Part Temperature Effects in Powder Bed Fusion Additive Manufacturing of Ti-6Al-4V

Submitted in partial fulfillment of the requirements for the degree of

Doctor of Philosophy

In

Mechanical Engineering

Brian A. Fisher

B.S. Mechanical Engineering, Brown University

M.S. Mechanical Engineering, Carnegie Mellon University

Carnegie Mellon University

Pittsburgh, PA

May, 2018

Dedication

To my wife, Elizabeth

Acknowledgements

I would like to thank my advisor and thesis committee chair, Professor Jack Beuth, for his guidance throughout my PhD. He has given me the push to move my research in new and exciting directions. I would also like to thank the other members of my committee, Professor Jonathan Malen, Professor Anthony Rollett, Professor Bryan Webler, and Dr. Brandon Lane for their advice and expertise.

I would like to acknowledge the financial support for this research, which came from four sources. The first is the National Institute of Standards and Technology (NIST) Measurement Science Innovation Program for Additive Manufacturing (MSAM) under project number GB131307, led by the University of Louisville. The second is the Office of Naval Research under project number N00014-14-1-0687. The third is the Pathways Program at NIST. The fourth is the NextManufacturing Center at Carnegie Mellon University (CMU). I would also like to acknowledge use of the Materials Characterization Facility at CMU supported by grant MCF-677785.

I would like to thank all of the members of the NIST Intelligent Systems Division. Without them, the work in this thesis on thermography would not have been possible. In particular, Dr. Brandon Lane was a tremendous resource for a myriad of topics and patiently explained (more than once) the fundamentals of thermal imaging to me. I would also like to thank Dr. Jarred Heigel, Dr. Ho Yeung, and Dr. Jason Fox for answering questions and assisting with experiments.

I would also like to thank my collaborators at the University of Texas at El Paso W.M. Keck Center for 3D Innovation for helping to make the work in this thesis on feedback control possible: Professor Ryan Wicker, Jorge Mireles, Shakerur Ridwan, and Israel Segura.

I would like to give special thanks to Luke Scime, and friend and discussion partner who kept me on my toes and pushed me to do my best work. His tireless efforts getting the additive manufacturing lab to where it is today made my time at CMU considerably easier and more productive. I would like to thank Dr. Sneha Narra for helping me set up and run the single bead experiments on the Arcam machine and act as a resource throughout my time at CMU. I would like to thank Nicholas Jones and Edgar Mendoza Jiminez for assisting with data collection and analysis. I would like to thank all of the students in Professor Beuth's lab group during my time at CMU, especially Dr. Jason Fox (again) and Dr. Zachary Francis for their guidance when I first started my PhD. I would like to thank Ross Cunningham and Recep Onler for their assistance and guidance with SEM imaging and light optical microscopy, respectively. I would like to thank Dr. Sandra DeVincent Wolf for her advice and insights.

This thesis is the culmination of a lifetime of encouragement. I could not have done it without my brother, Michael, acting as a role model and my parents, Suzanne and David, giving me the confidence and stability to pursue what I found interesting. Last, but in no way least, I would like to thank my wife, Elizabeth, for her love, support, and friendship throughout the entire PhD process (long hours, failed experiments and all).

Abstract

To ensure the widespread adoption of metal Additive Manufacturing (AM) processes, a complete understanding of the interactions between process variables is necessary. The process variables of beam power, beam velocity, deposition geometry, and beam diameter have been shown in prior works to have major effects on resultant melt pool and solidification characteristics, but this list is incomplete. Without accounting for part temperatures prior to deposition, unintended outcomes may result. In the current work, Ti-6Al-4V is studied in the Powder Bed Fusion (PBF) processes to gain an in-depth understanding of how part temperature interactions with other process variables affect physical properties of the process such as melt pool size and variability, part distortion, porosity, and microstructural characteristics.

This research is performed through a combination of finite element modelling, single melt track experiments, full part production, and in-situ monitoring in order to gain a full understanding of the underlying relationships between part temperature and part outcomes. In the Arcam Electron Beam Melting (EBM®) process, this knowledge is used to generate a feedback control strategy to constrain prior beta grain width to remain constant while part surface temperatures are allowed to vary. In the Laser Powder Bed Fusion (LPBF) process, deposition is investigated at elevated substrate temperatures and several findings show that unintended part temperature increases can lead to undesirable consequences while prescribed part temperature changes can increase the available processing window and allow for more uniform deposition. This work also shows that both global temperature changes due to substrate heating and local temperature changes due to the choice of scan strategy can be combined into one metric: the temperature encountered by the melt pool during deposition.

A combination of destructive and non-destructive characterization methods are utilized to understand and measure the changes to the melt pool and microstructural development that are seen during deposition. The feasibility of using a commercial high speed camera as a tool for thermography is characterized and the ability to discern cooling rates and thermal gradients within and surrounding the melt pool provide validation for trends in melt pool properties generated from simulations. This work provides a greater understanding of the role of part temperature during deposition and presents methodologies to account for the changes to the melt pool and resultant part due to both prescribed and unintended temperature changes during deposition.

Table of Contents

List of Tables

List of Figures

Chapter 1 – Introduction

1.1 Additive Manufacturing

Additive manufacturing (AM) is the process by which a part is built up with successive layers of material being added on top of previously deposited material, and has the ability to produce metal parts quickly, generate complex geometries, and keep scrap material to a minimum [1]. The increased design freedom afforded by AM over processes like forging and machining lends itself to a wide variety of applications, especially in the aerospace and medical device industries [2]. Of particular interest to industry is the ability to create conformal internal channels for enhanced heat transfer or mixing and lattice structures for mass reduction, heat transfer, and energy storage applications. Both of these design features are impossible or impractical to produce using traditional manufacturing techniques, but are easily accomplished using AM if the appropriate process and parameters are utilized.

All AM processes share some unique characteristics, and are a result of the fact that material is being added, not removed, to create a final part. The computer aided design (CAD) model for a part is generated, oriented, supported, and then sliced into layers or converted to G-code by software tailored to the particular process [3]. This data is then fed into the AM machine.

There are four main categories of metal AM processes. The first two are directed energy deposition (DED) processes: 1) Electron Beam Wire Feed (EBF3), and 2) Laser Powder Stream (LENS®). The last two are powder bed fusion (PBF) processes: 3) Electron Beam Powder Bed Fusion (EBM®), and 4) Laser Powder Bed Fusion (LPBF) [4]. Each of the 4 have particular strengths and weaknesses, but the majority of the differences between them stem from the area of process space that each inhabits. Figure 1-1 shows the area of process space that each process

inhabits, with arrows showing extended ranges. You can see that the directed energy deposition processes are low velocity processes with different power ranges, while the powder bed fusion processes are high velocity processes with generally different power ranges.

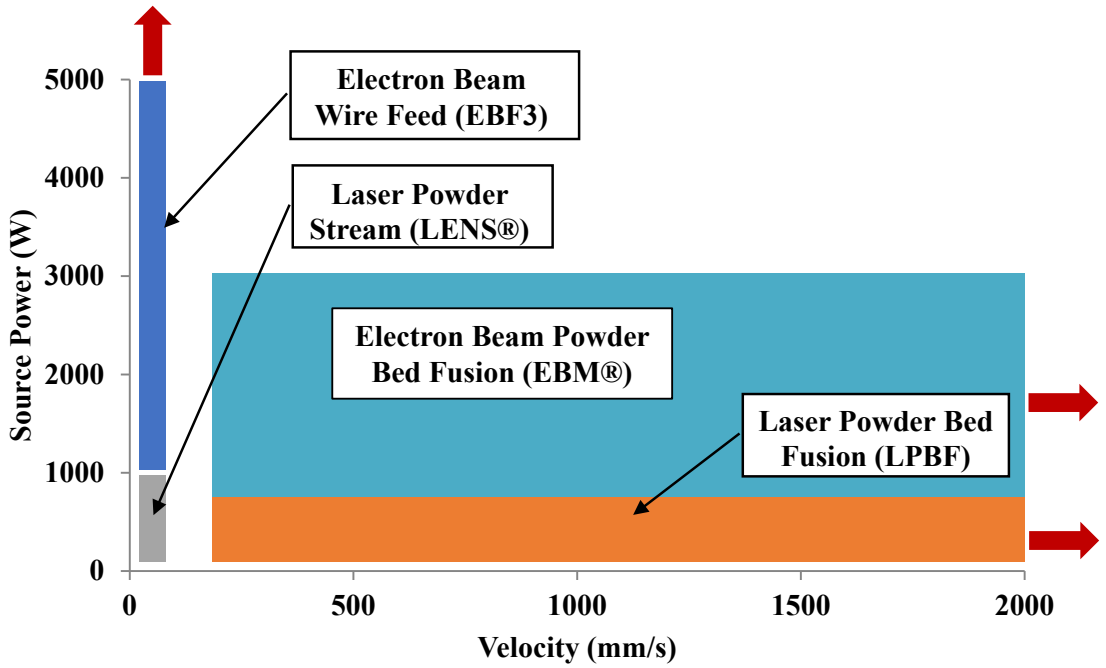

Figure 1-1: The four main categories of AM processes and the power and velocity space that each inhabits, adapted from Beuth et al. *[5]*.

All of these processes build a part by melting added material and substrate material into a molten pool, which is known as a melt pool. Several scan strategies can be employed, but the most common is what is known as a raster, where the melt pool forms parallel tracks to fill in a 2D slice of the part. The distance between parallel tracks is known as the hatch spacing, which must be matched to the melt pool dimensions and layer thickness in order to build dense parts [6].

The directed energy deposition processes are similar in their ability to add material to existing products with arbitrary geometries, and are therefore considered truly 3 dimensional processes. Due to the relatively low velocity range that each process inhabits, the melt pools are

usually large and the dimensional accuracy of the processes are not as good as the powder bed fusion processes [5], [7]. In the case of EBF3, the power is high and the added material is fed from a wire, allowing for high deposition rates and the production of large structures such as air-frame components [8]. The LENS process uses lower power and adds material by blowing powder into the melt pool, meaning that melt pools are smaller and material composition can be graded within a part [9].

The powder bed fusion (PBF) processes are generally at higher velocity and have smaller melt pools than the directed energy deposition processes. The PBF processes produce near-net shape components and have been used to produce highly complex shapes with minimal post processing. Material can only be built up in one axis, so material addition to existing products is limited to flat surfaces of parts that can fit in the machine's build tank. Powder bed fusion processes can therefore be considered '2.5' dimensional. The procedure for producing a part in the powder bed fusion processes is to spread powder over a baseplate using a rake, roller or blade, then use a heat source to fuse material in the layer that will become solid. The build platform is lowered by one layer thickness and the process is repeated until the part is complete. The part is then removed from the powder bed and post processed. Differences between the powder bed processes stem from the choice of heat source, and have significant consequences for each process.

The EBM process will generally have higher deposition rates, higher surface roughness, larger powder diameters and a higher part temperature [10]. Additionally, the use of an electron beam requires that the build chamber be at high vacuum, while the LPBF process generally uses an inert gas environment at standard pressure. A consequence of the high vacuum and high part bed temperature in the EBM process is that all of the powder in the build tank that is not melted is agglomerated (often referred to as 'sintered powder'). This sintered powder must then be

mechanically removed in a process similar to sand blasting[1]. There is no agglomeration of powder particles outside of the part in the LPBF process, so powders will flow freely and can more easily be removed from internal cavities. In addition, the elevated temperature in the EBM process produces parts with very little residual stress [11], while parts in the LPBF process generally have large residual stresses [12] that must be removed by heating in a furnace before the part can be removed from the build plate.

1.2 Motivation

The additive manufacturing process has historically been used in the production of prototype parts that give designers a 'looks like' model to aid in part production by more traditional manufacturing processes. The ability to produce complex shapes and iterate designs quickly is very useful. Recently however, the ability to produce parts of high enough quality, mechanical strength, and in sufficient volume using additive manufacturing has made this process viable for production as well as prototyping [2].

In order to use AM parts for production, an understanding of how parameter changes affect resultant part properties is critical. Two of the major process parameters for AM are power and velocity of the heat source. A thorough understanding of how these two parameters interact is vitally important and a large amount of research into these parameters has been done to date, but without taking into account part temperature during deposition, unintended build defects or microstructures may result.

[1] Instead of using sand or shot, the same powder material used for fabrication of parts is entrained in a high velocity air stream directed at the sintered powder. In this way, the sintered powder is broken up and can then be reused in future builds.

When producing AM parts the parameters used for melting must be closely controlled. Machine manufacturers, especially in the LPBF processes, try to print parts as quickly as possible to reduce overall build time and cost, meaning they use a high power and velocity with as wide a hatch spacing as possible during bulk melting without inducing large amounts of porosity in the part. This porosity, when found in areas of high stress, such as near the surface of a part, can act as crack propagation sites and lead to premature part failure, particularly under fatigue loading conditions [13]. Part failures are never good, but since the two major industries for additively manufactured parts are aerospace and medical devices, part failures are unacceptable. In order to avoid these issues, a greater understanding of how existing part temperature affects resultant part outcomes is needed.

This work focuses on the powder bed processes for a titanium alloy, Ti-6Al-4V (Ti64), commonly used in industry due to its high specific strength, good corrosion resistance, fatigue characteristics, and biocompatibility [14]. Powder bed processes are chosen because of their steady increase in popularity for complex part production [2]. In addition, these processes pose a large challenge with respect to repeatability and control of the process.

Part temperature is chosen as the focus of this research because of the lack of information available to users on its effects and interactions with other process parameters. It is important to characterize the response of a material to changes in temperature and understand the advantages and disadvantages of allowing or forcing that temperature to be outside the nominal ranges for the processes being studied. In addition, because of the variability seen in the powder bed processes, it is also important to be able to monitor parts on various time and size scales in order to ensure part quality and generate optimized process parameter sets.

1.3 Background

In order to ensure the widespread adoption of AM, the ability to control mechanical properties and qualify parts quickly is critical. Currently, machine manufacturers provide operators with only a few 'themes', or sets of process parameters, for an individual alloy [15], [16]. This constrains operators to create parts that have very specific properties that may not be ideal for the end use of a part. Systematic exploration of outcomes due to combinations of input parameters can be used to understand how to efficiently correlate input parameters to part outcomes and better utilize the full capabilities of an AM technology or a particular machine [5]. Machine manufacturers are beginning to understand this concept, and introducing add-on packages to allow users to manually input parameter modifications [16]. There is a lack of guidance from the machine manufacturers on optimal ways to change process parameters for specific applications, however, mostly because those interactions are unknown, not well characterized, or proprietary.

1.3.1 Ti-6Al-4V Microstructure

The material of interest in this research is Ti-6Al-4V (Ti64), which is a two phase, α-β titanium alloy that is commonly used in industry due to its high specific strength, good corrosion resistance, fatigue characteristics, and biocompatibility [1]. Ti64 solidifies as a fully beta (BCC) microstructure. Once the temperature drops below the beta transition temperature of around 975 °C [14], alpha (HCP) begins to be a stable phase. The aluminum stabilizes the alpha phase while the vanadium stabilizes the beta phase. Many different grain morphologies are possible depending on the local thermal gradients and cooling rates at and below solidification [17], [18].

If the cooling rate from the beta transus temperature of roughly 995 ˚C through the martensite finish temperature of roughly 725 °C [17] is too rapid, it is possible to form non-

equilibrium phases. At cooling rates of approximately 20-410 °C/s, an alpha phase called massive alpha (α_m) is formed [18]. Massive alpha is characterized by an almost diffusionless transformation of the original beta phase into the newly formed alpha phase, but is more globular in morphology [19] than the other commonly seen non-equilibrium phase, α' martensite. α' is also a diffusionless transformation from the original beta phase into the newly formed alpha phase, but has a strained lattice and is characterized by long orthogonally oriented plates that are acicular in nature [18], and has been observed at cooling rates at low as 18-20 °C/s and steadily increases in phase percentage as cooling rates are increased [17], [18]. α' martensite is generally what is seen as the as-build condition in the LPBF process.

Assuming that the cooling rate is slow enough, as the temperature drops below the beta transus temperature, alpha grains nucleate at the beta grain boundaries. These alpha grains grow along one of the prior beta grain crystallographic orientations and look needle like [14]. The result of this growth can be what is referred to as Widmanstatten, or "basket-weave" microstructure, which has a significantly higher percentage of alpha by volume [14]. This microstructure is generally representative of what is seen in the EBM process. This is only one of several grain morphologies seen in AM and welding processes [20], [21]. Another is colony alpha, which is also a diffusion based transformation and also has needle like alpha grains, but is characterized by alpha grains oriented in the same direction [14].

Most of the mechanical properties of Ti64 are mainly determined by the alpha grain size and morphology, including yield strength, tensile strength, ductility, and fatigue strength [14], [17], [22]. The prior beta grain size does become important for toughness [14], [23] and acts as a limit to the size of the alpha lamellae colonies [22]. α' and α_m are generally considered harder and less ductile than the equilibrium α-β microstructure [24].

1.3.2 Process Modelling

The two main avenues for understanding AM processes are modelling and experimentation. Research into AM modelling spans many different temporal and spatial scales. The complexity of the models employed is also varied. The least computationally intensive models are conduction based, analytical heat transfer solutions to a moving heat source. Rosenthal [25] utilized a point heat source, which created infinite temperature at the point of heat application. Eagar and Tsai [26] increased the accuracy of the model by allowing for a distributed heat source, but neither of these models allow for temperature dependent material properties or the addition of latent heat of fusion. These omissions can cause large deviations from experimental values, as Ti64 material properties change significantly between room temperature and melting temperature [27]–[29]. Because of the introduction of potentially large errors, these analytical models will not be used in this work.

Though computationally more expensive, finite element simulations of the melt pool (or molten material at any given time) provide considerably better agreement with experimental observations [30][31]. Extensive work has been done on this topic. The low end in terms of computing power are simple heat flow models that are fast and efficient to run for an entire part [32], [33]. These models can do a good job of simulating residual stress and part warpage, but do not give sufficient detail about material/heat source interaction, melt pool level phenomena, or temperature history at or near solidification. Intermediate models can give information about temperature history at solidification, but do not include the physical phenomena occurring within the melt pool itself, and so do not predict some important flaw mechanisms, such as keyholing [34]–[36] and balling [37].

The highest complexity models currently employed rely on particle level simulations that include fluid flows, solid/liquid and liquid/vapor interactions, and have resolution down to the order of single microns [38]–[41]. This level of detail allows the model to predict a great deal of physical phenomena about the melt pool, such as keyholing and spatter formation, but can only be practically employed for a very limited set of cases and only for a very small physical size [40]. All of these methods require some form of validation in order to be considered accurate, and this is generally accomplished with experimentation on actual AM machines. For a more complete list of the types of modelling work that has been done in the field, the reader is directed to the review papers by Seufzer [42] and DebRoy et al. [7].

This work utilizes intermediate complexity simulations that incorporate temperature dependent properties but do not include fluid flows within the melt pool in order to maintain adequate model accuracy without requiring excessive time or computing resources. As much as is practical, the simulations are validated with experimental results.

1.3.3 Effects of Process Parameters on Build Quality

Process mapping is a general framework for determining how AM processes behave throughout their useful ranges. The major process parameters are beam power, beam velocity, existing part temperature, beam spot size, layer thickness, and deposition geometry [5]. Early work into how process parameters affect resultant part outcomes utilizing the process mapping approach focused on residual stress, with research into other outcomes such as melt pool size and thermal gradients following [43]–[47]. There has been work over the past several years into how parameter changes affect melt pool size and resultant microstructure in the EBF3, and EBM processes [48], [49]. This approach has been extended to the LPBF process [37], [50], [51]. These concepts have

been scaled from single melt pools up to bulky parts, and show that there is continuity between the relationships seen at different levels of complexity. The common theme in all of this work is that simulation results inform a limited set of experiments, resulting in a greater understanding of a particular underlying physics. Recent results utilizing this method have shown that standard Arcam themes can be used to control microstructure in Ti64 bulky parts [52] and changing processing parameters in the EBM and LPBF processes can reduce porosity in Ti64 specimens [53], [54]. Also, adverse melt pool phenomena such as keyholing, lack of fusion, and balling can be mitigated by changes to the heat source diameter and profile [31]. The effect of temperature on the melt pool and resultant parts, however, has not been well treated in the existing literature.

A great deal of work in this area has also been done utilizing methods other than the process mapping approach, but again the effect of temperature is not well characterized in prior work. Defect generation and melt pool size has been characterized by Gong et al. [50], [55] for the powder bed fusion processes for Ti64 and found regions of process space where good material properties will likely be found based on beam power, beam velocity, hatch spacing, and beam diameter. Ladewig et al. studied the influence of shielding gas flow in the LPBF process and found that a weld plume above the melt pool and redistribution of material can change the local deposition conditions, affecting melt pool size and shape [56]. Fabbro et al. found that differences in ambient pressure affect the penetration depth of a laser during welding [57]. Kobryn et al. found that different processing conditions lead to different microstructural development for Ti64 in the laser powder stream process [58]. Puebla et al. found that increased scan velocity in the EBM process generated a finer α grain thickness, and that the top portion of each specimen had a courser α grain thickness than the bottom [59] most likely due to slower cooling from the beta transus temperature due to higher part temperatures. Klassen et al. found that varying process parameters

in the EBM process had a large effect on melt pool depth and the amount of vaporized material [60]. In addition, various methods for microstructural control have been presented, including variable scan strategies [61]–[63], build orientations [11], and part geometries [64].

1.3.4 Effects of Part Temperature on Build Quality

The existing temperature of a part before deposition can greatly influence the induced distortion (due to residual stress) in that part. It has been shown that increasing the heat input to a weld can lead to buckling of an I beam section due to an increased area of thermal contraction upon cooling [65] and preheating parts before welding can reduce distortion [66], [67]. The effects of existing part temperatures on residual stress have also been explored in additive manufacturing processes. Research by Klingbeil el al. [68] and Dai and Shaw [69] both found that an increase in substrate temperature will reduce distortion. Vasinonta et al. found that residual stress reduction in 316L stainless steel was accomplished by increases in substrate temperature due to thermal gradient and yield stress reductions [70]. Denlinger et al. found that adding dwell time between layers to allow for additional cooling in a laser DED process reduced distortion for IN625 specimens, but increased distortion for Ti64 specimens [71]. One explanation for this difference is the high temperature α-β phase transformation that happens at elevated temperature [72]. Dunbar et al. found that Inconel 718 distorted much more than Ti64 for the same conditions [72], again highlighting the difference in distortion of the two alloys. With the varying literature on distortion, one thing that does become clear is that an increase in initial substrate temperature will decrease part distortion due to a reduction in thermal gradients within the part.

Existing part temperature can also affect microstructures. Prior work in the EBM process has found a graded microstructure [73], [74], as well as graded mechanical properties [74], through

the height of a Ti64 build. Maintaining constant part temperature throughout a build has been suggested as a means of controlling microstructure [75], [76]. The basis for this microstructural control strategy is the grain growth equation [77, pp. 139–143]:

Equation 1

$$D^2 = D_0^2 + Kt$$

Where D is the final grain size, D_0 is the initial grain size, K is a constant dependent on temperature and boundary mobility activation energy (which will be material dependent), and t is time. This equation was derived for pure metals, but has been shown to hold true for Ti64 [78], and means that grain growth is faster as temperature is increased or as cooling rate is slowed. The authors investigated whether keeping the surface temperature of the build constant would keep the grain growth constant, and did so by changing melting parameters. While changing the melting parameters may keep the surface temperature constant, the change in melting parameters may also affect the cooling rate from solidification. Without accounting for this change in cooling rate, the method is incomplete. The author has also identified a lack of research with respect to the effects of part temperature during production in the LPBF process.

Characterization of process outcomes due to the effects of scan strategy have also been investigated. Because the scan strategy affects the local temperature fields around a melt pool, changing the scan strategy will change those temperature fields. Criales et al. studied scan strategies for nickel alloy 625 in the LPBF process and found that the melt pool is constantly changing size as the laser scans a single melt track (single bead) [79]. Tammas-Williams et al. found a higher density of porosity in EBM processed Ti64 at the edge of melt tracks [80]. Groeber et al. [81] found that the maximum substrate temperature encountered by a melt pool during the generation of a raster stripe is inset from the stripe boundary just after a beam turn around. While a great deal of work has been conducted that deals with part temperature, a comprehensive

understanding of the effect of part temperature on resultant part properties is still lacking, especially for Ti64.

1.3.5 Defect Formation Mechanisms

In order to reduce production time while maintaining precision, it is advantageous to produce parts with high power and velocity and with large hatch spacings [82]. This melt strategy has limits due to two defect formation mechanisms: keyholing and lack of fusion. Lack of fusion occurs when there is insufficient overlap between melt pools to fully melt all of the powder, generating irregularly shaped voids within the part. In addition, if the melt pool is too long relative to its width, liquid instabilities can cause the top surface of a melt pool to become unstable and try to form spheres, known as 'balling' [31], [37], [83], [84]. This phenomenon may induce porosity due to an uneven surface for subsequent powder layers. If the hatch spacing and/or powder layer thickness is not well matched to the melt pool size or the melt pool variability, areas of unmelted powder (lack of fusion) within a part can be produced. Tang et al. has shown that the melt pool overlap is a key consideration for the generation of fully dense parts [6].

If the energy density of the heat source is too high, keyhole porosity can be induced in parts [53], [54]. The term keyholing refers to the creation of a cavity under the beam spot that allows for considerably greater penetration of the laser or electron beam and an elongated cross sectional area of the melt pool [38]. Keyholing occurs when the depth of a melt pool is more than half of its width and signifies that surface tension and recoil pressure are starting to become significant factors in melt pool cross sectional shape [85]–[87]. Prior work has shown that keyholing is a specific phenomenon that exhibits a clear threshold based on the formation of a vapor depression under the heat source [88]. Keyholing can be detrimental because of the increased probability of

getting voids (pores) in the solidified material [53], [89], increased variability in melt pool dimensions [90], [91], and loss of alloying elements [90], [92].

Without an understanding of the effect of temperature on the melt pool size and shape, it is possible to induce defects in resultant parts by unintentionally changing the temperature encountered by the melt pool.

1.3.6 Thermal Monitoring

Direct monitoring of the deposition process can be a way to bridge the gap between modelling and experimentation with the goal of gaining model-level predictive ability while simultaneously incorporating all of the complexity of the actual process. There are two main scales on which this can be done: the build area scale and the melt pool scale. There is a great deal of information that can be gleaned from monitoring the entire build surface. This would mean looking at both the part surface and surrounding powder bed. In this way, temperature changes throughout the height of a build can be measured and tied back to resultant part properties. Infrared (IR) imaging systems designed to look at the build surface have been developed for the EBM process by Schwerdtfeger et al. [93], Dinwiddie et al. [94] and Rodriguez et al. [75]. Each developed a mechanism to shield the viewport from metallization, which occurs due to evaporation of metal during melting [75], [93], [94].

Spatial resolution is a concern when monitoring the entire build surface, however. More targeted monitoring is necessary to see what is occurring at the melt pool scale, which will be a very small fraction of the entire build surface at any given time. There is a large amount of prior research in this area from laser welding and other relatively low speed processes [95]–[98]. A review article on process monitoring for welding applications was completed by You et al. [99].

High speed melt pool monitoring in powder bed processes has also been investigated. Price et al. developed a NIR imaging system to look at the melt pool in the EBM machine [100]. Pioneering work in the LPBF process has been completed in Dr. Kruth's lab at the University of Leuven. This work utilized a custom built LPBF machine and optics that allowed for monitoring along the path of the laser (co-axial monitoring) [101]–[104], which gives a Lagrangian view of the melt pool. More recently, the National Institute for Standards and Technology (NIST) has developed a custom built LPBF machine with coaxial monitoring capabilities [105]–[107] and have incorporated both thermal and other sensors to gather data about the melt pool and solidification process [108]. Yadroitsev et al. also viewed the melt pool coaxially and was able to obtain temperatures within the melt pool [109]. A review paper on process defects and monitoring in powder bed fusion processes has been completed by Grasso et al. [110].

The hardware setups for coaxial monitoring require integration into the laser system, and are not practical to add to existing LPBF machines that are not designed to accept them. The other option for positioning sensors is to have them stationary, and allow the melt pool to pass by the fixed field of view (FOV) [111]. This monitoring strategy gives an Eulerian view of the melt pool and can be more easily incorporated into existing LPBF machines. Work by Heigel and Lane utilizing a fixed FOV infrared camera has shown that melt pool dimensions can be determined from solidification at the tail of the melt pool, that melt pool dimensions change drastically with successive melt tracks, and that powder does not affect the cooling of the melt pool for IN625 [112], [113].

By modelling of the laser interaction with a titanium substrate, Cho et al. found that significant evaporation of material can be expected for even relatively shallow melt pools, with the amount of evaporation increasing with increasing power density of the heat source [87]. The

maximum temperature under the heat source was limited to roughly 2725 – 2900 ˚C by the faster than exponential rise in vapor pressure of the metal above 2500 ˚C [87]. While the maximum temperatures did not quite reach the boiling point of titanium (3289 ˚C [87]), they were significantly closer to the boiling point of the material than the melting point (1680 ° C [87]).

The melt pool cross sectional shapes in Cho et al. [87] were relatively shallow, so it is likely that the maximum temperatures encountered for these melt pools is lower than what would be found in the vapor cavity of keyholing melt pools. Therefore, the maximum temperature for keyholing melt pools is likely very close to the boiling point of the alloy. The high liquid temperatures expected under the heat source and the hot vapor being ejected from the melt pool may obscure the relatively low temperature features like solidification due to the significantly higher thermal emission from the hottest part of the melt pool. These effects must be considered in order to understand what is actually being monitored when viewing a melt pool.

Kruth et al. showed how melt pools can change size when different substrate conditions are encountered [104], but a systematic study of how melt pool emission changes throughout available processing space has not yet been completed for Ti64 to the author's knowledge. Looking at the actual temperature of different parts of the melt pool during processing is valuable, but the ability to convert between camera signals and actual temperature has proven difficult in the LPBF process due to uncertainty about emissivity and plume formation, among other factors [36], [75], [111]. The difficulty in extracting information from melt pool monitoring is one reason for the slow adoption of feedback control strategies targeted at the melt pool.

1.3.7 Process Monitoring

Significant information about the build process can be gleaned from sensors that do not utilize thermal data. Scharowsky et al. used a high speed camera and laser illumination to characterize melt pool dynamics in the EBM process [114]. Bidare et al. was able to show denudation of powder and plume formation during LPBF using laser illumination and Schlieren imaging [115], [116]. Repossini et al. used a high speed camera to characterize the spatter signature of different process parameters in LPBF [117]. Several flaw detection methods utilizing powder bed images have also been employed [118], [119]. For a more complete list of the types of monitoring work that has been done in the field, the reader is directed to the review papers by Purtonen et al. [120], Tapia et al. [121], and Everton et al. [122].

It is clear that there are many ways that monitoring can detect inconsistencies in the process that may lead to flaws in the final part. Powder bed machine manufacturers are starting to realize this and offer monitoring hardware and software packages with their commercial machines due to the push from customers to have more information about how well the process is being controlled. Arcam has instituted LayerQam™ [123] in their newest machines and EOS has instituted EOSTATE™ [124], [125]. Both of these systems try to give the operator the tools to decide if a build was successful, but don't provide very much information about what the data that is being presented means. In order to gain a real understanding of how the process is being affected, there has to be a way to tie the sensor data back to physical attributes of the process in terms that can be easily incorporated into control strategies to mitigate undesirable outcomes.

1.3.8 Determining Temperature from Thermal Data

Since the top surface of powder bed processes are always changing due to material addition, it is necessary to use non-contact temperature measurements to obtain surface temperatures in-situ. There are a wide range of temperatures that can be encountered in powder bed processes, from room temperature up to the vaporization temperature of the alloy being studied [40], [87]. There is also a wide range of time scales over which temperatures are changing. Melt pool dynamics are on the order of microseconds [40] and temperature changes within a part (i.e. through its build height) are on the order of hours or days [120]. These constraints make it necessary to have different sensors that are tailored for looking at specific aspects of the process.

Non-contact temperature measurements rely on measuring the light emission from the target. If the target is emitting light as if it is a black body[2], its spectral radiance would be characterized by a form of Plank's Law and would be dependent on wavelength and temperature according to Equation 2 [126]:

Equation 2

$$L_\lambda(T) = \frac{c_1}{\lambda^5}\frac{1}{[\exp\left(\frac{c_2}{\lambda T}\right) - 1]}$$

where $L_\lambda(T)$ is spectral radiance measured in W/(sr*m^2*μm), c_1 and c_2 are the first and second radiation constants, respectively, λ is wavelength in μm, and T is temperature in K. When looking for the spectral radiance over a finite wavelength range, which is appropriate for thermal monitoring applications, Equation 2 can be integrated over the wavelength range of interest. Actual materials do not radiate as a black body, so a wavelength dependent emissivity (ε_λ) must be

[2] A black body is an idealized construct in which a surface emits the maximum possible amount of radiation according to Plank's law and absorbs all incident radiation. This means that a surface has an emissivity and an absorptivity of 1. In practice, no surface has an emissivity of 1, but it is possible to approach this condition using a black body source, which uses a cavity with a relatively small orifice to increase the radiance to mimic an emissivity approaching 1 [126].

included. It is often the case that the imaging system is not equally sensitive to all wavelengths within its range, so a weighting (w_λ) based on sensitivity must also be included. The ideal sensor response of an imaging system (S) should therefore be proportional to the spectral radiance as described in Equation 3 [127].

Equation 3

$$S \propto \int w_\lambda * \varepsilon_\lambda * L_\lambda(T)\, d\lambda + \beta$$

where β is an offset representing the noise floor of the detector.

One consequence of Equation 3 is that only certain temperature ranges are well suited to measurement by given camera detector chemistries because those chemistries are only able to detect certain wavelength ranges of light [128]. As the wavelength range used to measure temperature is shifted to shorter wavelengths, the minimum measureable temperature increases and the calibration curve for a given temperature range becomes steeper. The practical result of this is that temperatures below roughly 1000 °C brightness temperature[3] are not well suited to silicon based detectors, and infrared cameras should be used[4].

In a real thermal monitoring system, there will be optical filters, losses and aberrations in lenses, camera detector variability and non-linearity, absorption due to site glasses and participating atmosphere, etc. These factors will make the actual curve of signal value vs temperature reading specific to the particular camera setup and material being viewed. When all of these practical considerations are taken into account, an equation proposed by Sakuma and

[3] Brightness temperature refers to the temperature measured by a sensor that is calibrated to an emissivity of 1. This means that the measured temperature is as low as it could possibly be, since a material with an emissivity of 1 would emit the maximum possible amount of thermal radiation for a given temperature. Any material with an emissivity less than 1 would have to be at a higher temperature in order to generate the same amount of thermal radiation.

[4] The high speed camera used in this work has a high light sensitivity and the lower bound of the calibration curve generated as part of Chapter 6 is 1150 °C brightness temperature. While it is possible to lower the temperature range from what is presented in this thesis, infrared cameras are much better suited to detecting temperature ranges below 1000 °C brightness temperature.

Hattori (Equation 4) has been shown to fit a calibration curve to camera signal when viewing a black body source with a narrow wavelength band using a silicon detector [129].

Equation 4

$$F(T) = \frac{C}{\exp\left[\frac{c_2}{AT + B}\right] - 1}$$

where A, B, and C are fit parameters, and c_2 is the second radiation constant. This equation is applicable for a range of thermal monitoring applications, but becomes less accurate when the temperature range is large or the wavelength range of the detector's spectral responsivity is wide [130]. The calibration of the camera system in Chapter 6 shows that Equation 4 is an appropriate equation for the calibration curve of the high speed camera system used in this research. A discussion of the effect of emissivity on the detection of true temperature is presented in section 6.2.5.

1.4 Organization

There is a gap in the literature with respect to how existing part temperature affects solidification conditions and microstructural development of additively manufactured parts. Additionally, the connection between global part temperature (the temperature of the part away from material deposition) and local part temperature (dominated by scan strategy) has not been thoroughly investigated. This research focuses on how power, velocity, and part (substrate) temperature affect melt pool dimensions, solidification cooling rates, and microstructure for Ti64 to help fill the identified knowledge gaps. Thermal simulation, experimentation on EBM and LPBF machines, and thermal monitoring of the process are used.

This thesis consists of 7 chapters. The first chapter introduces additive manufacturing, provides motivation for the thesis, and gives background related to relevant research that has been completed in the areas of study presented in this thesis.

Chapter 2 characterizes the temperatures that can be expected during an EBM build and their implications for monitoring applications. Simulation and experiment is used to explore the relationship between existing part temperature, melt pool dimensions, and solidification cooling rates. This relationship is then used to generate a feedback control algorithm designed to keep solidification cooling rates constant while temperatures change. The algorithm is tested by integrating it into an existing thermal camera system at the University of Texas at El Paso and automating the system.

Chapter 3 explores the relationship between existing part temperature and melt pool dimensions in the LPBF process with the goal of successfully building parts at elevated temperatures. An insert into the EOS M290 at CMU is constructed in order to heat a substrate to elevated temperatures and single beads are deposited and characterized. Experimental results are compared to model simulations to gain a greater understanding of the trends seen in the data and those trends are used as the basis for further study in subsequent chapters of this thesis. Experiments on the EOS M290 at CMU and a prototype LPBF machine at NIST are also used as the basis for further work in subsequent chapters of this thesis.

Chapter 4 utilizes the work done in Chapter 3 to produce parts at elevated temperature. Bulky parts are characterized with respect to defect generation, distortion (part warpage), and microstructural development. Finally an industry relevant geometry is fabricated at both standard conditions and at elevated temperatures to validate the analysis.

Chapter 5 characterizes a current scan strategy used in LPBF processes. Temperature fields utilizing that scan strategy are simulated and a methodology for determining optimized parameters is developed with the goal of keeping melt pool cross sectional area more consistent. A case study developing parameters for the EOS M290 at CMU is then presented.

Chapter 6 characterizes the thermal emissions that can be acquired from a commercially available high speed camera utilizing two different LPBF machines and monitoring strategies. A correlation between total in-band thermal emission and melt pool cross sectional area is presented. Several methodologies for determining melt pool dimensions are presented and applied to the determination of melt pool dimensions for Ti64 in LPBF processes throughout power, velocity, and temperature space. An understanding of the thermal emission and melt pool dimension changes during a raster are explored based on this methodology and compared to model predictions from Chapter 5.

Finally, Chapter 7 presents conclusions and major contributions from the research in this thesis as well as recommendations for future work.

Chapter 2 - Solidification Microstructure Control in Electron Beam Melting of Ti-6Al-4V [5]

2.1 Background and Overview

The major manufacturer of electron beam powder bed fusion additive manufacturing machines is Arcam AB (Mölndal, Sweden) and has commercialized the technology under the term Electron Beam Melting (EBM®). To understand how well the EBM process is currently controlled, it is important to understand how it works. The internals of an Arcam EBM machine are shown in Figure 2-1. The EBM process begins by leveling a start plate on top of a bed of powder. A vacuum is then pulled within the build chamber and a very rapidly travelling electron beam is used to heat the plate to roughly 750 °C for Ti64. To create the beam, electrons are released by a heated filament, accelerated through a voltage potential, distributed symmetrically, focused, and directed by a series of electromagnetic lenses [123]. A thermocouple is positioned below the start plate to monitor build temperatures. The elevated temperature lightly agglomerates (sinters) the powder surrounding the start plate, fixing it in place throughout the build and increasing the electrical conductivity of the powders to the point where the incident electrons can efficiently flow to the machine's ground. A thin layer of powder is then spread across the surface of the build plate using a metal rake and agglomerated with the same rapid travel of the electron beam [123]. The electron beam is then used to selectively melt the powder in the areas dictated by the original CAD model. The build platform is lowered into the build tank by a specified layer thickness and more powder is spread. For the Arcam process, the layer thickness can be between 50 and 100 microns

[5] Sections of this chapter have been published in: B. A. Fisher, J. Mireles, S. Ridwan, R. B. Wicker, and J. Beuth, "Consequences of Part Temperature Variability in Electron Beam Melting of Ti-6Al-4V," *JOM*, 2017. DOI: 10.1007/s11837-017-2597-y

[131]. A heat shield is used as a sacrificial surface to reduce the deposition of metal vapor on other surfaces within the build chamber.

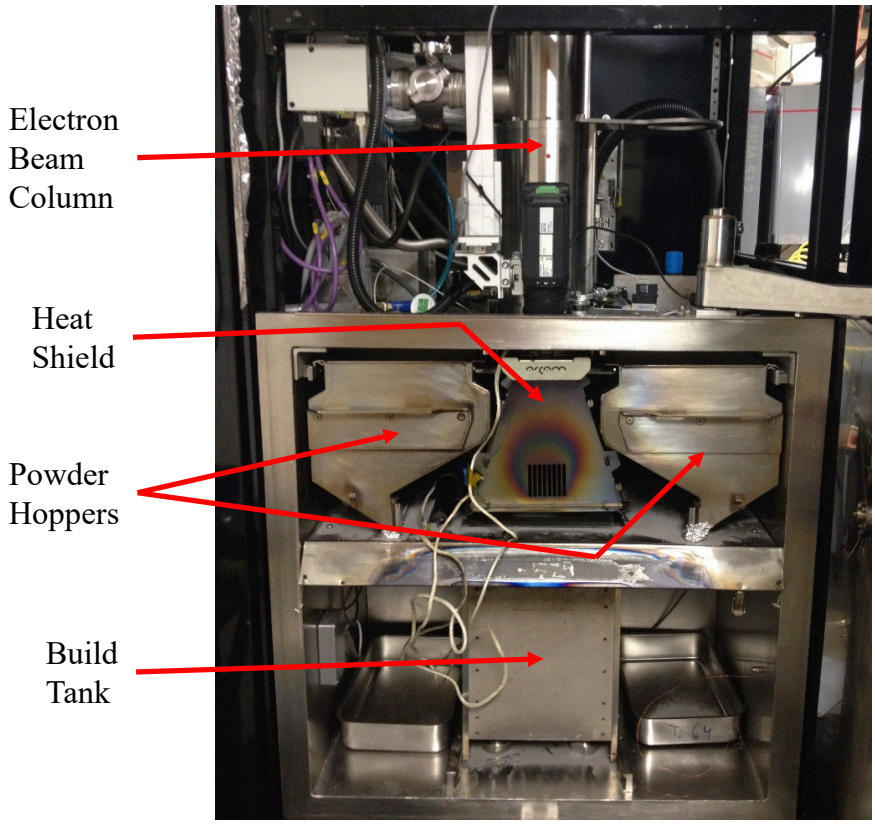

Figure 2-1: The internals of an Arcam A2 machine with select components labeled.

One major issue that has been investigated in the EBM process is temperature changes during a build [73], [74], [132]. In particular, excess temperatures can cause grain growth and 'part swelling' [63], [94], [133] in parts if not properly accounted for. In this chapter, the surface temperature history of industry relevant components is investigated for the EBM process using infrared thermography. Additionally, the melt pool area and solidification cooling rate response of Ti64 is investigated as temperature is changed using both finite element simulations and single bead experiments. This information is then used in the generation of a feedback control system on an Arcam A2 machine in order to constrain prior beta grain widths to be constant throughout the

height of a build. Build quality is assessed with respect to prior beta grain width (quantitatively) and part swelling (qualitatively).

Prior beta grain widths are used as the microstructural feature that the feedback control system holds constant because beta grains are produced at solidification and are less susceptible to changes due to the subsequent heating and elevated part temperature found during the EBM® process than other microstructural features of Ti64 [20]. This makes prior beta grains both a good metric for conditions at solidification as well as of interest to the AM community.

2.2 Methods

2.2.1 Process Mapping

Process Mapping is a method to determine the relationship between process parameters and process outcomes [5]. In this chapter, the process parameters of interest are power, velocity, and substrate temperature while the outcomes are melt pool cross sectional area and solidification cooling rate. To create a process map with curves of constant quantity of interest (melt pool area, solidification cooling rate, etc.), a grid of values across power and velocity space is generated from simulations of the melt pool. Experiments are then completed to validate the simulations. The initial parameter combinations (parameter sets) used may not fall directly on curves of constant quantity of interest, in which case the values at those parameter sets are piecewise linearly interpolated in order to find those curves. Prior research has shown that an effective absorptivity[6] is generally necessary to equate simulations to experiments [30], [31], [134]. The absorptivity of

[6] Effective absorptivity should change with the actual absorptivity, but is solely determined by the ratio of power used in simulations (section 2.2.2) to the power of the beam in experiments, and is adjusted until both melt pool cross sectional areas match. This means that the effective absorptivity value also includes all of the physics that is not included in simulations, but is not necessarily representative of the actual absorptivity.

the electron beam is considered agnostic to melt pool size[7] and the work in this chapter assumes a constant absorptivity of 85%, which is in the range found in literature for electron beam melting [30], [134], [135].

2.2.2 Finite Element Modelling

Finite Element simulations of the melt pool that run using the software package ABAQUS, originally developed by Soylemez [49] and refined by Fox [134] and Francis [31], have been modified and extended in this work to understand the relationship between changes in part temperature, melt pool cross sectional area, and solidification cooling rate over a wide range of process parameters. The model is based on conduction into the substrate and utilizes temperature-dependent material properties (see Appendix 7) [27]–[29]. Heat loss due to surface convection is not considered in the model since it has been shown to be insignificant compared to conduction [134], [136]. Convection within the melt pool is also excluded from the analysis, though it may have a small effect on melt pool dimensions [134], due to the uncertainty in the appropriate means of adding this effect to a model that does not include fluid flow. For simulations of the melt pool, radiation is not considered because research has shown that radiation on the model surface has little effect on melt pool size and shape [31], [134], [136].

Figure 2-2.A shows an example melt pool from the simulations conducted in this work. The heat source is modelled as a circular heat flux with a top hat distribution and a diameter equal to roughly 2/3 of the expected melt pool width, yielding simulations that run quickly while not

[7] The electron beam transfers its energy to a material via momentum transfer. While there is a difference in the percentage of momentum transfer (considered absorptivity in this work) based on the accelerating voltage of the electrons and the material's atomic number (due to the likelihood of scattering events), there should not be a difference between different power beams or different melt pool sizes for the same material since the accelerating voltage is constant [135], [190].

losing resolution with respect to solidification cooling rates or melt pool lengths and areas [31]. Three dimensional, 8 node linear brick elements (type DC3D8) are used and the melt pool always has a minimum of 10 elements across the width and through the depth to ensure convergence of the model [134]. The white arrow and white shaded area shows where the heat flux is applied, the yellow arrow shows travel direction (the positive *X* direction), the red dashed lines are the outline of maximum cross sectional area (in the Y-Z plane), and the green circle shows where cooling rates are extracted from the tail of the melt pool. The model is symmetric about the X-Z plane so the second half of the melt pool is replaced with an adiabatic boundary condition. The mesh is finest close to the melt pool to increase accuracy while keeping computation time to a minimum. Figure 2-2.C shows a cut view of the model at the point of maximum area and equates to the red dashed lines in Figure 2-2.A. Color in Figure 2-2.A and C represents the material above the solidus temperature, while dark grey represents fully solidified material.

The tail of the melt pool can be seen in Figure 2-2.B and is used to extract thermal gradients because the longest length scales, and therefore the greatest resolution given a constant element size, will be found there. These thermal gradients are then converted into cooling rates using the beam travel velocity. The color scheme for this picture is different from the other two in order to highlight the solidification region. The fully liquid region (above the liquidus temperature) is represented as light grey, the fully solid region (below the solidus temperature) is represented as dark grey, and the color in between shows the solidification region. The length along the top surface of the model is measured and converted to cooling rate using Equation 5.

Equation 5

$$CR = (V * (T_l - T_s))/D$$

Where *CR* is cooling rate (°C/s), *V* is beam velocity (m/s), *D* is solidification distance (m), and T_l and T_s are liquidus and solidus temperature (°C), respectively.

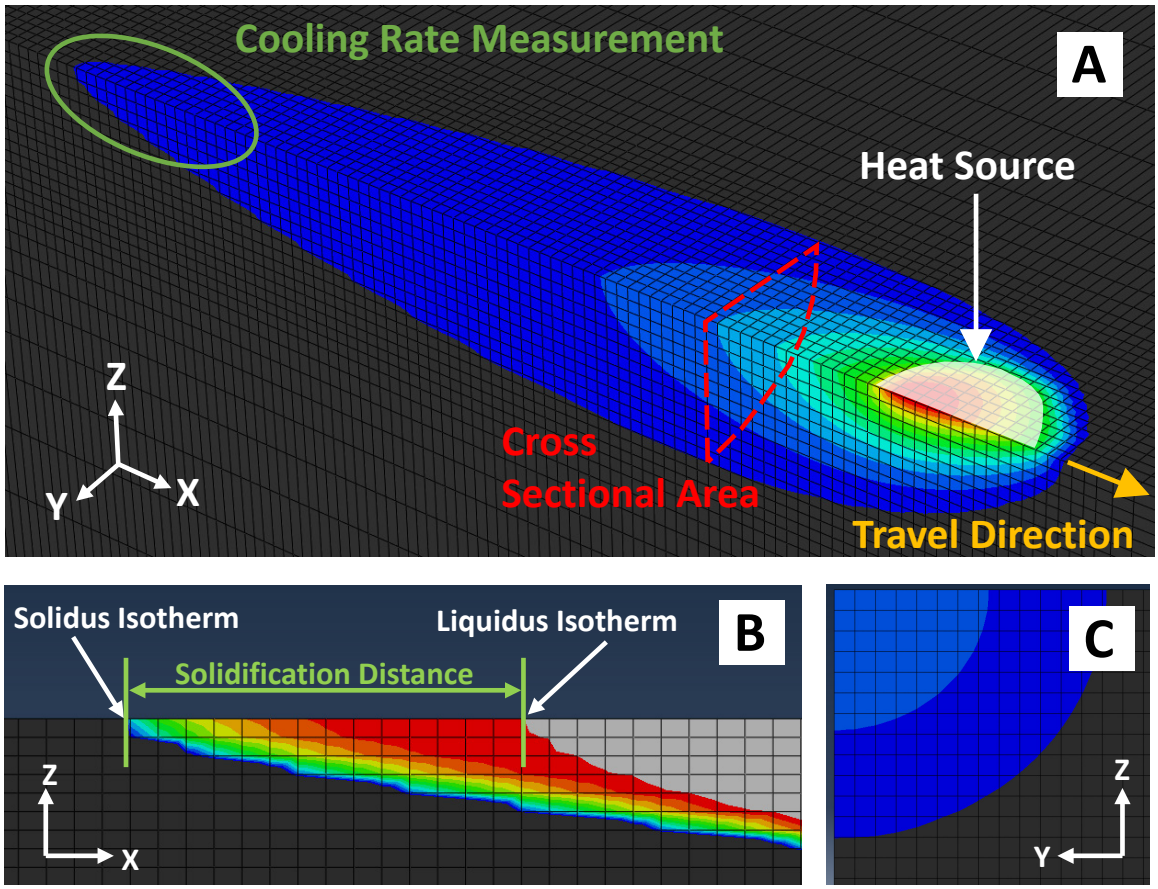

Figure 2-2: A) A sample finite element simulation of a melt pool. B) The tail of the melt pool showing the area between the liquidus and solidus temperatures. C) A view of the melt pool cross sectional area.

2.2.3 Single Bead Experiments

Single beads are deposited in an Arcam S12 (software version 3.2.132) machine at Carnegie Mellon University (CMU) on a series of 0.25 inch thick rolled Ti64 plates. The Arcam S12 and A2 machines are functionally very similar, though the A2 is a newer model. An example plate after deposition of single beads can be seen in Figure 2-3. A range of power and velocity combinations is used to generate a broad range of melt pool sizes. Each power-velocity combination is deposited at each of four substrate temperatures. In order to set the substrate temperature, the beam is used to heat the plate until the temperature is above the target temperature

by at least 50 ˚C as measured by a thermocouple welded to the center of the bottom of the plate. The beam is then turned off and the single beads are completed when the thermocouple temperature crosses the desired temperature. In all cases, the temperature read by the thermocouple is within 10 ˚C of the target temperature at the time of deposition. In order to eliminate the effect of local heating on each single bead, the melt order is designed to give at least 5 seconds between the deposition of adjacent single beads.

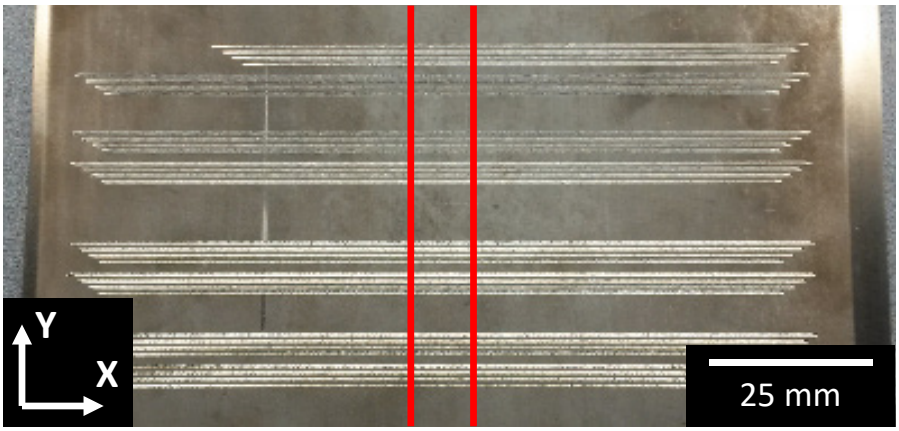

Figure 2-3: One of the plates from the single bead experiments completed in this chapter.

The power-velocity-temperature combinations along with the corresponding melt pool cross sectional areas can be found in Appendix 1. The single beads are cross sectioned in two locations in the steady state region of the bead[8] in the locations dictated by the red lines in Figure 2-3 using a wire electric discharge machining tool (wire EDM), mounted in Bakelite, and polished [137]. The polished samples are then etched by immersion for 30 seconds in Kroll's reagent [138] (2 mL HF, 6 mL HNO_3, 92 mL distilled water). Figure 2-4 is an example melt pool cross section from the Arcam S12 machine with the melt pool boundary highlighted in white. The view in Figure

[8] The length of the single bead tracks was set as at least 4 times the length required for the largest melt pool to reach steady state dimensions based off of finite element simulations. The steady state region of the bead was then defined as the center 25% of the track length.

2-4 corresponds to the Y-Z plane in Figure 2-2. The boundary has a flat top surface because the measurements are meant to determine the cross sectional area that is melted. Since the surface of the original substrate is flat, as evidenced by the good agreement between the existing substrate and the dotted white line on both sides of the melt pool in Figure 2-4, and no powder is added in these experiments, there is no material addition to the melt pool. It is common to see variability in the top surface profile of the melt pool due to liquid flow and surface tension effects [139]. By only measuring the area of material that has been melted, variability induced by surface effects are excluded from the analysis and trends in melt pool cross sectional area become more apparent.

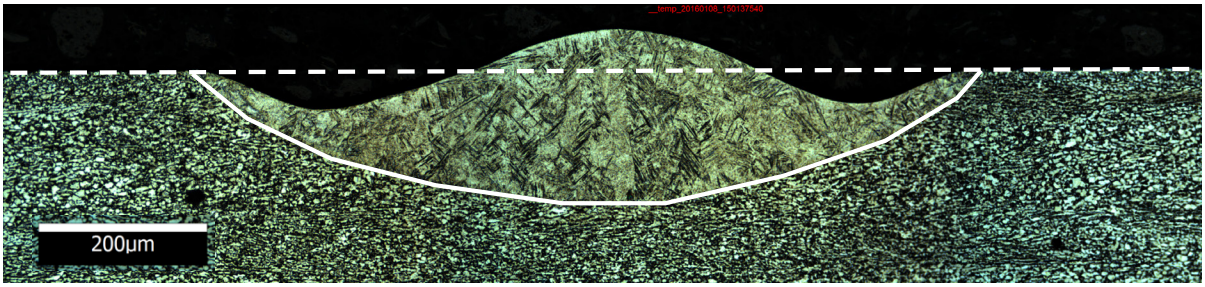

Figure 2-4: An example melt pool cross section from the Arcam S12 machine. The melt parameters were 639 W, 500 mm/s, and 800 °C substrate temperature. The area is measured between the solid white line and the dotted white line.

2.2.4 Temperature Monitoring

In order to look at the long time scale temperature changes at the surface of parts while they are being built, the University of Texas at El Paso (UTEP) has instrumented an Arcam A2 machine with a FLIR SC645 infrared (IR) camera and developed the software necessary to collect images at specified times during and after material deposition for each layer. To minimize the metallization of the viewport and provide the best possible imaging conditions, a shutter inside the build chamber has also been incorporated into the system. Coupled with prior research on view factors specific to the Arcam A2 machine and the emissivity of solidified Ti64, surface

temperatures can be extracted from IR images during a build. This information allows for the monitoring of absolute surface temperatures after a layer has been melted to within ±5% [140], [141]. Figure 2-5 shows the location of the thermal camera and shutter mechanism relative to the electron beam column as well as an example thermal image used in this research.

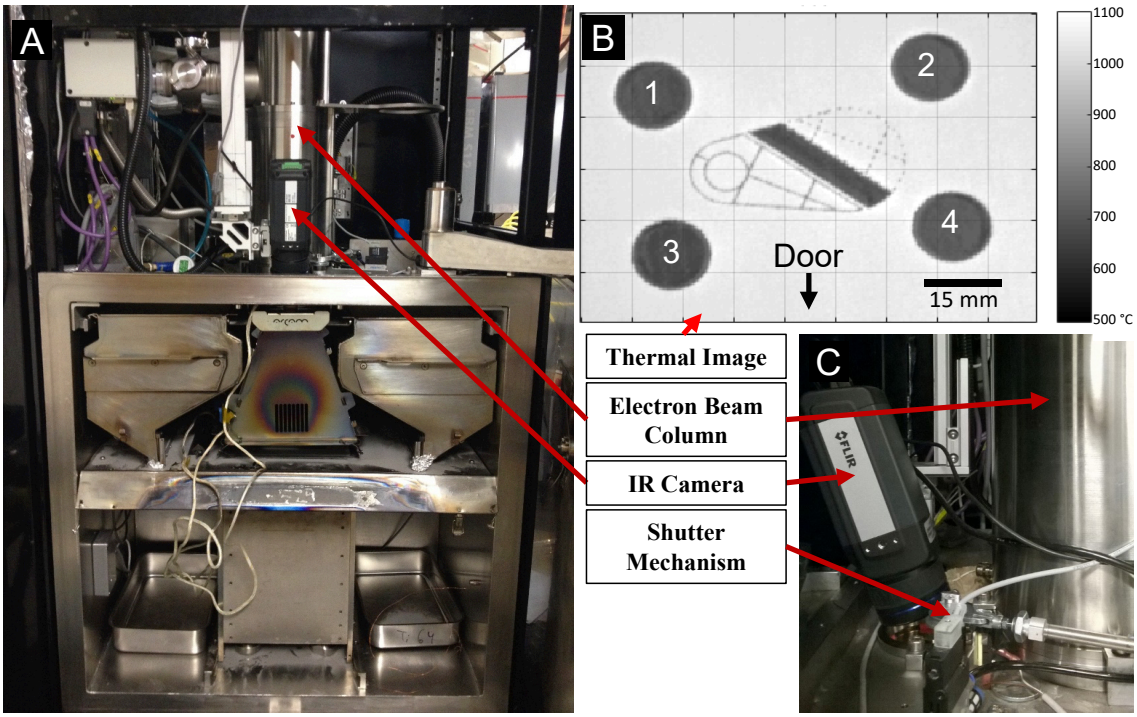

Figure 2-5: A) The front of the Arcam A2 machine with the door open. The camera is highlighted with a red arrow. B) Close up view of the thermal camera mounted above the chamber view port. C) An example thermal image taken with the thermal camera with scale and direction added.

2.2.5 Feedback Control Experiments

Section 2.3.2 shows that temperatures rise during an EBM part build. Prior research [75], [76] has tried to keep temperatures constant throughout the height of a build in order to keep microstructural features consistent. With the knowledge gained from process mapping in the EBM process (section 2.3.1), it is now possible to let temperature vary throughout the height of a build and account for that temperature change using a feedback loop to adjust power.

Arcam uses a thermal model of how temperatures will change during a build to account for thermal drift, but does not allow the operator to access the automatically adjusted parameters. Price et al. measured velocity and beam current for select cases and proposed a method of determining these parameters, but was not able to develop a comprehensive algorithm that could be utilized here [142].

To control or measure all of the major process parameters during an experiment, it is necessary to use manual settings instead of standard Arcam themes to produce test parts. This allows the operator to know exactly what parameters are being used and ensures that manual changes to parameters during a build are carried out as expected. The Arcam themes also account for changes in thermal conditions due to local geometry and free edges [80], but again the user is not given access to these changes. Therefore, using manual settings means that local geometry changes and free edges must be accounted for manually. This is achieved by building tubes around each test part to allow the raster turnaround to occur away from the test part. Contour passes were also disabled since surface roughness is not a concern in these experiments. Cylinders are chosen as the test parts for this experiment due to their simple geometry and constant cross section throughout their height, eliminating compounding variables from the experiment. Each cylinder is 20 mm in diameter, has a 2 mm gap between the cylinder wall and the tube inner wall, and each tube has a 2 mm thick wall. The target height for each build is at least 30 – 60 mm. These dimensions are chosen to generate bulky parts that will have a steady state grain size region at least 10 mm wide in the center of each cylinder based off of the parameters used in these experiments and prior work in the EBM process by Dr. Sneha Narra [143].

Figure 2-6 shows a CAD image of the experimental setup as well as a false color infrared (IR) image of the top surface of the build after a layer has been melted. The cylinders labeled

'Modified' (numbered 1, 3, and 5) have their powers changed based on the temperatures extracted from the IR images. The cylinders labeled 'Reference' (numbered 2 and 4) have constant parameters throughout the height of the build. IR images are taken after melting, but before powder spreading for each layer of the cylinders. Because of the vignetting caused by the camera angle relative to the sight glass into the Arcam chamber, as can be seen in Figure 2-6 left, the top two cylinder temperatures are not used in these experiments. In addition, due to the results of section 2.3.2, only the center cylinder temperature is used for the feedback loop. The temperature of the all of the cylinders is recorded using an emissivity of 0.26[9]. The seemingly higher temperatures surrounding each cylinder in Figure 2-6 is likely due to a difference in emissivity between the solid part and the surrounding powder, and not necessarily a difference in temperature.

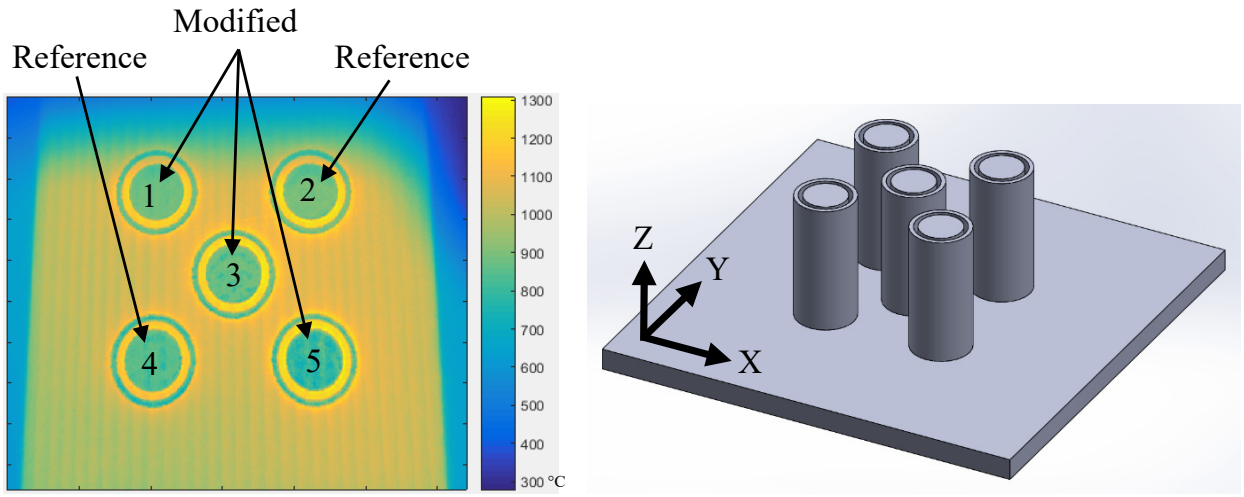

Figure 2-6: (Left) An example infrared image of the top surface of the build. The emissivity is held constant between the powder and solid surface in the image to highlight the solidified mateiral. (Right) The CAD model used to generate the beam path for the build.

[9] An emissivity of 0.26 is used to convert the infrared thermal images to true temperature based on prior work for this imaging system [140].

To implement the feedback loop, an existing program developed by UTEP [132] is modified to make the necessary parameter modifications within the Arcam software. Temperatures are measured by the thermal camera and fed into a Matlab program (MathWorks, Natick, MA) developed by the Author. The Matlab program automatically determines the last image taken before powder spreading for each layer, then extracts temperatures from a 12 pixel diameter area (16 mm^2) viewing the center of Cylinder 3 in Figure 2-6. The temperatures from each layer are then averaged over a preset number of layers and this average temperature is used to generate the power that is used for the Modified cylinders during the next interval.

Two builds (Experiment 1 and Experiment 2) are done with different process parameters. The automation of the feedback control loop was not accomplished until after Experiment 1 was completed. Therefore, Experiment 1 had the operator manually change the power used to melt the Modified cylinders during the build while Experiment 2 has the power changes automated. For Experiment 1, the power used to melt the modified cylinders is changed at roughly 5 mm increments (72 layers) throughout the height of a 30 mm tall build. Within each increment, the first 30 layers are used to allow temperatures from the previous change in power to equilibrate. The next 30 layers are used to collect IR images to extract an average surface temperature for the build at that height. The last 12 layers are used to manually analyze the images, extract temperatures, and determine the appropriate beam power change for the next increment. Experiment 1 uses 70 μm layers, a beam power of 556 W and a travel velocity of 500 mm/s. These build parameters are chosen to be close to the standard Ti64 theme for 70 μm layers on the Arcam A2 machine with software version 3.2.121.

For Experiment 2, the powers can be changed much more quickly because of the automation of the power change algorithm. For this reason, power changes are done at roughly 1

mm increments (14 layers) throughout the height of the build. As before, just after a power change, the temperatures are allowed to equilibrate, this time for only 4 layers, then IR images are collected for the next 9 layers, and the final layer is used to change the power[10]. Experiment 2 uses 70 μm layers, a beam power of 825 W and a travel velocity of 750 mm/s. These parameters are chosen in generate the same melt pool cross sectional area as Experiment 1, but with a deposition rate that is 50% faster[11]. By increasing the power and velocity of the beam, more heat is input to the system during deposition, and should therefore cause an increase in surface temperature during the build.

For both Experiment 1 and Experiment 2, each cylinder is cross sectioned throughout its height (X-Z plane) using a wire EDM, mounted in Bakelite, polished [137], and etched using Kroll's reagent [138]. Grain counts utilizing the Heyn Lineal Intercept Procedure [144] are done across the width of the center 10 mm of each cylinder (X direction) at 5 mm increments (Z direction) in order to detect any difference in grain widths through the height of each cylinder. At least 100 grains are measured to generate each data point. Sample micrographs taken from cross sectioned cylinders can be seen in Figure 2-7. The prior beta grain boundaries are highlighted in white and the direction of grain measurements is shown in red.

[10] All parameter changes must be instituted one layer before they take effect in software version 3.2.121.
[11] The change in deposition rate is generated by increasing the velocity of the beam by 50% and increasing the power to stay on the same line of melt pool cross sectional area based on the results in section 2.3.1.

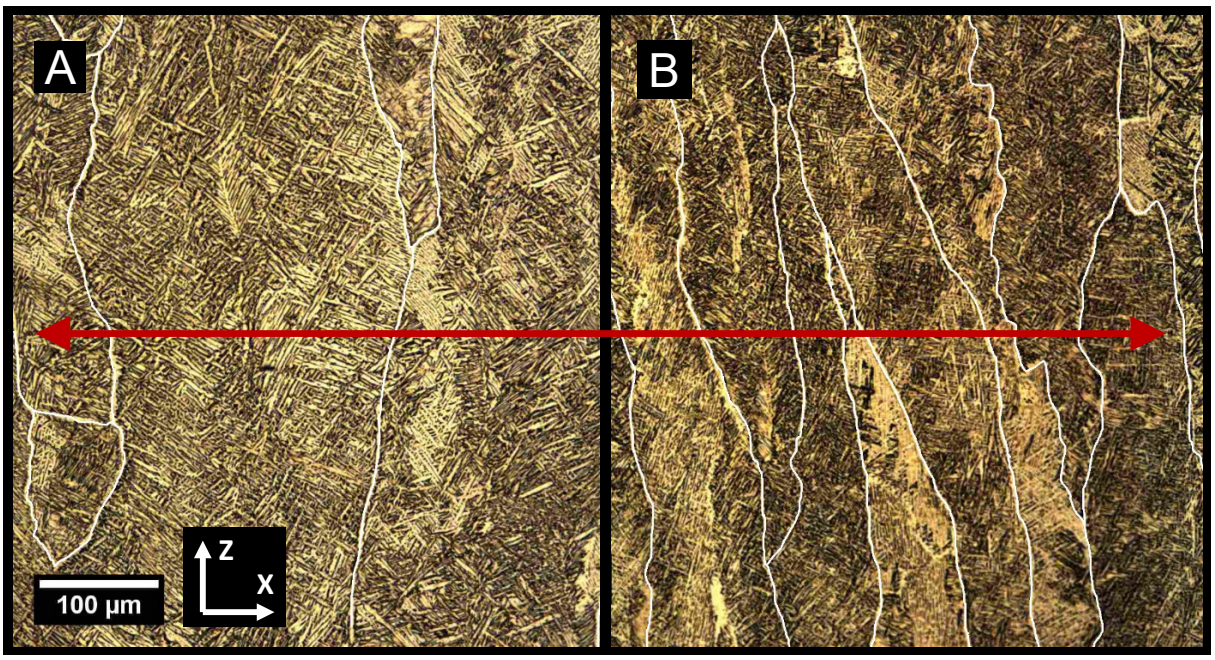

Figure 2-7: Micrographs taken from a Reference (A) and Modified (B) cylinder. Prior beta grain boundaries are highlighted in white. Grain counts are done horizontally across the columnar prior beta grains to get widths (*X* direction).

2.3 Results

2.3.1 Process Mapping for Temperature in the EBM Process

Process maps for both melt pool area and cooling rates at solidification are created for the Arcam process at 600, 800, and 1000°C from simulations of the melt pool. These substrate temperatures are based off of research by Mireles [132] and are meant to bracket the range of likely surface temperatures encountered during an EBM build. Curves of the same color correspond to the same quantity of interest. Solid lines represent 600 °C, dashed lines 800 °C, and dotted lines 1000 °C. Figure 2-8 shows that as substrate temperature increases, curves of constant area shift down and to the right on a power vs velocity process map, which matches well with what Fox found for the EBF3 process [134]. Figure 2-9 shows that as temperature increases, curves of constant solidification cooling rate also shift down and to the right on a power vs velocity process

map, but the curves shift farther for constant solidification cooling rate than for constant area[12]. An example of the utility of these process maps is the determination of the parameters for Experiment 2 in section 2.2.5.

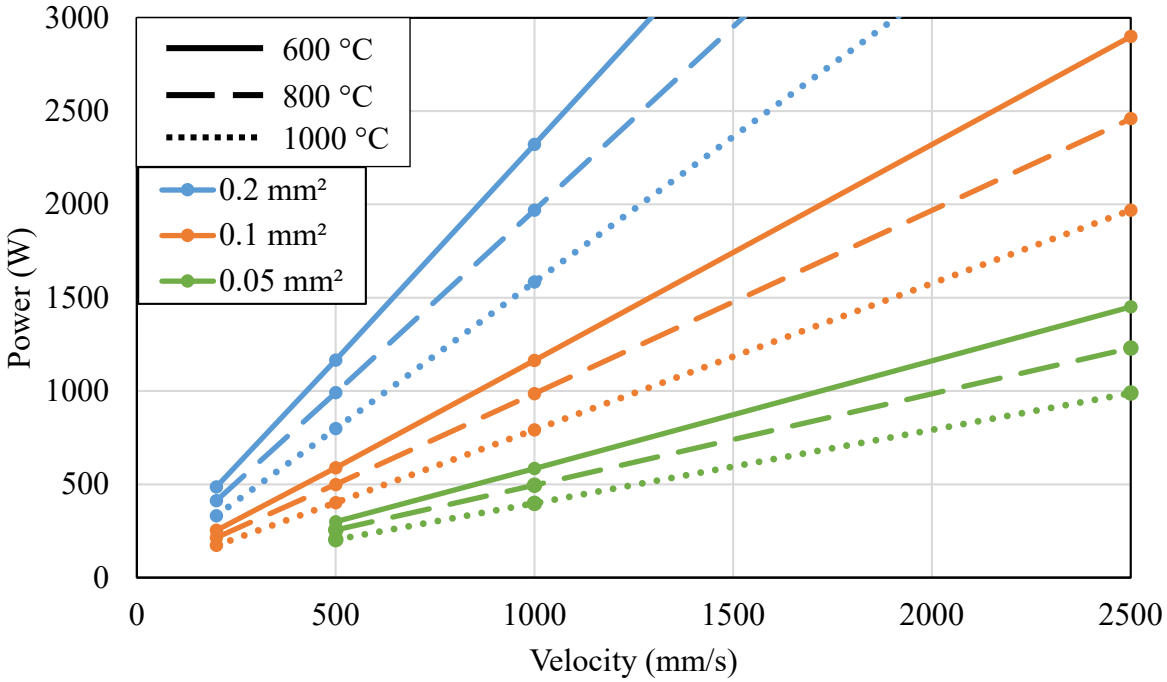

Figure 2-8: Plot of curves of constant area in the Arcam process. Each curve of the same color represents the same area, but at a different part temperature.

[12] Note that the difference between lines of constant cooling rate in Figure 2-9 is 4X, while the difference in lines of constant area in Figure 2-8 is only 2X. This change is made to allow the data to be presented within the available process window for the Arcam A2 and S12.

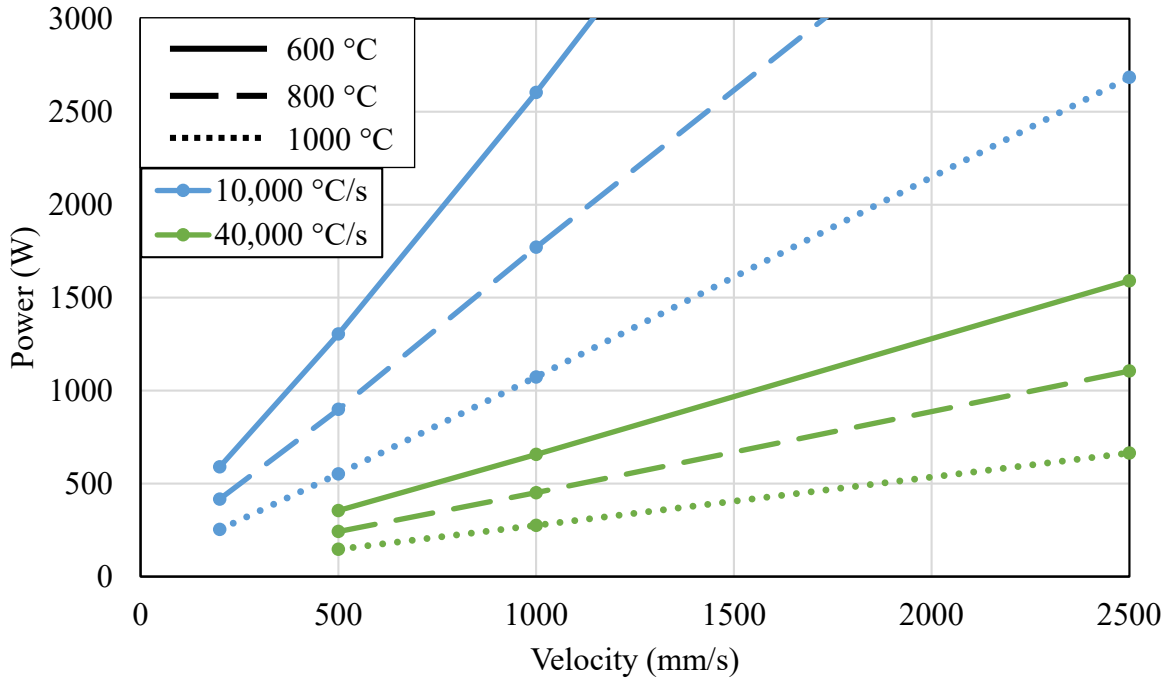

Figure 2-9: Plot of curves of constant cooling rate in the Arcam process. Each curve of the same color represents the same cooling rate, but at a different part temperature.

Figure 2-10 shows the results of the single bead experiments. Each purple dot represents a melt pool cross section, while the orange dots are simulation results. There is very good agreement between experiment and simulation, showing that simulation is correctly predicting how melt pool cross sectional area changes with substrate temperature across power-velocity space. To generate Figure 2-10, the self-similar lines in Figure 2-8 are collapsed to a single curve by normalizing the melt pool area to the predicted value for each power-velocity combination at 750 °C.

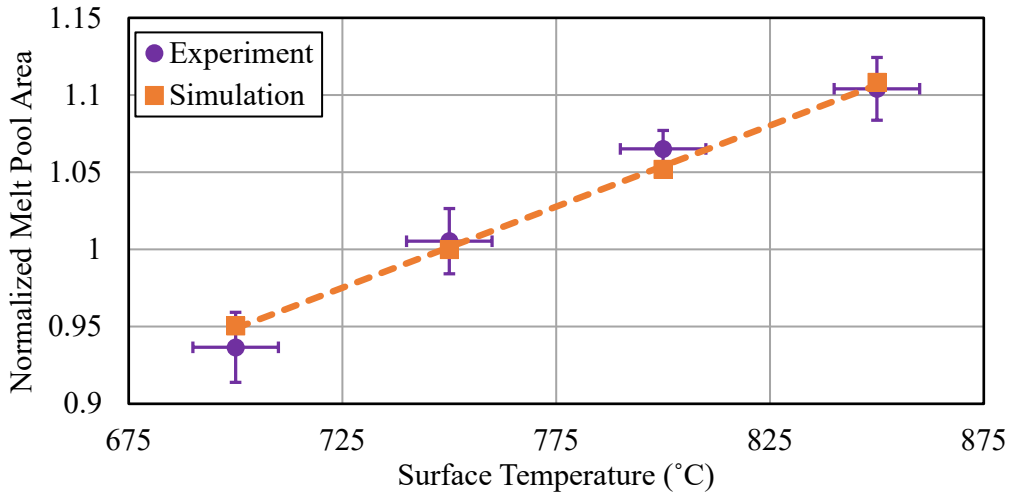

Figure 2-10: Plot of normalized melt pool area vs substrate temperature. All values are normalized by the areas from simulation for that power and velocity combination at 750 ˚C. The vertical error bars are the 95 % confidence intervals on the mean melt pool cross sectional area. The horizontal error bars are the substrate temperature uncertainty during deposition.

The process mapping results are then used to generate Figure 2-11, showing lines of constant solidification cooling rate and constant cross sectional area on a plot of normalized power vs substrate temperature (from simulations). The power required to maintain the same metric of interest is normalized to its value at 750 °C. In other words, if a certain power-velocity combination were used to generate a melt pool at 750 °C, what percentage change in power would be required to maintain that metric of interest (either melt pool cross sectional area or solidification cooling rate) as substrate temperature is changed and velocity held constant. The power axis has been normalized to show that the curves are independent of velocity for the range of velocities used in this section (roughly 500 mm/s to 800 mm/s). This means that though the absolute power changes necessary to keep cooling rates constant change with velocity, the underlying thermal problem is independent of velocity. Lines of constant solidification cooling rate (blue and green) have a steeper slope than lines of constant melt pool cross sectional area (orange and purple), meaning

that larger changes in power are necessary to keep solidification cooling rates constant than are necessary to keep melt pool areas constant.

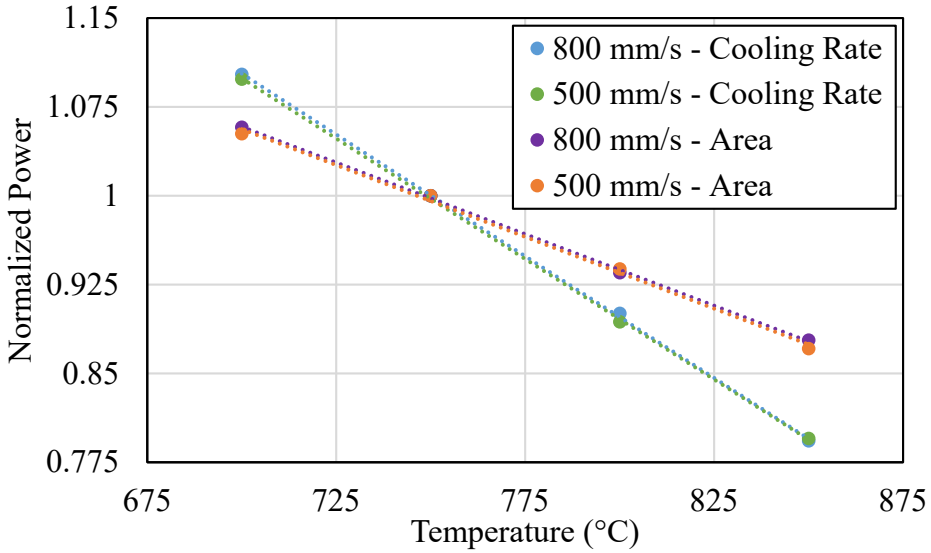

Figure 2-11: Plot of normalized power vs part temperature for the Arcam process generated from simulation results for both melt pool cross sectional area and solidification cooling rate. The dotted lines are best fit lines.

To evaluate the relationship between temperature change and resultant part properties like prior beta grain width, a framework is required that equates input parameters to prior beta grain widths. A link between prior beta grain widths and melt pool areas has already been established by Gockel [30] and Narra [52] and shows that prior beta grain width scales with the square root of melt pool area for Ti64 and that constant melt pool areas have constant cooling rates at solidification. This link was refined by Francis [31] to note that this relationship holds when the melt pool cross sectional shape does not vary considerably. The results from Figure 2-11 add to the existing understanding because prior work did not explore the effect substrate temperature changes.

When substrate temperatures are allowed to vary, the thermal problem becomes more complicated. As the substrate temperature rises, the difference between the solidus temperature and the substrate temperature decreases, reducing thermal gradients in the material. Figure 2-11 shows that the melt pool cross sectional area is less affected than the solidification cooling rate by the changes to thermal gradients, likely due to the significantly higher thermal gradients in the *YZ* plane relative to the *X* direction[13] [48]. Once a new substrate temperature is established, however, it is again true that lines of constant melt pool area match with lines of constant cooling rate. According to Equation 1 from section 1.3.4 and prior work [30], [31], [52], prior beta grain widths should track with cooling rate. Therefore, the curve of solidification cooling rate in Figure 2-11 is used to maintain constant prior beta grain widths in section 2.3.3.

2.3.2 Temperatures in the EBM process

An initial assessment of temperatures at the top surface of the Arcam A2 powder bed during fusion is conducted to determine how temperatures change within a single layer. A 15 mm diameter cylinder is continuously monitored at 20 Hz using the thermography setup described in section 0. Figure 2-12 shows the temperatures extracted from the IR images for one layer by averaging a 12 pixel diameter (16 mm^2) area at the center of the cylinder. The maximum temperatures detected by the camera were roughly 1300 °C even though melting is occurring because the temporal and spatial resolution of the thermal camera are not adequate to see melt-pool scale phenomena.

The squares in Figure 2-12 represent temperature data taken from the solid cylinder surface while the triangles represent data from the cylinder surface covered with powder. The emissivity

[13] From Figure 2-2, the melt pool cross sectional area is measured in the *YZ* plane while the solidification cooling rate is extracted at the tail of the melt pool along the *X* direction.

of solid and powdered Ti64 in this process has previously been determined to be 0.26 and 0.5 for the camera system, respectively [141], so these values are used to convert thermal information to temperatures. Both the cooling of the solidified surface and the heating of the powder during the agglomeration step appear to converge toward the same temperature, showing that the temperature derived from the last image taken before powder spreading is a good representation of the temperature just before fusion of the next layer. The highlighted area labeled 'Shutter Open' illustrates when the camera views the top surface of the build if monitoring of a substantial portion of a build is attempted. This means that future applications do not have to continuously monitor the process to determine the surface temperature of a build before deposition, but will instead only need the temperature that the previously deposited layer cooled down to before spreading of the subsequent layer.

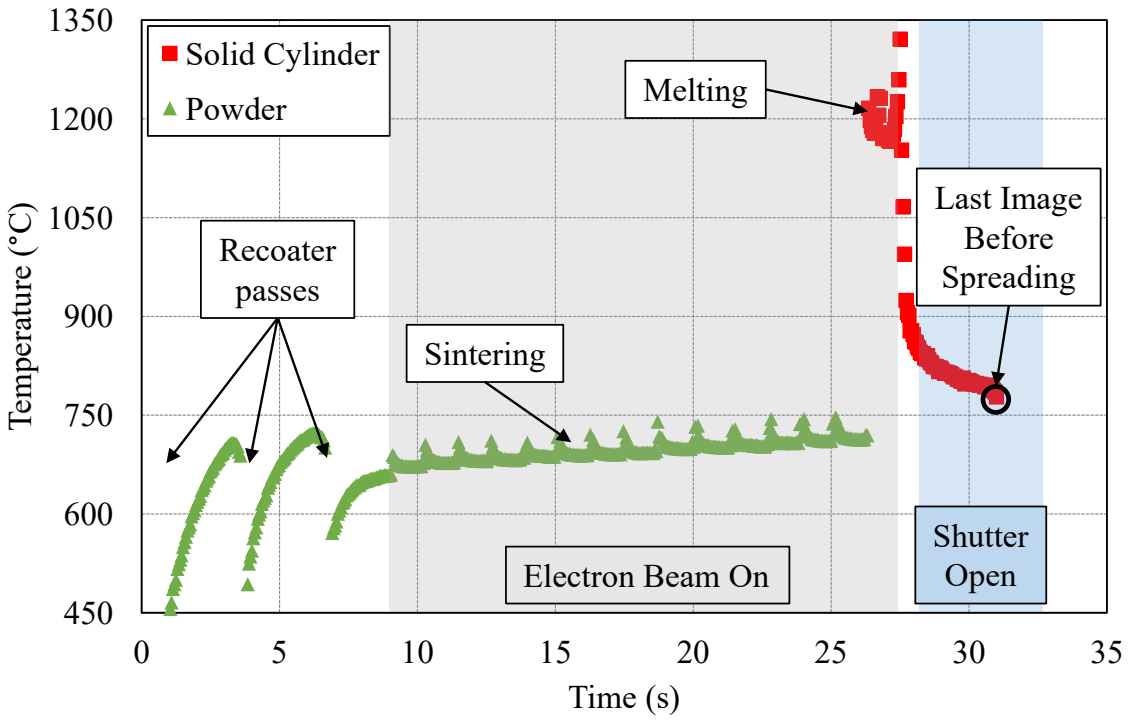

Figure 2-12: Temperature vs time plot extracted from thermal images taken at 20 Hz. The data is taken continuously for a single layer. Time on the *X* axis starts at the beginning of powder spreading for the layer.

To determine how surface temperatures may change during an EBM build, UTEP took thermal images of a 12 mm tall Ti64 build of 4 cylinders that were well dispersed within the build volume of their machine. A representative thermal image from this build can be seen in Figure 2-13. The build was conducted using Arcam supplied Ti64 powder and the standard Ti64 theme for 50 μm layers on the Arcam A2 machine with software version 3.2.121. Additionally, the build was made using a standard Arcam build plate and temperature measurements were taken at build heights greater than 3mm to avoid transient effects in initial layers of the build. A shutter system was used and images were only taken when the electron beam was off in order to minimize metallization of the camera viewport [141]. While continuous monitoring is preferred because it allows for accurate tracking of temperatures both before and after fusion, metallization of the viewing window when the electron beam is active makes this impractical for entire builds [141]. The build layout and fabrication was conducted by researchers at UTEP, but all subsequent analysis of the build presented in this work was done by the Author.

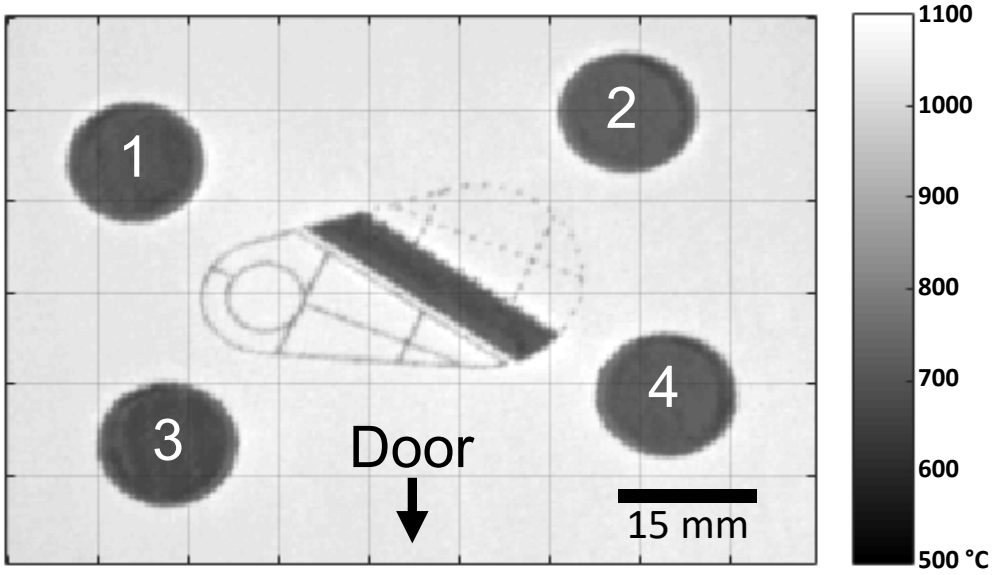

Figure 2-13: An example thermal image of the build used to determine surface temperature variation during and EBM build.

With the understanding that temperatures before spreading and after heating should be similar, the temperature of the solidified cylinders just before powder spreading is used as the substrate temperature for the subsequent layer. As with the continuous monitoring, temperatures are extracted by averaging a 12 pixel diameter area at the center of each cylinder. The results of tracking surface temperature from a build height of roughly 3.5 mm to 8.25 mm are shown in Figure 2-14 and have a clear upward trend in surface temperature. The build plate temperature rapidly decreases from a maximum of 780 °C at the start of the build to 600 °C at 3.5 mm build height, then slowly decreases throughout the rest of the build. This thermocouple temperature profile is representative of what is found during an Arcam A2 or S12 build and shows that as build height increases, the thermocouple below the build plate in the Arcam machine becomes a progressively worse indication of surface temperature.

Simulations are used to generate the right-hand y-axis in Figure 2-14, which shows that the observed surface temperature rise could change the average prior beta grain width by more than 5% over the interval measured. The baseline of 100% on the right-hand y-axis represents the predicted prior beta grain width at the build plate thermocouple temperature of 575 °C and assumes that all other process parameters are held constant. In this case, the true effect on microstructure cannot be adequately determined from part temperature alone because Arcam’s 'standard parameters' include proprietary control software that changes process parameters automatically based on a feed forward thermal model [15]. The data presented here only show about one hour of build time, while builds may last for tens or even hundreds of hours.

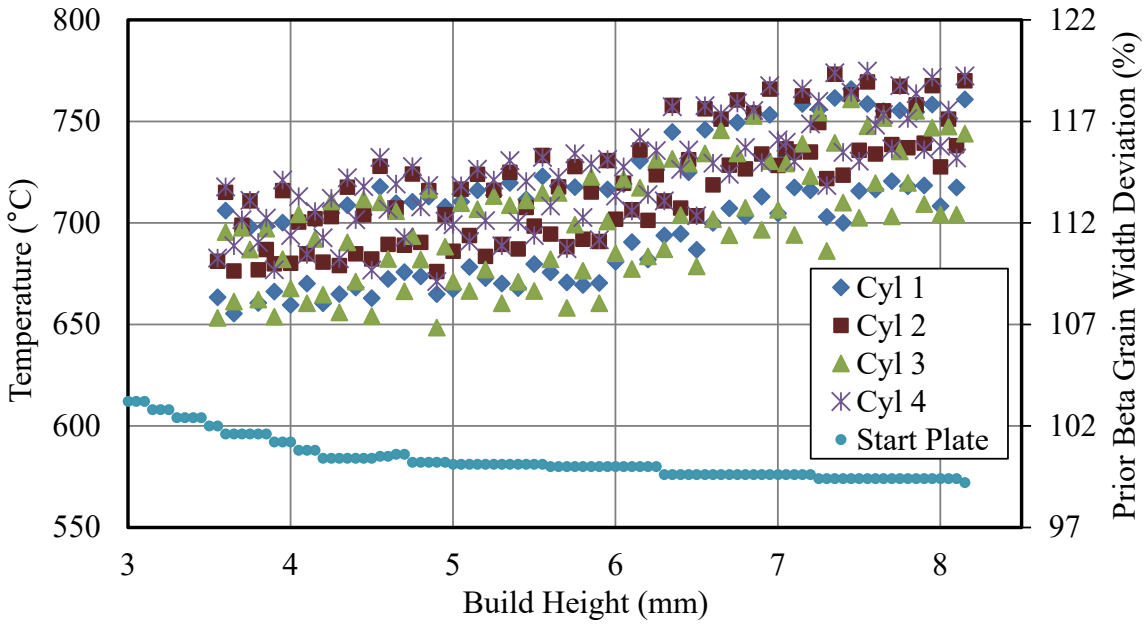

Figure 2-14: Experimental temperatures plotted against build height for four cylinders produced with standard Arcam parameters in an Arcam A2 machine. The left y-axis is temperature and right y-axis is the percentage increase in predicted prior beta grain width if increased temperatures are not accounted for.

Figure 2-14 is generated using one image taken just before powder spreading for each layer. However, multiple images are taken for each layer between when fusion ends and when spreading occurs (the 'Shutter Open' segment in Figure 2-12) so further data analysis on surface temperatures for this build is possible. Figure 2-15 shows the temperature profile for each cylinder for four consecutive layers at a build height of roughly 4 mm. Time zero is set at when the first image for a given layer is acquired. In cases *A*, *C*, and *D* in Figure 2-15, this first image is taken before the shutter is fully open, so the temperature derived from that image is excluded. It is clear that there is a complicated thermal situation occurring during the last stages of part cooling since some cylinders are increasing in temperature during the time period measured, likely a result of heat transfer in the system being fast enough that heat can flow from relatively hot spots generated

during fusion to relatively colder spots on the time scales being measured. In addition, there seems to be a cyclic nature to which cylinders are cooling and which ones are heating. This can be explained by the 90 degree rotation in scan direction between successive layers. Depending on which direction scanning occurs for a given layer, the amount of time between material fusion and when images are taken is different for each cylinder. This time difference is cyclic with a period of four layers, and will therefore not affect the average temperature trends seen in Figure 2-14, but account for the trends seen in Figure 2-15.

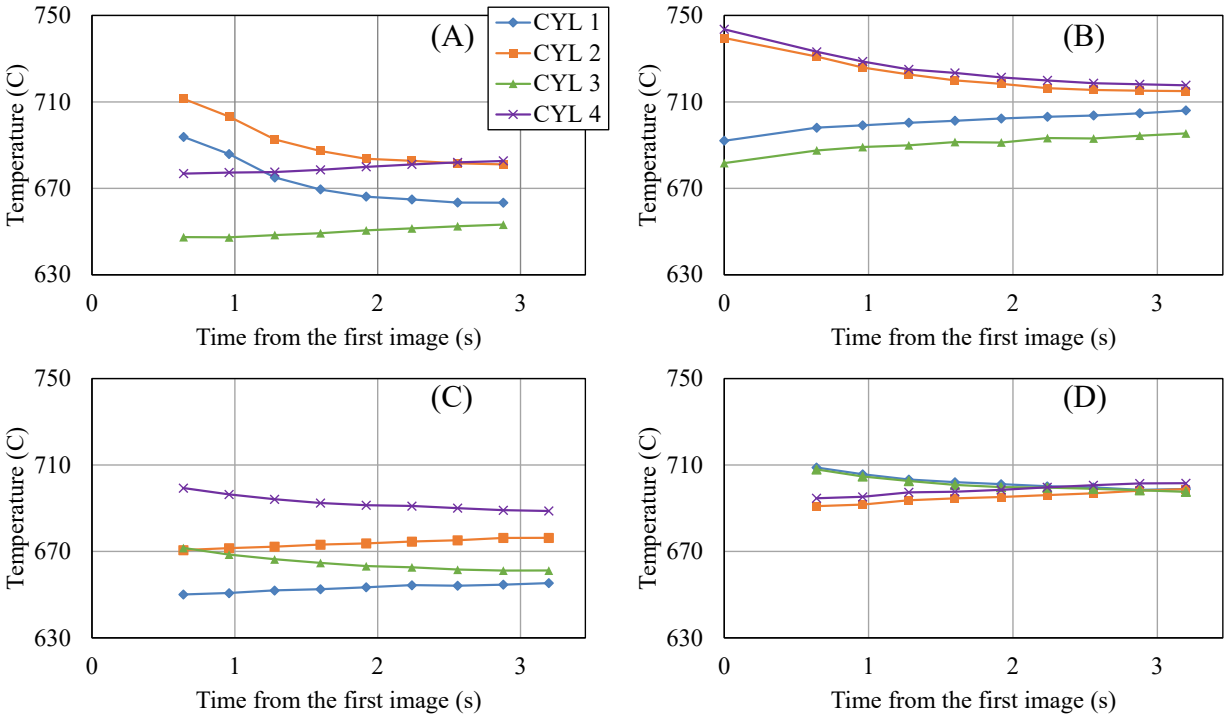

Figure 2-15: A-D show the temperature of each cylinder plotted against time since the first image is acquired for four consecutive layers around 4 mm total build height.

When all of the individual cooling curves are aggregated, an important result emerges. Figure 2-16 shows the maximum temperature difference between the four cylinders for each fusion

layer as a function of the time since the first image is acquired for that layer[14]. Each data point equates to one thermal image. A best fit exponential curve is fit to the data and has a 1/*e* time constant of 4.3 seconds. Because the time between layer fusions for even the simple part used for continuous monitoring is roughly 32 seconds (Figure 2-12), Figure 2-16 suggests that surface temperature variations induced during fusion should be reduced to insignificant levels before the start of the next layer and do not need to be considered in future monitoring applications. For example, using the curve from Figure 2-16, it would only take 6.6 seconds for the average spatial variation in cylinder surface temperature to drop to 10 °C, which would roughly equate to a 1% change in prior beta grain width between cylinders if sustained.

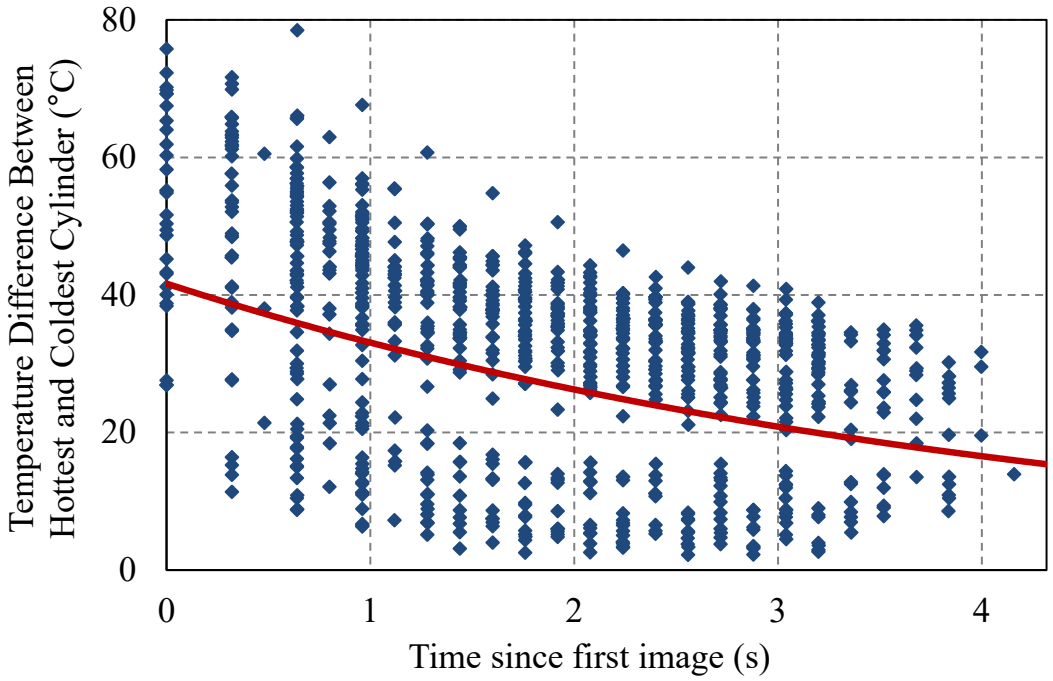

Figure 2-16: Plot with time on the *X* axis and temperature difference between the hottest and coldest cylinder on the *Y* axis. Time is measured from when the first image is taken for each layer.

[14] For clarity, this means that the coldest cylinder temperature is subtracted from the hottest cylinder temperature for each image in order to determine the temperature difference between cylinders for that image. In this way, the total spread of temperatures between cylinders is determined, and this spread is what is presented in Figure 2-16.

The cylinders are then cross sectioned and grain counts completed using the procedure outlined in section 2.2.5. The result of the grain counts can be seen in Figure 2-17. No clear trend in prior beta grain width with height is seen, though the temperature rise seen in Figure 2-14 suggest that there should be an upward trend. Arcam has a proprietary mechanism to control velocity throughout a build [52], so it is difficult to determine what the actual process parameters used for deposition of the cylinders. This leads to the conclusion that taller samples and the ability to build parts with known power and velocity are required to see microstructural changes induced by temperature changes, which is the focus of section 2.3.3.

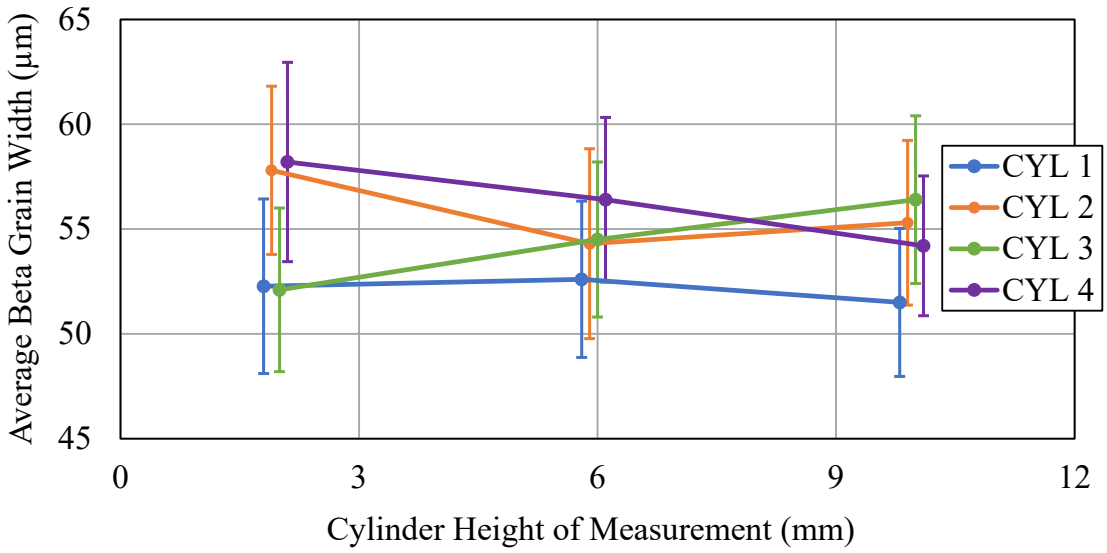

Figure 2-17: Plot of average prior beta grain width against cylinder height for standard cylinders in the EBM process. The error bars shown are the 95% confidence intervals on the mean.

2.3.3 Solidification Microstructure Control of Bulky Parts

The average temperatures extracted from the infrared images for Experiment 1 are presented in Figure 2-18. The red line shows the average temperature over each 5 mm power increment for Cylinder 4 while blue lines show the average temperature over each 5 mm power

increment for Cylinders 3 and 5 (Cylinders 1 and 2 are not used because of vignetting in the images). The error bars represent 95% confidence intervals on the mean temperature for each increment. It is clear from the data that the temperature measured by the thermocouple under the baseplate is a progressively worse representation of surface temperature as the build progresses, which is the same result as was found in section 2.3.2. It is also clear that the surface temperatures of the cylinders that do not have their powers adjusted are higher than those that did, meaning that the power changes used to account for increases in temperature have the added benefit of reducing the magnitude of the temperature changes.

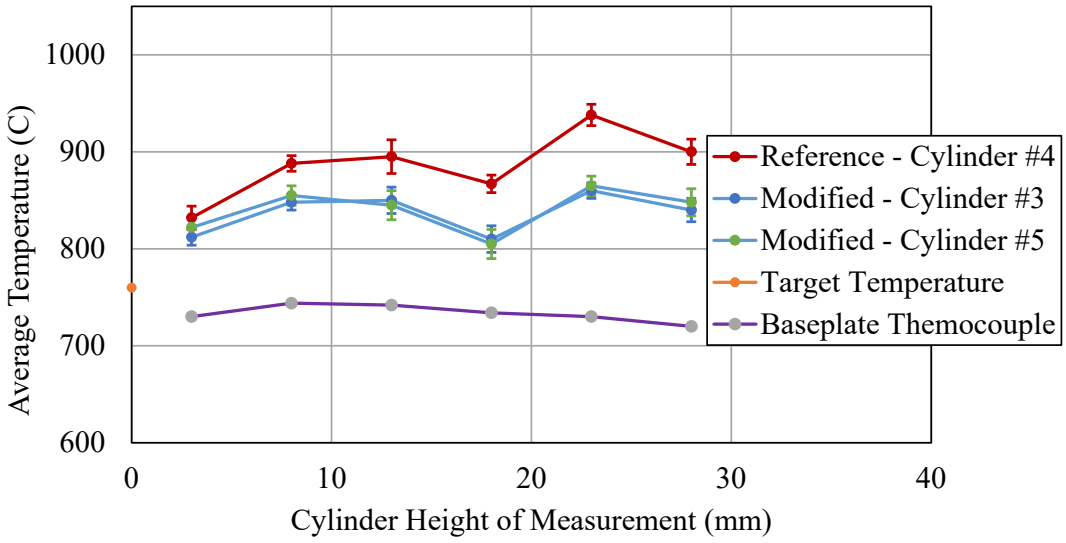

Figure 2-18: Plot of surface temperature vs cylinder height for Experiment 1. The red line represents the reference cylinder surface temperatures (Cylinder 4), the blue lines represent the modified cylinder surface temperatures (Cylinders 3 and 5), and the purple line represents the baseplate thermocouple temperature. The target baseplate temperature is shown in orange. The temperature and cylinder height scales are chosen to match up with Figure 2-19.

This difference in surface temperature throughout the height of the build also indicates that one of the results in section 2.3.2 requires further explanation. In section 2.3.2, surface temperature differences are shown to dissipate before the next layer is deposited when the melt parameters for

all of the parts are the same. That result is confirmed in this section, though it may not hold true when parts have considerably different power inputs. The difference in temperature measured in this section only shows the initial cooling from solidification, however. It is likely that the temperature field would have become more uniform during spreading and heating of the next layer, possibly to the point that the temperatures in this case would also have equilibrated before deposition of the subsequent layer. Further experimentation is needed to confirm this theory.

Figure 2-19 shows the temperatures extracted from the infrared images for Experiment 2. Once again, the temperature measured by the thermocouple under the baseplate is a poor representation of surface temperature as the build progresses. The surface temperatures of the cylinders that do not have their powers adjusted are higher than those that did, and the temperatures seen in this build are higher than those seen in the previous build. The greater increase in temperature is expected due to the higher deposition rate (and therefore higher power input).

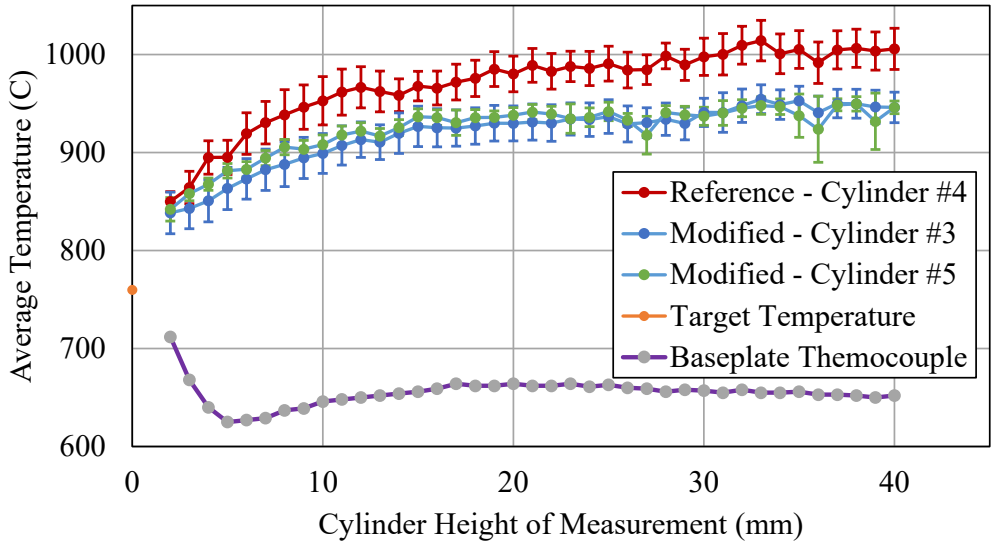

Figure 2-19: Plot of surface temperature vs cylinder height for Experiment 2. The red line represents the reference cylinder surface temperatures (Cylinder 4), the blue lines represent the modified cylinder surface temperatures (Cylinders 3 and 5), and the purple line represents the baseplate thermocouple temperature. The target baseplate temperature is shown in orange.

Surface temperature changes result in changes to thermal gradients around the melt pool, which alters cooling rates and ultimately the microstructure of the part. Therefore, changes in surface temperature of the part are expected to cause changes in microstructure if not accounted for. The modified cylinders are built with beam powers corrected based off of observed surface temperatures during the build with the goal of keeping solidification cooling rates consistent throughout the height of the build. The reference cylinders have constant parameters throughout the build, with the understanding that cooling rates should change as surface temperatures change. All of the cylinders, however, have the same starting parameters.

Figure 2-20 shows the results from the grain counts for Experiment 1. As with the temperature plots, the red lines represent the reference cylinders and the blue lines represent the modified cylinders. The error bars represent 95% confidence intervals on the mean temperature for each increment. The individual grain widths are variable, but the trend in average beta grain width is compelling. There is a clear upward trend in average beta grain widths for the reference cylinders that is not seen in the modified cylinders.

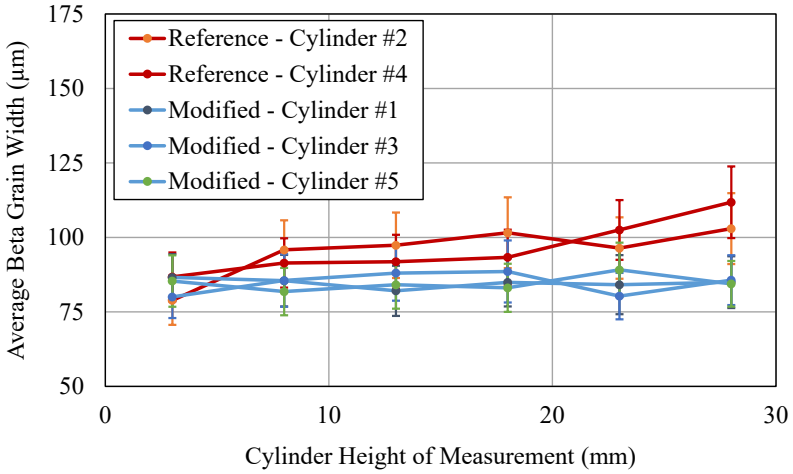

Figure 2-20: Plot of average beta grain width vs height of the measurement. Reference, or unmodified, cylinders are shown in red while modified cylinders are shown in blue. The error bars shown are the 95% confidence intervals on the mean.

Figure 2-21 shows the results from grain counts for Experiment 2. The 95% confidence interval on the mean shows a significant difference between the modified and reference cylinders. In Experiment 2 the overlap in error bars is practically non-existent above a build height of 2 mm, showing an even greater difference between the modified and reference cylinder prior beta grain widths than was seen in Experiment 1.

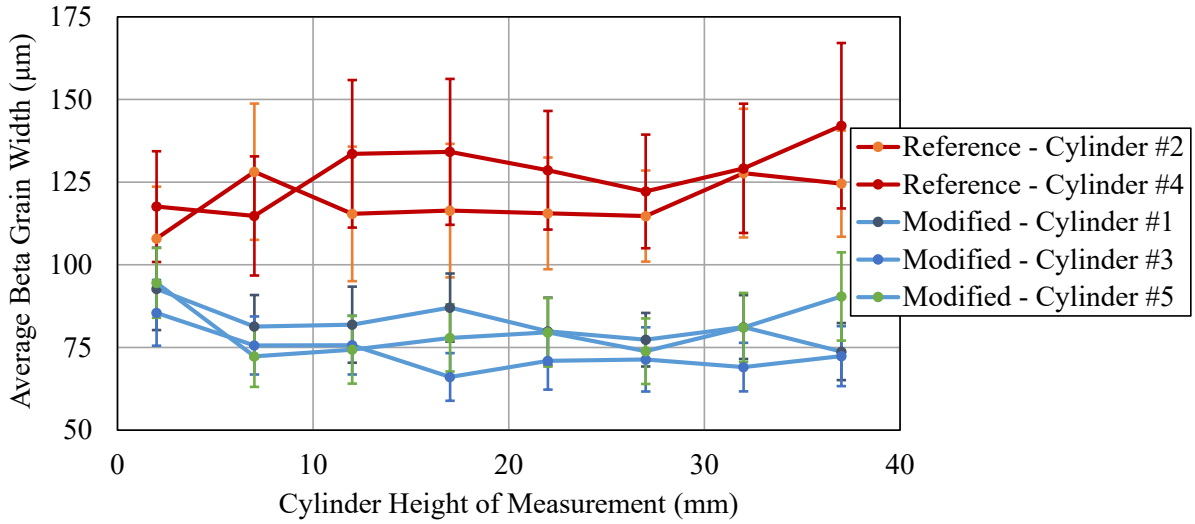

Figure 2-21: Plot of average beta grain width vs height of the measurement. Reference, or unmodified, cylinders are shown in red while modified cylinders are shown in blue. The error bars shown are the 95% confidence intervals on the mean.

Because more power is used for Experiment 2 than Experiment 1, the higher temperatures seen in Figure 2-19 than in Figure 2-18 is expected. You can also see that the grain sizes for the reference cylinders are larger for Experiment 2 than for Experiment 1, but the grain sizes for the modified cylinders are the same between the two experiments. This shows that by controlling solidification cooling rate as temperatures change, solidification microstructure is also controlled. In Experiment 1, all of the grain sizes start out at roughly the same value and then diverge. In Experiment 2, the two sets of grain sizes have diverged before the first grain width measurement.

This is likely due to the reduction in the power change interval from 5 mm to 1 mm and the increase in heat input overall. In Experiment 2, the first power change happens before the first grain counts, while in Experiment 1, the first power change happens after the first grain counts[15].

2.3.4 Part Swelling

There is no noticeable difference in the top surface profile between the reference and modified cylinders in Experiment 1. This suggests that even with the lack of power control for the reference cylinders, there is not enough heat input to cause part swelling. When the deposition rate is increased, however, there is a noticeable difference between cylinders with power control (Modified) and those without (Reference). Figure 2-22 shows the cylinders from Experiment 2, where the deposition rate is increased by 50% from Experiment 1. The reference cylinders have significant swelling of the top surface of the build while the modified cylinders do not have any noticeable swelling. This leads to the conclusion that the decrease in power input used to account for an increase in surface temperature has the added benefit of keeping the power density low enough to avoid part swelling.

[15] The first grain measurement for each experiment is taken at a height of at least 2 mm so that the grain size is not influenced by grain structure in the stainless steel baseplate. Work by Dr. Sneha Narra showed that the distance required for prior beta grain width to fully change after a step change in parameters will depend on the melt pool cross sectional area difference between the initial and final states. For the grain size differences in this work, 2 mm is an appropriate distance [143].

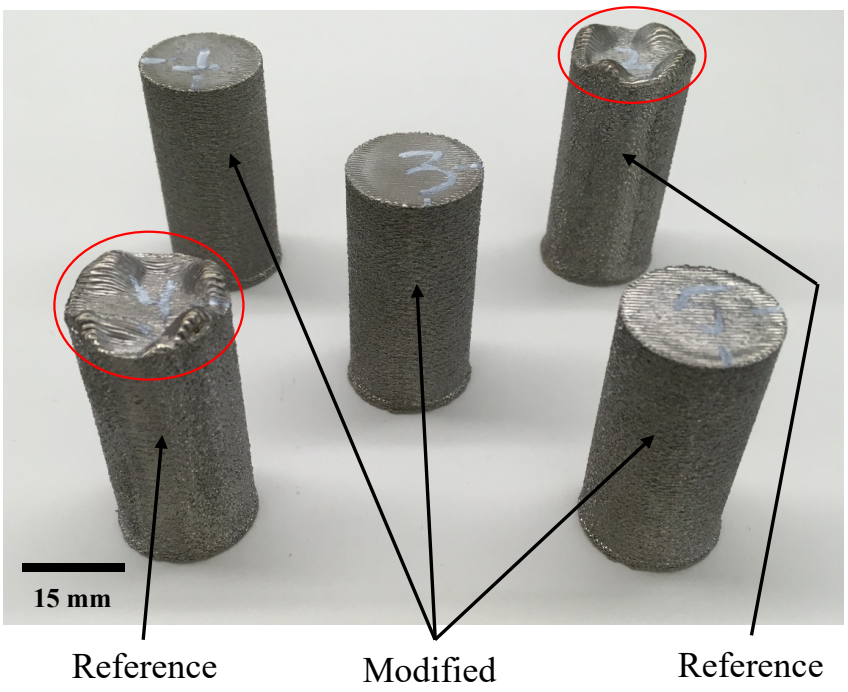

Figure 2-22: Image of the cylinders from Experiment 2 clearly showing part swelling in the reference cylinders, highlighted in red, that is not present in the modified cylinders.

It is clear that excess heat input causes a lack of dimensional tolerance that can be significant, and a better understanding of the underlying mechanisms is necessary to avoid this phenomenon. The term "swelling" may be a misnomer, however, since it is found in this work that the lack of dimensional tolerance on the top surface of the reference cylinders (Figure 2-22) does not lead to significant porosity, as can be seen in fig___. The likely mechanism for this lack of dimensional tolerance is that the excess surface temperature reduces cooling rates and increases the length of the melt pool to the point where balling of the liquid surface occurs and generates perturbations in the top surface of the part. In the modified cylinders, the solidification cooling rate was held constant, meaning that the melt pools were not able to grow to the same extent. Given that the variation in surface height seen in fig ___ is several millimeters, and therefore considerably more than what could be created by liquid pooling in an individual layer, it is also likely that the flexible

metal rake used to spread powder in the EBM process may generate an area of deeper powder behind a perturbation in the surface of the part. This would progressively increase the prominence of that surface feature by introducing excess material during deposition of the next layer.

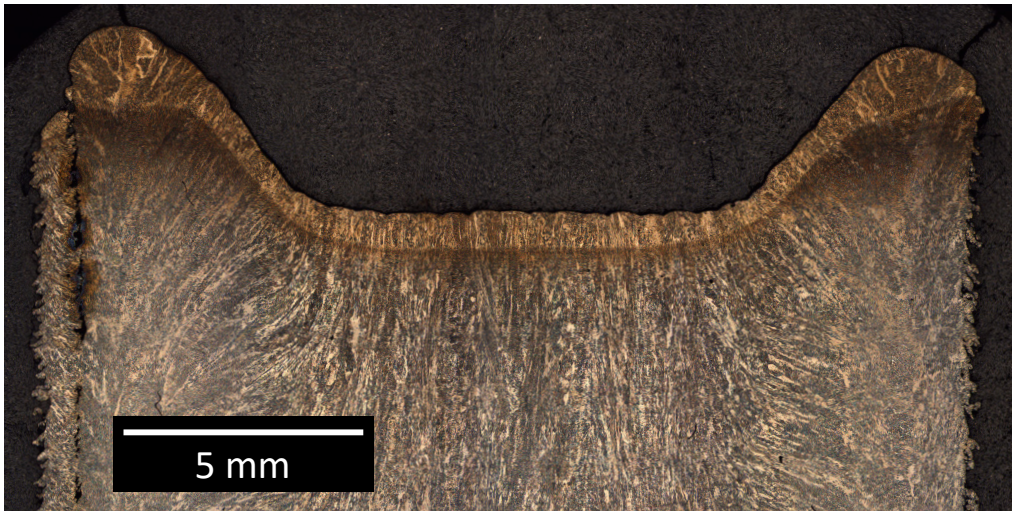

Figure 2-23: Cross sectional image of the top section of a reference cylinder from Experiment 2. The several millimeter tall "swelling", or lack of dimensional tolerance, is readily apparent.

2.4 Discussion

In this chapter the effect of substrate temperature on melt pool cross sectional area and solidification cooling rates is determined in the EBM process for Ti64 through simulations and experiments. Simulations based off of previous work [31], [49], [134] are run using ABAQUS and experiments are done on the Arcam S12 machine at CMU. The trend in melt pool areas from single bead experiments matches very well with those found from simulations, and suggests that the trends in solidification cooling rate from simulations is also accurate.

To determine how temperatures change during an EBM part build, thermal images are taken continuously during fusion for single layers as well as after fusion over a significant portion of an entire part build. To reduce metallization of the viewing window, continuous monitoring is

not employed for entire part builds. For a representative part build, surface temperatures rise while the start plate thermocouple readings fall, meaning that start plate temperatures are a poor indicator of part surface temperatures and should not be used for feedback control.

Complicated temperature profiles are seen following fusion of each layer and suggest that bulk heat transfer in the system is fast enough to affect neighboring part temperatures before fusion of a subsequent layer. When all of these temperature profiles are aggregated, it becomes clear that temperature anomalies, or 'hot spots', generated during fusion of a layer dissipate before fusion of the subsequent layer. Thus, a feedback control system for controlling solidification microstructure could be based on average surface temperature measurements, ignoring spatial variation in surface temperature. Subsequent results show that this finding should be further explored when there is a significant difference in heat input between different parts within a build.

The trend in solidification cooling rates with substrate temperature from simulations is then used to generate a feedback control strategy to keep prior beta grains constant through the use of power changes between layers during a part build. This feedback control is successfully implemented on an Arcam A2 machine at UTEP and shows that prior beta grains can be held constant throughout the height of a build by controlling solidification cooling rates. The temperatures increase during the builds in which the control strategy is implemented, but to a lesser extent than if no control is implemented. When the deposition rate is increased from nominal, the control strategy is still able to keep the prior beta grain size constant, further validating the control strategy. The control strategy also has the secondary effect of eliminating the swelling seen in the cylinders that did not have their powers controlled (reference), and shows that swelling can be mitigated even as surface temperatures increase throughout the height of a build.

Chapter 3 - High Temperature Evaluation of Select Laser Powder Bed Fusion Processes

3.1 Background and Overview

There are many laser powder bed fusion (LPBF) machines, made by several manufacturers. This chapter focuses on the EOS M290 (EOS GmbH, Krailling, Germany)[16] at CMU and the prototype system to the current Additive Manufacturing Metrology Testbed (AMMT) [105], [106] developed by NIST. LPBF works in a similar fashion to EBM, but uses a laser beam as a heat source instead of an electron beam and does not use the laser beam to heat the start plate or the powder during the build. In addition, the powder size distribution is smaller[17], the layer thickness is generally smaller, the melt pool size is generally much smaller, and deposition occurs in an inert gas environment as opposed to a vacuum.

Heating of the build is usually accomplished using a resistive heating element in the build platform. In the case of the EOS M290, heating is available up to a maximum of 200°C [145], which is in line with other manufacturers. Powder is typically spread from a feed hopper by a hardened steel blade attached to the re-coater assembly. Any excess powder ends up in the collector hopper on the opposite side of the build tank. Mirrors are attached to galvanometers capable of high accelerations to direct the laser radiation and an F-Θ lens is used to change the focal plane from spherical to flat so that the focal plane of the laser coincides with the build plane [56]. The standard temperature feedback is the same as the Arcam machine: a thermocouple underneath the

[16] While the EOS trade name for the EOS process is Direct Metal Laser Sintering (DMLS®), the process is still a form of Laser Powder Bed Fusion (LPBF).

[17] The standard Arcam Ti64 powder has a nominal size distribution between 45 and 105 μm in diameter [73] and has an average particle diameter of 60 μm [191], while the standard EOS Ti64 powder has an average particle diameter of 36 μm [191].

build plate. A vacuum is not pulled in the chamber as it is deemed unnecessary for deposition to occur (unlike in the EBM process). Instead, an inert gas (in these experiments, argon) is blown across the top surface of the build to carry away deposition byproducts and reduce oxidation of the exposed metal. Figure 3-1 shows the Argon gas outlets and inlet, collection hopper, build plate, feed hopper, and re-coater assembly inside the EOS M290.

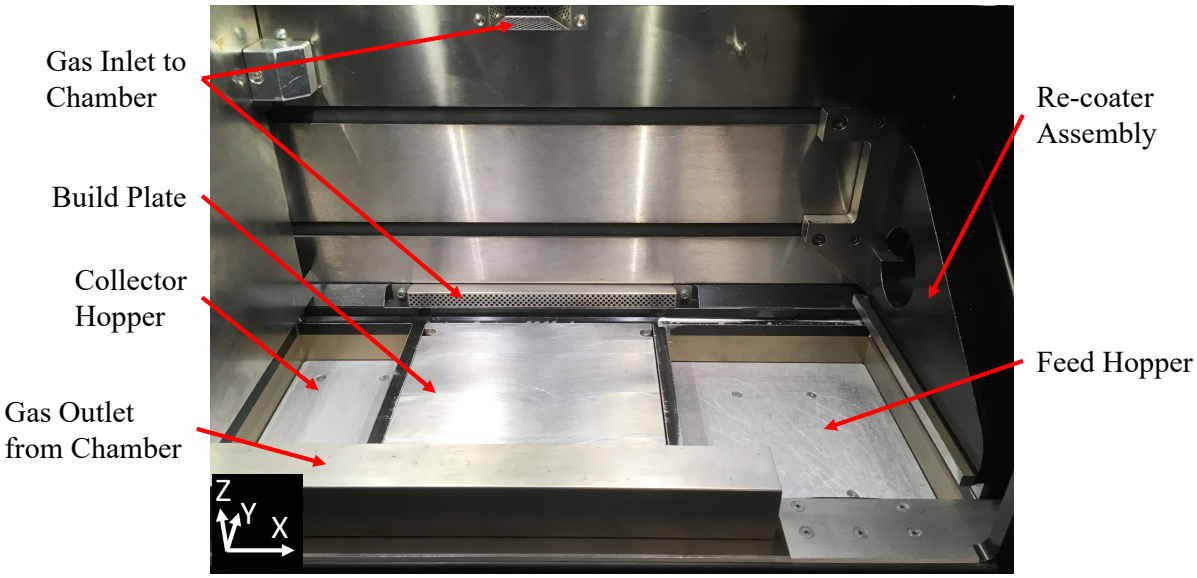

Figure 3-1: An image of the build chamber in the EOS M290 with select components labeled.

A well-known limitation of the LPBF process is the introduction of significant residual stresses in a part during deposition. These residual stresses have been shown to cause varying levels of part deformation depending on the material used, geometry of the part and the support structures employed [146], [147]. If the support structures are not adequate for the geometry being printed, the part may fail during deposition due to impacts with the re-coater blade or a loss of tolerance in the overall part geometry [119]. An increase in part temperature during deposition can relieve residual stress, though temperatures below certain levels will not do so quickly enough to stress relieve a part during production. For most AM suitable alloys, the temperature required to

stress relieve a part during production is considerably above the EOS M290 limit of 200 ˚C [14], [148], [149]. At the time of this writing, there is only one commercial LPBF machine manufacturer that has an option for a high temperature build plate to the Author's knowledge [150].

An important material attribute of Ti64 is its stress relaxation behavior. Schmidt and Wood [151] showed that both temperature and time are important considerations for resultant residual stress levels in parts. From their findings, part temperatures above roughly 600 °C stress relieve Ti64 in a matter of minutes, and is the reason that parts made in the Arcam process are generally considered stress-free. A complicating factor in understanding the distortion of AM parts is the relationship is between substrate temperature and residual stress in a part being printed when the substrate temperature is not high enough to stress relieve on short timescales. Two aspects of LPBF that complicate the prediction of this relationship are the cyclic nature of temperatures at a single location within a part and the temperature-dependent thermal contraction of a part. Mukherjee et al found that Ti64 is more susceptible to thermal strain than IN625 or SS316L [152]. Several authors have found spatially varying, thermally induced, residual stresses in AM parts [32], [68], [69], [71].

Both the laser passing over adjacent material within a single layer and the deposition of subsequent layers contribute to cyclic temperature profiles with peaks above the nominal substrate temperature. As substrate temperatures are increased, the temperature difference between solidification and the existing part temperature is decreased, reducing the amount of local part shrinkage due to cooling. In addition, as the substrate temperature is increased, the yield stress of a material will decrease, limiting the maximum induced residual stress within a material [70], [153]. Therefore, an increase in substrate temperature acts to reduce the initial residual stress as well as allow the stress in the part to relax more quickly. Given all of these complicating factors,

temperatures up to at least 500 °C are be explored to determine their effect on part distortion, melt pool dimensions, microstructure and deposition quality in LPBF parts.

In this chapter, the development of an insert (module) for the EOS M290 that allows for the production of parts at temperatures up to 500 °C is presented. This insert is then used to characterize Ti64 single beads produced at a wide range of power, velocity, and part temperature combinations in the EOS M290. Characterization of melt pool dimensions and the variability that can be expected in single beads without the use of powder is determined and this information informs subsequent experiments on the prototype system at NIST. The results from this chapter are used to build parts at elevated temperature in the EOS M290 (Chapter 4), inform the development of a methodology to produce optimized scan strategies for LPBF processes (Chapter 5), and in the characterization of thermal emission from the melt pool using a high speed, visible light camera in both the EOS M290 and NIST prototyping system (Chapter 6).

3.2 Methods

3.2.1 High Temperature Insert Design

The maximum substrate temperature that can be attained in the EOS M290 is 200 °C. In order to determine the effects of elevated temperature in the LPBF process, an insert for the EOS M290 is developed that is capable of heating a small build plate to at least 500 °C. The major design considerations for the construction of an insert to increase the usable substrate temperature range of the EOS M290 is that the existing hardware within the machine cannot be exposed to temperatures above 200 °C, spreading of powder during part production is not affected, and that none of the existing hardware (except for consumable items) or software needs to be modified. For

these reasons, it is necessary to design an insert that would ‘bolt on’ to existing hardware while being controlled separately from the existing software.

The author chose to add a resistive heater to a thermally conductive carrier and bolt a build plate to that carrier in order to attain the required 500 °C substrate temperature. High temperature, thermally conductive cement is used to bond a resistive ring heater to the build plate carrier and a PID temperature controller is used to maintain the temperature of the build plate. Thermally isolating the build plate carrier from the existing build chamber is accomplished using ceramic standoffs. In order to house this assembly within the existing build chamber, the new build plate must be smaller than the existing build plate. A usable build area of 72 mm by 72 mm is chosen in order to be large enough to build parts of interest, small enough to easily fit inside the existing build chamber, and sized to work with a commercially available heater. The smaller build area requires that a plate (called the ‘capping plate’) be mounted to the build chamber and surround the new build plate to allow powder to be spread over the new build plate as opposed to falling into the gap created between the new build plate and existing build chamber.

To power the heater and get feedback about temperatures, wires for power and thermocouples are routed under the re-coater blade and out one of the existing ports in the EOS M290 chamber. The wires could have been routed through the existing build carrier and out the back of the build tank, but this was deemed unnecessarily intrusive and would have detracted from the ‘bolt on’ nature of this device. The AC power wires and the thermocouples are separated from each other in order to reduce noise in the thermocouple signal. High temperature polyamide tape is used to seal gaps between the capping plate and the build chamber and a woven, flexible, carbon fabric is used to act as a seal between the capping plate and the Ti64 build plate to keep as much powder from falling below the capping plate as possible. A wall around the edge of the Ti64 build

plate is printed as part of each build in order to maintain the powder seal between the capping plate and the Ti64 build plate.

A 500 W resistive ring heater is chosen based on availability and expected performance[18]. Stainless steel 410 is chosen as the plate carrier material due to its high strength at temperatures up to at least 500 °C, thermal expansion coefficient similar to Ti64, and relatively high thermal conductivity [154]. Low carbon steel is chosen for the capping plate because of its commercial availability and ease of machining. In order to ensure that the re-coater blade does not impact the wires or thermocouples that are added to the system, sections of the re-coater blade are ground down to increase the gap between the re-coater assembly and the build chamber walls in select locations[19]. The placement of the ground down sections is chosen to avoid the areas of the build plate where an even powder layer is required.

The high temperature insert is shown in Figure 3-2 with select components labeled. Figure 3-3 shows the high temperature insert installed in the EOS M290 build chamber. It is bolted to a standard build plate that mounts to the ceramic standoffs. Type K, 30 gauge thermocouples with glass fiber insulation (Omega Engineering, Stamford, CT) are welded to select locations on each Ti64 build plate using a HotSpot 2 Thermocouple Welder (DCC Corporation, Pennsauken, NJ) in order to monitor the temperature of the build plate and provide feedback to the temperature controller.

[18] Simple thermal calculations to determine the amount of heat lost to the surroundings were conducted to generate a rough estimate for the heater power requirements. Only a select few heater options are readily available, so the most appropriate was chosen.

[19] The re-coater blade is considered a consumable item in the EOS M290, and is easily and routinely replaced during normal operation.

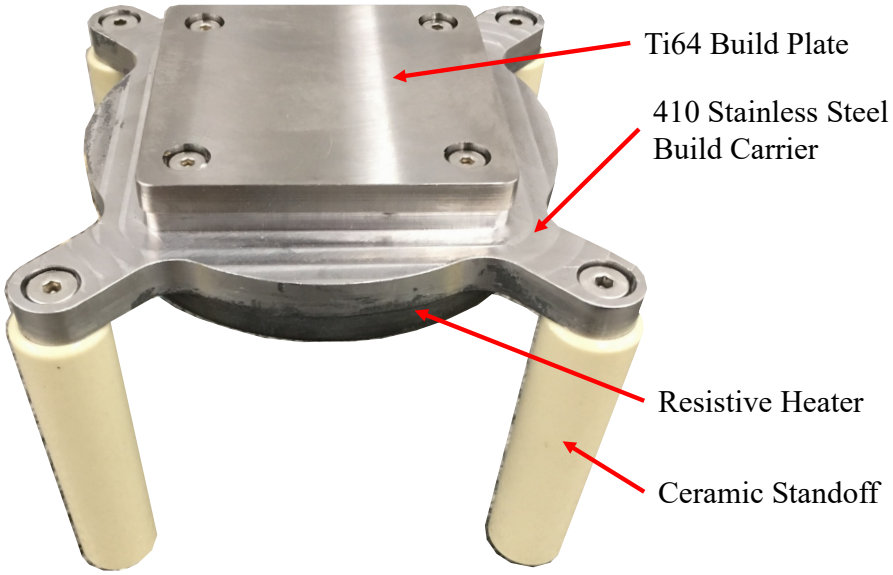

Figure 3-2: The high temperature insert with various components labeled.

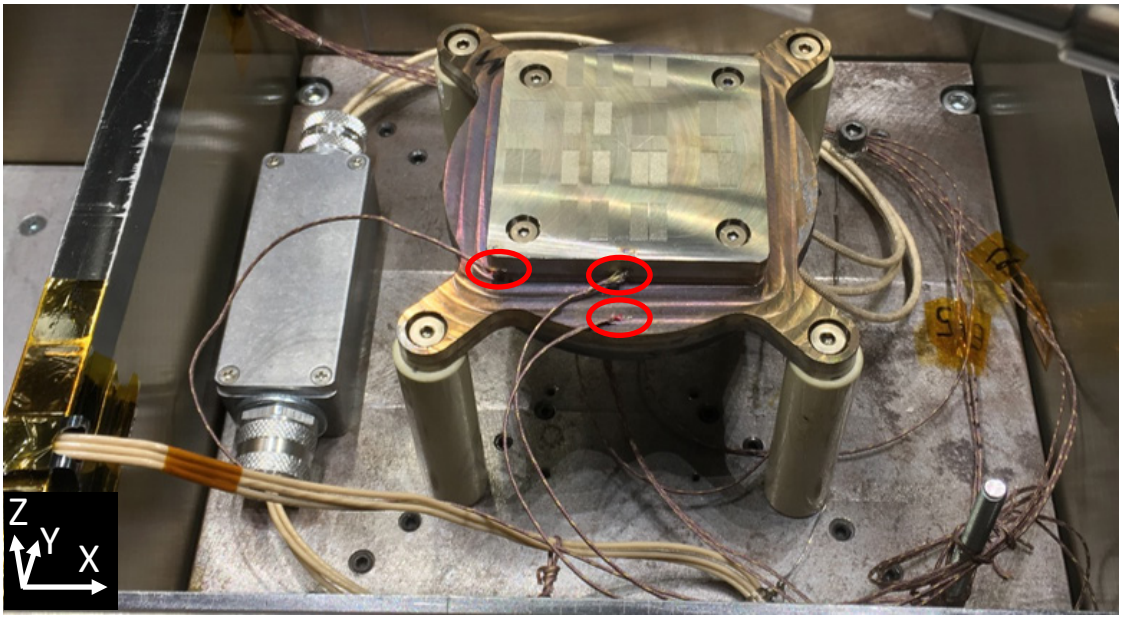

Figure 3-3: The high temperature insert bolted to an existing build plate within the EOS M290 build chamber with power and thermocouple wires shown. The thermocouples are welded to several locations on the build plate and build carrier (circled in red) to test the heat distribution in the system during initial characterization.

Figure 3-4 shows the capping plate, polyamide tape, and carbon fabric installed. The thermocouples and power wires enter the build chamber via the left wall to minimize the effect on powder spreading (since the re-coater spreads from right to left, or the –X direction). The red highlight in the image shows the locations where the ground down re-coater blade will affect spreading.

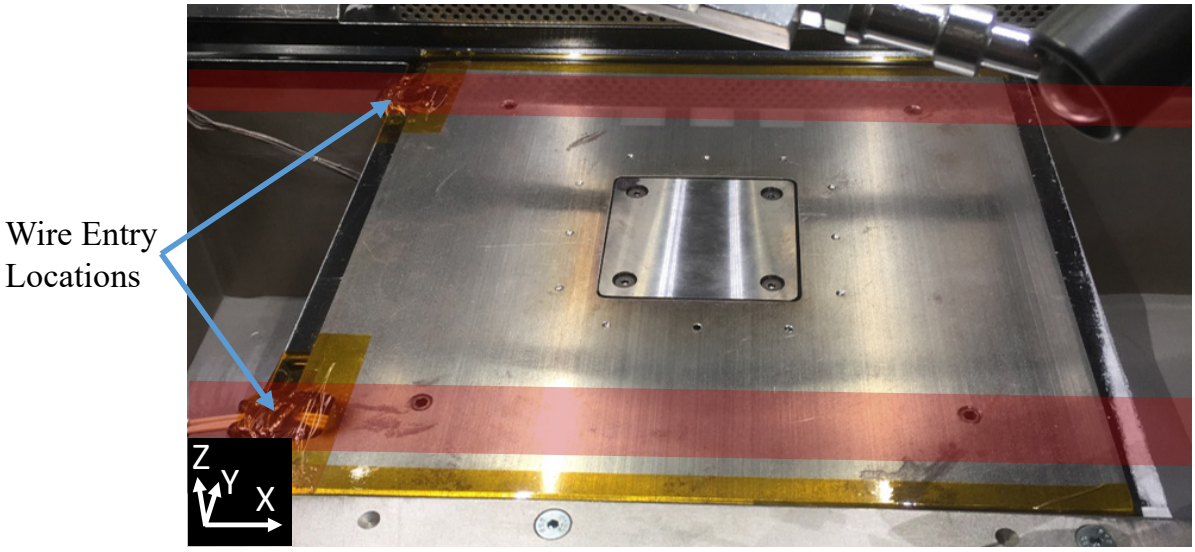

Figure 3-4: The high temperature build plate showing through the capping plate within the EOS M290 build chamber. The setup in this image is ready for powder to be spread. The red highlights show the locations where the powder spreading will be impacted due to the ground sections of the re-coater blade.

Figure 3-5 shows one of the sections where the re-coater blade is ground down to increase the gap between the existing build chamber and the re-coater mechanism. The red highlight in this image matches with the red highlight in Figure 3-4.

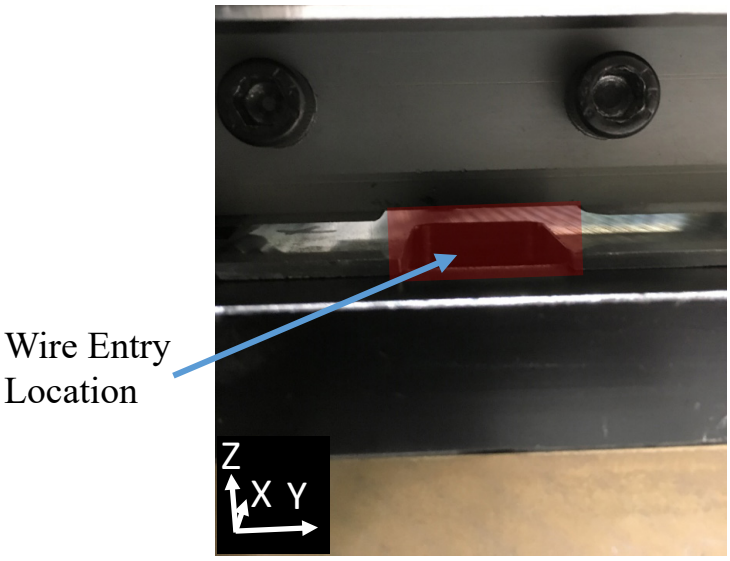

Figure 3-5: Slots cut in the tool steel re-coater blade line up with the access holes for wiring in the capping plate to allow enough clearance to ensure that wires are not impacted during the printing process. The red highlight corresponds to the red higlight in Figure 3-4.

3.2.2 Process Mapping

The same process mapping approach that was used in Chapter 2 is used in this chapter. Please refer to section 2.2.1 for more information.

3.2.3 Finite Element Modelling

The same finite element simulations that were used in Chapter 2 are used in this chapter. Please refer to section 2.2.2 for more information.

3.2.4 Single Bead Experiments at CMU

Using the high temperature insert, successive single beads are generated on a machined plate without powder at 36 power-velocity-substrate temperature combinations (parameter sets). As with the Arcam single bead experiments in Chapter 2, powder is excluded from this experiment in order to more accurately determine melt pool cross sectional area and reduce uncertainty in the measurements. In order to understand the variability in each melt pool cross section without having to serial section the samples, 20 single bead tracks are generated for each parameter set. For ease of measurement the single beads are only separated by 275 μm, however, heating from adjacent scan tracks is eliminated via a custom scan strategy. Successive scan tracks are separated by at least 5 mm and adjacent scan tracks are separated by at least 60 seconds to ensure that the substrate temperature during deposition is always at the expected value[20].

The plate is then sectioned in the center of each scan track[21] perpendicular to the laser path using a wire EDM, mounted in Bakelite, and polished [137]. The polished samples are then etched by immersion for 30 seconds in Kroll's reagent [138] (2 mL HF, 6 mL HNO_3, 92 mL distilled water). Figure 3-6 shows the plate before sectioning and representative cross sectional images after etching.

[20] To keep the substrate temperature constant for all single beads, a single scan track for each power-velocity combination at a specified temperature is deposited, then a delay is initiated, then the next set of scan tracks are deposited adjacent to the first. This procedure is repeated 20 times in order to get 20 tracks for each power-velocity combination. The temperature of the plate is then changed and the procedure repeated such that all power, velocity, substrate temperature combinations end up on the same plate, seen in Figure 3-6.A.

[21] As with the EBM single beads, the length of the EOS single bead tracks is set as at least 4 times the length required for the largest melt pool to reach steady state dimensions based off of finite element simulations. The steady state region of the bead is then defined as the center 25% of the track length. For these experiments, the absolute track length is 10 mm.

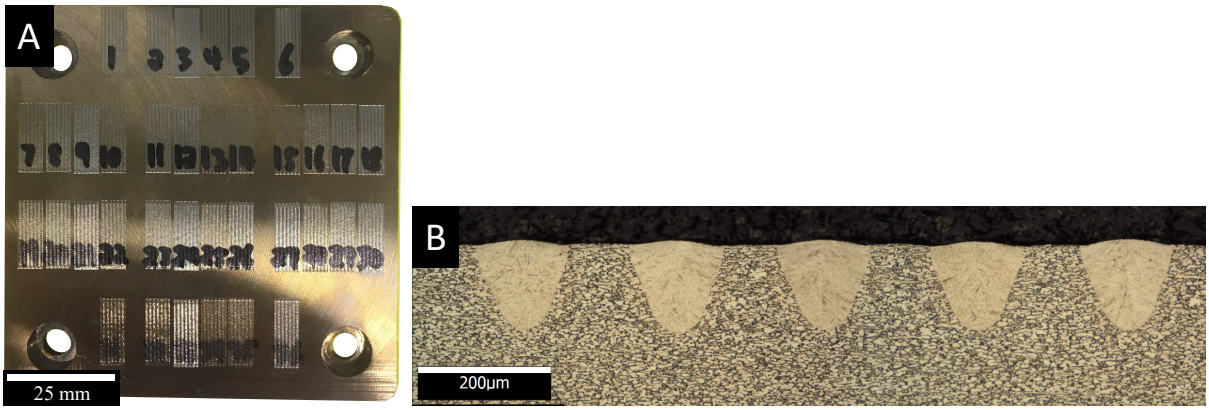

Figure 3-6: A) Top view of the Ti64 build plate after single bead tracks have been deposited. The plate is 2.8" square. B) A representative sample of single beads for EOS nominal parameters (280W, 1200 mm/s, 35 °C plate temperature).

The 12 power-velocity combinations used to generate the single beads are chosen to span the range of process parameters that would likely be employed in a LPBF system with a similar beam profile, powder size distribution, and layer thickness to those used for the default parameter set for Ti64 in the EOS M290. Unlike prior process mapping work, the parameter sets are chosen to be targeted in order to reduce the total number of necessary melt pool cross sections. The standard parameters used by EOS for bulk melting of 30 µm layers (280 W, 1200 mm/s, hereafter referred to as 'nominal parameters') and 60 µm (340 W, 1250 mm/s) layers are included so that direct characterization of the standard parameters is available. Figure 3-7 is a plot of those combinations in power-velocity space. Each combination is deposited at target temperatures of 25, 300, and 500 ˚C, chosen to span the temperature range of interest in this work.

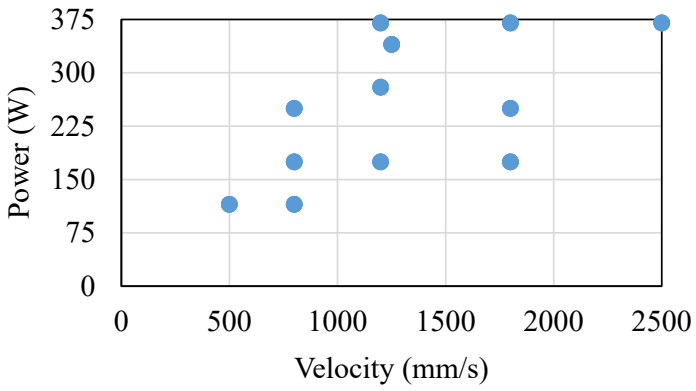

Figure 3-7: The process parameters used to deposit single beads at each substrate temperature.

The resultant melt pool cross sections are imaged using an optical microscope and the melt pool cross sectional area is recorded for each track. As in Chapter 2, melt pool area is measured from the existing substrate surface in order to accurately measure the amount of material that is melted by the laser pass[22]. The standard deviation for the melt pool area sampling error is measured to be between 0.9% and 2.1%[23], while the standard deviations of the melt pools are measured to be between 1.7% and 5.2%[24]. This shows that the overall melt pool area variation is very low, and in most cases close to the measurement error. The standard deviations are used to generate 95% confidence intervals for the average melt pool area of each parameter set. The process parameters, width, depth[25], and area, along with standard deviations for these values, can be found in Appendix 2 for each parameter set.

[22] For a more in depth explanation of the reasoning behind this measurement strategy, please refer to section 2.2.3.
[23] Measurement error estimates are done by sampling the same melt pool 20 times and generating a standard deviation. Three parameter sets are used to generate the range of error estimates presented above, chosen to span a range of melt pool sizes: keyholing (370 W, 1200 mm/s), nominal parameters (280 W, 1200 mm/s), and small (175 W, 1800 mm/s).
[24] Standard deviations are generated from the areas measured for each of the 20 melt pools for each parameter set.
[25] Melt pool width refers to the maximum width of the melt pool cross section and is found at the surface. Melt pool depth refers to the maximum depth of the melt pool from the original substrate surface.

The thermocouple placement for the single bead experiments at CMU are shown in Figure 3-8. These locations are chosen to give a good representation of the span of temperatures across the plate surface. Those temperatures can be seen in Table 3-1.

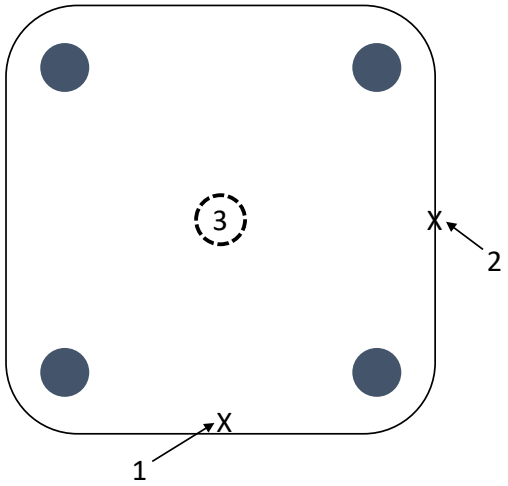

Figure 3-8: Thermocouple locations on the build plate for single bead experiments. Thermocouple 1 is welded to the top of the plate and thermocouple 2 is welded to the side of the plate, both at the locations indicated by an x. Thermocouple 3 is welded to the bottom of the plate in the location indicated by the dashed circle.

Table 3-1: The average temperature and standard deviation over the time that the single beads are deposited for each thermocouple.

Thermocouple #	Target Temperature (°C)	Actual Temperature (°C)	Standard Deviation in Actual Temperature (°C)
1	25	28.9	0.04
2	25	30.4	0.07
3	25	30.7	0.03
1	300	276	1.0
2	300	290	0.8
3	300	298	0.8
1	500	476	4.2
2	500	496	3.4
3	500	500	2.5

The target temperatures for the experiments were 1) 25 °C, 2) 300 °C, and 3) 500 °C. The actual temperature for 1) is roughly 30 °C. The small spread in temperatures between thermocouples show that the data acquisition system does not induce any systemic errors. The small standard deviation for each thermocouple shows that the heat imparted by the laser during deposition is not significant and the noise in the data is low. The average temperature for 2) is between 275 °C and 300 °C. The average temperature for 3) is between 472 °C and 503 °C. The temperature range for 2) and 3) is not insignificant, but in each case the surface temperatures are likely more uniform and toward the lower part of the range since thermocouples 2 and 3 are not welded to the top surface of the plate and the resistive heater is located on the bottom of the plate.

3.2.5 Single Bead Experiments at NIST

Experiments are also conducted at NIST on the prototyping system developed as a precursor to NIST's current Additive Manufacturing Metrology Testbed (AMMT) [105][106]. An analysis of this data is included here in order to compare to monitoring results in Chapter 6. The monitoring capabilities associated with the EOS M290 and NIST prototyping are fundamentally different, and the ability to compare ex-situ experimental results (generated in this chapter) to data gathered in-situ (Chapter 6) from both machines is very important.

The only notable modifications to the prototyping system are the addition of a heater and thermocouples welded to the Ti64 substrates used for the experiment[26]. Argon is pumped into an acrylic enclosure, called the 'purge box', which surrounds the heater and substrate. A window on the top of the purge box is specifically designed to allow the laser to pass through it. The

[26] The thermocouples and method of attachment are the same as in section 3.2.4. The Ti64 plate size was 70 mm long by 30 mm wide by 3 mm thick. Those dimensions were chosen in order to use readily available material at the time of the experiment.

experiments are conducted when the oxygen percentage in the purge box is measured to be below 1000 ppm[27]. Figure 3-9 shows the purge box with the front panel removed, and select components labeled. Figure 3-10 shows a schematic of the Ti64 substrate, single bead locations and direction, and sectioning locations.

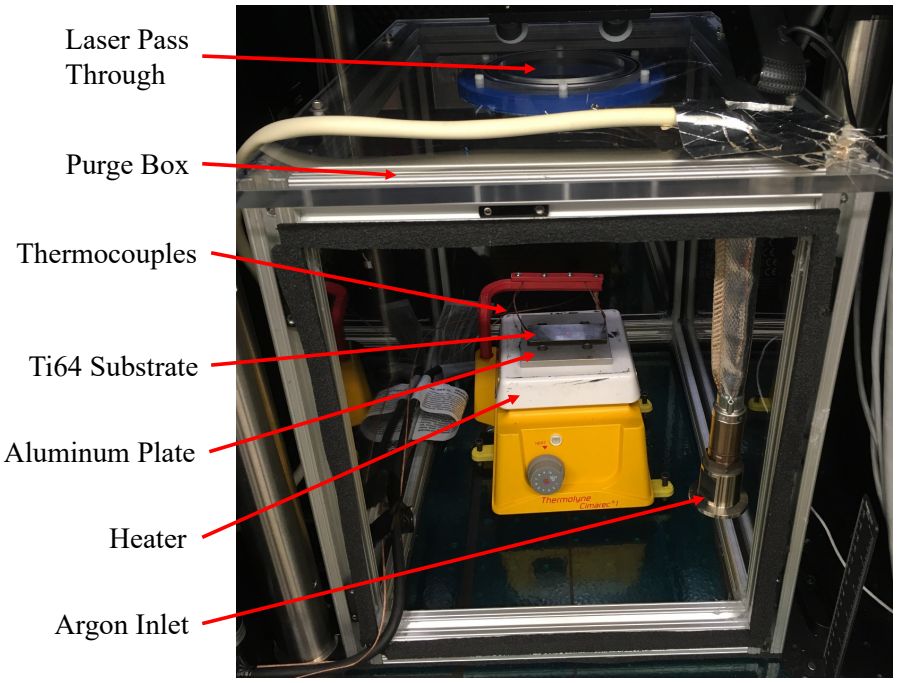

Figure 3-9: Experimental setup for NIST single bead experiment with select components labeled.

[27] 1000 ppm is chosen as the upper limit for oxygen concentration in order to coincide with the conditions during deposition in the EOS M290, which also has an upper allowable oxygen limit of 1250 ppm O_2 for the laser to fire, but generally operates below 1000 ppm during deposition.

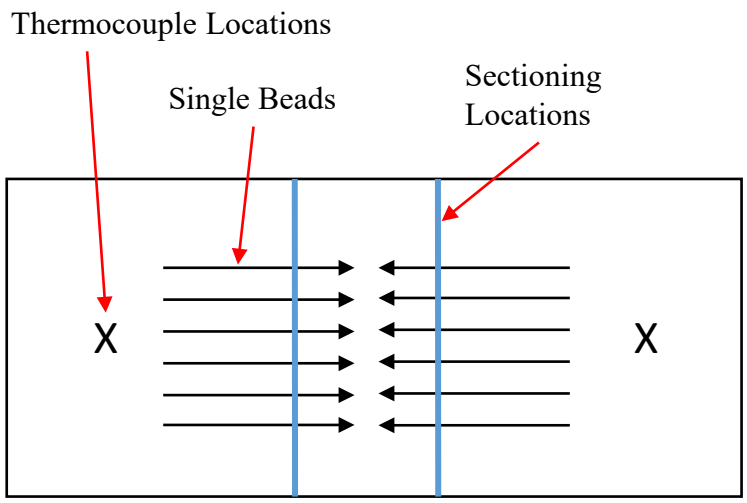

Figure 3-10: Schematic of the single bead, thermocouple, and cross section locations for the experimental plates used for the NIST single bead experiment.

Data acquisition is not developed for the thermocouple assembly, and the heater does not have an external temperature controller. Temperatures are read manually using a handheld type K thermocouple reader (Part # HH12B, Omega Engineering, Stamford, CT). In order to attain the target temperature, the heater is turned on until the substrate temperature is above the target temperature by at least 20 ˚C. The power to the heater is then turned off and the laser scans are completed when the thermocouple temperature crossed the desired temperature. In all cases, the temperature read by the thermocouples is within 10 ˚C of the target temperature. The maximum attainable substrate temperature is 480 °C, so the target temperatures for single beads are set as 25 °C, 300 °C, and 450 °C.

An F-θ lens is not used in these experiments, so the laser is focused to a sphere, not a plane. In addition, the profile of the beam had not been characterized at the time of the experiment. A characterization of the depth of focus of the laser was done, however, by Jason Fox at NIST and the results of that characterization are used to lay out the single bead experiment. Specifically, the

depth of focus is defined as the focal length range over which the melt pool width did not vary by more than 10%[28]. The individual tracks for this experiment are laid out on the substrate such that the locations were cross sectional area is taken is within the depth of focus at locations of steady state melt pool geometry[29]. Because of the area constraints and the low variability seen in the single beads done on the EOS machine (section 3.2.4) only one single bead and only one melt pool cross section is generated for each parameter set.

3.3 Results

3.3.1 Simulation Process Map

A process map, based on simulations, for melt pool area is created for the LPBF process at 35, 300, and 500°C. Curves of the same color correspond to the same quantity of interest. Solid lines represent 35 °C, dashed lines 300 °C, and dotted lines 500 °C. As was the case in section 2.3.1, Figure 3-11 shows that as temperature increases, curves of constant area will shift down and to the right on a power vs velocity plot.

[28] The characterization completed by Jason Fox results in a usable substrate area with a diameter of 50 mm. This is more than enough to complete the necessary single bead experiments.
[29] Single bead track length is set as at least 4 times the length required for the largest melt pool to reach steady state dimensions based off of finite element simulations. The steady state region of the bead is then defined as the center 25% of the track length.

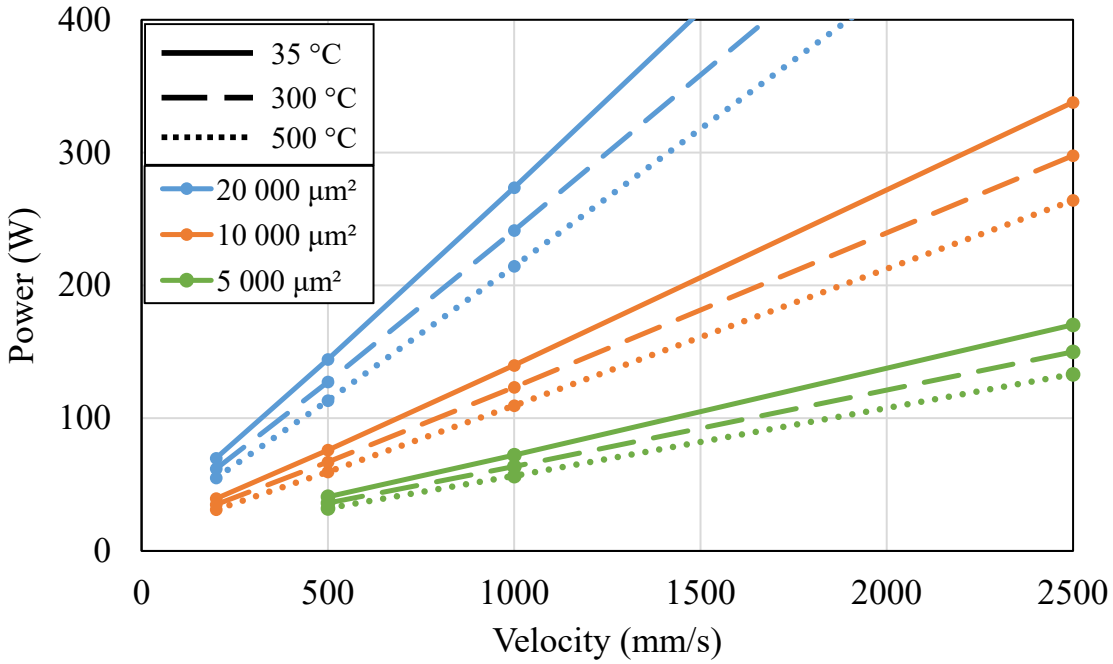

Figure 3-11: Plot of curves of constant area in the EOS process from finite element simulations. Each curve of the same color represents the same area at a different substrate temperature. A constant absorptivity of 1 is assumed for all curves.

3.3.2 EOS Experimental Process Map

The data in Appendix 2 can be used to generate lines of constant area through process space, allowing a machine user to easily tailor the melt pool size for a given application and understand the sensitivity of melt pool area to process inputs. Figure 3-12 shows a process map with three lines of constant area generated from linear interpolation of the experimental results at 35 °C. Each line is chosen to be different from the preceding line by a factor of 50%. The error bars on the interpolated points are generated by replacing the average experimental areas with the top and bottom values of the 95% confidence intervals for each data point and re-running the interpolation. The dotted lines are the best fit lines to the interpolated average points, and the solid lines are the curves of constant area generated from finite element model (simulation) results. The values attached to each line are the effective absorptivity necessary to make the simulation results match

with the experimental results. It is clear that the slope of the best fit lines matches very well with the curves generated from simulations. The effective absorptivity increases as the melt pool cross sectional area increases, which matches with previous work [30], [31], [134]. This is likely a result of the increase in actual absorptivity with an increase in melt pool cross sectional area due to the greater effect of internal reflections of the laser in the vapor cavity [155].

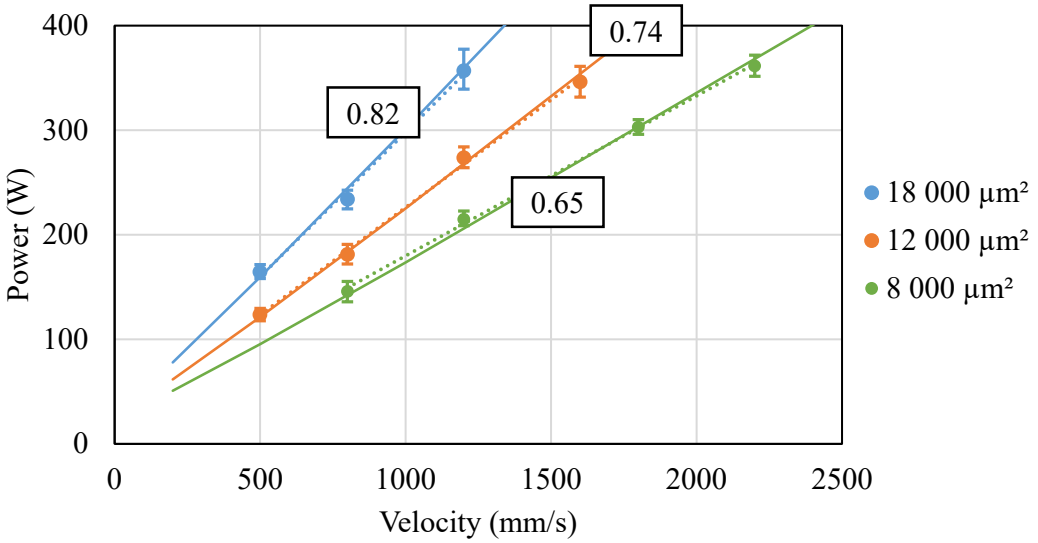

Figure 3-12: Curves of constant area for the EOS M290 at 35 °C. The boxed numbers represent the effective absorptivities that give the best agreement between the simulated and experimental curves.

The same figures can be made for melt pools at 300 ˚C and 500 ˚C (Figure 3-13 and Figure 3-14, respectively). It is clear that the curves of constant melt pool area are shifting down and to the right as the substrate temperature is increased, as was seen in Chapter 2. This result is expected because it shows that as the substrate temperature increases, the energy density necessary to generate an equivalent melt pool area decreases.

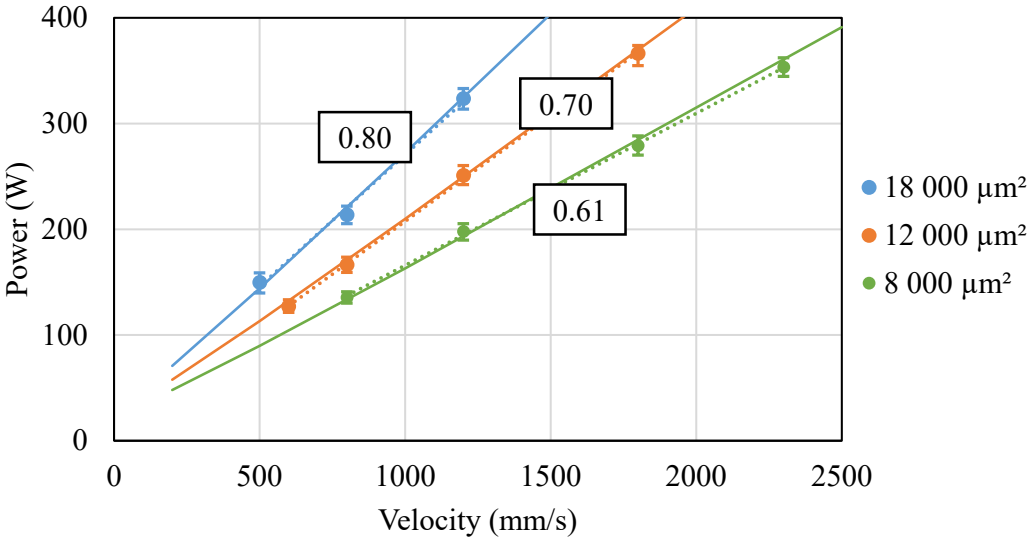

Figure 3-13: Curves of constant area for the EOS M290 at 300 °C. The boxed numbers represent the effective absorptivities that give the best agreement between the simulated and experimental curves.

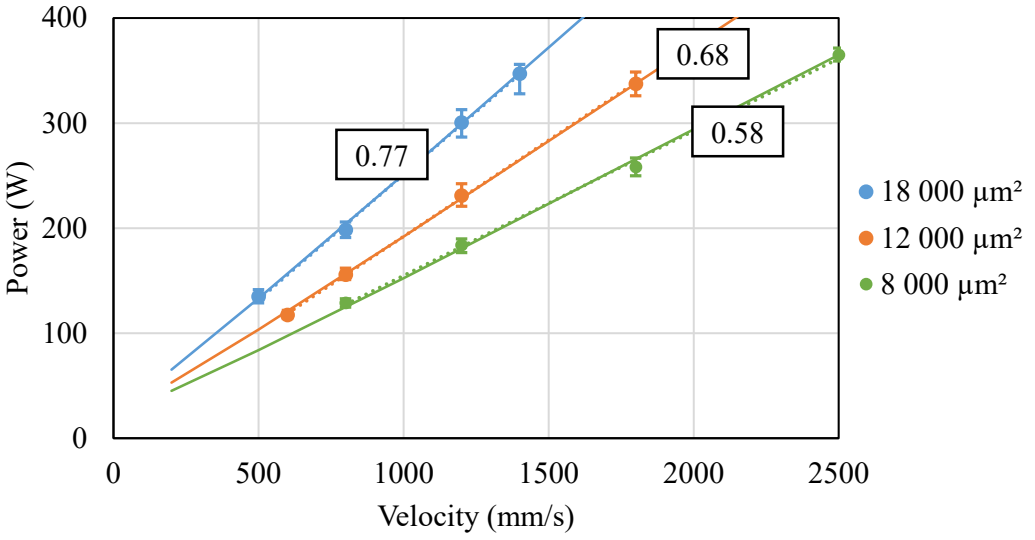

Figure 3-14: Curves of constant area for the EOS M290 at 500 °C. The boxed numbers represent the effective absorptivities that give the best agreement between the simulated and experimental curves.

There is a difference in the appropriate effective absorptivity to use, depending on substrate temperature, as can be seen in Figure 3-15. The error bars in this figure are generated by determining the effective absorptivity necessary to match the upper and lower bounds of the experimental error bars in Figure 3-12, Figure 3-13 and Figure 3-14. The trend is a reduction in effective absorptivity with an increase in substrate temperature, though the absolute changes are small, and on the order of the size of the error bars.

Though relatively small, this decreasing trend in effective absorptivity with increasing substrate temperature shows that the conduction-based simulations are slightly overestimating the melt pool area increases induced by substrate temperature increases and is likely due to the lack of fluid flow in the melt pool model. Fluid flow would increase the effective thermal diffusivity of the liquid by moving the superheated liquid from under the beam spot toward the edges of the melt pool, thereby transferring heat more efficiently than conduction alone. An increase in substrate temperature would reduce the thermal gradients throughout the melt pool and surrounding material. Fluid flow would reduce the effect of substrate temperature because the actual thermal gradients seen in the melt pool would not change as much as the conduction based simulation predicts. Because the change in effective absorptivity is small, the fluid flows in the melt pool are having a considerably lower effect on melt pool cross sectional area than conduction, and by equating simulations to experiments, the effect of fluid flow in the melt pool can be accounted for by knowing what effective absorptivity to use in the model.

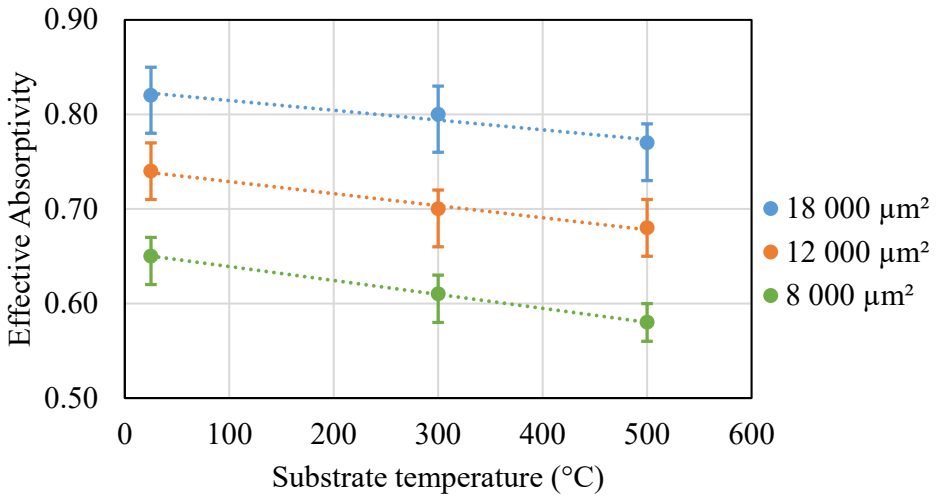

Figure 3-15: A plot of effective absorptivity with substrate temperature for different melt pool cross sectional areas.

Aggregating the data from the experimental and simulation process maps at each substrate temperature, Figure 3-16 shows how cross sectional melt pool area changes with substrate temperature. The average melt pool area for each parameter set is normalized by its value at 35 ˚C, the *Y* error bars represent one standard deviation on the mean normalized area, and the *X* error bars show the range of temperatures from section 3.2.4 for the experimental data. A best fit parabolic curve is fit to each data set and the equation for the simulation curve is displayed at the bottom of the plot. It becomes clear that regardless of original melt pool cross sectional area or parameter set, the percentage increase in cross sectional area with temperature follows a single master curve. Another important point is that the trend lines for simulation and experiment fall on top of each other, and neither data set has a significant amount of scatter. The change in effective absorptivity necessary to match the data in Figure 3-15 shows that the simulations are not capturing all of the physics of the process, but the small effective absorptivity differences coupled with Figure 3-16 show that the simulations do a very good job of capturing the changing melt pool behavior.

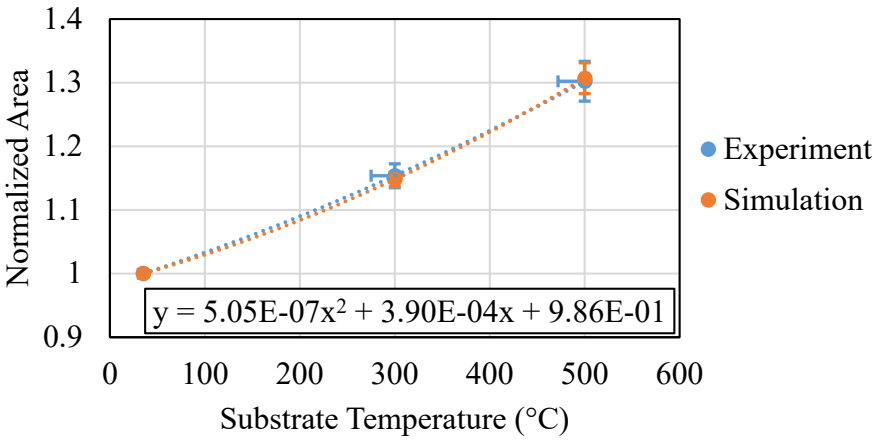

Figure 3-16: A plot of nomalized melt pool cross sectional area with substrate temperature when process parameters are not changed to account for substrate temperature increases. The blue curve is from experiment and the orange from simulation.

Figure 3-16 can be used to determine the change in power or velocity required to keep melt pool area constant as substrate temperatures are increased. The author concentrates on changing power because power changes are simpler and more computationally efficient to implement into a scan strategy than velocity changes for the LPBF process[30] [3]. Figure 3-17 shows the simulation curve from Figure 3-16, but instead of determining how melt pool area changes for constant power and velocity, this figure shows how power must be changed to keep melt pool area constant. Again, a best-fit parabolic curve is fit to the data and the equation is displayed at the bottom of the plot. Figure 3-17 can be used in a control system to keep melt pool area constant if the temperature that the melt pool encounters is known. Figure 3-17 is equivalent to Figure 2-11 and follows the same trend.

[30] Power changes are simpler to implement because the absolute values can be fed directly to the laser. Velocity changes, however, would require the calculation of the variable accelerations of the scanning mirrors needed to implement those velocity changes.

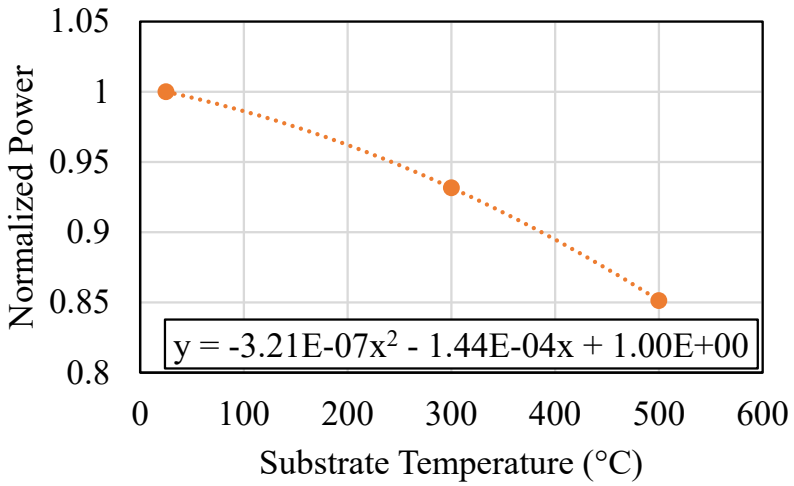

Figure 3-17: A plot of normalized power with substrate temperature in order to keep melt pool area constant. The curve is generated from simulation data.

A curve for constant solidification cooling rate is not included in this chapter because of the uncertainty as to the actual absorptivity of the laser that should be used to match simulation to experiment for cooling rates[31]. Solidification cooling rates should track with the amount of heat that needs to be removed from the melt pool, and will therefore track with actual absorptivity as opposed to effective absorptivity. This topic will be explored in greater detail in Chapter 5. What can be presented is the trend in solidification cooling rate with substrate temperature from simulation, presented in Figure 3-18. The solidification cooling rate for each parameter set is normalized by its value at 35 ˚C and the error bars represent one standard deviation on the mean normalized solidification cooling rate.

[31] The difference between effective absorptivity and actual absorptivity, along with the uncertainty it induces in simulated temperature fields, will be discussed further in Chapter 5.

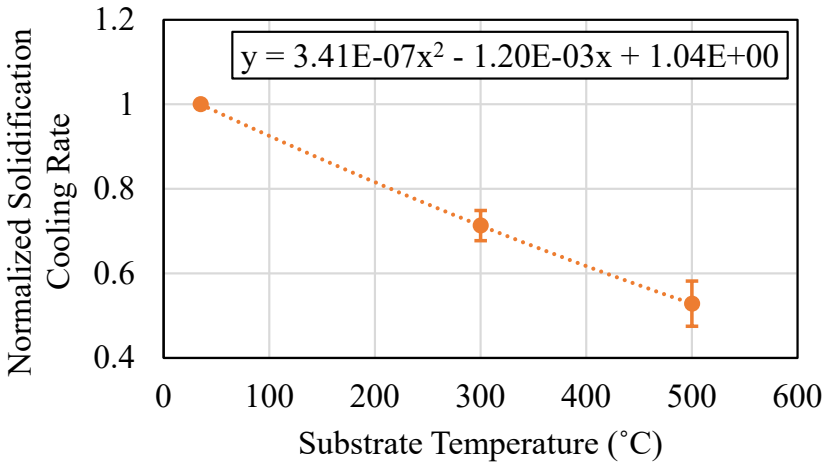

Figure 3-18: A plot of normalized solidification cooling rate with substrate temperature. The curve is generated from simulation data.

3.3.3 Aspect Ratio Changes

To determine if porosity would be more likely for Ti64 printed in the EOS process at elevated temperature, an understanding of melt pool cross section aspect ratios is necessary. In this work, aspect ratio is defined as *2*D/W*, where *D* is the depth of the melt pool and *W* is the width of the melt pool. This metric is chosen because it yields a value of 1 when the melt pool is semi-circular. Values less than 1 indicate wide, shallow melt pools, while values greater than 1 indicate that the vapor depression induced by the laser spot is intense enough to create a melt pool cross section that would be impossible to develop by conduction alone [85]. If the melt pool aspect ratio becomes too high, inadequate liquid flow during melt pool solidification will tend to leave voids toward the base of the melt pool cross section [38]. Therefore, there should be an aspect ratio above which keyholing porosity becomes likely.

It has already been determined that an increase in substrate temperature increases melt pool cross sectional area. Figure 3-19 is the normalized experimental melt pool aspect ratio as substrate

temperature is increased, and shows that the melt pool aspect ratio increases with substrate temperature as well, but not as quickly as melt pool area increases with substrate temperature (Figure 3-16).

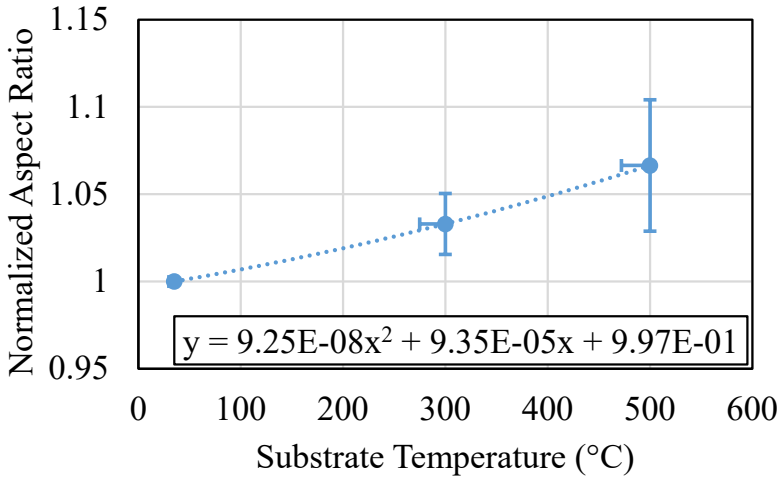

Figure 3-19: A plot of normalized aspect ratio with substrate temperature from experiment.

This result makes physical sense because of the different mechanisms that affect melt pool area and aspect ratio. Melt pool area increases will be due to deeper penetration of the heat source, slower heat conduction into the solid material (due to lower thermal gradients), and a lower temperature difference between the existing (substrate) temperature and the solidus temperature. However, aspect ratio increases should only be due to deeper penetration of the heat source. Changes to thermal gradients into the solid (due to increases in substrate temperature) and a lower temperature difference between the substrate temperature and the solidus temperature should not significantly affect aspect ratio because both width and depth of the melt pool would be affected in the same way[32].

[32] The heat equation [192, p. 85] predicts hemispherical isotherms (and therefore an aspect ratio of 1) for a point heat source. Therefore, the substrate temperature does not factor into melt pool cross sectional shape when only considering conduction.

The comparison between Figure 3-16 and Figure 3-19 shows two important trends: 1) As substrate temperature is increased, the melt pool area at which a given aspect ratio will occur increases and 2) As substrate temperature is increased for the same power and velocity combination, the aspect ratio will increase. These two trends have important implications for process development. The first shows that if the melt pool area needs to be increased without increasing the melt pool aspect ratio, the substrate temperature should be increased and the power adjusted accordingly. This gives a machine operator greater flexibility to choose process parameters that suit the individual application. In particular, this suggests that build rate can be increased without inducing keyholing porosity because the melt pool shape will stay more semi-circular for larger melt pools. The second trend shows that if a change in substrate temperature is not accounted for by changes to other process parameters (e.g. power), then the melt pool aspect ratio will increase, possibly inducing keyholing porosity. Taking both trends together, unintended changes to substrate temperature may induce porosity while controlled changes to substrate temperature can eliminate porosity.

It is important to note, however, that none of the parameter sets used here generated keyholing porosity in the single bead cross sections. This means that either the aspect ratio necessary to induce keyholing porosity in Ti64 is greater than what is seen in this research or porosity is induced, but none of the 20 melt pool cross sections happened to be in locations where a pore is present.

3.3.4 Balling Characterization

An experimental characterization of balling is also completed on the single beads conducted on the EOS M290. This gives a general range over which the introduction of instabilities in the top surface of the melt pool will occur, but likely over-estimates that range due to the lack of powder in the experiments[33]. Figure 3-20 shows an example transition from a stable melt pool cross section to a balling cross section taken from the single beads conducted on the EOS M290.

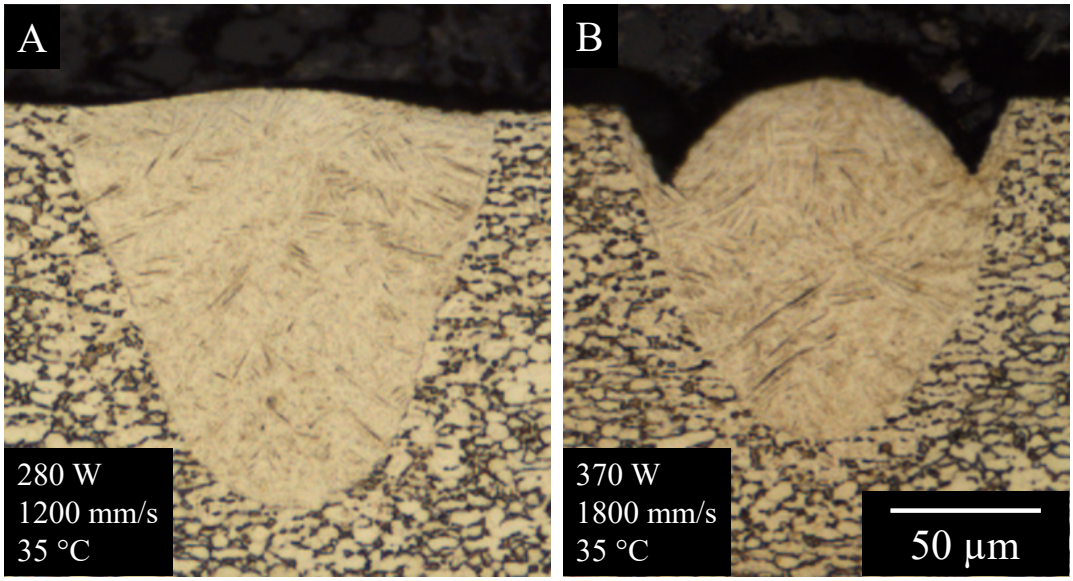

Figure 3-20: Two melt pools of roughly the same cross sectional area. (A) A stable melt pool cross section. (B) A balling melt pool due to the circular shape of the melt pool surface and steep undercuts at the edges of the melt pool.

The experimental parameter sets are not densely populated enough to see differences in the balling region of process space with changes in substrate temperature since, in all cases, the transition from stable melt pools to balling occurs between 1200 mm/s and 1800 mm/s. Prior work

[33] Powder has been shown to increase the likelihood of balling because of the agglomeration of powder particles on top of the melt pool surface. This phenomenon is often described as being due to poor 'wetting' and has the effect of increasing the depth of the deposit without significantly affecting its width. Because the added material is not as readily secured to the existing substrate, it is more likely to form a concave shape, or 'bead up' (balling) [37].

has shown, however, that balling will occur when the melt pool width to full length (W/FL) ratio drops below a value of roughly 0.32 [31], [37], [84], which in all cases presented here equates to a velocity between 1200 mm/s and 1800 mm/s[34]. This means that the current experimental results are in agreement with literature values. In addition, simulation results (Figure 3-21) show that the width to full length ratio will decrease with increases to substrate temperature because lower thermal gradients preferentially increase the length of the melt pool. This suggests that as substrate temperature is increased, the transition from stable melt pools to balling melt pools will occur at lower velocities for a given power. Because the power needed to maintain a constant melt pool area will decrease with increasing substrate temperature, however, the transition from a stable melt pool to a balling melt pool will not necessarily occur at lower velocities for a given melt pool cross sectional area. Further experimental investigation of the change in the onset of balling as substrate temperature is changed should be completed to understand these competing effects.

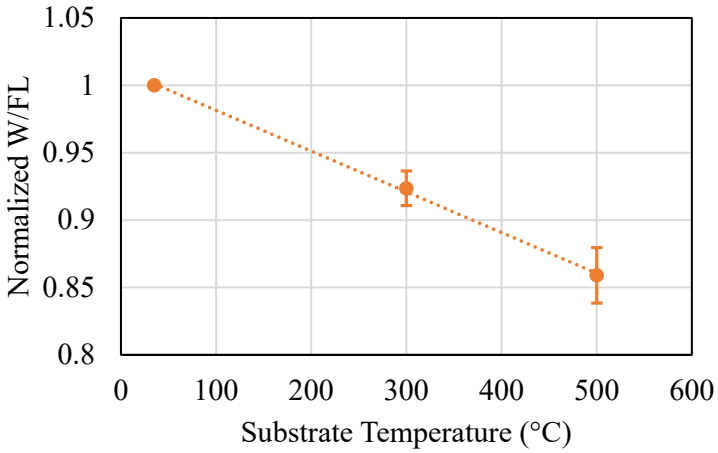

Figure 3-21: Plot of normalized width to full length ratio with substrate temperature from simulations.

[34] Using the widths measured from experiment and the lengths calculated from simulation.

While instabilities in the melt pool surface (balling) may increase surface roughness, this roughness does not translate into porosity unless it induces lack of fusion due to incomplete spreading or excessive powder layer thicknesses. The parameter sets in Chapter 4 will include balling melt pools to determine the effect of balling on porosity in bulky parts.

3.3.5 NIST Experimental Process Map

Figure 3-22, Figure 3-23, and Figure 3-24 are process maps created for the NIST testbed from the experimental data in Appendix 3 as well as finite element simulations of the melt pool. Curves of constant area from simulations are the solid lines, interpolated melt pool areas from single bead experiments are points, and best fit curves to the experimental points are the dotted lines. Each line is chosen to be different from the preceding line by a factor of 100% in order to better span the full range of possible process parameters for this machine[35]. The effective absorptivities used to match up curves of constant area from simulations with the experimental data points are displayed next to each curve. It is clear that the melt pools from the NIST machine have a much lower effective absorptivity when compared to equivalent melt pools from the EOS machine, and implies a wider beam diameter [31].

[35] The larger jumps between lines for the NIST Process Map as opposed to the EOS Process Map is due to the larger span of process parameters chosen in order to explore the full extent of processing space for the NIST machine (whereas the goal for the EOS machine was to focus on melt pools that are currently being used to produce parts).

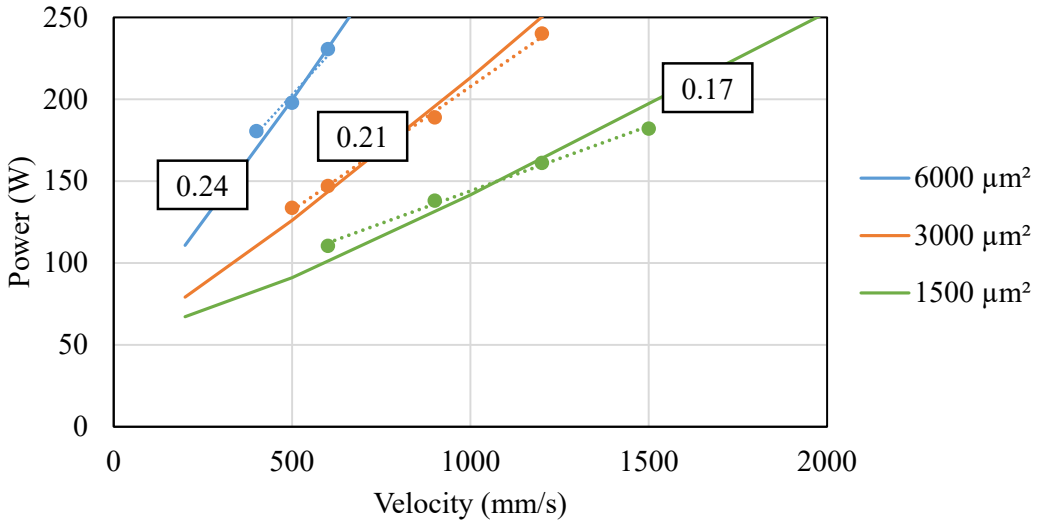

Figure 3-22: Curves of constant area for the NIST testbed at 35 °C.

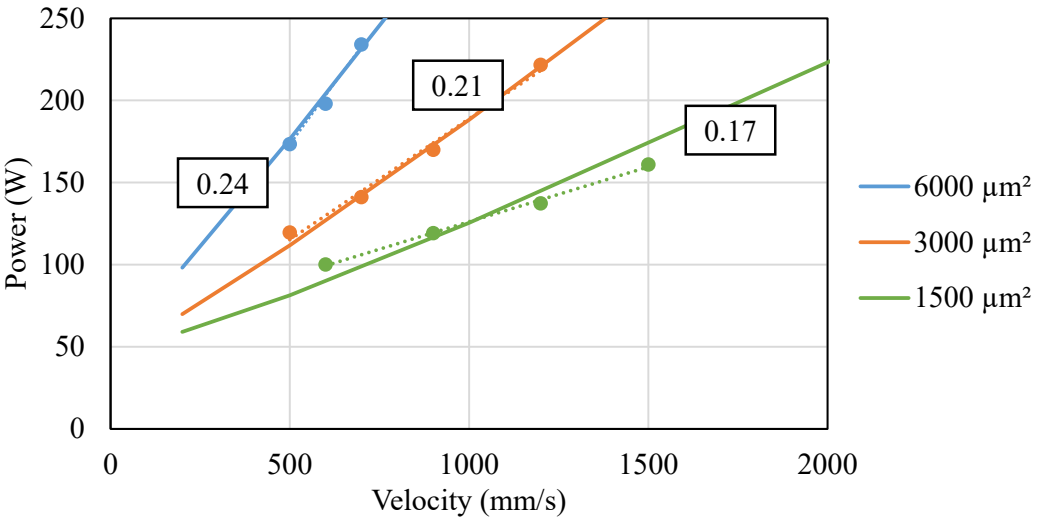

Figure 3-23: Curves of constant area for the NIST testbed at 300 °C.

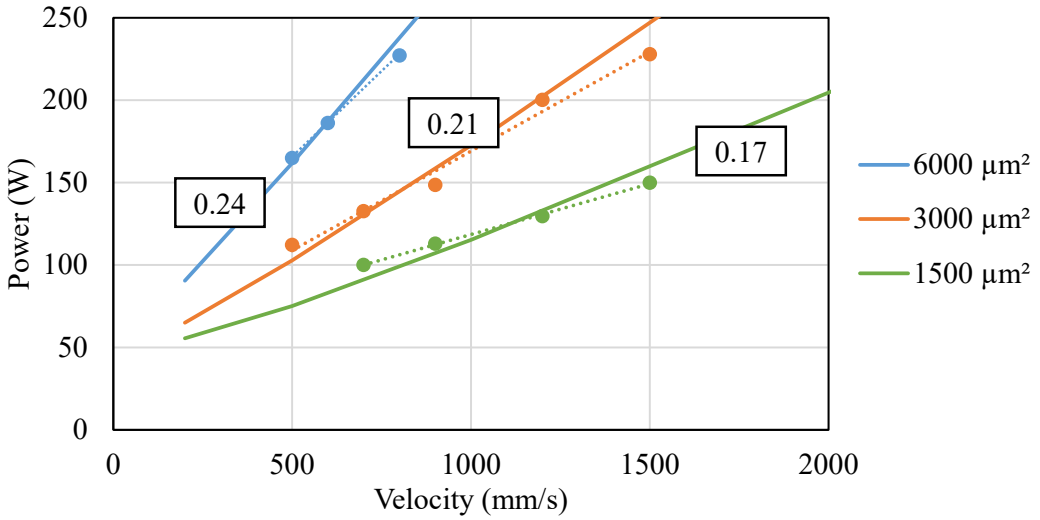

Figure 3-24: Curves of constant area for the NIST testbed at 450 °C.

For these process maps, the effective absorptivity does not seem to change between temperatures. This is possibly because there is only one melt pool cross sectional area at each parameter set, thereby increasing the uncertainty of the measurement to the point where a difference in effective absorptivity is be distinguishable. The simulated 1500 µm² curve of constant area does not match the slope of the experimental data as well as the other curves, probably due to the beam being wider than the melt pool width for these parameter sets [31].

The beam diameter of the EOS M290 at CMU has been measured to be a Gaussian profile and about 90µm in diameter using the D86 definition [31], meaning that assuming the beam profile is Gaussian, 86% of the beam energy is within the given diameter [156]. The beam diameter and profile of the laser beam on the NIST prototyping testbed had not been characterized at the time of the experiments presented in this research, and subsequent adjustment to the laser optics makes characterization of the laser beam for these experiments impossible. The beam diameter can have a large effect on melt pool cross sectional area even if all other parameters are held constant because the shape of the melt pool cross section will be affected. Francis [31] showed that melt

pool aspect ratio has a large, but predictable, effect on the melt pool area relative to a simulation that assumes a semi-circular melt pool cross section. It is clear from the differences in effective absorptivity (and therefore melt pool area for the same parameter set) between the experiments conducted at NIST and those conducted at CMU that the beam profile must be considerably different. This analysis shows that while effective absorptivities may be affected by melt pool shape, and therefore each laser powder bed machine will have its own curves of constant area, the trends with power, velocity, and substrate temperature gleaned from simulations still hold true.

3.4 Discussion

In this chapter, the feasibility of generating parts in the EOS M290 at elevated temperature is explored due to the potential reduction in residual stress that would accompany increases in temperature. 500 ˚C is identified as an appropriate maximum temperature for exploration since strain relaxation is significant starting around this temperature. No commercially available options existed for the EOS M290 at the time of this work, so a custom system that is capable of raising substrate temperature to 500 ˚C is developed. While to date, this system has only been used for the research presented in this thesis, the ability to substantially raise substrate temperature in the EOS M290 has wide ranging applications for both Ti64 and other alloys.

Single beads are deposited in order to generate experimental process maps that can be used for part production at elevated temperature. In addition, simulations of the melt pool are generated and the effective absorptivity necessary to match simulations with experiments is determined. Simulated trends are shown to match well with experimental trends, showing that simulations can be used to understand how melt pool dimensions change in response to substrate temperature changes in more complex systems. The trend in melt pool aspect ratio with substrate temperature

is also used to determine that increases in substrate temperature can be advantageous when accounted for by changes to other parameters, but are detrimental if unaccounted for (the same finding as Chapter 2). In addition, regions of process space that are likely to generate balling melt pools are identified and will be explored further in Chapter 4 to determine their effect on porosity in parts.

Process maps are also generated for the NIST AMMT prototyping system and the differences in effective absorptivities between the two machines, likely due to a difference in beam diameter, is highlighted. In both machines, substrate temperature has a large effect on the melt pool cross sectional area.

The work in this chapter acts as the basis for subsequent chapters. Specifically, the process maps for the EOS M290 will be used to generate the parameter sets for producing parts at elevated temperature in Chapter 4. The understanding of how melt pool cross sectional area changes with substrate temperature will be used in the generation of optimized scan strategies for LPBF processes in Chapter 5. The characterization of experimental results from single beads in both the EOS M290 and NIST AMMT prototyping system will be used to compare to data extracted from thermal images in order to understand what information is useful to acquire in-situ in Chapter 6.

Chapter 4 - Laser Powder Bed Fusion Part Fabrication at Elevated Temperatures

4.1 Background and Overview

The goal of this chapter is to show that an increase in substrate temperature during deposition in the LPBF process can lead to more design freedom and less post processing. A reduction in the residual stress during deposition allows for less support structures, and therefore more complex geometries and easier removal of those supports. In addition, a reduction in residual stress may require a shorter or lower temperature post build stress relief, saving time and money. The reduction of post processing is important due to the large percentage of total part cost that post processing represents [157], [158].

In order to realize these goals, the effect of elevated substrate temperature deposition on distortion, build quality, microstructure, and mechanical properties of Ti64 parts produced in the LPBF process is necessary. The heating insert described in Chapter 3 is used in the EOS M290 to produce bulky parts[36] at progressively higher substrate temperatures. Those bulky parts are then sectioned to determine distortion on the cut surface (the lower the distortion, the lower the overall residual stress in the material). The introduction of porosity due to increases in substrate temperatures is then be analyzed. Microstructural features are characterized using both BSE imaging and X-ray diffraction (XRD). Finally, Vickers hardness testing is performed to determine any differences within the as-built parts and between parts in the as-built and heat treated conditions.

[36] Bulky parts refer to parts that do not have any thin features or complex geometries, and are meant to reduce the degrees of freedom in the experiment. In this case, the bulky parts chosen are cylinders.

While it is possible to stress relieve parts after they have been printed, the amount of support structure necessary to stop a part from distorting during production is directly related to the amount of residual stress induced in that part during deposition. The results from the single bead and bulky part builds are used to produce an industry relevant part geometry (in this case, a compressor blade section) at standard and elevated substrate temperature, and the amount of support structure required to eliminate distortion is characterized.

For the microstructural characterization in Chapter 2, the feature of interest was prior beta grain widths due to the elevated surface temperatures in the EBM process[37]. As a result of the relatively low temperature part bed during production in the LPBF process, the formation of the alpha grain structure within Ti64 will progress to completion on very short timescales (even at a substrate temperature of 500 ˚C) [17], but can still be impacted or modified by subsequent deposition during part production. In addition, solidification cooling rates are much faster than in the EBM process due to the lower heat input and lower part bed temperature. Due to the larger effect on mechanical properties [14], [17], [18], the alpha grain structure is the microstructural feature of interest in this chapter.

[37] The surface temperatures in the EBM process were determined to be between roughly 700 °C and 1000 °C (sections 0 and 2.3.3), hot enough for the majority of the alpha grain microstructural development to happen after the build has completed.

4.2 Methods

4.2.1 Bulky Part Builds

Using the information gleaned from single bead experiments in Chapter 3, parts are generated at elevated temperatures in order to determine both the feasibility of the high temperature insert to produce parts and the advantages of increasing substrate temperature during deposition. In particular, the parts are analyzed with respect to distortion, porosity, microstructural development, and hardness. Bulky cylinders with dimensions of 12.5 mm in diameter by 15 mm tall are chosen in order to eliminate geometry and edge effects as compounding factors in the analysis while still being small enough to be easily sectioned and analyzed. A Ti64 build plate is used as a substrate to build the cylinders, and the cylinders are generated at each of four substrate temperatures. The same STL file is used for each build, but the parameter sets are changed between builds. The build conditions and justification for the parameters that are used can be found below. The actual parameters for the builds can be found in Appendix 4. The experiment is designed to test 1) the effect of a change in substrate temperature, 2) the effect of constant melt pool area as substrate temperature is changed, and 3) the effect of a 2X decrease in melt pool area from the nominal condition as substrate temperature is changed.

Substrate Temperature Set Points (condition #):

1) The build plate is attached to the existing build plate to provide enhanced heat transfer to keep the substrate temperature as close to 35 ˚C as possible.
2) The build plate is attached to the heating insert, but there is no active heating needed after the initial set point of 150 ˚C is attained.
3) The build plate is attached to the heating insert and is set for 300 ˚C.

4) The build plate is attached to the heating insert and is set for 500 ˚C.

Parameter set list (parameter letter) [38]:

A) This cylinder is meant to be the control. The EOS M290 Ti64 nominal power and velocity for 30 μm layers is used. This parameter set is the same for all condition numbers.

B) The same parameters as parameter letter *A* are used in condition 1, but power is adjusted based on the expected substrate temperature in conditions 2 through 4 in order to maintain melt pool area at the same level as parameter letter *A* in condition 1.

C) The velocity is decreased until the power matches that of parameter letter *F* in condition 1, but the melt pool area matches that of parameter letter *A* in condition 1. The power is then adjusted for conditions 2 through 4 based on the expected substrate temperature in order to maintain the melt pool area at the same level as parameter letter *A* in condition 1.

D) This cylinder is also meant to be a control, and the parameter set is the same for all condition numbers. However, the target melt pool area is ½ of that for parameter letter *A* in condition 1. The power is kept the same as parameter letter *A*, but the velocity is increased until the new target melt pool area is attained.

E) The same parameters as parameter letter *D* are used in condition 1, but power is adjusted based on the expected substrate temperature in conditions 2 through 4 in order to maintain melt pool area at the same level as parameter letter *D* in condition 1.

F) The velocity is kept the same as parameter letter *A*, but the power is decreased until the target melt pool area is the same as parameter letter *D* in condition 1 (recall that this power

[38] The hatch spacing for the smaller melt pool area cases were calculated using the equations derived in Tang et al. [6]. The hatch spacing can only be adjusted in 10 μm increments in the EOS software, so the closest width available that had at least as much overlap as parameter letter *A* in condition 1 was chosen.

is then used as the target power in parameter condition *C*). For conditions 2 through 4, the power is adjusted to maintain the melt pool area the same as parameter letter *D* in condition 1.

The parameter set graph for condition 1 is presented in Figure 4-1 and the parts produced at condition 1 can be seen on the Ti64 build plate in Figure 4-2. Note that cylinders *D* and *E* have beam velocities well within the balling region of process space defined from the single bead experiments in 3.3.4. The green dotted lines show the power or velocity matching described in the parameter set list above.

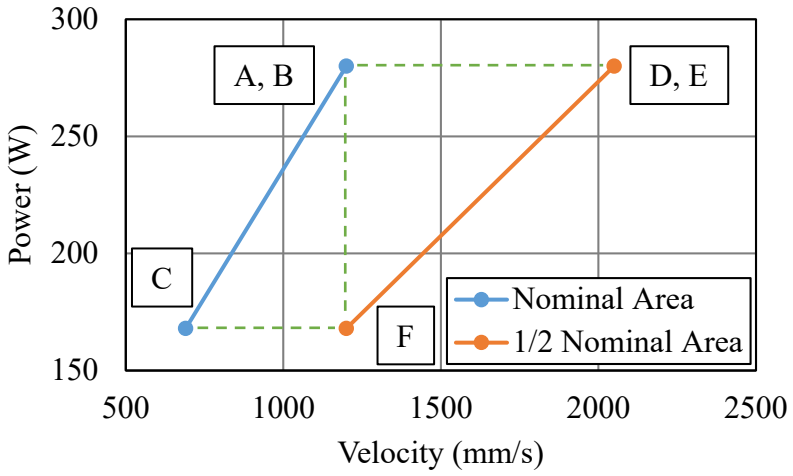

Figure 4-1: Process parameters for bulky part build in condition 1. The points are the parameter sets used and the labels designate which parameter letter the point represents.

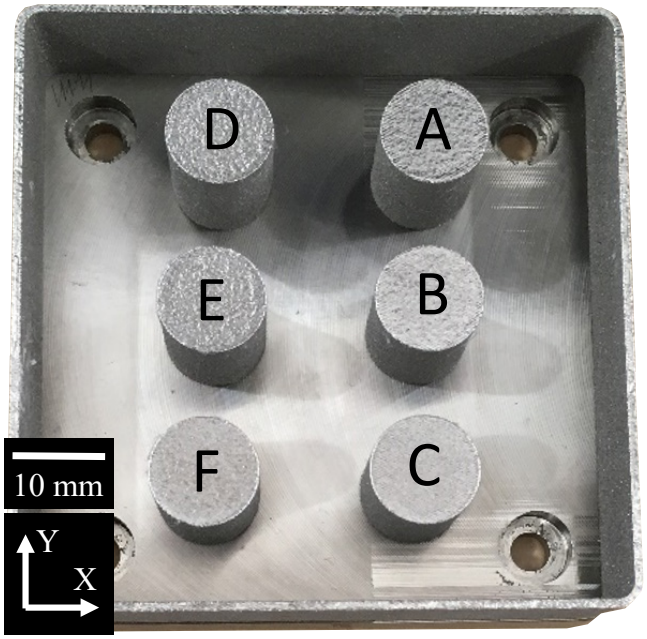

Figure 4-2: Bulky part build at condition 1.

The cylinders are relatively short and the geometry is not changing through the height, so the substrate temperature is expected to be a good representation of the top surface temperature during deposition as well as the part temperature throughout the build. The validity of this assumption is explored in the section 4.3.1. As discussed in section 3.2.1, a wall is printed around the border of the build plate for each build to keep the powder from falling under the capping plate.

4.2.2 Distortion Measurement

Each cylinder is cut down its centerline using a wire EDM[39]. The cut surfaces are then measured using an Alicona InfiniteFocus optical microscope at 5X magnification to generate a profile with a stated spatial resolution of 8 μm in the *YZ* plane and 4 μm in the *X* direction. The blue line in Figure 4-3 represents the location of surface profile measurement for the center cylinder.

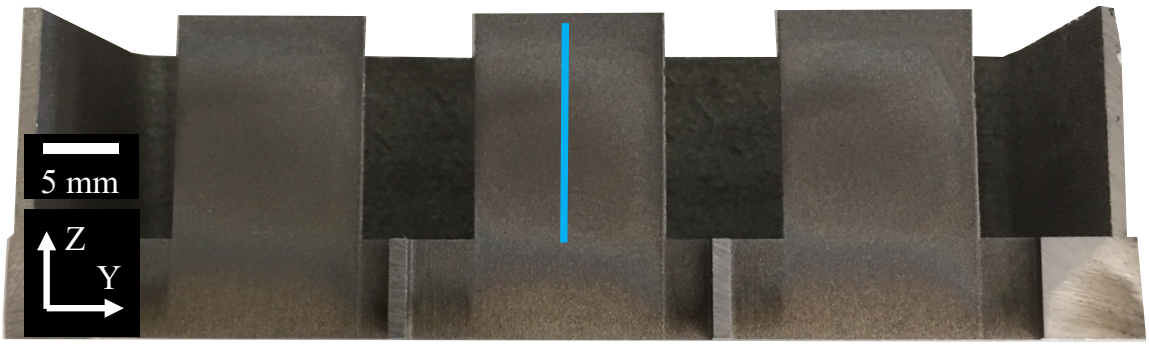

Figure 4-3: Example EDM cut surface with blue line indicating the location of the surface profile extracted for the center cylinder in the image. The axes shown in the figure correspond to the build axes during deposition.

A representative surface profile can be seen in Figure 4-4 with the red line indicating the stripe of 10 pixels in the *Y* direction that were then averaged at every *Z* height to generate a curve of distortion in the *X* direction with cylinder height. The plot of distortion in the *X* direction with cylinder height taken from Figure 4-4 can be seen in Figure 4-5. A parabola is fit to the distortion measurement for each cylinder, and gives very good agreement with the experimental data.

[39] The wire current and feed rate for the EDM were set to be conservative to ensure that no wire breaks occurred during the cuts. Each cylinder was cut with a single pass of the wire and no removal of material from the cut face occurred after the initial cut face was generated. A single pass of the wire is important because any subsequent passes of the wire would remove excess material from the cut surface after distortion of the cut surface occurred, potentially reducing the measured distortion.

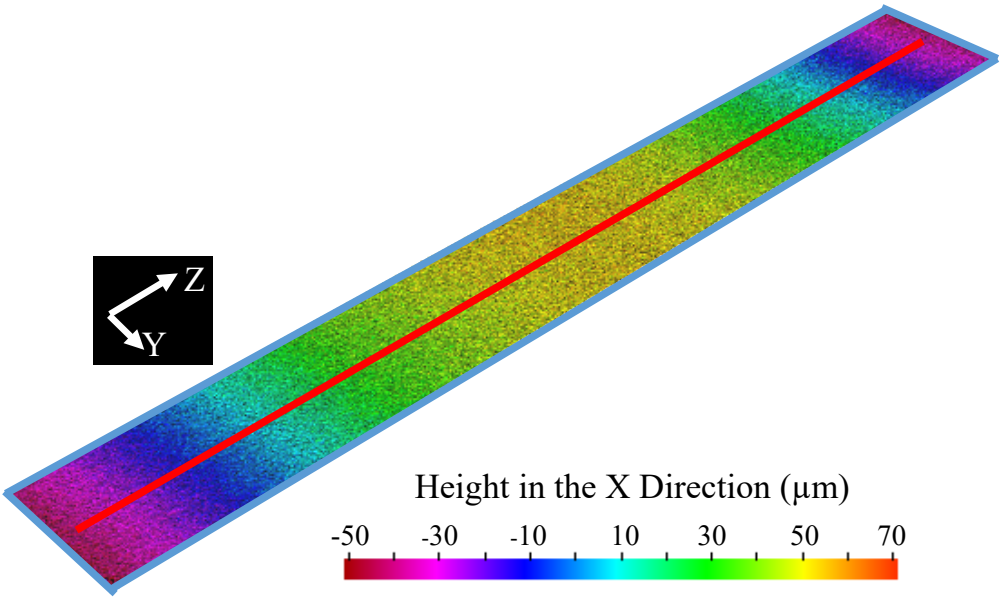

Figure 4-4: An example surface height profile that corresponds to the blue line in Figure 4-3. The red line shows the location of the line scan used to determine total distortion for that cylinder (Figure 4-5).

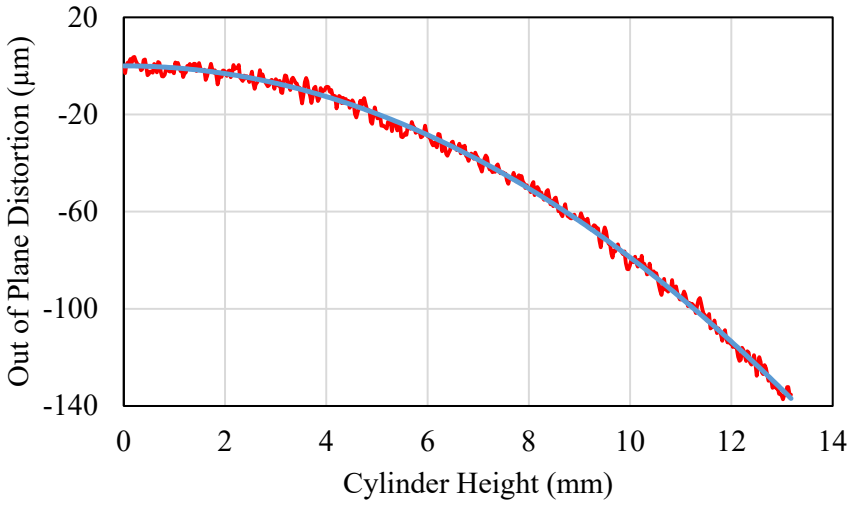

Figure 4-5: Example plot of out of plane distortion (X direction) with cylinder height of the measurement (Z direction). The red curve shows the experimental data and the blue curve shows a parabola fit to the experimental data. The original surface height data from Figure 4-4 has been rotated to give a slope of zero at a cylinder height of 0 mm.

Before the cut, the residual stresses within the cylinders are balanced. As soon as the cut face is generated, however, the forces in each side of the cylinder are no longer balanced and a new equilibrium geometry is established in response to the change in stress field. The resultant parabolic shape of the cut surface is related to the original stresses in the cylinders [159]. Figure 4-6 shows a schematic of the how the unbalanced stresses will cause distortion on the cut surface. The red arrows in the figure are meant to represent the stress directions that would be required to generate the measured distortion if those stresses were being induced externally, and are used for visualization purposes only. Because each cylinder is cut in the same location and the original geometry of each cylinder is the same, a comparison between the stress states present within the cylinders can be made by looking at the distortion of the cut surfaces. The larger the distortion of the cut surface, the higher the original residual stresses in the cylinder.

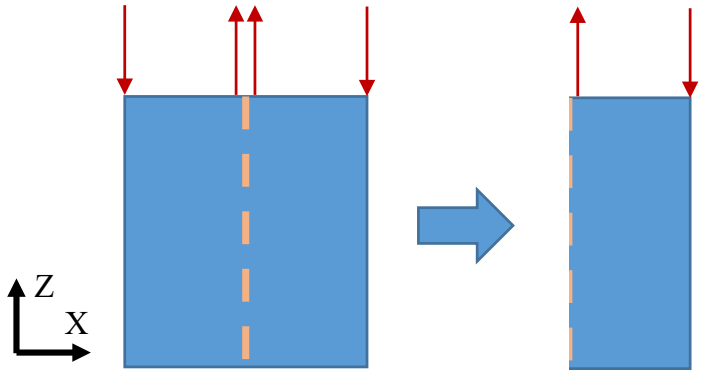

Figure 4-6: A schematic representation of the distortion of the cylinder after the cut surfaces are made by the wire EDM. The red arrows are stresses and the dotted orange line is the cut location. The stresses are no longer balanced after the cut is made.

4.2.3 Porosity Measurement

The biggest concern when modifying parameters is the introduction of porosity into the part, but porosity can be avoided by understanding how to avoid both keyholing and lack of fusion. As stated earlier, the hatch spacing for the modified parameters is scaled to have at least as much overlap as the nominal parameters, so lack of fusion should not be an issue. The other factor would be the introduction of keyholing porosity into parts due to the increases in substrate temperature during deposition.

To determine if porosity is induced in the cylinders, after distortion measurements were taken on the cut surfaces described in the previous section, the cylinders are mounted in Bakelite, polished, and imaged using an optical microscope. The microscope settings are adjusted to get high contrast between voids and the polished surface. The resultant micrographs have a scale of 1.75 μm/pixel, so the minimum pore size that is considered in the analysis is 5.25 μm in diameter[40]. A Matlab code generated by Luke Scime [160] is used to determine the total amount of porosity on the cut surface by thresholding the microscope images such that the pores are differentiated from the surrounding polished surface and the relative area fractions are determined[41]. Figure 4-7 shows an example image from the analysis. The cylinder surface has been thresholded to be either a pore (black) or the existing surface (white) and a grey overlay is added to show the region of interest. The edges of a part, defined as within 200 μm of a boundary, are not considered in the analysis. The cylinders generated in condition 2 are excluded from this analysis due to their similarity to condition 1.

[40] Though the Nyquist criterion would suggest that 2 pixels are adequate to resolve a point [193], the author chose to count pores that are at least 3 pixels in diameter as the minimum pore size to reduce the incidence of false positives in the analysis.

[41] The area/area ratio of pores is stereologically equivalent to the volume/volume ratio of pores [194, p. 9].

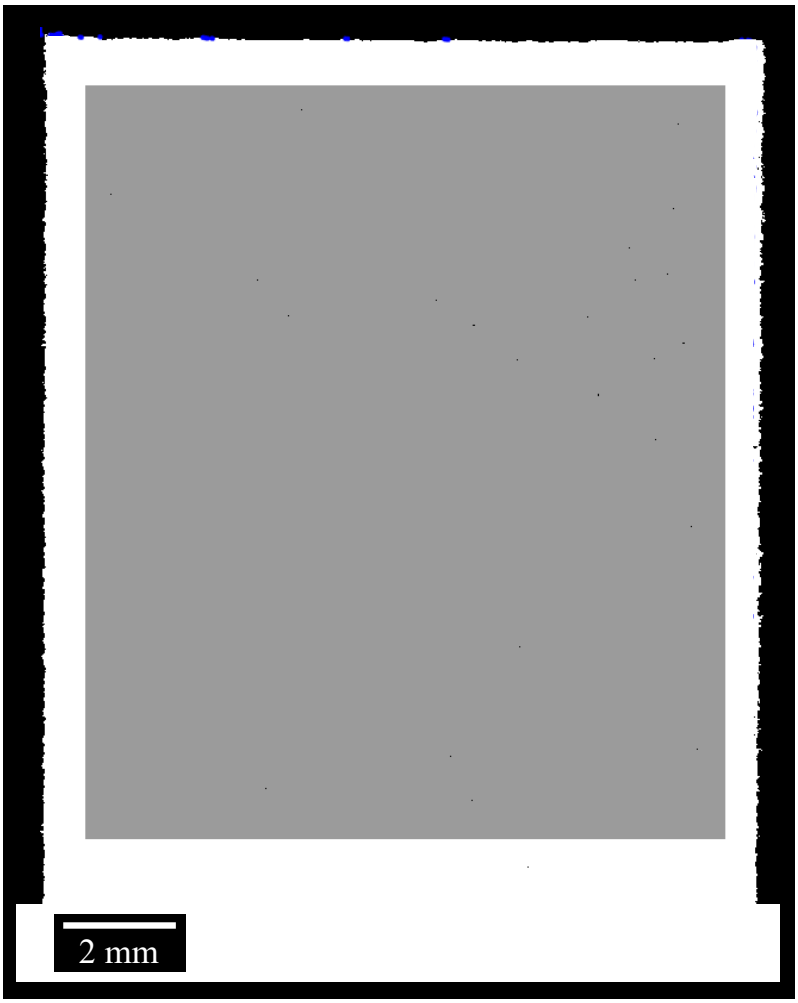

Figure 4-7: Thresholded image of a cylinder cut surface used to determine pore volume fraction. The porosity is determined within the grey area in the image.

4.2.4 Microstructure Characterization

While the single bead characterization tells us very useful information about what process parameters to use to generate a part, a microstructural characterization of the resultant parts is still necessary. In addition, because it is important to determine the differences between as-built and stress relieved samples, one half of each cylinder underwent the EOS recommended heat treatment

for Ti64[42]. These samples were then mounted in Bakelite and the cut surfaces were ground and polished. The stress relieved samples are differentiated from the as-built samples by adding a "_SR" to the existing cylinder reference.

Backscatter electron (BSE) images are obtained for select cylinders using the FEI Quanta 600 FEG SEM (FEI Company, Hillsboro, OR) in the Materials Characterization Facility at CMU. BSE imaging works by detecting the high energy electrons that are elastically scattered by the atomic nuclei of the atoms in the target material. Contrast in BSE images is derived from two main sources: grain orientation (electron channeling contrast) and atomic number of the constituent atoms (Z contrast) [161]. Grain orientation affects the BSE signal because if the planes in the crystal structure align with the incident beam, the beam will penetrate much deeper into the crystal before impacting an atom and the scattered electrons will be much less likely to escape the material, making the signal much lower than it would otherwise be. *Z* contrast is important because the likelihood of a backscattering event increases with the atomic number of the nuclei in the target material. In Ti64, the three main elements are titanium (atomic number = 22), aluminum (atomic number = 13), and vanadium (atomic number = 23). Vanadium is preferentially segregated into the beta phase while aluminum is preferentially segregated into the alpha phase [17], meaning that the beta phase will have a stronger signal in BSE images.

X-ray diffraction (XRD) using the Panalytical X'Pert Pro MPD X-Ray Diffractometer (Panalytical Company, Almelo, Netherlands) in the Materials Characterization Facility at CMU is also conducted on the cut surfaces in order to determine which crystal phases are present in the samples. XRD works on the principle that the crystal structure of a material will dictate the incident angle of an X-ray beam that produces a strong diffraction signal [162]. This signal is detected as a

[42] The samples are heated in an argon environment to 650 ˚C and held for 3 hours, then cooled to room temperature.

voltage and recorded as ‘counts’. The absolute number of counts is not important since it is dependent on the machine and choice of settings, but the relative number of counts will determine peak locations, relative intensities, and peak breadth [163]. The angle at which peaks are detected are recorded as ‘2Θ’ angles because both the X-ray source and detector will be at Θ degrees relative to the sample surface [162]. The most prominent diffraction peaks for α-Ti have values of 35.4°, 38.6°, and 40.4° and correspond to the (100), (002), and (101) planes, respectively [164], [165]. The most prominent diffraction peak for β-Ti has a value of 39.7° and corresponds to the (110) plane [166], [167]. Literature data is used to identify the diffraction peaks because of a lack of information available for Ti64 in the International Centre of Diffraction Data (ICDD) database. In addition, α’ martensite has been shown to have similar diffraction peak locations to α-Ti, indicating that the α and α’ have a similar crystal structure, though the α’ peaks are less intense and broader, signifying that the lattice is distorted [133], [168]. The samples in this work are examined using a Cu target as the radiation source at 45kV and 40mA. The diffraction angle range (2Θ) is set to include all of the peaks mentioned above (33° to 43°) with a step size of 0.02° and a scan speed of 0.5 °/min.

4.2.5 Hardness Testing

Vickers hardness testing is then done on the cut faces to determine the difference in hardness between the parameter sets and substrate temperatures. This testing method is a fast, inexpensive, and relatively non-destructive way to determine basic material properties. Vickers hardness works by indenting the target surface with a very hard, pyramid shaped, indenter (in this case, diamond) with a specified force. The amount of plastic deformation in the target material is measured from above by determining the projected area of the indent and prior knowledge about

the indenter geometry. Equation 6 [169] is then used to generate a number that is correlated to the yield stress of the material.

Equation 6

$$HV = 1.8544 * P_1/d_1^2$$

Where HV is Vickers hardness, P_1 is the indentation force (kgf) and d_1 is the average diagonal length of the indentation (mm).

For this work, a ZHV10 hardness tester (Zwick Roell Group, Ulm, Germany) is used to generate 10 indents at a height of 9 mm (Z direction) and within 2 mm (in the Y direction) of the center of each cylinder. A 5 kgf load is applied with a dwell time of 15 seconds and each indent is spaced at least 500 μm from any other indent. The resultant indents are then imaged using an Alicona Infinite Focus optical microscope at 50X magnification to determine the indent dimensions. All test conditions comply with ASTM E384-11 [169]. An example indent image can be seen in Figure 4-8.

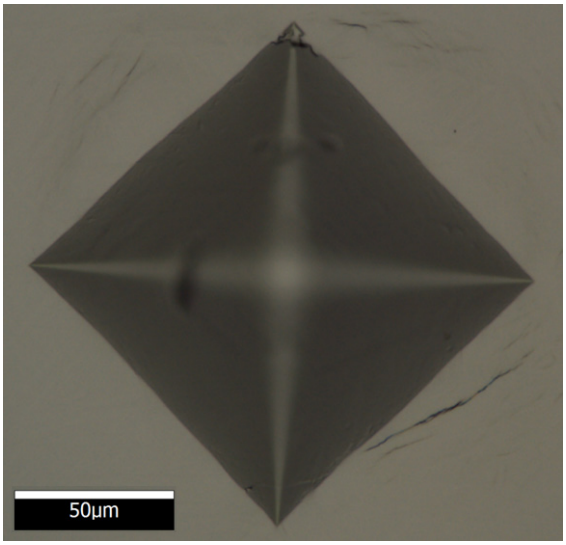

Figure 4-8: Example image of a Vickers hardness indent on the polished face of a Ti64 cylinder used in this work.

4.2.6 Industry Relevant Geometry

To determine how well the substrate heating reduced the need for supports, a section of a generic compressor blade[43] is used as the industry relevant geometry to test. A picture of the compressor blade printed in Ti64 on the EOS M290 at CMU as part of a previous project can be seen in Figure 4-9. The blade was printed vertically, with the build direction in *Z*. The area highlighted in red shows the flange section of the compressor blade. Even through the blade finished printing, it is clear that the flange section deformed considerably, likely due to delamination of the flange section from the supports during the build. The distortion is considerably greater than one layer thickness, so it is likely that the majority of the distortion happened when a higher portion of the build was being deposited due to the steady buildup of residual stress in the part.

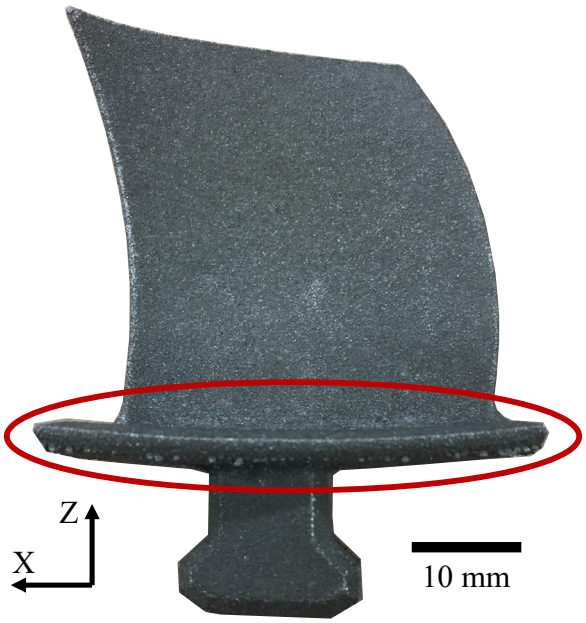

Figure 4-9: A compressor blade geometry, generated as part of a previous project, is used as the basis for this work.

[43] The STL for the compressor blade was distributed by GE as part of an America Makes project. The design is non-proprietary and meant to be representative of geometrical features that are of interest to industry.

Because the distortion of the flange section in Figure 4-9 occurred during printing of the blade section of the part, the geometry printed for this project included a significant portion of the blade section as well as the flange section. Not all of the blade geometry was included, however, in order to keep build time and costs down. A CAD image of the geometry used in this work can be seen in Figure 4-10 as grey material with the support structure shown in red. The flange starts at a height of 2.5 mm and the total height of the component is 15 mm.

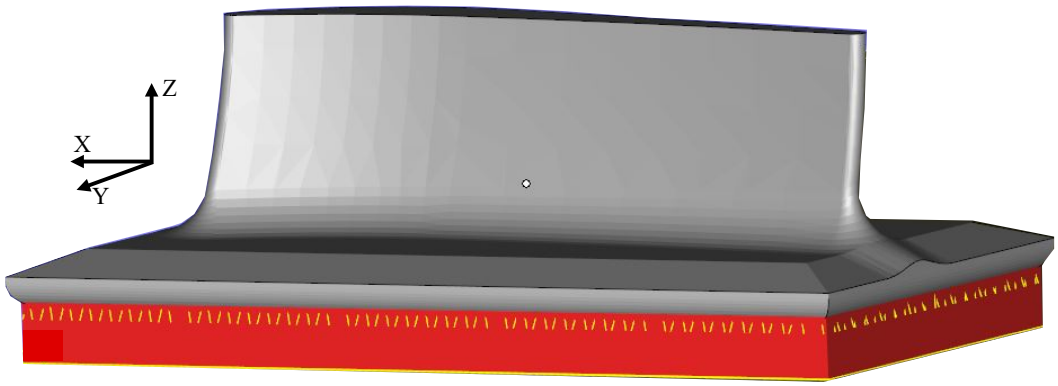

Figure 4-10: CAD image of the compressor blade section printed in this work (in grey) with the supports in red.

The original print of the compressor blade (Figure 4-9) used teeth at the connection of the supports to the flange section of the part to facilitate support removal. Using the original print as a guide, the support structures in Figure 4-11 are generated in Magics 20.02 (Materialise NV, Leuven, Belgium) to produce parts using the standard parameter set (including the standard substrate temperature) for the EOS M290 for 30 µm Ti64 layers with EOSPrint V1.6. Each image in Figure 4-11 is taken from EOSPrint and shows a representative portion of each of the supports at the connection to the flange section of the compressor blade in red with the outline of the first layer of the flange in blue.

The first support structure (Figure 4-11.A) is labeled ‘standard’ because it is the default ‘block’ supports generated by Magics. There are teeth supports for the interior of the flange section and those interior supports are broken up into 5 mm square blocks to facilitate support removal. The outer perimeter of the flange section has a solid border for strength since the perimeter supports are likely to experience the highest tensile loads due to residual stress buildup within the part. The second support structure, labeled ‘Modified 1’ (Figure 4-11.B), is the same as the standard supports in every way except the block size for the interior supports have been reduced to a 2.5 mm square. The third support structure, labeled ‘Modified 2’ (Figure 4-11.C), is the same as the standard supports in every way except the solid border around the outer perimeter of the flange section has been replaced with teeth supports to make support removal easier. The final support structure, labeled ‘Modified 3’ (Figure 4-11.D), incorporates the changes seen in Modified 1 and Modified 2: the block size for the interior supports have been reduced to a 2.5 mm square and the solid border around the outer perimeter of the flange section has been replaced with teeth supports. The standard support structure is the strongest and therefore least likely to allow the part to distort while Modified 3 is the weakest and therefore most likely to allow the part to distort.

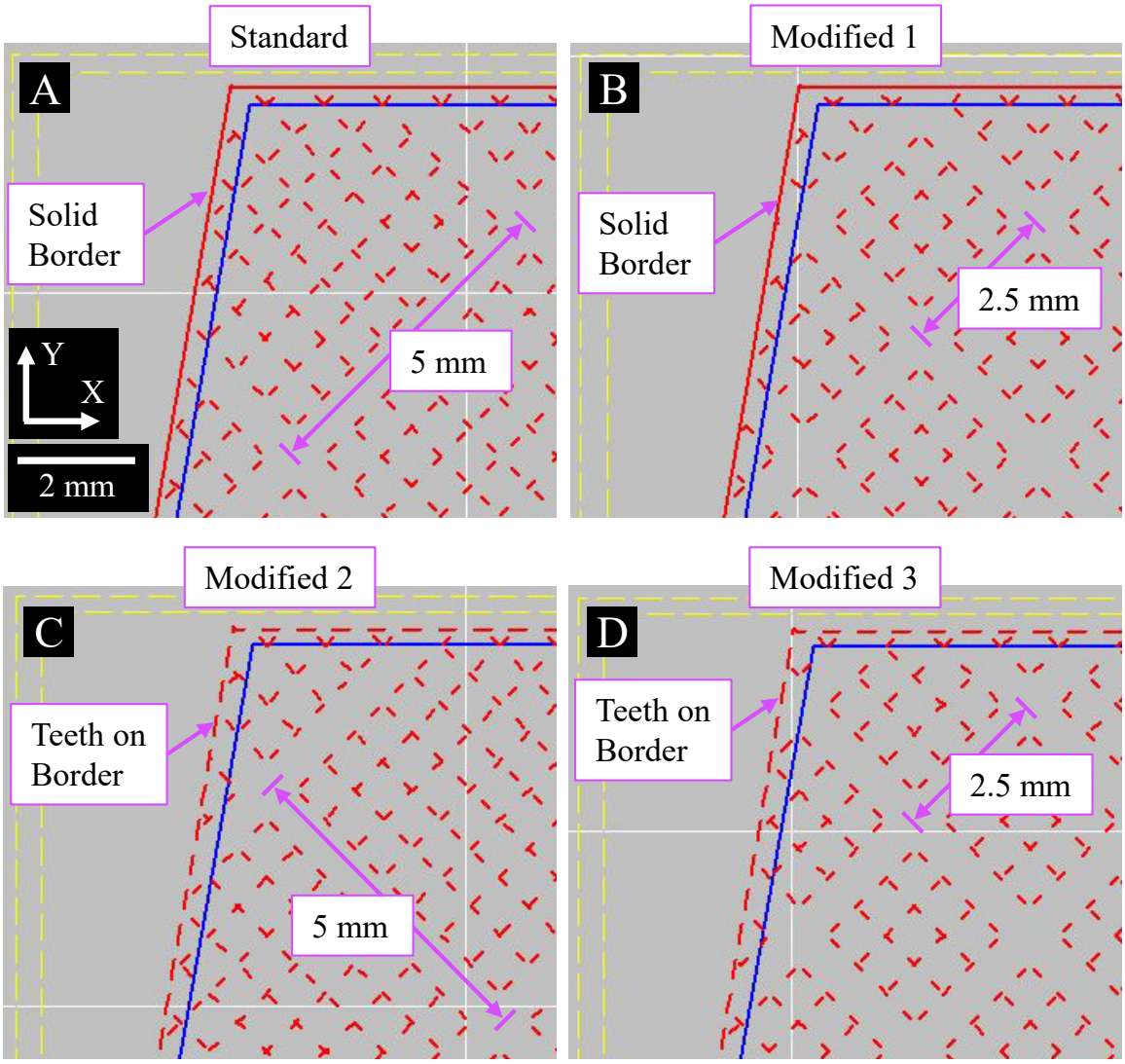

Figure 4-11: Support structures showing the connection between the supports and the flange section of the compressor blade.

The results of this build are then used to determine the parameter sets and support structures for deposition of the compressor blade section at a substrate temperature of 500 ˚C. The STL file for the compressor blade section is not changed in any way between the builds, so the level of improvement in distortion with the increased substrate temperature can be characterized.

4.3 Results

4.3.1 Temperature Distributions

The thermocouple placement is shown in Figure 4-12. These locations are chosen to give a good representation of the span of temperatures across the substrate. Temperatures for the cylinder builds are shown in Table 4-1. Due to the thermal isolation of the high temperature insert, the lowest temperature that can be sustained during a cylinder build (as a result of the heat input from the laser) is roughly 160°C.

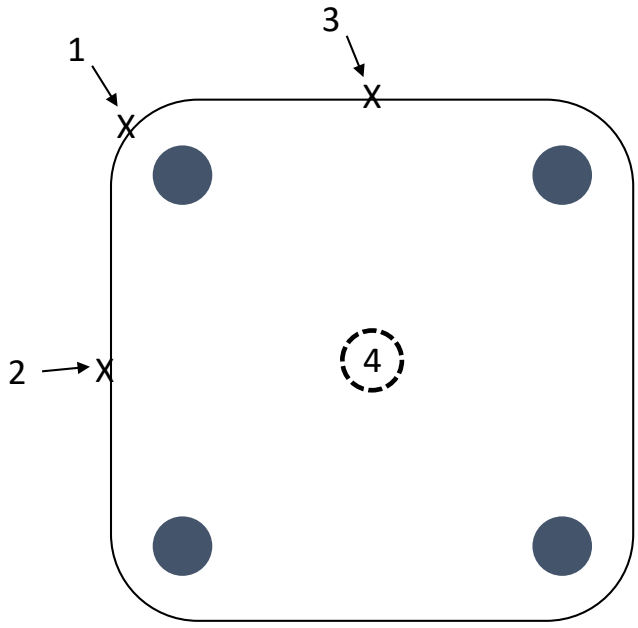

Figure 4-12: Thermocouple locations on the build plate for the cylinder builds. Thermocouple 1 is welded to the side of the build plate at an edge, thermocouples 2 and 3 are welded to the side of the build plate in the center of a side, all at the locations indicated by an x. Thermocouple 4 is welded to the bottom of the build plate in the location indicated by the dashed circle.

Table 4-1: Temperature distribution during deposition of cylinders.

Thermocouple #	Target Temperature (°C)	Actual Temperature (°C)	Standard Deviation in Actual Temperature (°C)
1	35	60	5.5
2	35	58	3.8
3	35	57	3.2
4	35	58	2.1
1	150	155	5.7
2	150	161	4.8
3	150	160	4.5
4	150	166	4.2
1	300	291	3.8
2	300	305	2.8
3	300	303	3.1
4	300	311	2.4
1	500	487	4.8
2	500	515	3.2
3	500	518	4.3
4	500	533	3.5

The target temperatures for the cylinders were 1) 35 °C, 2) 150 °C, and 3) 300 °C and 4) 500 °C. The actual temperature for 1) was between 54 °C and 66 °C. The difference in temperatures between the target and actual temperature is due to the insufficient heat transfer into the bulk to keep the temperature any lower, but should be representative of the actual temperature at a similar location in a standard build. There was no heating during this build. The average temperature for 2) is between 148 °C and 170 °C. There is no heating during this build after getting the substrate to the set point temperature before starting the build. This was not by design, the equilibrium temperature stabilized at this value. The average temperature for 3) is between 287 °C and 313 °C. The average temperature for 4) is between 482 °C and 537 °C. The temperature range for 3) and 4) extends above the target values because the heater set point was increased in order to maintain the build plate surface temperature as close to the target value as possible. The temperatures

reported here are for the substrate during deposition of the cylinders. The temperature of the top surface of the cylinders is not measured, but is likely similar to the substrate temperature due to the heat input from the laser and short height of the build (see below).

The same analysis is done for the industry relevant geometry of a compressor blade section. The thermocouple locations are the same as for the cylinder builds for the 500 °C build (Figure 4-12), but thermocouples are not attached to the build conducted at the standard conditions since that build is printed on a standard build plate. The temperatures can be seen in Table 4-2.

Table 4-2: Temperautre distribution during production of industry relevant component.

Thermocouple #	Target Temperature (°C)	Actual Temperature (°C)	Standard Deviation in Actual Temperature (°C)
1	35	-	-
2	35	-	-
3	35	-	-
4	35	-	-
1	500	465	8.2
2	500	495	3.4
3	500	490	6.3
4	500	515	2.9

All of the temperatures reported so far have been for the substrate during a build because thermocouples couldn't be attached to the part itself during deposition. In order to understand the temperature gradient within a part due to heating from below, the author attached thermocouples to the compressor blade build after deposition, but while the part and substrate were still bolted to the heating apparatus.

Thermocouples are attached to several locations on the compressor blade build, including the top of the build plate (build height of 0 mm, thermocouple 1), the top of the flange section (build height of 5 mm, thermocouple 2), and the top of the blade section (build height of 15 mm, thermocouple 3), the edge of the build plate (thermocouple 5), and under the build plate (build

height of -6.5 mm, thermocouple 4). Figure 4-13.A shows a picture of the build with the thermocouples attached and before powder is added and the capping plate is put in place.

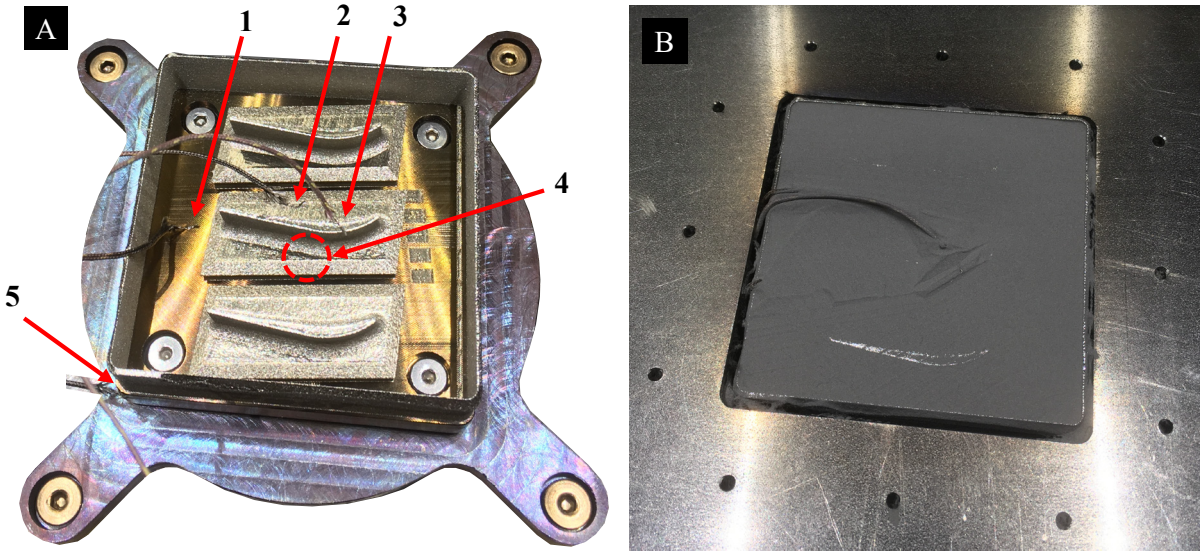

Figure 4-13: A) A picture of the build plate, build carrier, compressor blade sections and thermocouples attached. B) The same view after powder was added and the capping plate replaced.

The parts are then buried in powder up to the top of the turbine blade section to mimic the conditions during a build as closely as possible (Figure 4-13.B). This test is meant to bracket the low end of the possible surface temperatures because there is no heating from the laser and the compressor blade section is a fairly thin part compared to the cylinder builds (so heat transfer from the substrate will not be as substantial). However, because a part is not being printed in this scenario, there is no forced argon flow over the top surface of the build. The EOS software only allows gas flow over the plate during printing, and it was not possible to mimic that gas flow for this test. Moving argon would have wicked more heat from the top surface than argon moving under natural convection, so this would have acted to pull surface temperature down. With these competing factors considered, this test should give a good indication of what the top surface

temperature likely was toward the end of the build (when the temperature would have deviated farthest from the substrate temperature). With the lower temperature thermal monitoring capabilities currently being developed at CMU, future work will be able to accurately determine the top surface temperatures during a build that employs substrate heating.

Figure 4-14 shows the temperature profile from the time that the resistive heater is turned on until the build reaches steady state temperatures. The time required for the system to come up to temperature is roughly 30 min. The cylinder builds each takes roughly 3 hours and the compressor blade build takes roughly 2 hours, so the system transfers heat faster than the parts are produced.

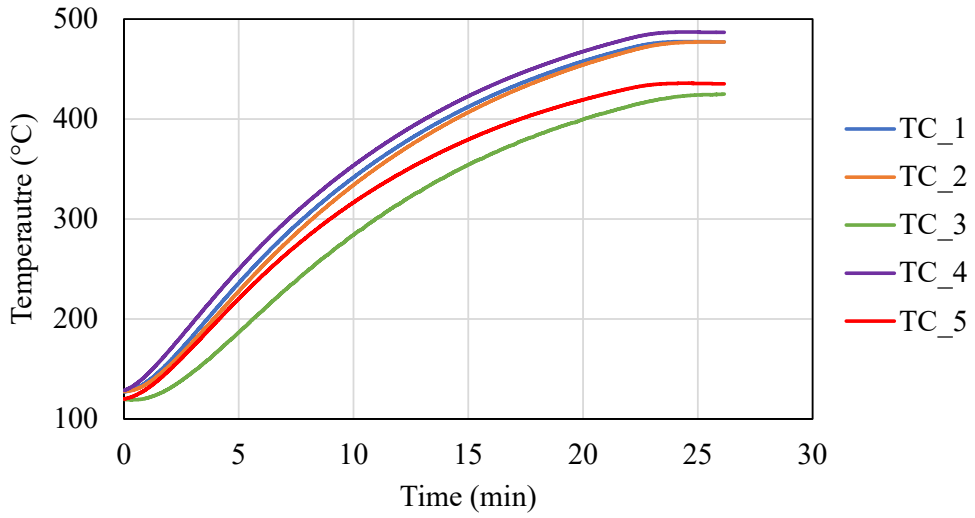

Figure 4-14: Heating profile for thermocouples welded to the compressor blade build.

It is clear that the temperatures for thermocouples 1, 2, and 4 track very closely together throughout the experiment, meaning that there are very low thermal gradients from the bottom of the plate through the top of the flange section (a height of 11.5 mm). Thermocouple 5 (welded to the edge of the plate) starts heating at the same rate as 1, 2, and 4, but then levels off to a lower temperature, consistent with the spread in temperatures seen during part builds. Thermocouple 3

is welded to the top of the compressor blade section and shows both slower heating and a lower equilibrium temperature than lower in the build. The temperature difference is not drastic even though the cross section is small, however. In addition, the spread in temperatures in the *Z* direction (thermocouples 1, 2, 3, and 4) is similar to the spread in temperatures in the *XY* plane (thermocouples 1 and 5 in this experiment as well as the spread in temperatures measured during the part builds at 500 °C). This indicates that the spread in temperatures measured during builds is representative of the temperature difference throughout the height of each build.

4.3.2 Distortion Characterization

The maximum out of plane distortion from each best fit parabolic curve (Figure 4-5) is used to generate Figure 4-15. The first thing that becomes clear is that there is a downward trend in distortion with temperature starting from condition 1. Stress relaxation will only occur on the time scale of minutes to hours at temperatures over roughly 400 ˚C [151], meaning that the reduction in distortion seen at low substrate temperatures (conditions 1 through 3) must be from lower induced residual stress, since stress cannot be relieved after deposition at these temperatures. Between condition 3 (300 ˚C target substrate temperature) and condition 4 (500 ˚C target substrate temperature) there seems to be a slope change in the data and the distortion drops more quickly. This makes physical sense since stress relaxation would start to become the dominant stress reduction mechanism at temperatures around 500 ˚C. The curve for each cylinder seems to be going to zero at slightly different temperatures, but all curves will hit zero distortion around 525 ˚C to 625 ˚C, which makes physical sense based on the stress relief times and temperatures for Ti64 [151].

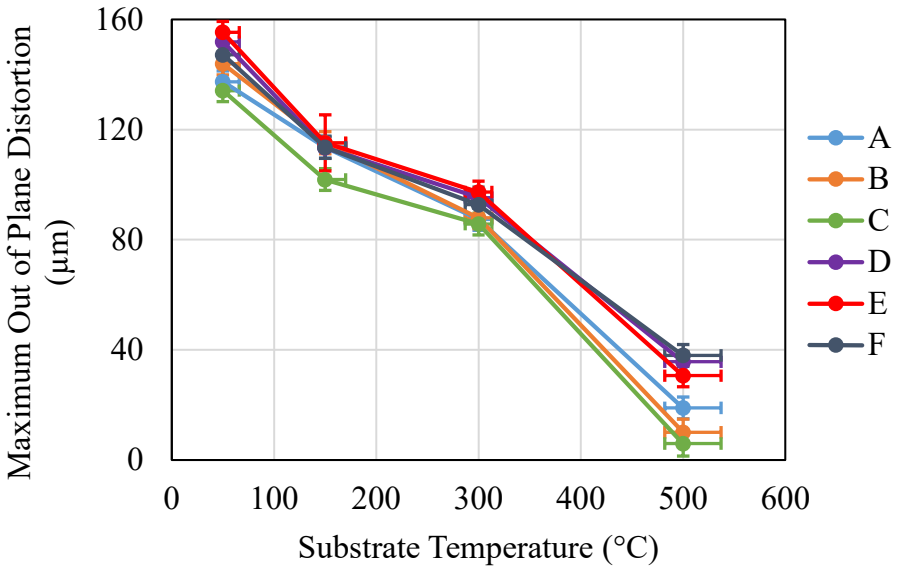

Figure 4-15: The maximum out of plane distorition with substrate temperature. The error bars in the *Y* direction are 1 standard deviation on the data used to generate each best fit parabolic curve. The error bars in the *X* direction are the temperature distribution from Table 4-1.

Another trend in the data, though significantly less pronounced than substrate temperature, is that for the same substrate temperature, the cylinders with larger melt pool cross sectional areas (cylinders A, B, and C) have lower distortion than those built with smaller melt pool cross sectional areas. The higher heat input for the larger melt pools lowers thermal gradients throughout the cooling process and keeps the surrounding material hotter for longer. Both of these effects act to reduce distortion.

4.3.3 Porosity Characterization

Figure 4-16 shows the volume fraction of porosity (in %) for each cylinder for conditions 1, 3, and 4. The error bars on temperature are omitted for clarity. The only sample that has noticeably higher porosity than the others is sample 1_C, but a volume fraction of porosity of 0.01% is still very low. It is, however, interesting to note that as temperature is increased,

parameter letter *C* has a reduction in porosity even through the melt pool area and hatch spacing should be constant. From section 3.3.2, the aspect ratio of the melt pools should be decreasing (or becoming more semi-circular in cross section) as substrate temperature increases for constant melt pool area, suggesting that the more semi-circular cross section was better able to maintain a fully dense part.

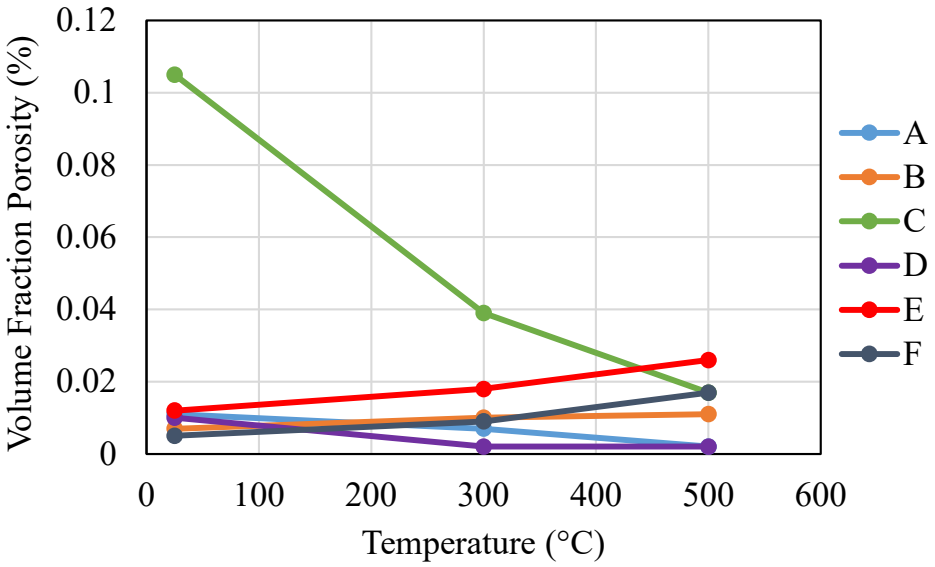

Figure 4-16: Porosity volume fraction (%) for all of the cylinders printed at different substrate temperatures.

Prior work has tried to avoid printing with parameters that induce balling in single bead experiments due to the large variability in the top surface profile of the melt track [37], [170]. The lack of porosity found in cylinders produced with parameter letters *D* and *E* indicate that while the balling phenomenon is occurring due to the process parameters chosen, balling is not inducing significant porosity. This indicates that avoiding balling melt pools may not be as critical as previously thought as long as the melt pool dimensions and hatch spacing are chosen to generate a sufficient overlap during deposition.

While a large surface area (at least 120 mm^2) is analyzed for each cylinder, the relatively small number of pores found for most cylinders suggests that characterization methods that sample the part in three dimensions (such as X-ray computed tomography or serial sectioning) would be a more appropriate means of determining differences between levels of porosity in the parts, if any exist.

4.3.4 Microstructure Characterization

A microstructural characterization of all cylinders printed with parameter letter *A* in both their as-built and stress relieved conditions is conducted to determine the effect of elevated substrate temperature on microstructural features[44]. This set of cylinders is chosen to show the progression of microstructures that are generated when the only parameters being modified are substrate temperature and post build stress relief (the process parameters used for deposition are all the same). Figure 4-17 shows BSE images for each of the as-built conditions at 1400X and 5000X magnification.

[44] The author would like to acknowledge Ross Cunningham and Edgar Mendoza Jiminez for their assistance in acquiring the BSE images shown in Figure 4-17 and Figure 4-19.

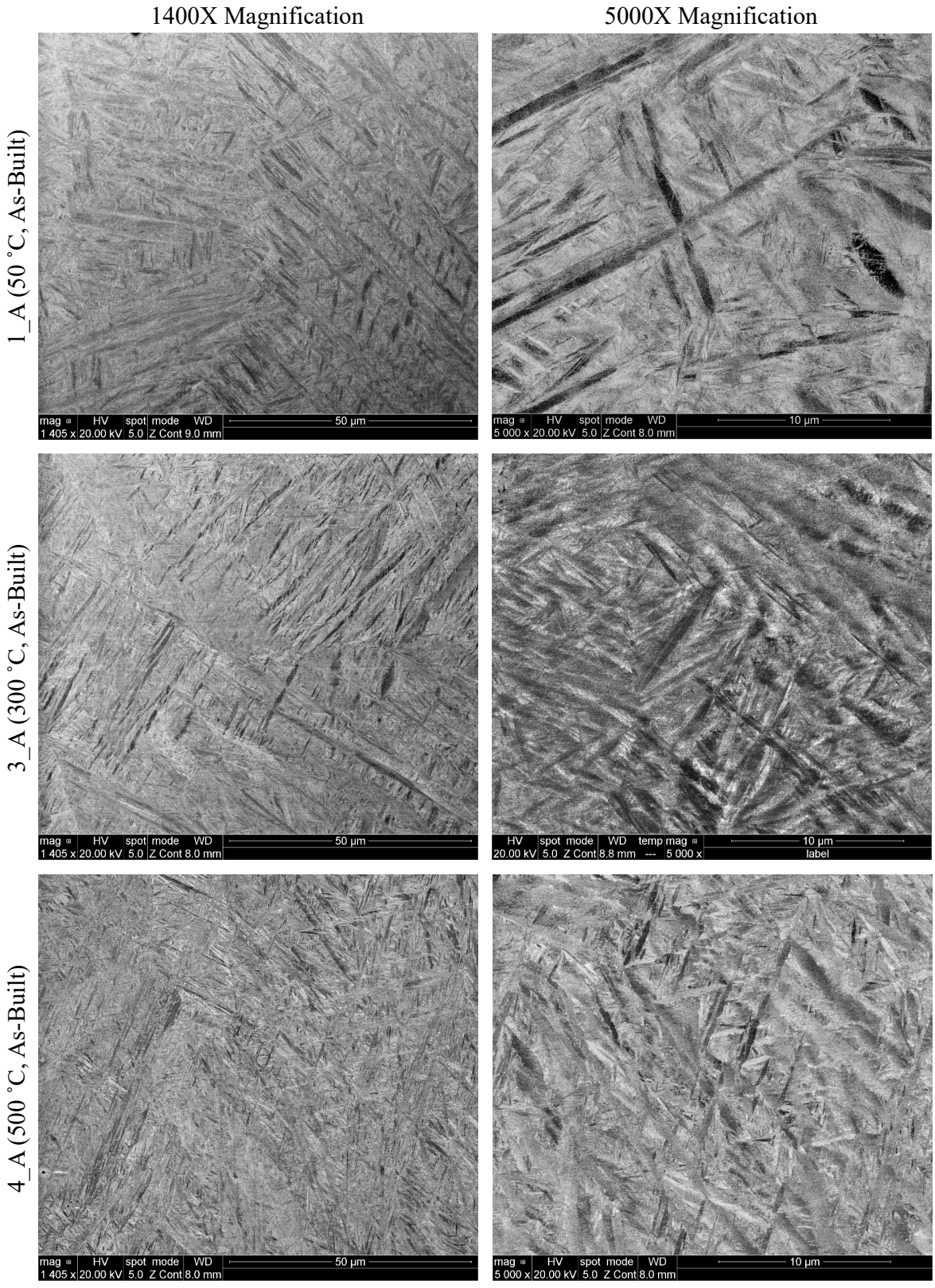

Figure 4-17: Cylinders printed with paramter letter *A* in their as-built condition.

All of the as-built cases (Figure 4-17) look to be almost entirely α' martensite [171]. Recall from Chapter 1 that α' martensite is the dominant microstructure at cooling rates in excess of roughly 410 °C/s [17], [18]. From the single bead simulations presented in Chapter 3, even when the substrate temperature is 500 °C and large melt pools are generated, the cooling rate at the martensite start temperature of 725 °C (the martensite finish temperature [17]) is at least an order of magnitude larger than 410 °C/s. This suggests that α' martensite will form during deposition until substrate temperatures approach those seen in the EBM process (above 700 °C), though further testing would be required to confirm this finding.

While it may be difficult to discern in Figure 4-17, there are small light features outlining some of the martensitic needles in sample 4_A, as can be seen in Figure 4-18. These features are likely beta precipitating out of the martensite as it decomposes and suggests that there is at least a small amount of breakdown of the martensite in the 500 ˚C as-built case that is not seen in the lower temperature cases (1_A and 3_A).

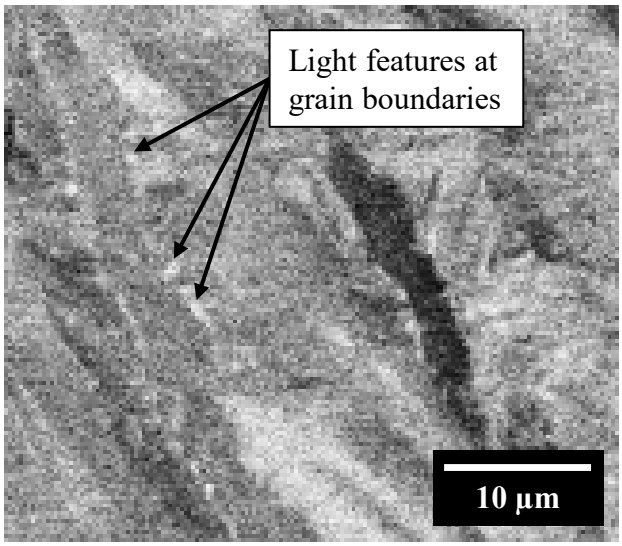

Figure 4-18: An enlarged section of the BSE image of sample 4_A taken at 5000X magnification. Light features can be seen at many of the grain boundaries.

The slight breakdown of the martensite in the 500 °C as-built cylinder means that an advantageous phase transformation from martensite to fine α/β has been initiated in-situ, but is not significant enough to substantively change the microstructure during part production. This also suggests that the temperature required to decompose martensite is lower than the substrate temperature required to forgo the generation of martensite during deposition. For this reason, Ti64 martensite decomposition is more important than martensite formation when determining the as-built microstructure for parts produced using high substrate temperatures.

Figure 4-19 shows the BSE images for each of the stress relieved conditions at 1400X and 5000X magnification. It is clear that the stress relieved samples look considerably different than their corresponding as-built samples.

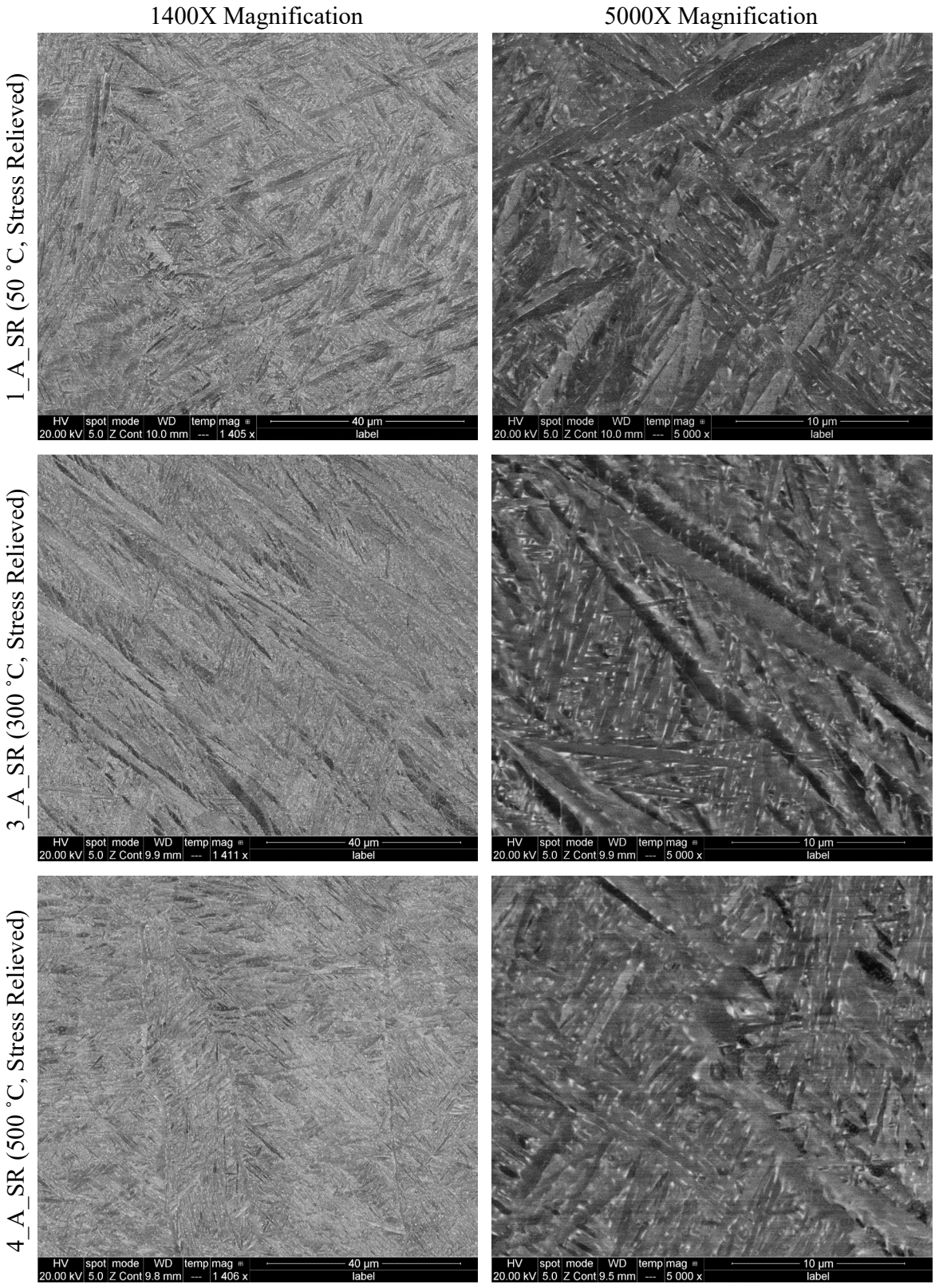

Figure 4-19: Cylinders printed with paramter letter *A* in their stress relieved condition.

All of the stress relieved samples (Figure 4-19) look to be α/β lamellae, as the white spots (beta) are much more noticeable and interspersed with a uniformly dark matrix (alpha) [172]. The beta precipitates delineate the alpha grain boundaries, but are also present within alpha grains. This morphology, coupled with the difference between the as-built and stress relieved grain morphologies, leads to the conclusion that the stress relieved cases likely show significantly decomposed martensite.

Alpha grain width is quantified in the stress relieved cases utilizing the Heyn Lineal Intercept Procedure [144], and can be seen in Figure 4-20. At least 75 grains are measured to generate each data point. There is not a significant difference in the alpha grain widths for cylinders printed at different substrate temperatures, indicating that the substrate temperature during deposition is not a significant factor in the alpha microstructural development during stress relief as long as martensite is formed at solidification and not broken down during the build[45]. The similarity between the post stress relieved samples suggests that any post processing steps already developed for as-built material can still be used when printing at elevated temperature.

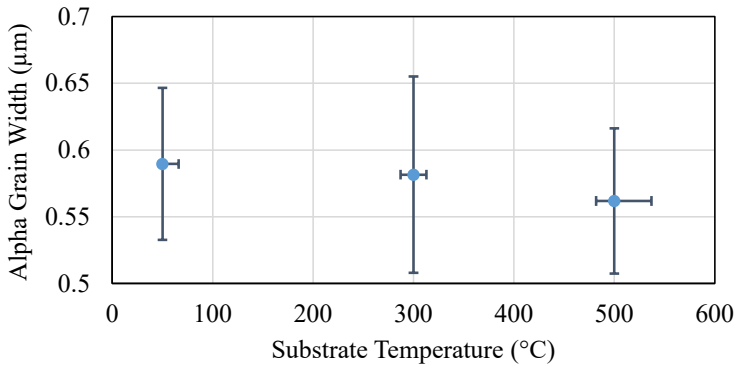

Figure 4-20: Alpha grain widths for the cylinders printed with parameter letter *A* in their stress relieved condition. The *Y* error bars are the 95% confidence interval on the mean grain width and the *X* error bars are the range of substrate temperatures measured during deposition.

[45] It is clear from a comparison to EBM fabricated Ti64 samples that the as-built microstructure is considerably different due to the significantly elevated substrate temperature during a build [74], [195].

Grain counts are not done in the as-built condition due to the uncertainty as to the location of the grain boundary for a majority of the grains. While there are several well defined grains in these images, the majority of them have diffuse boundaries that are difficult to interpret. In addition, the grain sizes do not look to be significantly different from the stress relieved cases.

X-ray diffraction (XRD) is used to confirm the findings from the BSE imaging. Figure 4-21 shows the XRD profiles for the cylinders printed with parameter letter *A* in both their as-built and stress relieved conditions. The grey vertical bars show the locations of the expected alpha peaks while the purple vertical bar shows the location of the expected beta peak [166], [167].

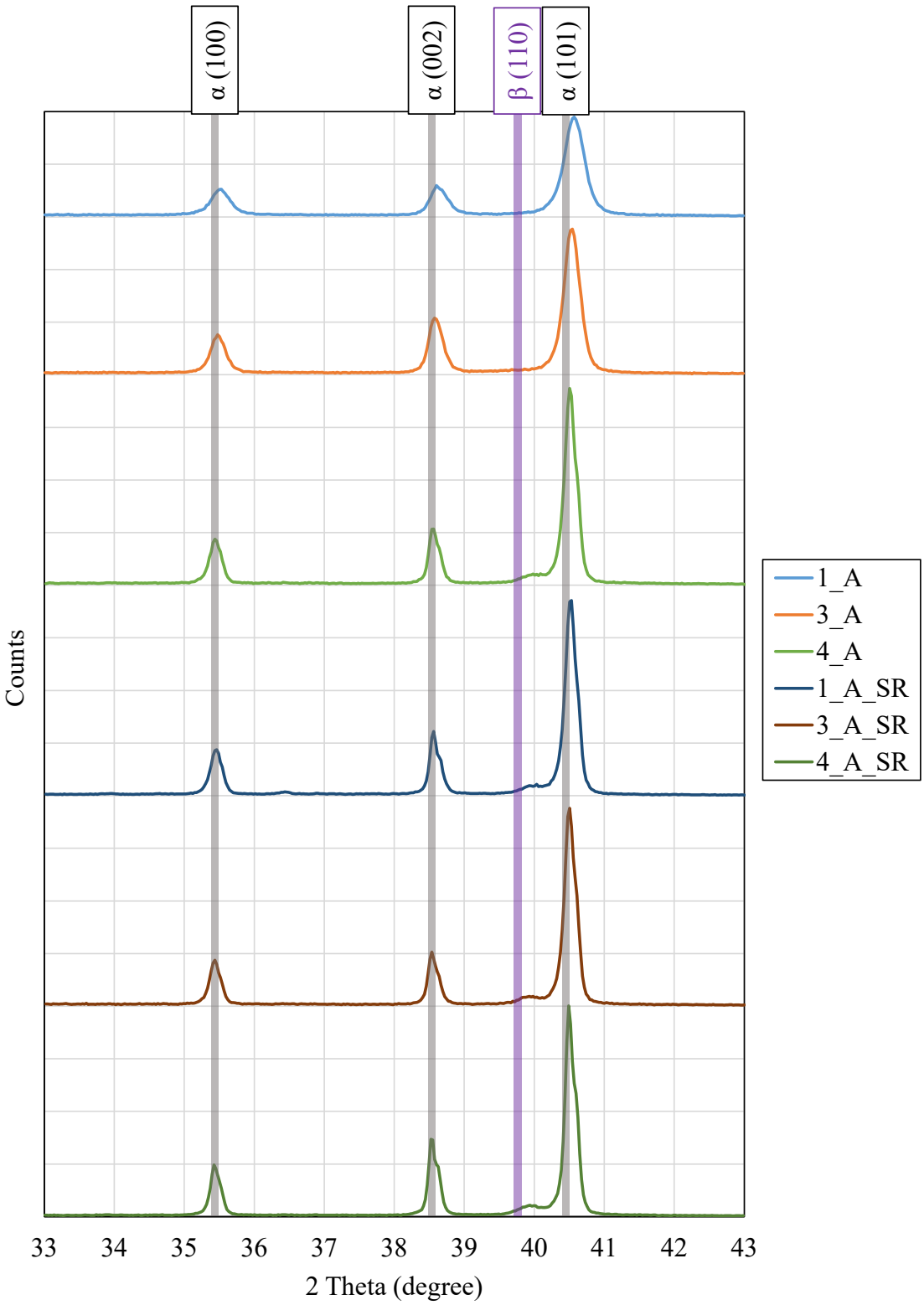

Figure 4-21: XRD results for cylinders produced with parameter set *A* in their as-built and stress relieved conditions. The expected peak locations are highlighted in grey and purple.

The differences between cylinders can be better seen when the individual XRD scans are overlaid. From Figure 4-22 it is clear that as the substrate temperature during deposition is increased, the alpha (or α' martensite) peaks become more intense, narrower, and shift to shorter 2Θ angles[46]. Taken together, this suggests a reduction in lattice distortion, and can be caused by a reduction in residual stress and/or a reduction in the concentration of martensite [133], [168]. In addition, samples 1_A and 3_A do not have a detectible beta peak, while sample 4_A does. This lends credence to the BSE image analysis proposing that there is at least a small degree of breakdown in the α' martensite into alpha and beta.

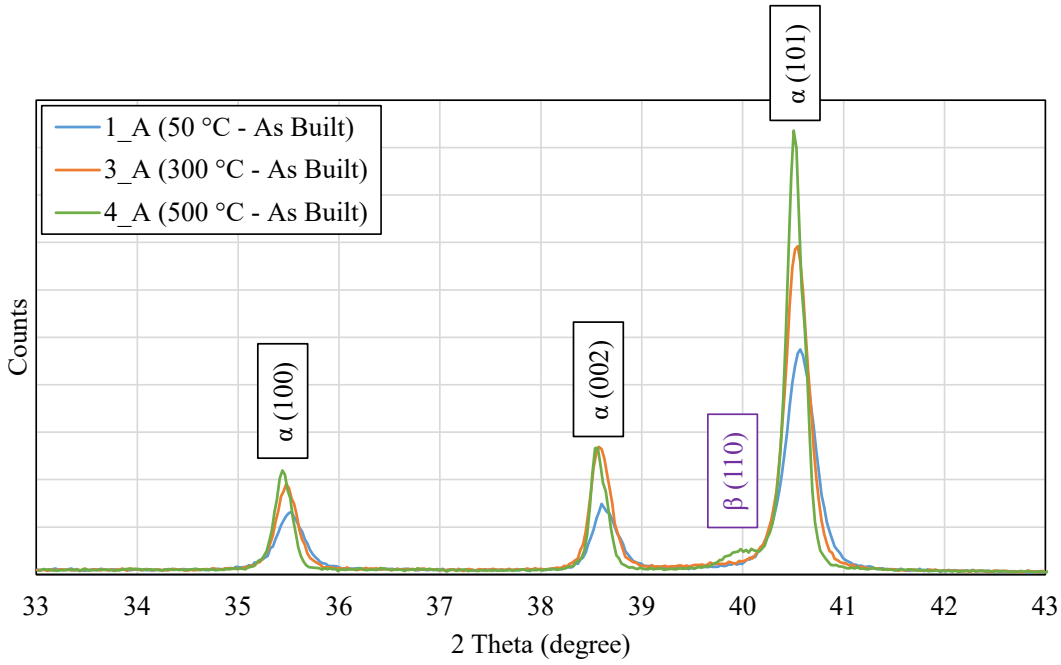

Figure 4-22: XRD results for cylinders produced with parameter set *A* in their as-built condition overlaid on the same axes.

Figure 4-23 shows XRD results for the stress relieved samples added to Figure 4-22. From Figure 4-23, it becomes clear that there is no significant difference between the XRD peaks for

[46] A peak shift to shorter 2Θ angles specifically indicates an increase in lattice parameter [162].

sample 4_A and all of the stress relieved samples. This is in contrast to the BSE images, in which the stress relieved samples are almost completely broken down into α and β, while sample 4_A is still almost entirely α' martensite. The discrepancy between the BSE and XRD results is most likely due to the small size of the β grains [163, p. 262] (on the order of 10s to 100s of nm) reducing the sensitivity of the XRD detections to the point where differences in phase composition are not discernable. The difficulty in detecting the β phase is evident by the exceedingly small β peak in even the most intense detection.

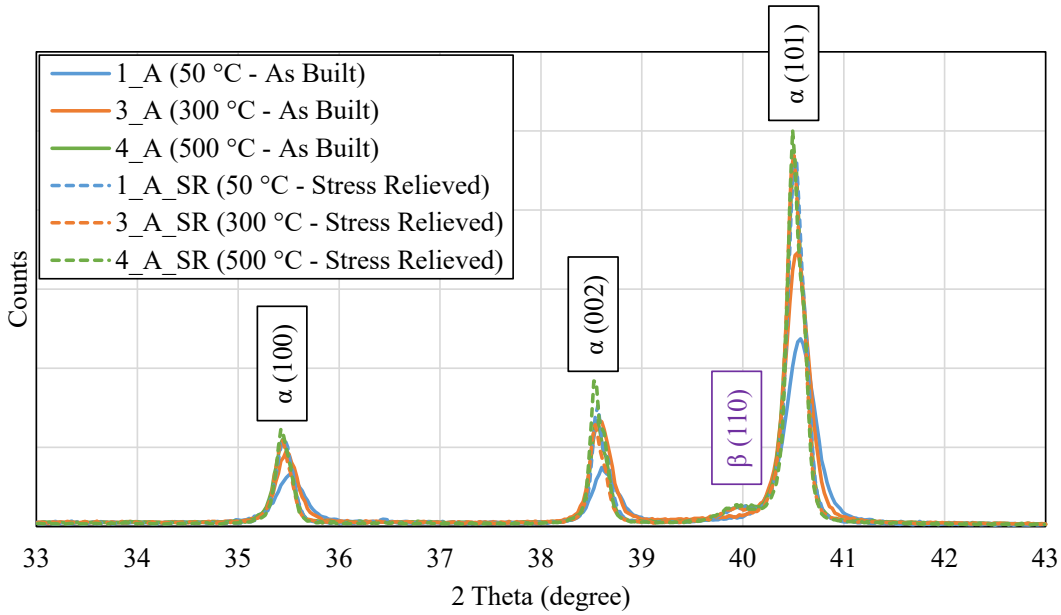

Figure 4-23: XRD results for cylinders produced with parameter set *A* in their as-built and stress relieved condition overlaid on the same axes.

4.3.5 Hardness Characterization

Vickers hardness testing is then done on the cylinders. Figure 4-24 shows the hardness values for all samples tested in their as-built condition. No clear trend emerges from the data, showing that both increased substrate temperature during deposition and changes to process parameters do not significantly affect hardness of the printed parts. Coupled with the

microstructural characterization, the hardness values suggest that there is not significant enough breakdown of the martensite in any of the as-built samples to affect the bulk hardness of the sample[47]. This is an important result because it suggests that as long as martensite is the dominant phase in the part after deposition, the hardness (and therefore tensile strength [169]) of the material will not be affected significantly. More in depth testing would be necessary to determine the material property differences between the samples, if any exist.

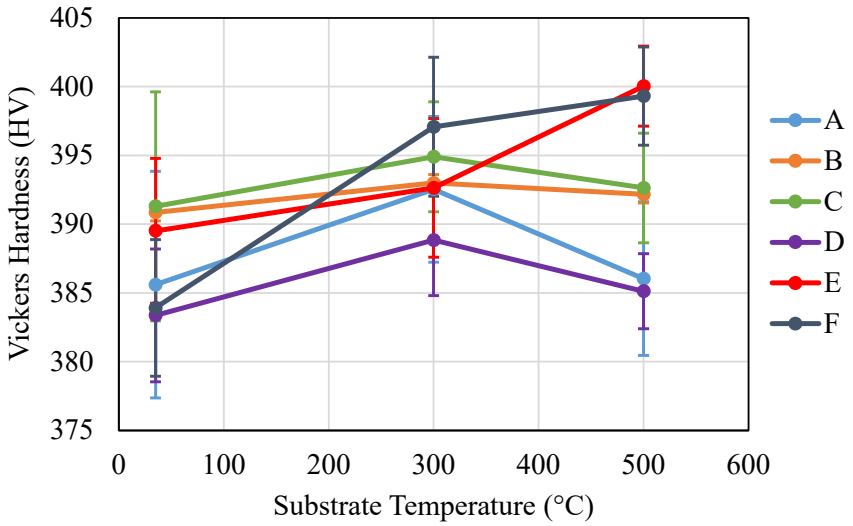

Figure 4-24: The Vickers hardness (HV) values for all cylinders in the as-built condition. The *X* error bars are omitted for clarity. The *Y* error bars are one standard deviation on the mean value.

To understand the effect of post processing on hardness, the hardness values for the parameter letter *A* cylinders in both their as-built and heat treated condition are compared, as can be seen in Figure 4-25. The Ti64 substrate hardness (in the original, rolled condition) is also measured and can be seen in red. The grey highlight in this figure shows the range of hardness

[47] All of the Vickers hardness indents were between roughly 150 and 175 μm on a diagonal. This distance is large enough to span several deposited layers and include 100s of alpha grains, so the author believes the hardness values are representative of the overall properties of the material.

values from Figure 4-24. It is clear that the stress relieved sample has significantly lower hardness than any of the as-built samples. In addition, the substrate hardness value and literature values agree and are both significantly lower than either the as-built or stress relieved samples. These findings, coupled with the microstructural analysis, suggest that the martensite mostly or completely breaks down during stress relief and the resultant α/β microstructure is not as hard as the as-built martensite, but harder than wrought or rolled material. In addition, the lack of a significant trend in hardness with temperature for both the as-built and stress relieved conditions suggests that the microstructure is not changed significantly by the substrate temperature at which the cylinder is printed [7], in line with findings in the previous section.

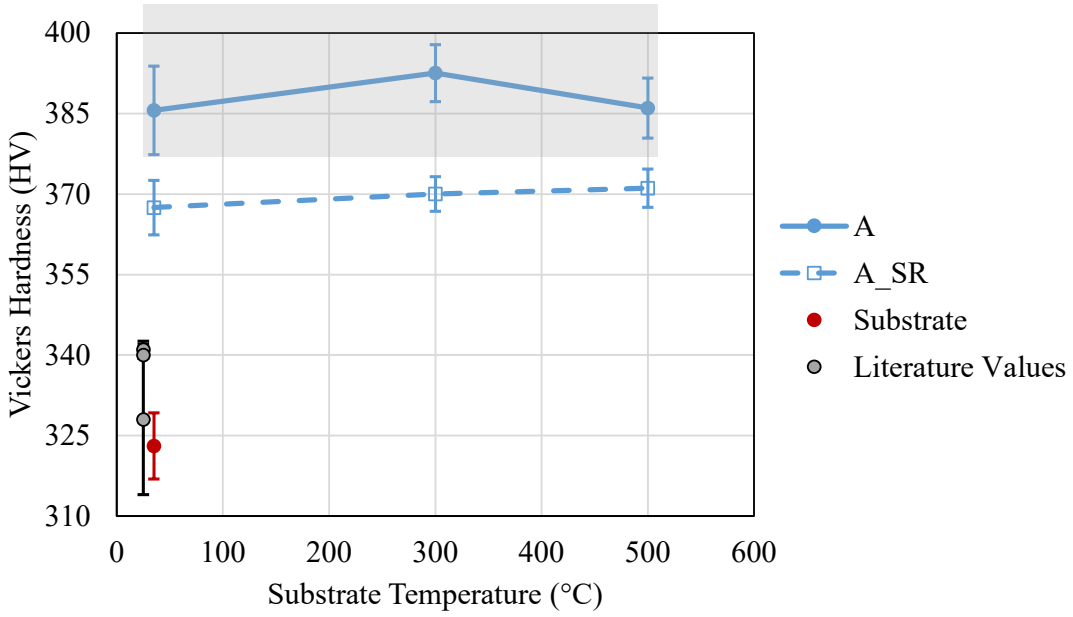

Figure 4-25: The Vickers hardness (HV) values for the cylinders printed with parameter letter *A* in both the as-built and stress relieved conditions, shown in blue. The rolled substrate hardness is shown in red. The grey highlight represents the hardness range in Figure 4-24. The grey points with black error bars are hardness values found for wrought and rolled Ti64 from literature [24], [173], [174]**. The *X* error bars are omitted for clarity. The *Y* error bars are one standard deviation on the mean value.**

4.3.6 Industry Relevant Geometry Fabrication

The results of the standard parameter compressor blade build (with a substrate temperature of 35 ˚C) can be seen in Figure 4-26. It is clear in all four of the images that there is delamination of the flange section of the compressor blade from the supports. In the case of the standard supports, there is a crack running along the junction between the flange and the supports, but there does not seem to be significant distortion of the flange. Modified 1 also has a crack running along the junction between the flange and the supports, but there is further degradation of the supports and does seem to be distortion at the edges of the flange. Modified 2 and Modified 3 have significant delamination of the flange from the supports at the junction between the support teeth and the flange and have a significant amount of distortion of the top surface of the flange.

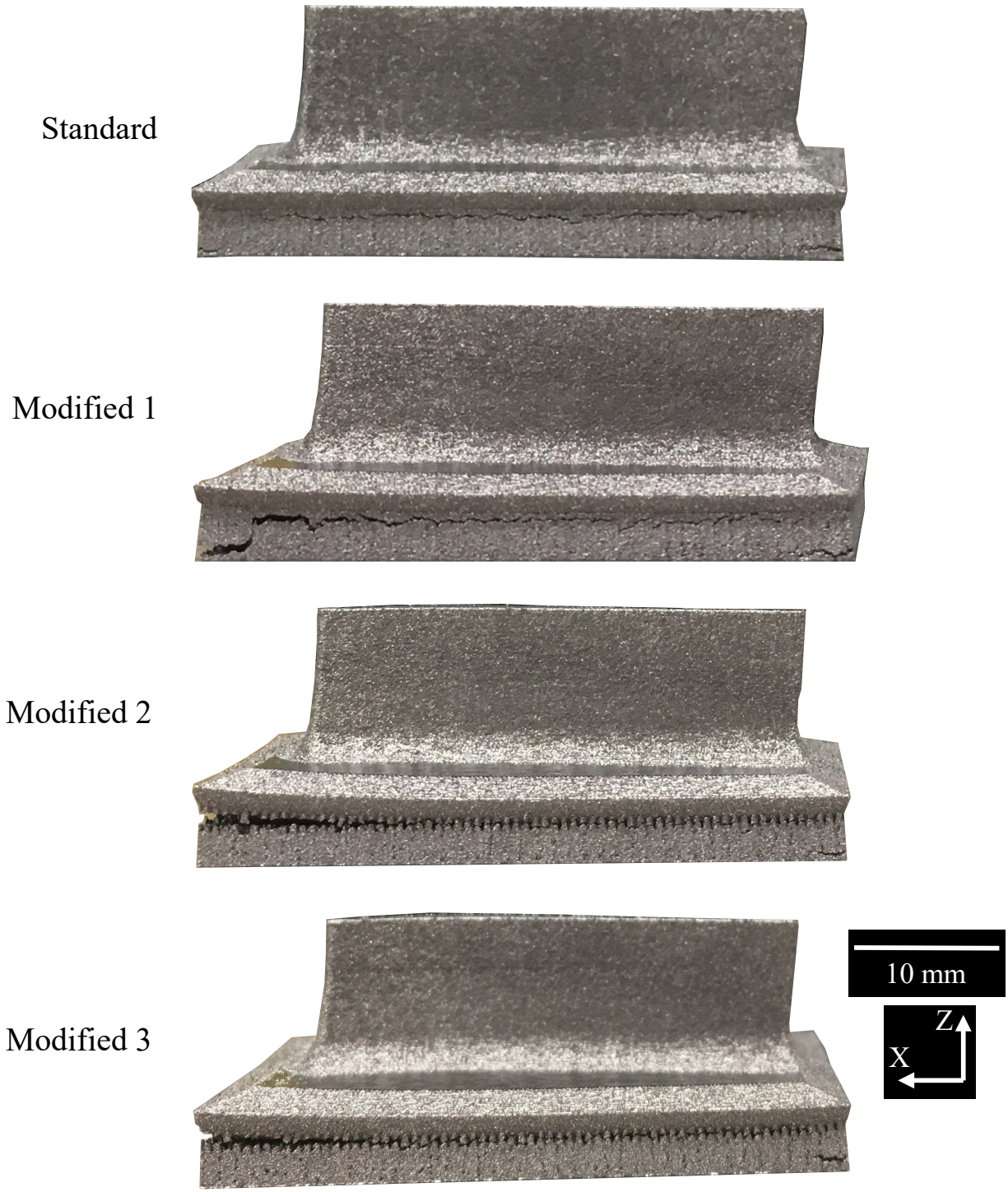

Figure 4-26: The results of the low temperature build of the compressor blade section (using EOS M290 nominal parameters).

A surface profile of the Modified 3 flange is taken to quantify the amount of distortion that is generated during deposition, and is presented in Figure 4-27. The red line in Figure 4-27.A shows the location of the surface profile on the top of the flange section of Modified 3 (a build height of 5 mm). Figure 4-27. B shows the surface profile image and the blue line represents the location where 10 pixels in *Y* were averaged at every *X* location in order to generate the plot seen in Figure 4-27.C.

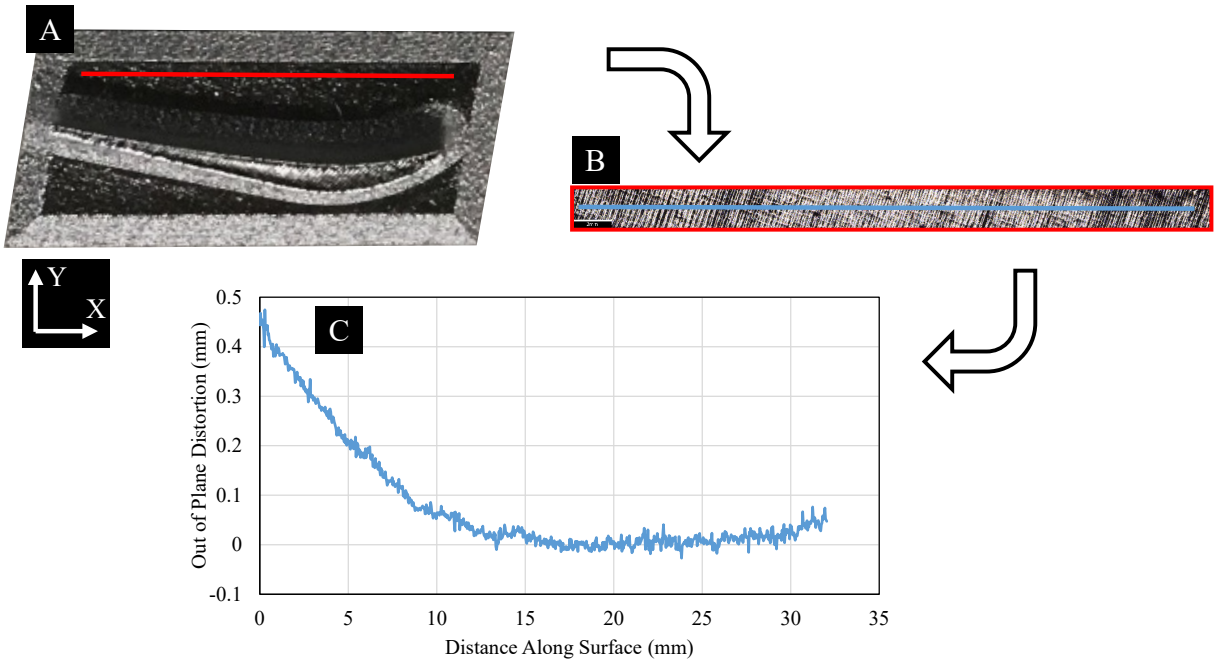

Figure 4-27: The surface profile taken from the flange section of the low temperature compressor blade build for the weakest supports (Modified 3). Out of plane distortion is measured in the *Z* direction.

An analysis of this build using Luke Scime's powder spreading anomaly detection software [119] is then completed by Luke Scime, and only two notable anomalies are detected. The first is for Modified 2 and the second for Modified 3. The powder around Modified 3 is disturbed for two

layers at a build height of 11.58 mm[48]. This height equates to a horizontal dark band in Modified 3 and shows that there is movement of the underlying part between deposition of subsequent layers. Both the dark band and the anomaly detection can be seen in Figure 4-28.

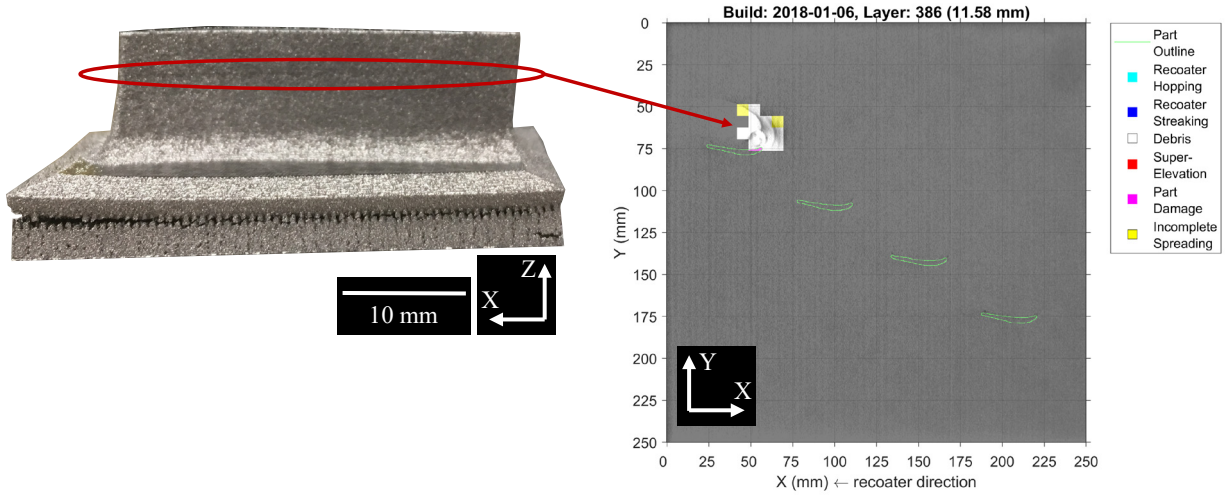

Figure 4-28: A side view of the Modified 3 compressor blade section with the red circle highlighting a dark band across the part at the same height that an anomoloy is detected in the spreading images.

The distortion and delamination of the originally flat section of Modified 3 is shown to be roughly 500 µm (Figure 4-27), which is equivalent to almost 17 build layers (one layer thickness is 30 µm). This means that if the distortion occurred at one time, or 'popped' off of the supports all at once, then the build should have failed due to the re-coater impacting the part. Therefore, it is clear that the majority of the distortion happened slowly over at least tens of layers, and probably hundreds of layers. This behavior suggests that even if the induced residual stress is high when material is deposited, as long as that stress is relieved on the timescale of tens to hundreds of layers (minutes to hours), then that residual stress should not induce distortion in the overall part.

[48] A further discussion of the powder spreading results for this build can be found in Luke Scime's doctoral dissertation [160].

The fact that there is an anomaly detection severe enough to disturb the powder bed, however, is an indication that the delamination is not completely gradual. When inspecting the final part, there is a detectable line in the surface of the part that corresponds with the height of the anomaly detection, as can be seen in Figure 4-28. This anomaly detection must be caused by the release of stored residual strain as the part separated from a portion of the supports, partially denuding the powder around the part. Therefore, it is likely that the distortion happened in steps, with the detected anomaly at 11.58 mm merely the largest of these steps, releasing enough energy to disturb the powder bed.

From the results of the low substrate temperature build, the parameters for the build at 500 ˚C are determined and three cases are chosen. The first case, labeled HT-1, keeps the process parameters the same as the low temperature build and uses standard supports, but at the increased substrate temperature. The second case, labeled HT-2, lowers the beam power to keep the melt pool cross sectional area the same as the low temperature builds (based on the results from Chapter 3, 238 W), and keeps the standard supports. The third case, labeled HT-3, uses the same power as HT-2 and the same supports as Modified 3. HT-3 is as close to a direct comparison with Modified 3 as possible because the build geometry (both part and supports) and the melt pool cross sectional area are the same. In addition, the residual stress held in the flange section of HT-3 would have to be considerably reduced in order for HT-3 to print successfully since there is such significant delamination and distortion in the low temperature build.

Figure 4-29 shows a picture of the three compressor blade sections with the wall used to facilitate printing removed for clarity. All three compressor blade sections built successfully with no distortion of the flange section of on any of the three.

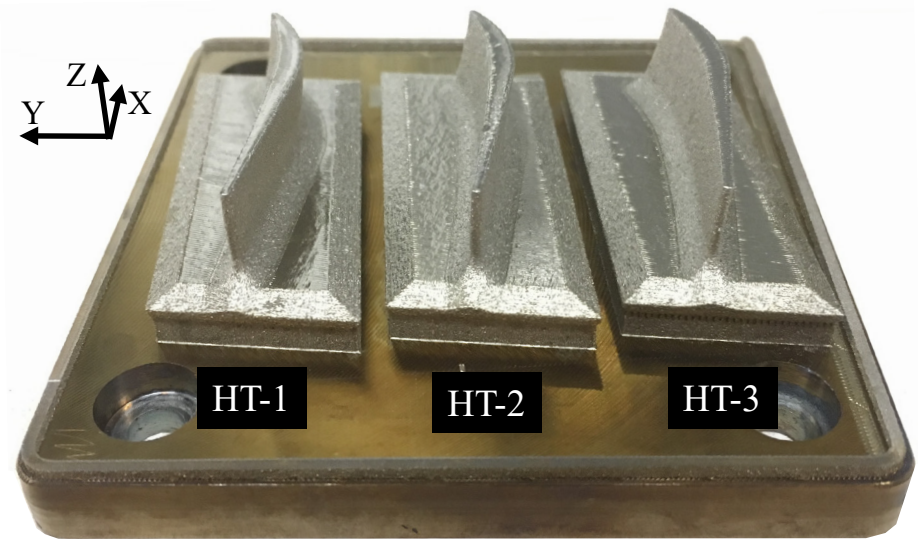

Figure 4-29: High temperature compressor blade section build.

A side view of HT-3 can be seen in Figure 4-30. It is clear that the flange section did not delaminate from the supports and that the teeth connecting the flange section to the supports are intact.

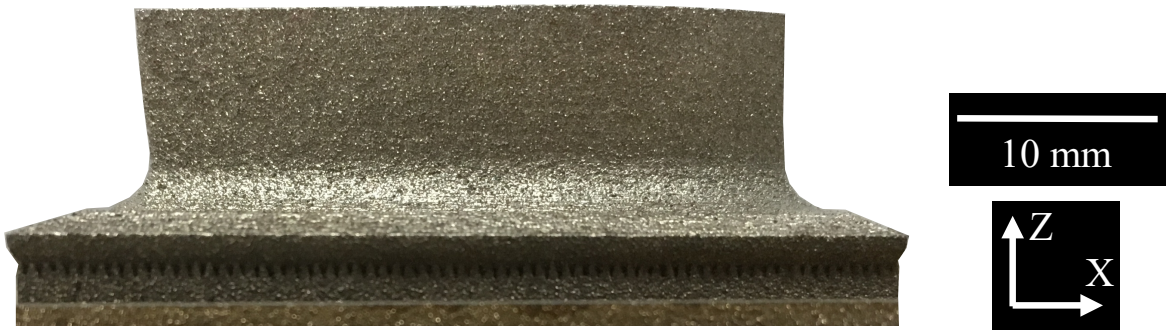

Figure 4-30: Side view of HT-3 showing the teeth supports intact.

To quantify the amount of distortion on the top surface of the flange section of HT-3, a surface profile is taken following the same procedure outlined in Figure 4-27. Figure 4-31 shows the measured surface profile of HT-3 relative to Modified 3 and shows that there is no trend in the

surface profile; while there is 'noise' caused by the uneven surface due to the individual rasters, there is no average height change across the sample. Since there is no change to the geometry of the part or supports and the melt pool size is held constant between the parts printed at different temperatures, this shows that the increase in substrate temperature successfully reduced the residual stress in the compressor blade section (an industry relevant geometry) to a level that is easily constrained by relatively weak and easily removable supports.

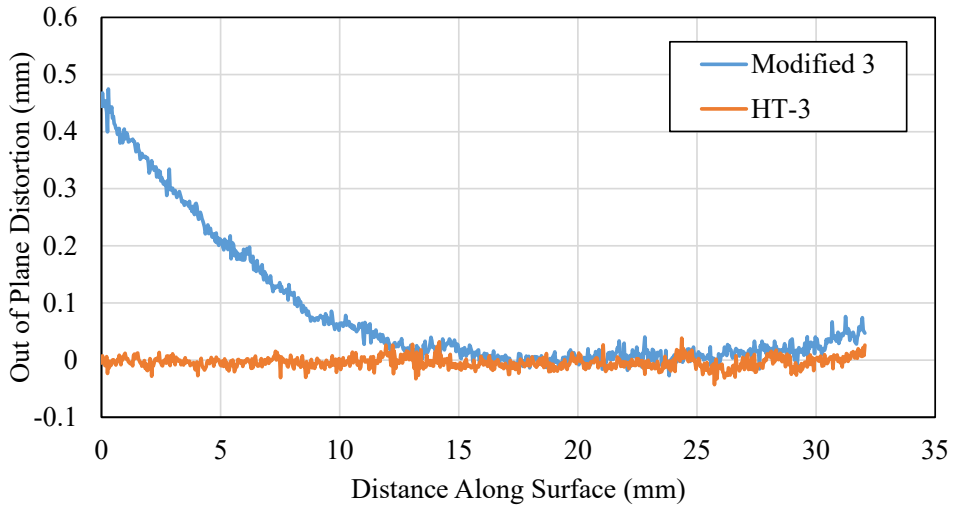

Figure 4-31: Out of plane distortion (elevation change, *Z* direction) for identical compressor blade sections printed at the nominal temperature (Modified 3) and at 500 ˚C (HT-3).

4.4 Discussion

In this chapter, the feasibility and inherent advantages of printing parts at elevated temperature in the EOS M290 (a standard, industrially relevant, LPBF machine) is demonstrated. Utilizing the characterization work done in Chapter 3, process parameters are developed to maintain constant melt pool cross sectional areas as substrate temperatures are increased. Parts utilizing these process parameters are produced at elevated temperature without the introduction of adverse microstructures, porosity or a reduction in hardness.

Cut surfaces within a part have progressively less distortion as the substrate temperature used for printing is increased. Extrapolating the maximum distortion curve generated in this work predicts residual stress free parts at substrate temperatures of roughly 500-600 °C. This behavior suggests two physical mechanisms. The first is a reduction in induced residual stress as substrate temperature is increased due to a reduction in thermal gradients around the melt pool and reduction in yield strength of the material. This mechanism does not have a threshold temperature, meaning that its effect will progressively increase from room temperature up to the melting temperature of the alloy. The second is stress relaxation [151], which will have a highly non-linear effect with temperature and starts to add to the distortion reduction in these experiments between a substrate temperature of 300 °C and 500 °C. This finding is in agreement with the strain relaxation behavior of Ti64, which predicts that distortion will not be seen in parts above roughly 600 °C [151]. This behavior is also the reason that the ASTM suggested stress relief temperature for grade 5 titanium (Ti-6Al-4V, Ti64) is 650 °C [175].

Since residual stress is significantly reduced during deposition of a part, the fixturing (support) requirements for parts to print successfully becomes significantly less constraining and the ability to print parts with more easily removable supports becomes possible. This allows for an increase in part complexity as well as a reduction in post processing, making a wider range of industrially relevant parts both more feasible and less expensive to produce.

The as-built microstructure for parts produced at a 500 °C substrate temperature is shown to be similar to that of as-built material for nominal conditions with the notable exception that there is at least a small degree of martensite breakdown into α/β. After stress relief, all of the sample microstructures look very similar and the alpha grain widths are not significantly different, meaning that printing at a substrate temperature of 500 °C allows for close to residual stress free

parts while still getting the same microstructural advantages of the existing LPBF process; namely high strength and the ability to decompose the as-built martensite into a fine α/β lathe with the suggested furnace profile for stress relief.

The lack of porosity in the high velocity melt pools indicates that avoiding balling may not be as critical as previously indicated as long as the melt pool dimensions and hatch spacing are chosen to generate a sufficient overlap during deposition. This result has significant implications for deposition speed, since an increase in velocity allows for an increase in deposition speed for the same melt pool cross sectional area. While more work is necessary to fully vet this conclusion, if balling is shown to be acceptable during part production, significant increases in deposition speed are possible using existing systems.

The production of a compressor blade section at nominal parameters (35 ˚C substrate temperature) displays the need for a reduction in residual stress as a means to reduce the amount of supports needed to produce a part successfully. In order to keep the flange section of the compressor blade flat during normal deposition (at a substrate temperature of 35 °C), solid supports surrounding the parts are necessary, and even then there is significant cracking of those supports. That same part, when produced at a substrate temperature of 500 ˚C, requires considerably less supports (that are more easily removed) and has no detectable distortion.

Chapter 5 – The Effect of Scan Strategy on Local Part Temperature in Laser Powder Bed Fusion

5.1 Background and Overview

Any scan strategy will affect the local temperatures within a part due to the movement and travel history of the heat source, and there are several scan strategies that can be employed to efficiently fuse a layer during LPBF. The most efficient scan strategy in terms of deposition speed is a raster pattern, meaning that a beam turns around at the end of a single bead and passes back parallel to its previous track at some set distance (hatch spacing) perpendicular to the travel direction (see Figure 5-1). This scan strategy is widely used in powder bed processes. If all of the laser passes were in the same direction instead of alternating directions, the temperature field that is seen by the melt pool would be more temporally uniform [12], but the total time to fill in a layer would be significantly increased because of the extra movement required by the scanning optics[49].

There is quite a bit of variation in the macro scale scan strategy, however, which will also have an effect on the local part temperature encountered by the melt pool during deposition [12], [69], [159]. The EOS software (EOSPrint Versions 1.5 and 1.6) uses stripes that are filled in using a raster scan strategy [81]. Every layer, the direction of the stripes changes by 67 degrees. When a melt pool gets to the edge of the stripe, the laser is turned off for a specified amount of time to allow the mirrors that direct the laser to decelerate, change direction, and accelerate. Figure 5-1 shows a schematic of the default scan strategy used in the EOS process with an enlarged section highlighting the individual raster scan tracks and beam turnaround. The edges of stripes are in blue, the individual raster scan tracks (raster passes) in green, and the beam turnaround is in brown.

[49] The galvanometer mounted mirrors would have to turn around twice for every melt pass for laser passes in the same direction, but only once for a raster scan pattern.

The nominal stripe width for Ti64 is 5 mm, but on the edges of parts, it is possible for the stripe width to be reduced significantly, as highlighted in red. In these cases, abnormally high substrate temperatures are expected due to the shorter time between passes of the heat source [113].

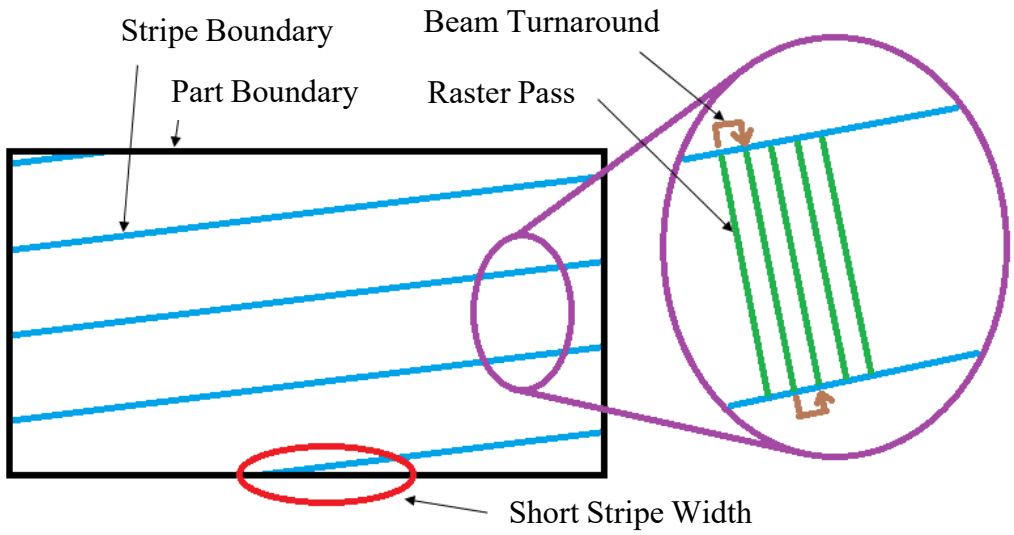

Figure 5-1: Scematic of the scan strategy employed by the EOS M290 to melt a single layer of a part.

From Chapter 3 and Chapter 4, it is clear that increasing substrate temperature during deposition can reduce distortion and increase melt pool cross sectional area. The current chapter will characterize the local heating that is induced during a raster scan strategy with and without substrate heating to understand what temperatures are attained locally within a part and what effect that may have on deposition.

Local temperatures within a part have been shown to be important, as varying scan strategy has an effect on part distortion [68], [69]. This effect is not lost on machine manufacturers, as EOS reduced the stripe width when printing Ti64 relative to other materials because of its propensity to distort [16], [145], [152]. As with part edges, as a stripe becomes thinner, the time between laser passes in a given area becomes shorter causing more local heating. In addition, the beam

turnaround during a raster has been shown to be very important from a final part quality standpoint due to its effects on part edge elevation [176], defect formation and microstructural development [81]. In the EBM process, the effect of beam turnaround has been identified as enough of a problem that the Arcam software implements a 'turning function' to accommodate the excess heat encountered at the edges of parts [80]. The author proposes that a turning function would also be valuable in the LPBF process in order to mitigate the effect of unintentional local part temperature elevation and variability due to the choice of scan strategy.

In this chapter, the time required for the melt pool to solidify is determined in order to compare that value to the time allowed by the EOS software (EOSPrint Versions 1.5 and 1.6) for the beam to turn around at a part edge. In this way, a recommendation for the beam off time (or the amount of time that the laser beam is off at the end of a raster pass) can be made based on process parameters. This time is then used in finite element simulations of raster stripes in order to understand how temperatures are changing along a single track and as a stripe progresses. A methodology to determine an optimal laser beam power profile for raster stripes is generated utilizing this temperature information and the relationships between power and melt pool area generated in Chapter 3. Finally, a stripe is produced on the EOS M290 and the variability in the melt pool at the edge of a stripe is analyzed.

5.2 Methods

5.2.1 Beam Turnaround and Time Required to Solidify

The EOS software allows for a delay at the beam turnaround called 'skywriting'. The time that the beam is off at the edge of a raster changes depending on whether skywriting is on or off. The software does not, however, tell the user what the off times are or whether they are variable.

In order to characterize the amount of time that the beam is off at the edge of a raster as parameters change, the beam off times are measured with a high speed camera and high magnification lens[50] at 100 kHz with an integration time[51] of 260 ns. The two notable exceptions to the existing camera setup for these experiments is the reduction in magnification by a factor of four[52] and the replacement of the existing filter with a neutral density filter that reduces the amount of light from all wavelengths that is allowed to hit the camera detector. This filter protects the camera detector, but does not preferentially attenuate the laser wavelength. While it is unclear if the camera detector is sensitive to the laser wavelength or just the emitted light from the melt pool, the camera signal did decrease from saturation to the noise floor in a maximum of two frames in all cases and results in a very definable signal on and off. This gives the uncertainty about beam off time as ±20 µs. An example progression of images showing a beam turnaround with skywriting enabled can be seen in Figure 5-2. The beam off time corresponding to the image progression seen in Figure 5-2 is 550 µs.

Figure 5-2: An example progression of high speed images used to determine the amount of time the beam is off for various geometries and process parameters.

[50] This camera setup is described in section 6.2.2.
[51] The Photron Mini AX200 uses an electronic, global shutter. This means that it takes the data from all pixels at the same time for each image, and the voltage built up in each pixel is returned to zero between images. Integration time refers to the amount of time that pixels are accepting photons for each camera image and is analogous to 'shutter speed'.
[52] Since spatial resolution is not needed, but temporal resolution is very important, the magnification of the system is reduced in order to reduce the number of active pixels in the camera while maintaining the required field of view. Reducing the active pixels allows for a considerably higher frame rate.

The effect of geometry on the beam off time is also taken into account by looking at the time for the beam to turn around when the angle between the beam travel direction and the part edge is not 90 degrees. The scan pattern used for these tests can be seen in Figure 5-3. The laser starts at the bottom right (labeled START) and finishes in the upper left (labeled END). Each turnaround is numbered. This scan pattern is used at several power and velocity combinations in order to determine if the EOS software takes process parameters into account when determining the beam off time. The results of the beam off time measurements are separated into two groups and the average value for each group is used as the beam off time[53]. Turnarounds 1, 3, 5, 7, and 9 make up group 2 and occur at an edge that is not perpendicular to the beam travel direction, while all of the other turnarounds make up group 1, which do occur at an edge that is perpendicular to the beam travel direction.

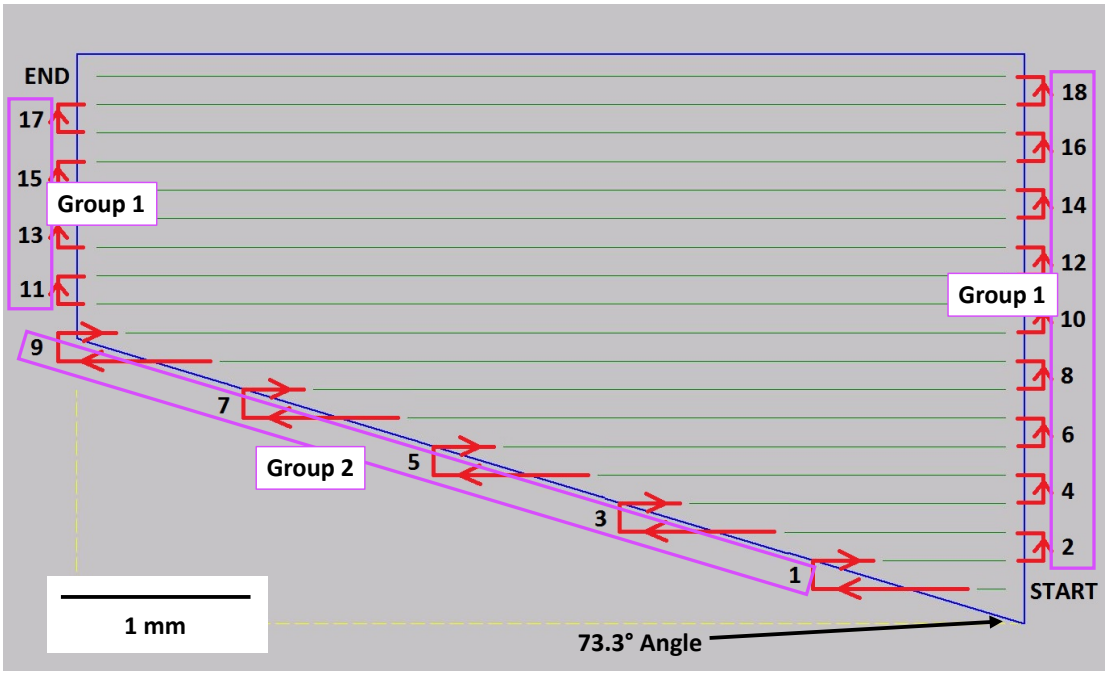

Figure 5-3: The scan pattern used to determine the beam off time as parameters and geometry change. The group 1 and group 2 (discussed in the text) are highlighted.

[53] The average is then rounded to the nearest 10 μs due to the temporal resolution of the measurement.

The same finite element simulations that were used in Chapter 2 are used in this chapter. Please refer to section 2.2.2 for more information. Once a steady state melt pool is formed, the heat source is turned off and the time for all of the nodes to drop below the solidus temperature is measured. The time step in each model is set such that there are at least 50 steps between the time the heat source is turned off and the time that the maximum temperature falls below the solidus temperature.

5.2.2 Raster Stripe Simulations

To determine the temperature that a melt pool would encounter during a raster scan strategy, a long single bead simulation is run in order to get the temperatures behind the melt pool for a prolonged period of time. The temperatures at a location one hatch spacing from the centerline of this simulation in the *Y* direction are determined as the heat source passes by. A representative simulation with a point representing the location from which temperatures are extracted (red point) is shown in Figure 5-4. A representative curve generated from those temperatures is shown in Figure 5-5. Groeber et al. [81] found that the maximum substrate temperature encountered by a melt pool is inset from the stripe boundary just after a turn around. The temperature profile in Figure 5-5 shows the same behavior, which is due to the time required for heat to diffuse from the previous raster pass.

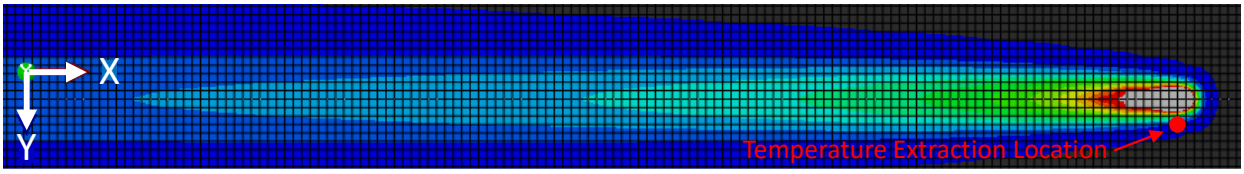

Figure 5-4: Long single bead simulation used to generate the temperature profile for a single raster pass. The melt pool is in light grey, the initial substrate temperature in dark grey, and the solid state temperatures above the initial substrate temperature in color.

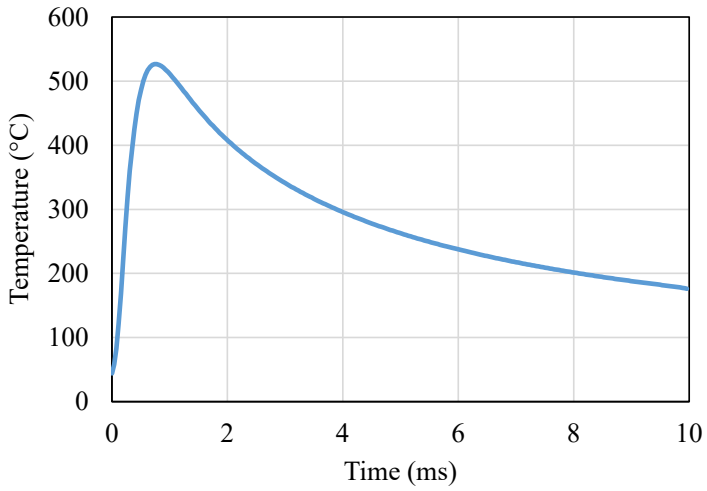

Figure 5-5: An example temperature profile one hatch spacing away from the previous raster pass, equating to the temperature seen by the red point in Figure 5-4. Time on the X axis refers to the time since the previous heat source passed adjacent to that point.

These simulations are very similar to the simulations in section 2.2.2, but the mesh size in these simulations is increased to accommodate the larger spatial domain on reasonable timescales. Since the melt pool dimensions are no longer of interest in these models and the resultant temperature profiles have the same shape as prior research [81], this was deemed an acceptable tradeoff.

Previous raster passes will affect the temperatures encountered by the melt pool, so the ability to simulate an entire stripe is also necessary. Figure 5-6 is an example image of a multi-pass simulation that is used to determine how temperatures evolve throughout a stripe. The melt pool is in grey. The red arrow shows the stripe propagation direction, which is perpendicular to the beam travel direction in yellow. The white arrow represents the heat source and the locations where temperatures are extracted are shown in green. Color represents temperatures below solidification. The beam off time determined from section 5.2.1 is used as the delay at the end of each pass.

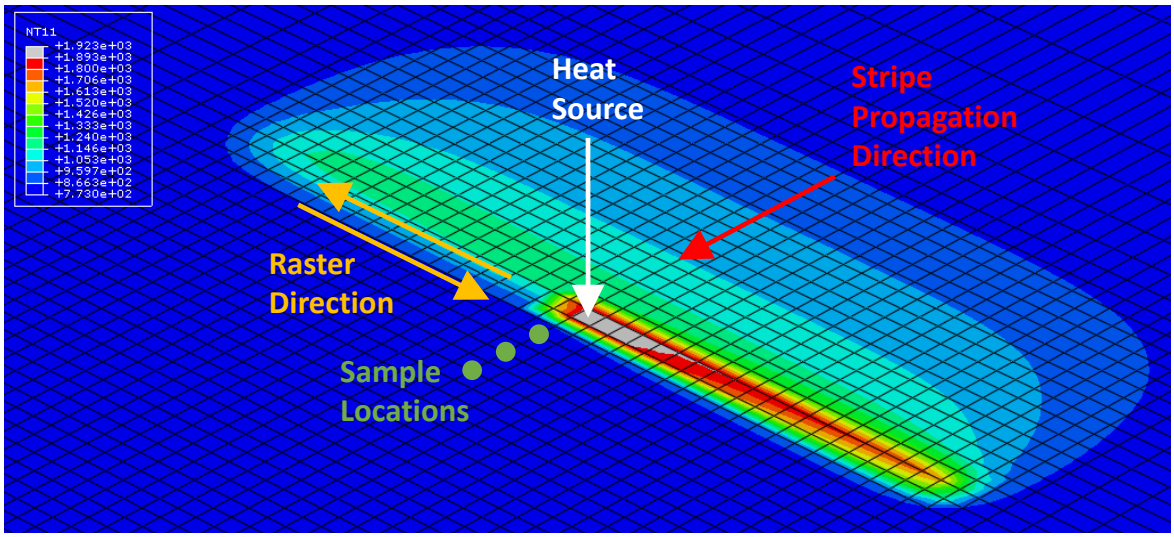

Figure 5-6: An example simulation of multiple passes of the laser to simulate a raster stripe.

Again, the mesh size in these simulations is increased to accommodate the larger spatial domain to be simulated. Since the model is only determining how specific locations of a stripe heat up with successive passes of the melt pool, and therefore the temperatures of interest are changing relatively slowly, this was deemed an appropriate tradeoff. The temperatures within the raster are measured in Chapter 6 and show good agreement to the simulations generated in this chapter, validating the choice of mesh size.

Figure 5-7 shows an example plot of temperature vs time for a fixed location at the centerline of a raster stripe. A time of zero is set to be before any heat reaches that location. The melt passes leading up to the fixed location are labeled 'Previous Beam Passes' while the melt passes after passing over the fixed location are labeled 'Subsequent Beam Passes'. The red dot in Figure 5-7 highlights the temperature used as the present beam pass. At each beam pass, the present beam pass temperature is extracted and used to generate Figure 5-8, which shows the temperature rise along the centerline of a stripe as it progresses. Each data point in Figure 5-8 is the temperature at the centerline of the stripe just before the melt pool passes over that position for each raster pass.

This means that each data point in Figure 5-8 comes from the data in a figure like Figure 5-7, but for a different location along the centerline of the raster stripe. A raster number of 1 means that it is the center of the stripe in front of the first melt pass, and is therefore the temperature of the original substrate. A raster number of 2 means that it is the center of the stripe in front of the second melt pass, etc.

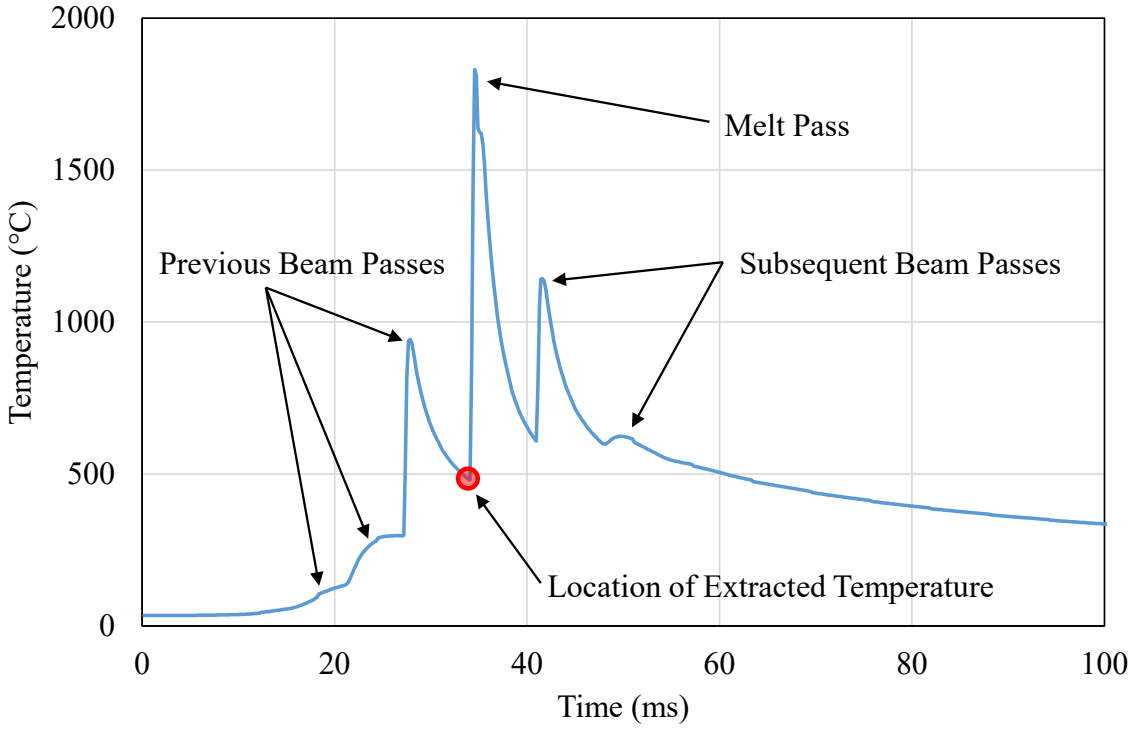

Figure 5-7: The temperature profile for a single location at the center of a raster stripe for the simulations described in Figure 5-6 with select features highlighted.

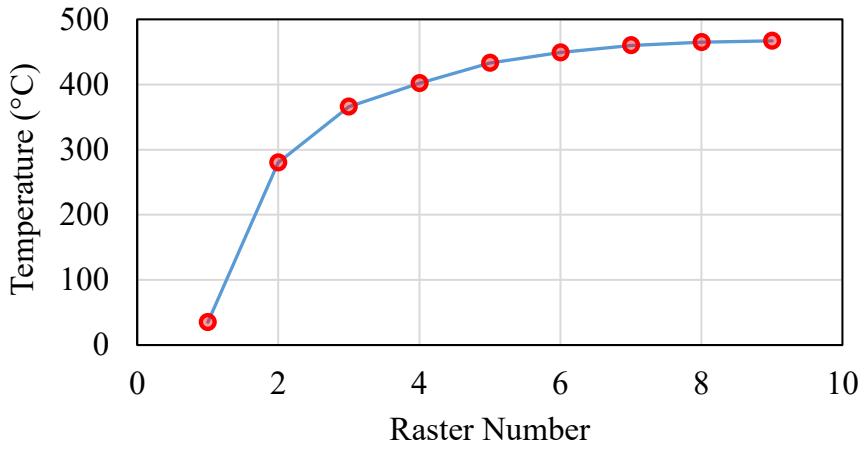

Figure 5-8: An example of the temperature encountered by the melt pool at the center of a stripe as that stripe progresses.

The temperatures encountered by the melt pool are based on the amount of energy absorbed by the beam during the generation of the stripe. This means that instead of using an effective absorptivity that is determined by comparing melt pool cross sectional area to conduction based simulations (Chapter 3), the actual absorptivity of the laser must be used for accurate temperature profiles to be generated. Trapp et al. found that the actual absorptivity of 316L stainless steel varied between roughly 30% and 80% depending on the melt pool morphology (conduction mode melting vs severe keyholing), and that there was a steep increase in absorptivity as the melt pool transitioned between these regimes [155]. The cross sectional shape of the Ti64 melt pools generated in the EOS machine using the parameters from Chapter 3 are in this transition region (though closer to conduction mode melting than severe keyholing), and therefore the actual absorptivity of the laser is uncertain. Kwon et al. found values for the absorptivity of 1070 nm laser radiation on a Ti64 substrate of roughly 40%, relative to 30% for 316L stainless steel [177]. A comparison of these findings suggests that the absorptivity of Ti64 will not be below 40% for the LPBF process. Since the laser absorptivity increases to a maximum of 80% for severely

keyholed 316L stainless steel samples, this value was taken as the maximum absorptivity of the laser for Ti64 as well.

The upper limit found for 316L stainless steel was used for Ti64 without a correction since the upper limit of absorptivity should be more dependent on internal reflections of the laser within the vapor cavity of the keyhole than on the properties of the material. In addition, none of the melt pools simulated in this chapter would generate a severe keyhole, so 80% was deemed a safe upper bound. Without specific information on the actual absorptivity of the laser for the parameters and materials used in this chapter, the author has bracketed the true absorptivity range as being between 40% and 80%.

5.2.3 Power Profile Generation

A beam power vs part temperature relationship for the LPBF process was determined in section 3.3.2 that can be used to keep melt pool area constant even as substrate temperature is changed. Using the temperature information generated from the simulations introduced in section 5.2.2, the optimal power to use at any location within a stripe can be determined in order to keep melt pool area constant. Beam power is controlled in this work because power changes are simpler and more computationally efficient to implement into a scan strategy than velocity changes[54] [3].

The steps in determining the optimal power profile for a raster stripe are shown in Figure 5-9. Plot *A* is the power profile from section 3.3.2, plot *B* is the single track temperature profile (Figure 5-5), and plot *C* is the buildup in heat along the centerline of the stripe (Figure 5-8). Plot *D* shows the result of combining plots *A*, *B*, and *C*, and is the optimal power profile to use for

[54] Power changes are simpler to implement because the absolute values can be fed directly to the laser. Velocity changes, however, require the calculation of the variable accelerations of the scanning mirrors needed to implement those velocity changes.

deposition of a raster stripe. The steps in the process are as follows: plot *C* is used to determine the substrate temperature to plug into plot *B* for that raster number, the resultant temperature profile is then plugged into plot *A* in order to generate plot *D*. To generate a power profile, the following process parameters need to be set: starting beam power, beam velocity, beam off time, hatch spacing, stripe width, and beam diameter[55]. For the work in this chapter, all process parameters that are being held constant are set as the value used for the nominal parameters for Ti64 on the EOS M290 for 30 µm layers.

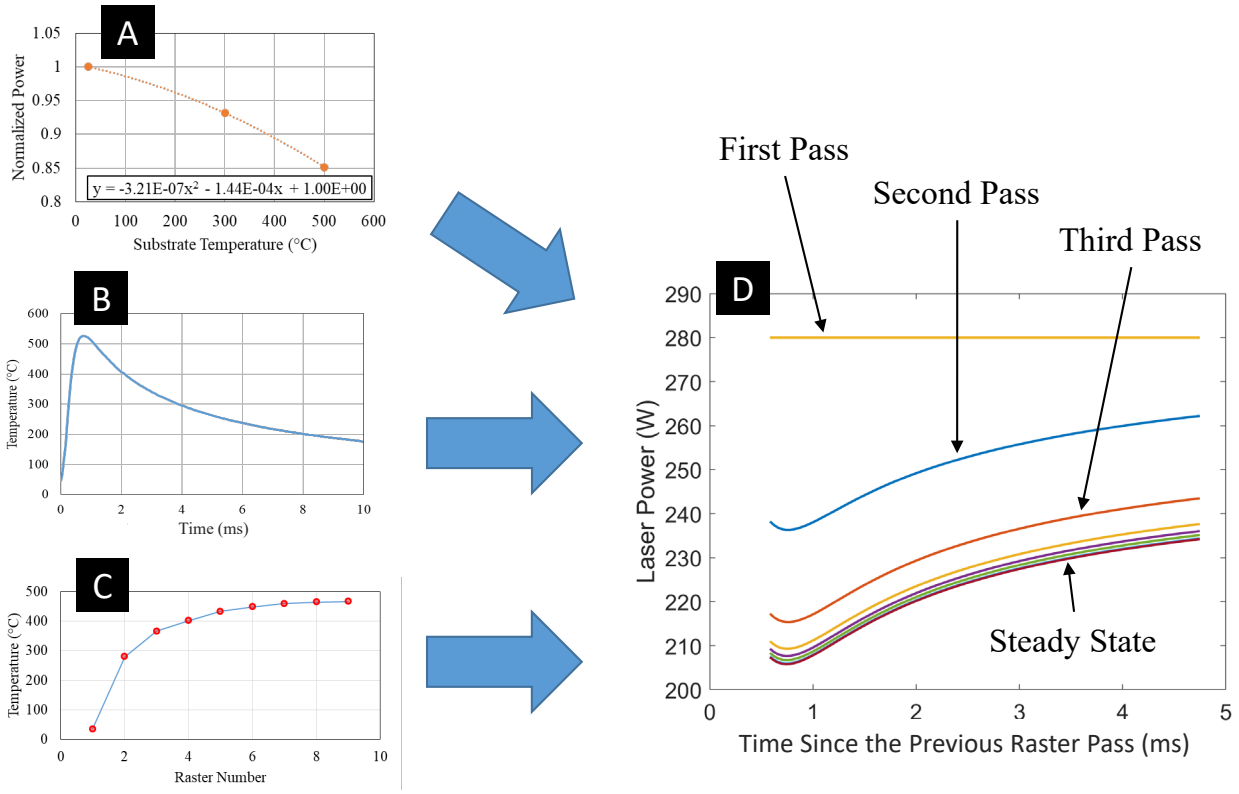

Figure 5-9: A schematic of the steps required to determine the power profile that should be used to keep melt pool area constant as a stripe progresses.

[55] Beam diameter needs to be set because it affects the shape of the melt pool cross sectional area and therefore the absorptivity of the laser.

5.2.4 Raster Stripe Deposition

To test the validity of the temperature profiles determined from simulations, a series of raster stripes are deposited on a Ti64 substrate and cross sectioned at varying distances in from the edge of the stripe. Due to the limitations of the EOS software, power cannot be varied during deposition of a stripe. Instead, the stripe is deposited with nominal Ti64 parameters for 30 μm layers and the melt pool areas are compared to those predicted from simulation. In order to look at several distances into the edge of the stripe without having to employ serial sectioning, five identical stripes are deposited such that their ends are offset from each other (in the *Y* direction) by 200 μm. A wire EDM then cut a straight line through all of the stripes (in the *X* direction). Figure 5-10 shows an image of the re-assembled Ti64 substrate after the cut was made, showing the location of the cut relative to the stripes. The stripes are offset from each other in the *Y* direction so that the EDM cut is at a known distance in from the edge of the raster.

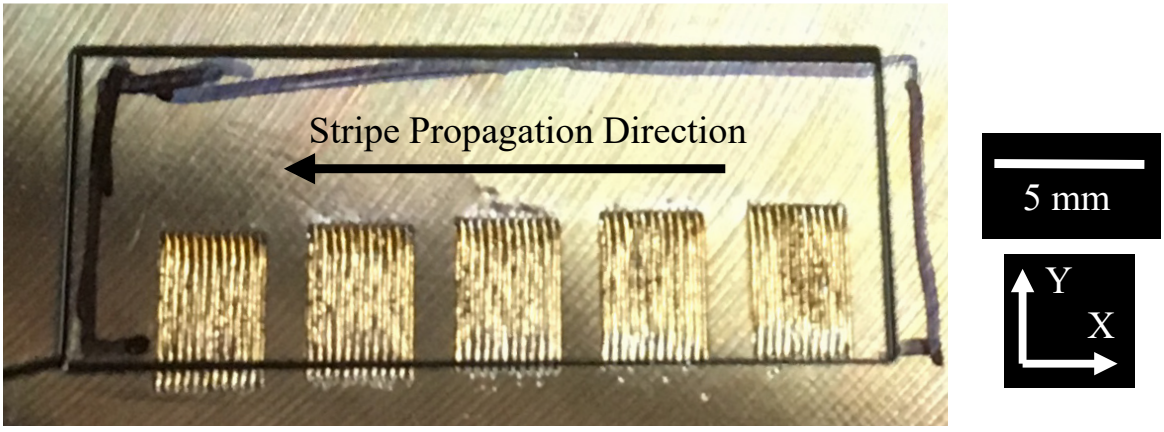

Figure 5-10: Image of the stripes after the wire EDM cut.

5.3 Results

5.3.1 Beam Turnaround Behavior in the EOS M290

The beam off times are measured and the time for simulated melt pools to solidify are determined. The individual results can be found in Appendix 5. The amount of time that EOS turns off the beam at the edge of a stripe does not change significantly as process parameters change. This is true with and without skywriting activated, leading to the conclusion that skywriting only adds a fixed delay to the beam turnaround and does not account for changes to the melt pool. Figure 5-11.A shows the time to solidify from simulations performed at a 35 °C substrate temperature assuming a constant laser absorptivity at the low end of the bracketed range (40%) for clarity. Figure 5-11.B shows the measured beam off time for group 1[56] beam turnarounds conducted at a 35 °C substrate temperature.

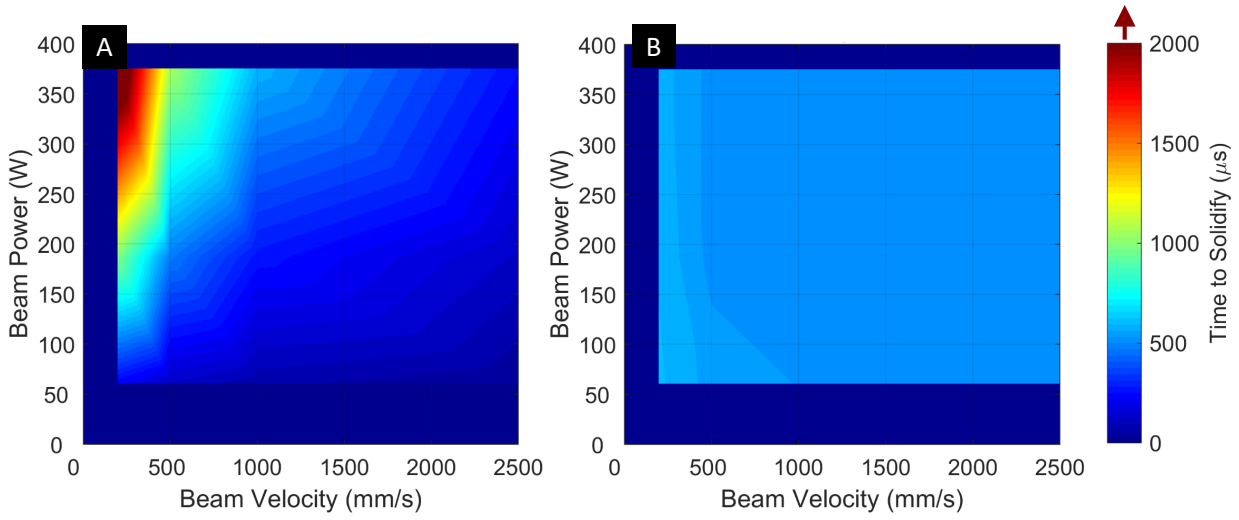

Figure 5-11: A) The simulated time to solidify at 35 °C assuming a laser absorptivity of 40% and B) the measured beam off time in the EOS M290. Both plots have the same scale bar.

[56] Note that group 1 refers to beam turnarounds that occur at an edge that is perpendicular to the beam travel direction.

It is clear by comparing the two charts that there is room for optimization of the beam off time based on the time it takes for the melt pool to solidify. There is no change in velocity while the beam is on and the power is not being changed at the end of scan tracks either [81], meaning that the EOS control software does not account for changes to substrate temperature with their standard process parameters.

The beam off time when skywriting is employed is around 500-600 μs and happens to be roughly the same amount of time that it takes for melt pools around nominal conditions to solidify[57]. This may not be the optimal criterion for how long the beam should be off, however, since it means that the beam is starting a new melt pool adjacent to material that is either still molten or close to the melting temperature of the alloy. If the previous melt pool is still molten when the beam turns back on, undesirable fluid flows or spatter formation may be generated due to excess liquid adjacent to the current melt track. If the previous melt pool has fully solidified, but is still close to melting, then the new melt pool may be excessively large or the wrong shape if not accounted for by changes to other process parameters. In addition, the simulated time to solidify spans almost two orders of magnitude for the parameters used, so a beam off time of 550 μm may be far from optimal for non-standard power and velocity combinations or when part temperatures have changed.

The simulations also looked at the time required for the melt pool to solidify as the substrate temperature increased. The results of those simulations can be seen in Figure 5-12. The time to solidify increases substantially with substrate temperature. To understand this change, the time required for a melt pool to solidify is normalized to its value at 35 °C and plotted in Figure 5-13,

[57] The time to solidify for nominal parameters (at a 35˚C substrate temperature) assuming an absorptivity of 40% is roughly 410 μs. The likely temperature at the edge of the stripe, taken from Figure 6-48, is roughly 300 ˚C, which increases the time required to solidify to roughly 510 μs. Both of these times represent the bottom of the range for time to solidify because an absorptivity of 40% is the bottom of the absorptivity range discussed in section 5.2.2.

and shows that the percentage increase in time to solidify is almost independent of the power-velocity combination used to generate the melt pool. This means that as substrate temperature is increased, the melt pool will stay liquid for longer and the possibility of starting the next track before full solidification of the previous track increases. It also means that the particular process parameters used to melt do not change the percentage increase in time required for the melt pool to solidify, making it easier to incorporate this change into a control strategy. Experimental verification of the time it takes for a melt pool to solidify will be presented in section 6.3.5.

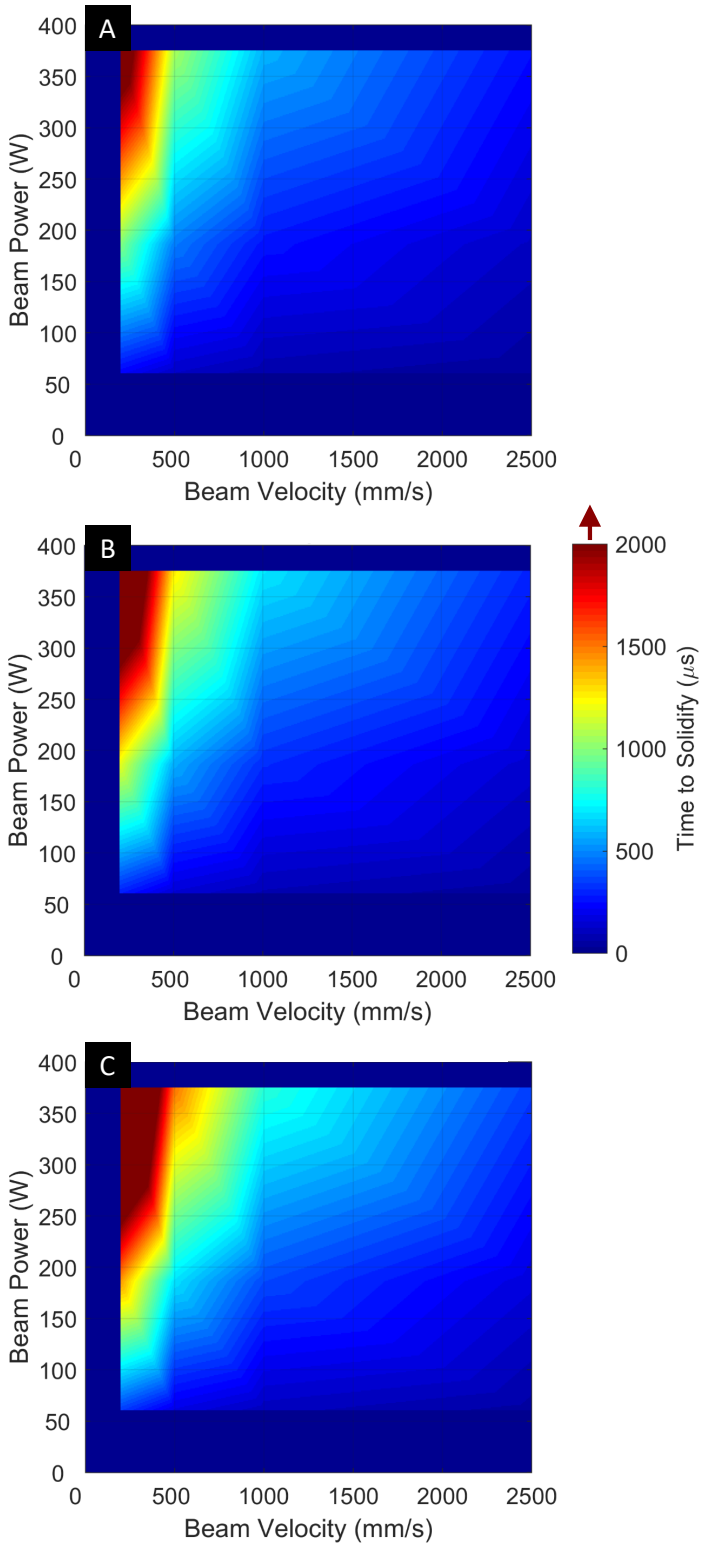

Figure 5-12: The simulated time required for the melt pool to solidify at different substrate temperatures: A) 35 °C, B) 300 °C, C) 500 °C.

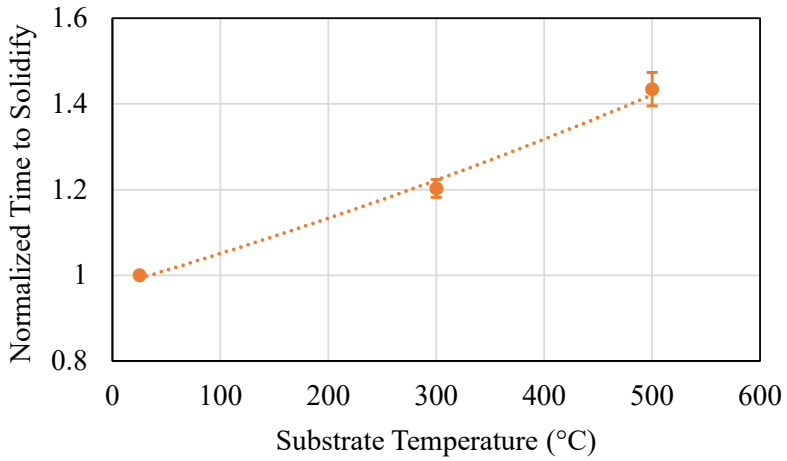

Figure 5-13: Simulation results for normalized time to solidify for a range of power-velocity combinations at different substrate temperatures. An exponential best fit line is shown for reference. The error bars in the *Y* direction are one standard deviation on the mean.

Up until this point, only the experimental data from group 1[58] has been presented. When the group 2 beam off times are analyzed, it becomes clear that the beam off times for group 2 are longer than those for group 1 by a roughly constant factor of 80 µs (refer to Appendix 5). This is likely a result of the longer travel distance required by the laser optics while the beam is off to reach the location of the subsequent scan track (see Figure 5-3), but as with skywriting, seems to be a fairly constant delay and not based on process parameters. While it is unlikely that this added delay has a significant effect on local part temperatures because of its small magnitude relative to the total beam off time, the EOS software has implemented a delay to facilitate laser optics movement that may affect local part temperatures, and should be characterized. Once again, there is room for optimization when non-standard process parameters are being developed.

[58] Group 1 refers to beam turnarounds that occur at an edge that is perpendicular to the beam travel direction while group 2 refers to beam turnarounds that occur at an edge that is not perpendicular to the beam travel direction.

5.3.2 Single Track Temperatures

Figure 5-14 shows the temperature profiles for the absorptivity bounds (40% and 80%) at several substrate temperatures for the EOS Ti64 nominal parameters for 30 µm layers[59]. The power used to generate each melt pool is scaled to keep the cross sectional area constant based on Figure 3-17. It is clear that there is a large spread in temperature for the same substrate temperature due to the 2X difference in absorbed power. It is also clear that at all times, the temperature is higher for higher substrate temperature at the same absorptivity.

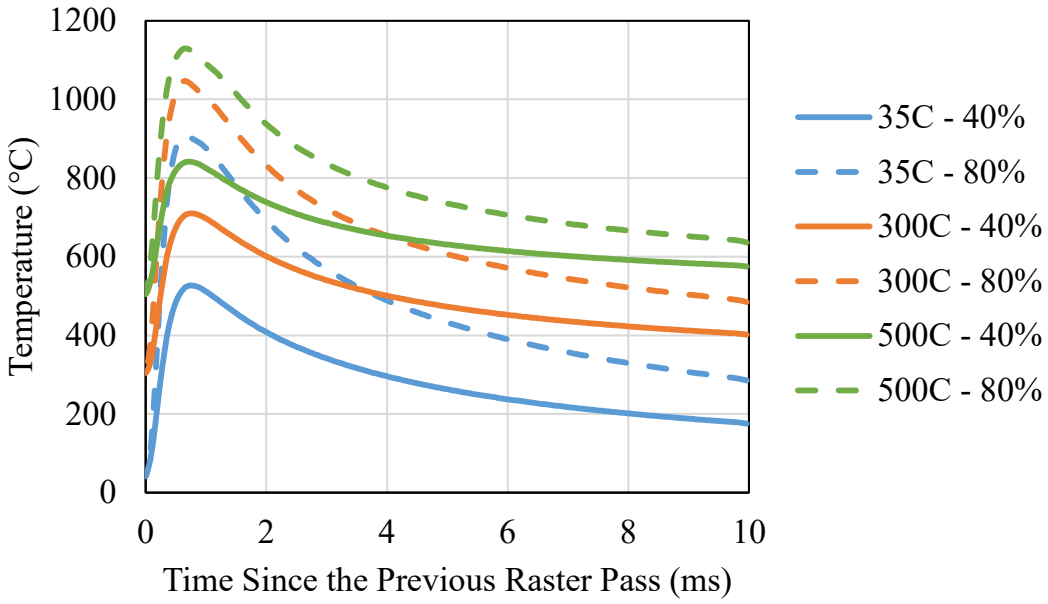

Figure 5-14: The temperature profile encountered by a melt pool as a function of time since the prior melt pool passed. Solid lines are for an absorptivity of 40% and dotted lines are for an absorptivity of 80%. Three initial substrate temperatures are shown and the power used to generate the melt pool is scaled to create the same melt pool cross sectional area at each substrate temperature.

[59] The velocity in the model is 1200mm/s, the power at a 35 ˚C substrate temperature is 112 W and 224W (280 W multiplied by either 0.4 or 0.8). At elevated substrate temperature, the power is further reduced in order to maintain the same melt pool cross sectional area as the 35 ˚C case.

Further analysis, shown in Figure 5-15, reveals that for a constant absorptivity, the temperature rise (or temperature difference between the original substrate temperature and the measured temperature) decreases as the substrate temperature increases. Similarly, the temperature difference between an absorptivity of 40% and 80% decreases as the substrate temperature increases, shown in Figure 5-16, meaning that at a higher substrate temperature, the temperature uncertainty induced by the absorptivity range is lowered. Both trends are likely a result of the decreased power input needed to maintain the same melt pool cross sectional area, the reduced thermal gradients around the melt pool[60], and the increased thermal diffusivity of Ti64 at elevated temperature [27].

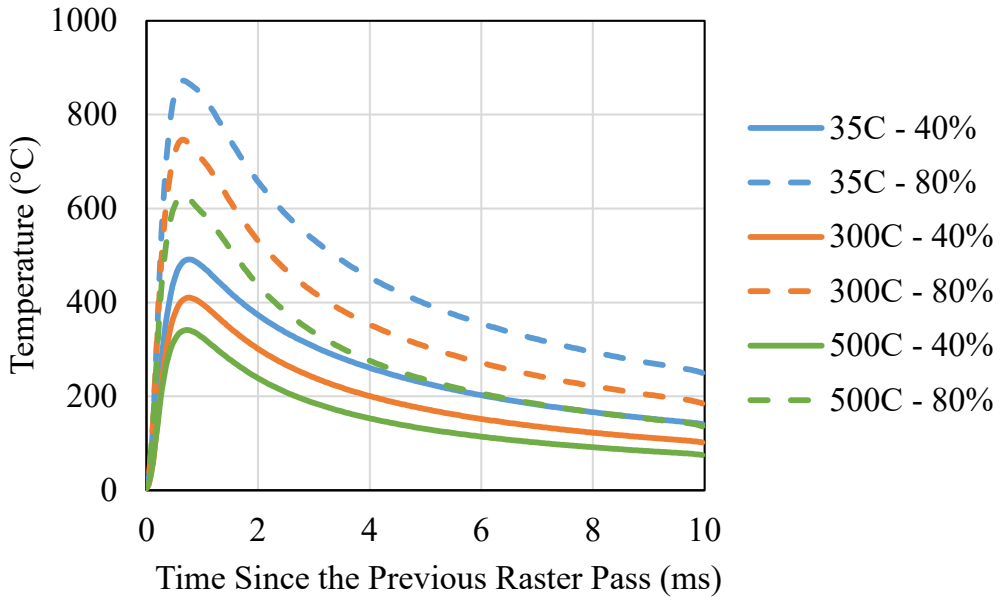

Figure 5-15: The same temperature profiles as Figure 5-15, but with the temperature difference relative to the initial substrate temperature, so only the local heating is shown. Note that the higher the substrate temperature, the lower the local heating above the original substrate temperature.

[60] The reduced thermal gradients around the melt pool at elevated substrate temperature are a result of the reduction in temperature difference between melting and the substrate temperature.

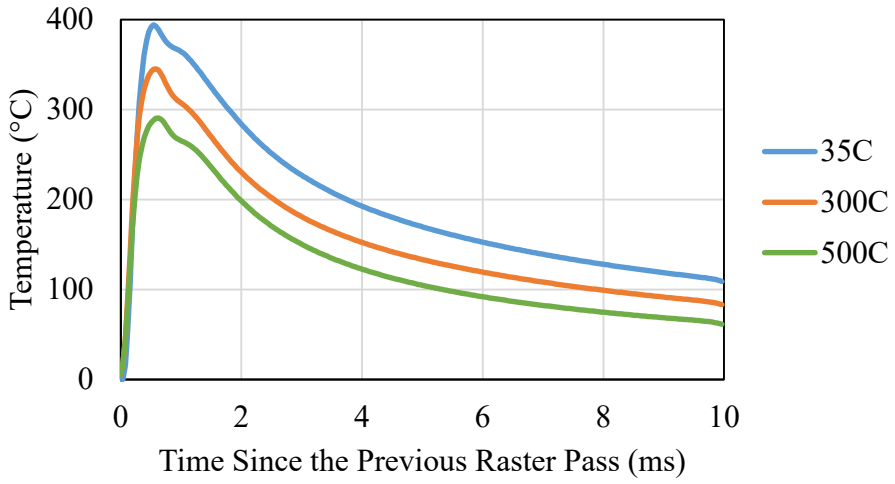

Figure 5-16: A plot of the temperature uncertainty (induced by the absorptivity uncertainty) with time for each of three substrate temperatures, showing that as substrate temperature is increased, the uncertainty in temperature decreases.

5.3.3 Temperatures and Optimized Power as a Raster Stripe Progresses

Once the temperature profile for a single track has been determined for various temperatures, this information can be fed into the model of an entire raster stripe. To determine the temperatures that are generated by the current EOS scan strategy with nominal Ti64 30 μm layer thickness parameters, a constant power and velocity with a 550 μs beam off time at the edge of the stripe is used[61]. The resultant temperatures along the centerline of the model are then fed back into the single track temperature profile model developed in section 5.3.2 in order to generate a temperature profile for each individual track within the raster. The simulation of the stripe is then re-run. At this point, the power is changing at every step in the model based on the centerline

[61] 550 μs is used for the beam off time to mimic the EOS M290 scan strategy when skywriting is active, and is not changed for simulations at different substrate temperatures. A constant beam off time is used instead of one that increased with substrate temperature to reduce the degrees of freedom in the analysis, but from section 5.3.1 the beam off time increases can be calculated.

temperatures from the previous model iteration and the single track temperature profile from section 5.3.2.

The temperatures along each track are generated by using the centerline temperature for that track as the substrate temperature to plug into the single track temperature profile. In this way the resolution of the stripe simulation is made course enough to run quickly, but the single track temperature profile and melt pool cross sectional areas are generated from more detailed simulations. The temperatures from the previous stripe simulation iteration are fed into the current iteration until a steady state temperature along the centerline of the raster stripe is reached, at which point the model has converged. The temperatures from any other location in the stripe can also be extracted using the same method, and are used in sections 5.3.4 and 6.3.6.

Figure 5-17 shows a subset of Figure 5-14, but with regions highlighted. Note that for the 5 mm wide stripe represented here, each pass only takes 4.72 ms[62]. The majority of the temperature increase due to diffusion of the heat from the previous melt track occurs while the beam is off (red shading). This means that when the next melt pool is formed, the substrate temperature is close to its maximum value. Recall that the beam off time of 550 μs (0.55 ms) was only slightly longer than the time required for the previous melt pool to solidify, though interestingly, a doubling of the beam off time would only slightly reduce the local temperature that the current melt pool would encounter because of the delay in heat diffusion from the previous melt track to the current one. It is incomplete, however, to say that changing the beam off time would not have a substantive effect on part outcomes. The longer the beam is off (equating to a shift to the right on Figure 5-17), the lower the local temperature encountered by the melt pool would be throughout the entire stripe.

[62] 4.72 ms = 0.55 ms for the beam turnaround + 4.17 ms for the raster pass (4.17 ms = 5 mm stripe width / 1.2 m/s beam velocity)

The red dotted line in Figure 5-17 shows the time that equates to the center of the stripe for each track, and the red solid line shows the time that equates to the opposite edge of the stripe for each track (or the end of that track). It is clear that the temperature from the previous track affects the temperature encountered by the current melt track throughout the entire stripe width. This means that local heating is not just a stripe edge phenomenon and must be accounted for throughout the full stripe.

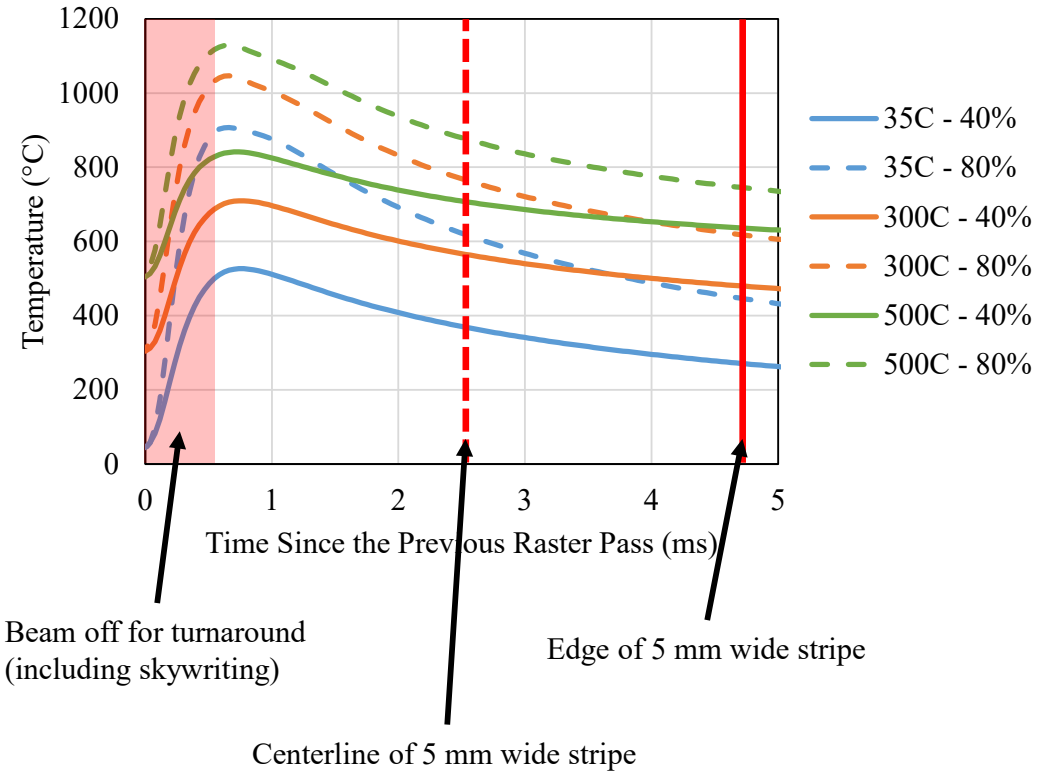

Figure 5-17: Temperature profiles from Figure 5-14 with overlays showing the start, middle, and end of a track for a 5 mm wide stripe.

The simulation of a raster will be unique to the choice of starting power, beam velocity, beam turnaround time, absorptivity of the heat source, substrate temperature, and hatch spacing. Therefore, four different cases are presented here. The nominal parameters for the EOS M290 for 30 µm layers are used as the basis for the parameters. The starting power is 280 W for a substrate

temperature of 35 °C, the velocity is 1200 mm/s, the beam off time is 550 μs, and the hatch spacing is 140 μm. The four cases have a starting substrate temperature of either 35 °C or 500 °C and use an absorptivity of either 40% or 80% (in order to bracket the range of possible absorptivities).

Figure 5-18 shows the centerline temperatures from each of the four cases for each iteration until steady state is reached. In all cases, the first iteration (utilizing a constant power at every step to represent what is done currently by the EOS M290) has the highest centerline temperatures. Iteration 1 overestimates the temperatures that the melt pool encounters and therefore underestimates the necessary power required to keep melt pool area constant for Iteration 2. Iteration 2 underestimates the temperatures and so on. Successive iterations quickly converge to a final temperature profile. Note the difference in temperature scale for each case. In all cases, the centerline temperature profiles after convergence are lower than their corresponding temperature profiles when a constant power is used, showing that by accounting for local heating during deposition, temperature swings during the deposition of a raster stripe are mitigated as well.

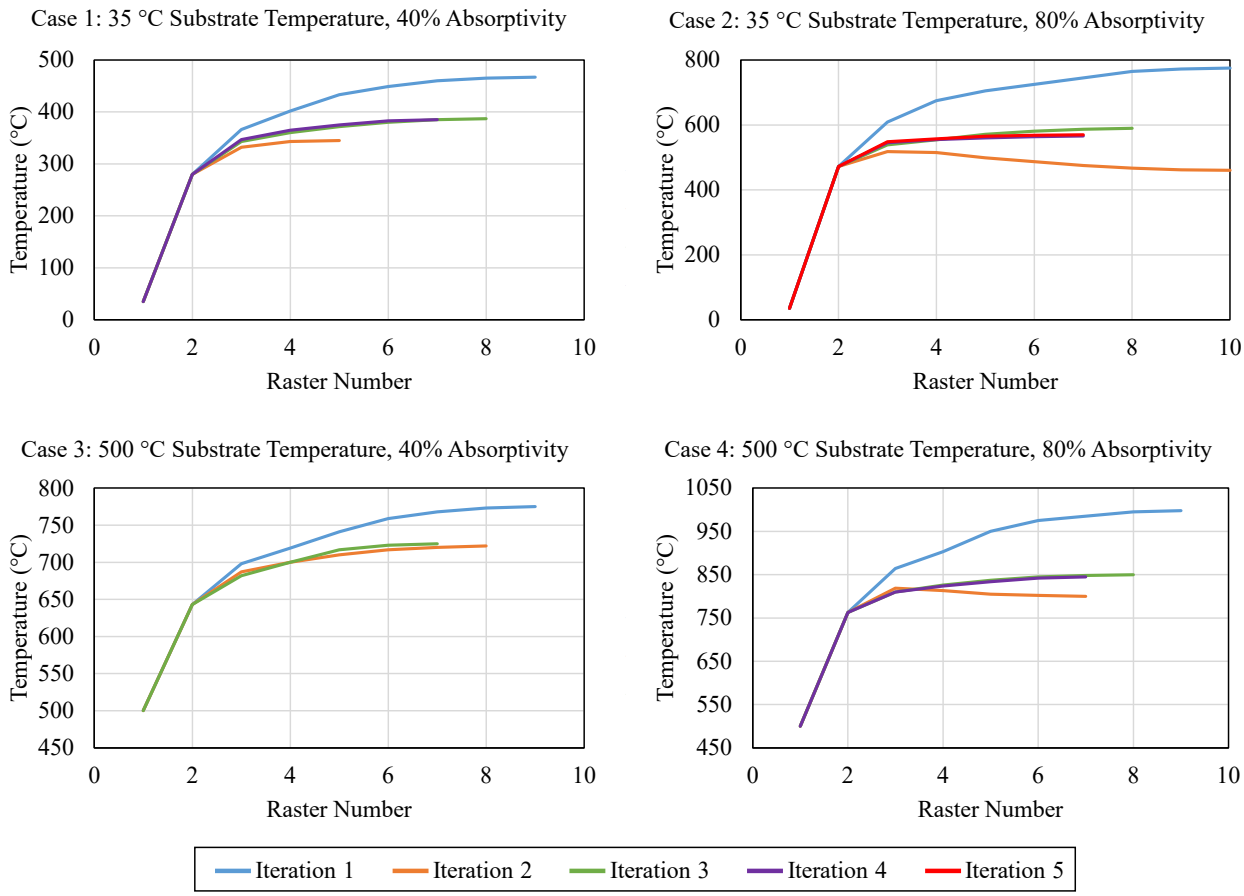

Figure 5-18: The centerline temperatures for each iteration for each case. Note the change in temperature scale in each case.

It is clear that there is a large spread in the centerline temperature of a stripe based on the amount of heat input (due to the range in absorptivity). To highlight the temperature differences seen once the models have converged, Figure 5-19 shows the final iteration for each case on the same axes. The centerline temperature for the stripe with a substrate temperature of 500 ˚C (Cases 3 and 4) is always higher than the centerline temperature for the stripe with a substrate temperature of 35 ˚C. However, as was seen with the single track temperature case, the centerline temperature increases more for the 35 ˚C case than it does for the 500 ˚C, showing that the temperature will be more variable for the lower substrate temperature because of the higher power input needed to

generate the same melt pool cross sectional area. This means that by increasing the substrate temperature and accounting for that temperature increase with a decrease in beam power, the local part temperature can be kept more constant during deposition.

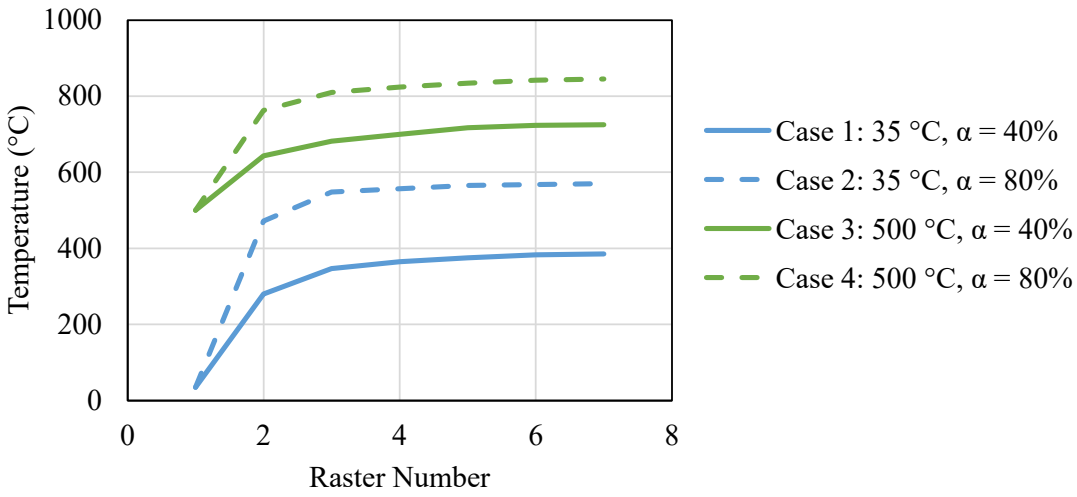

Figure 5-19: Centerline temperatures once the model has converged for each of the four cases presented in Figure 5-18.

The beam power profile once the model has converged is optimized to keep the melt pool area constant as the stripe progresses. Figure 5-20 shows what this optimized beam power profile would look like for Case 1. Note that the power is constant for the first raster pass since the substrate temperature would also be constant. The beam power profile for the second raster pass would then be based only on the single track temperatures determined in section 5.3.2. From the third raster pass until a steady state is reached, the excess heating from the generation of the raster stripe must be accounted for. The beam power profile is generated for the times that the beam is on, which corresponds to the *X* values discussed in Figure 5-17.

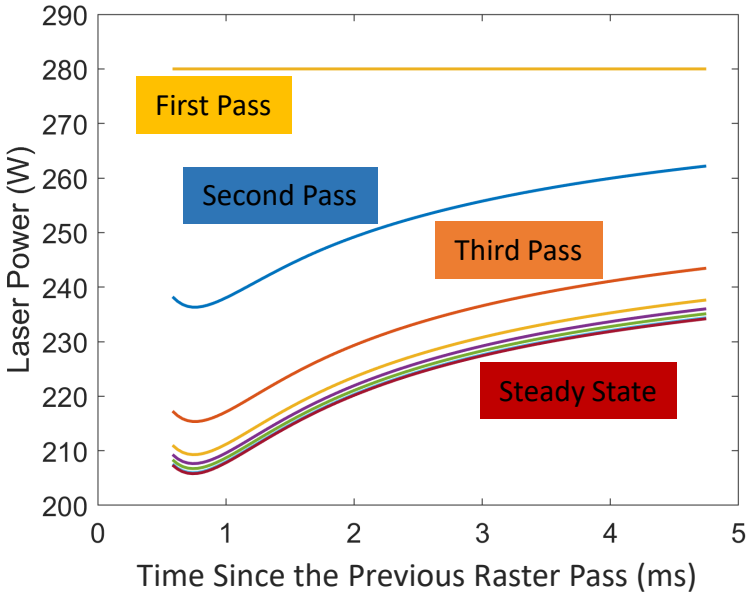

Figure 5-20: The power profile for Case 1. The first pass is equivalent to a single bead and has a constant power, but all subsequent passes has constantly varying power within a raster pass, even once a steady state centerline temperature is reached for the stripe.

Since the melt pool cross sectional area is not increasing throughout the raster stripe (as it would if the power were held constant), it may be necessary to reduce the hatch spacing or increase the initial starting power to account for the lack of melt pool area increase that is normally found. However, because the melt pool cross sectional area is less variable, the factor of safety on the melt pool overlap can be reduced without increasing the likelihood of lack of fusion porosity. In addition, because of the relatively few raster passes needed to get to a steady state temperature profile (less than 10 in all cases), the majority of a stripe would follow a single power profile, and would therefore be computationally efficient to implement into a control software.

5.3.4 Melt Pool Areas at the Edge of a Raster Stripe

After sectioning the stripes in the *X* direction, an image is taken from above showing the top surface of those stripes and the depth of polishing (Figure 5-21). The goal of using different stripes to probe progressively deeper into each stripe is accomplished, as can be seen from the polished and etched cross sections (Figure 5-22).

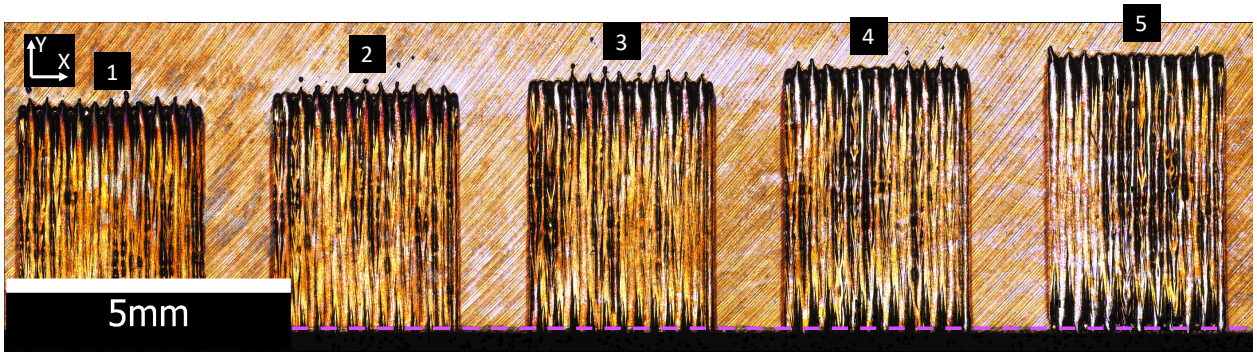

Figure 5-21: The stripes before mounting and polishing. The depth of polishing (75-100 µm) is represented by the pink dotted line.

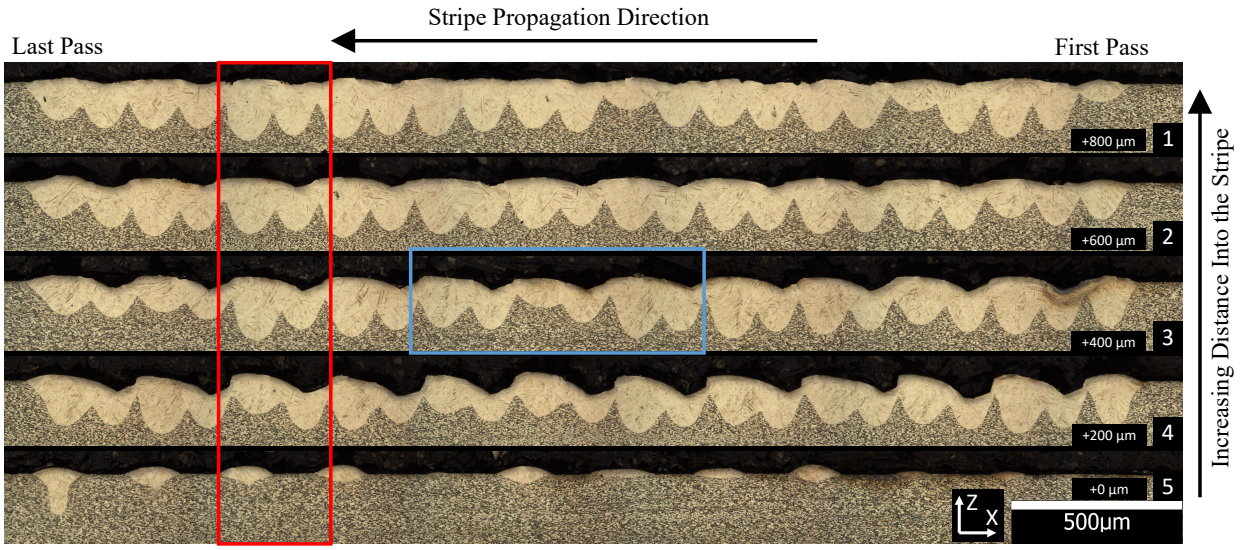

Figure 5-22: The polished surface of each stripe showing the melt pool cross sections, stripe propagation direction, and depth into the stripe.

It is clear from Figure 5-22 that there is a periodic nature to the melt pool heights, and that this periodic nature decreases in intensity with increasing distance into the raster stripe. The red box in Figure 5-22 shows the location where the images are extracted for Figure 5-23. The melt pool on the left in each image is super-elevated from the melt pool on the right of each image and the difference in height becomes smaller as the distance into the stripe increases (from left to right in the image progression in Figure 5-23). This is caused by the fluid flows within the melt pool. The left melt pool in each image shows the start of a track, while the right melt pool in each image shows the end of the subsequent track. Liquid is pushed out from under the beam spot (due to recoil pressure and evaporation) [85] and sucked toward the back of the melt pool (due to surface tension, or Marangoni, effects) [40], both of which act to create excess liquid at the start of the track and therefore a depleted region at the end of a track.

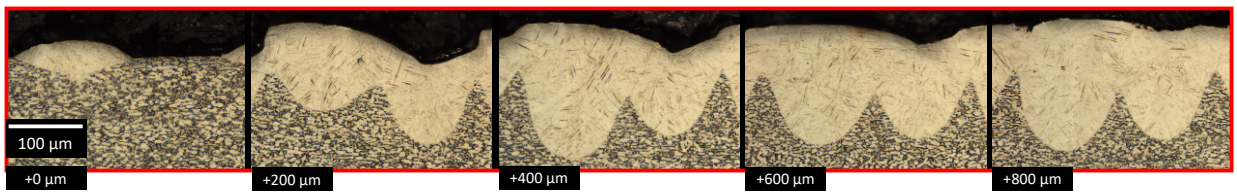

Figure 5-23: A series of images, each 200 µm deeper into the raster stripe, taken from the red highlighted region in Figure 5-22.

Figure 5-22 also shows that the depth of the melt pools can be significantly variable. The region of Figure 5-22 highlighted in blue is extracted and shown in Figure 5-24. The melt pools highlighted in purple in Figure 5-24 are much smaller than the surrounding melt pools. The origin of this variability is unknown, though it suggests perturbations in the absorbed energy or beam profile of the laser that was not seen in the single beads. These anomalously small melt pools are

seen at all distances into the stripe as well as randomly distributed in terms of raster pass number[63], and makes analysis of this data set with respect to melt pool depth and area difficult.

Figure 5-24: Image section taken from the blue highlighted box in Figure 5-22. The purple circle in this image highlights anomalously small melt pools.

To understand how the melt pool cross section changes as a stripe progresses, a line across the original substrate surface is drawn and depth measurements are taken from this line to the base of each melt pool to look at only the amount of material that is melted and not include the fluid flows while the material is molten. This is the same measurement method as was used for the single bead measurements in Chapter 2 and Chapter 3. Melt pool depth is measured instead of cross sectional area because individual cross sectional areas cannot be determined with a high enough level of certainty due to the overlap of the melt pools. Unlike IN625 [79] and AlSi10Mg [178], which exhibit contrast at the extents of the melt pool and therefore make it possible to discern melt pool boundaries in bulk material, determining the melt pool boundaries in LPBF Ti64 requires contrast with the substrate grain structure. This means that any overlaps in melt pool cross

[63] The first pass at +800 µm in from the edge of the stripe is anomalously small, while the other small melt pools are fairly evenly distributed throughout the rest of the data. Because each cross section came from a different stripe, it is not possible to track individual anomalies through the progression of images to determine any periodicity along the raster direction. Future work should employ serial sectioning and in-situ monitoring to determine the origin of these anomalously small melt pools.

sectional area will cause significant uncertainty in the shape of individual melt pools and therefore precludes an analysis of melt pool cross sectional area for the stripes.

Figure 5-25 shows the experimental depth of the melt pools seen in Figure 5-22 as well as the expected depth of the melt pools from simulation (represented by a yellow overlay). To generate the expected depth, the depth found for the nominal case from single bead experiments in Chapter 3 (128 µm) is used as the depth for the first raster pass. All subsequent passes are generated by multiplying this value by the melt pool area increase and aspect ratio increase predicted from the trends seen in Chapter 3[64]. The upper and lower bounds of the yellow overlay are generated from the simulated temperatures for an absorptivity of 0.4 and 0.8 respectively.

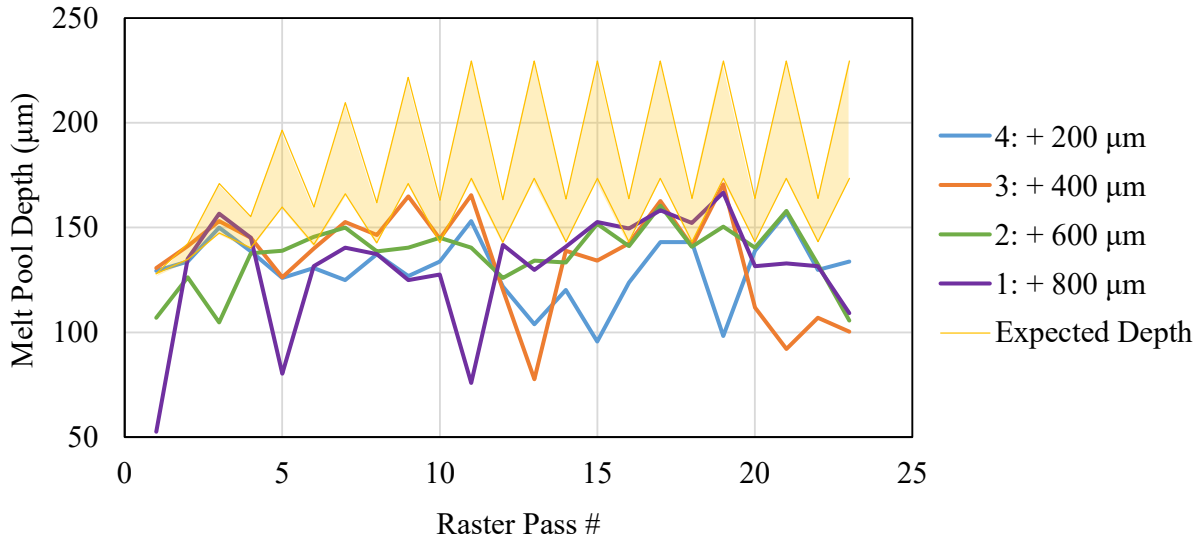

Figure 5-25: Melt pool depth for the cross sectional images shown in Figure 5-22. +0 µm is omitted because there are not enough melt pool cross sections visible.

[64] The temperatures used to find the change in depth are taken from the simulations of the first iteration for Cases 1 and 2. Only one location (400 µm in from the edge of the stripe) is chosen for the expected melt pool cross sectional area due to the similarity in the temperatures between 0 µm and 800 µm from the edge.

The range of depths calculated from simulated temperatures shows a large range depending on the absorptivity value used. The lower range agrees most closely with the measured depths, though the measured depths are still generally less than predicted. The lack of an increase in average depth with increasing raster pass number (along the *X* axis in the plot) suggests that the variability and fluid flows within the melt pool are obscuring any trends in melt pool depth that may be present due to increases in substrate temperature as the stripe is deposited. Another feature of the experimental melt pool depths that seems to be obscured by the measured depth variability is periodicity in the depth. It is clear from the expected depths that there should be a succession of small and large melt pools. This trend can be seen for some of the experimental melt pools at some locations, but is not a dominant feature in the measured depths.

An important result from these data is that the melt pool depth becomes close enough to steady state to be within the uncertainty in the data within 200 μm from the edge of the stripe, which is on the same length scale as the width and depth of the melt pools and is less than the simulated melt pool lengths. The short distance required to get to a steady state melt pool cross sectional area means that the simulations reported in this chapter should represent the actual melt pool cross sectional area starting very close to the stripe edge, and therefore the power profiles generated should be valid for close to the entire stripe width.

This same stripe is analyzed in section 6.3.6 with respect to thermal gradients at the edge of the stripe and shows that the temperature distributions predicted from the methodology presented in section 5.3.3 are accurate.

5.4 Discussion

In this chapter, the time required for the beam to turn around (beam off time) in the EOS M290 is shown not to vary significantly with changes to processing parameters. The time for the melt pool to solidify, however, is shown to vary significantly with changes to processing parameters, and highlights an avenue for optimization of the current scan strategy. The beam off time used by the EOS software is well matched to the nominal parameters, however, so this value is adopted for subsequent simulations of the temperature fields during a raster stripe. The presented methodology easily allows for the beam off time to be altered in order to develop an optimized beam power curve for non-nominal process parameter combinations.

Both single tracks and raster stripes are simulated in this work to determine the temperature field throughout a raster stripe. This work shows that beam power needs to be constantly controlled throughout the width of a stripe (i.e. the length of the raster pass), not just at the edge of the stripe. The power needed to keep melt pool area constant given a certain substrate temperature (generated in Chapter 3) is then used to convert the simulated temperature profile into a power profile that keeps melt pool cross sectional area constant during lasing of a stripe. This power profile has the additional effect of reducing the increases in local temperatures which occur during deposition of a stripe. A further reduction in the variability in temperature during deposition can be attained by increasing the starting substrate temperature due to the reduction in beam power needed to maintain the same melt pool cross sectional area. Combining these two results, a user can increase build rate by using larger melt pools while simultaneously reducing temperature and melt pool cross sectional area variability throughout a single raster pass as well as from one raster pass to the next. The effect of which would be a lower probability of both lack of fusion and keyholing porosity because the melt pool dimensions would be more closely controlled.

The beam power profile generated using this methodology can be used in the parameter generation software for a LPBF machine to account for local heating caused by a raster scan strategy before the part is built. Since the majority of each stripe would have a single power curve, this methodology is relatively computationally efficient to implement. The power profile generated in this chapter is similar to the turning function in the Arcam EBM software (a continuously variable function designed to maintain melt pool area during a raster [80]) and shows that the control of local temperatures proposed in this work can be implemented into commercial metal AM processes.

The experimental raster stripes show that there are other sources of variability beyond substrate temperature that are generating uncertainty in melt pool dimensions. The first is fluid flow within the melt pool. Liquid is pushed out from under the beam spot (due to recoil pressure and evaporation) [85] and sucked toward the back of the melt pool (due to surface tension, or Marangoni, effects) [40], both of which act to create excess liquid at the start of the track and a depleted region at the end of a track. The other source of uncertainty is less well defined and is likely due to perturbations in the absorbed energy of the laser. Since these perturbations are not seen in the single beads conducted in Chapter 3, it is likely that they arise from the interaction of the laser with the plume or other ejected material from previous raster passes. A discussion of plume formation and verification of the simulated temperature fields is presented in Chapter 6.

Regardless of the source of variability, it is clear that there is significantly more variability in the melt pool cross sectional dimensions in the raster stripes than in the single bead deposits from Chapter 3, especially at the edge of a raster stripe. Chapter 4 suggests that the overlap in subsequent layers accounts for the variability in the melt pool when process parameters are chosen correctly, as evidenced by the close to pore-free builds over a variety of process conditions. The

elimination of substrate temperature as a contributor to melt pool cross sectional area changes should keep the melt pool more uniform throughout the deposition of a raster stripe, and a reduction in melt pool variability would allow for a decrease in melt pool overlap and an increase in deposition speed.

The potential void formation mechanisms seen in this work are likely due to fluid flow within the melt pool during transient melt pool regimes (the beginning and end of a track, or the edges of a strip). Excess temperature at the edges of a stripe may be inducing keyholing porosity and the beam turn off causes a collapse of the vapor cavity that may also cause porosity at the edge of a stripe [88]. In addition, the variability in surface height seen at the edges of a stripe would require greater penetration of the subsequent layer in order to fully fuse all of the material. All of these factors suggest that the most likely location of porosity formation is the edge of a stripe, similar to the findings by Groeber et al. [81].

Chapter 6 - High Speed Videography of Select Laser Powder Bed Fusion Processes [65]

6.1 Background and Overview

This chapter will assess whether a visible light, high speed camera can be used to extract information about Ti64 melt pools in the LPBF process. The camera will be used to show that melt pool metrics of interest can be determined directly from thermal information even when spatial information is not available. The utility of the camera when spatial information is required will then be explored. The applicability of different methods for determining the melt pool boundary will be evaluated and the camera will then be used to understand how melt pool dimensions, thermal gradients and solidification times change when substrate temperature increases.

6.1.1 Melt Pool Monitoring

The implementation of tools to monitor the melt pool in metal additive manufacturing (AM) processes is widely considered essential to the adoption of those processes for advanced part production [121]. The fusion process is so variable that even when nominal deposition parameters are implemented, flaws in the resultant part are possible [54][40], making it essential to monitor the process on the length and time scales needed to detect flaws. Laser powder bed fusion (LPBF) is particularly difficult to monitor because of the small length scales, with melt pools roughly 50 μm to 250 μm wide [55], and short time scales, with melt pool phenomena occurring over roughly 10 μs to 100 μs [40][88]. The most promising solution to reliably obtain melt pool scale

[65] Sections of this chapter have been published in: B. A. Fisher, B. Lane, H. Yeung, and J. Beuth, "Toward Determining Melt Pool Quality Metrics vis Coaxial Monitoring in Laser Powder Bed Fusion," *Manufacturing Letters*, 2018. DOI: 10.1016/j.mfglet.2018.02.009

information in the LPBF process is to align sensors along the optical path of the laser, also called coaxial monitoring [95], [103], [109]. In doing so, spatial coordination of the sensors with the melt pool is guaranteed, allowing for more targeted data collection.

The majority of melt pool monitoring tools that are commercially available utilize this coaxial monitoring technique [179]–[181]. The current hardware is capable of recording copious amounts of data; however, the associated software packages rely on the user to draw their own conclusions from those data. Picking out anomalies, or even understanding what information is important to consider, is difficult without an informed framework that ties sensor outputs to part quality metrics. If a LPBF machine does not have coaxial monitoring capabilities, it is very difficult to add this capability. Generally, add-on monitoring capabilities are incorporated into existing machines in the form of fixed field of view (FOV) sensors.

In-situ monitoring may reduce the need for destructive testing by detecting, and possibly correcting, flaws during deposition. Because of the small spatial and temporal scales that laser powder bed processes occur on, resolving powers below 20 μm and frame rates of at least 5-10 kHz are advantageous. These requirements lend themselves to silicon based photodetectors because they are considerably less expensive and more capable than other photodetector chemistries[66]. Silicon based photodetectors are used in 'visible light' cameras, and are sensitive to wavelengths of light between roughly 400 nm and 1000 nm. In most applications, visible light cameras record reflected light, not light generated by the object being viewed. However, because a Ti64 melt pool is roughly between 1600°C [27] and 3300°C [38], [182], there is enough emission

[66] Infrared cameras generally use InGaAs, InSb, or a microbolometer to detect thermal radiation [128]. The high speed camera used in this work can take 6,400 images per second at 1 megapixel, and was purchased for roughly $50,000. The author was unable to find an infrared camera with comparable capabilities, but was able to determine that an infrared camera capable of frame rates more than one order of magnitude lower than the camera used in this work currently sells for over $100,000.

below 1000 nm that a visible light camera can be appropriate for detecting the emitted light (thermal radiation).

6.1.2 Image Analysis Approaches to Determine the Melt Pool Boundary

There are two main techniques to determine the solidification boundary of a melt pool from above. The first is to compare the actual dimensions of a melt pool measured ex-situ to the dimensions of the melt pool generated by thresholding the image at a particular pixel value. The pixel value that gives the best agreement with the known dimensions (from ex-situ measurements) is then chosen as the pixel value for solidification. This technique can be done directly with pixel value, and does not require the camera to be calibrated to temperature. Calibrating a camera in the temperature range for solidification of Ti64 requires access to specialized equipment that is not readily available[67], so this work started by exploring the possibility of determining the isotherm for solidification by matching width in melt pool emission to width from measuring melt pool cross sections ex-situ. This isotherm should equate to a pixel intensity value (reported in "Digital Level", or DL), which can then be used to threshold thermal images to determine melt pool dimensions.

The second approach utilizes the discontinuity in cooling associated with solidification. It is well documented that there is a plateau, or at least a discontinuity (significant and sudden change in slope), in the temperature profile at the tail of a melt pool due to the release of latent heat of fusion during metal solidification. Doubenskaia et al. [183] monitored Ti64 melt pools during laser cladding in the wavelength range of 3-5 μm and used a drop in the cooling rate at the tail of the

[67] The high temperature black body used in this work is property of NIST, see section 6.2.5. The use of a calibrated light source to act as a substitute for a black body source is currently being utilized by NIST for the AMMT [107].

melt pool to determine the solidification isotherm. Yadroitzev et al. [109] monitored Ti64 melt pools in a coaxial configuration in a custom built LPBF machine at a wavelength of 0.8 μm, and showed that there is a discernable plateau in temperature. These results may not transfer to the current work, however, because the parameters used for melting were in the low power, low velocity region of process space (20-50 W and 100-300 mm/s) and the LPBF machine used was significantly different than the EOS M290. More recently, Heigel and Lane [112] monitored IN625 melt pools in the LPBF process using a high speed (1800 frames per second) thermal camera in the wavelength range of 1.35-1.6 μm and was able to discern a discontinuity in the slope of the cooling curve by finding a minimum value in the cooling curve's second derivative.

These researchers utilized different viewing angles, laser beam profiles, and wavelength ranges for detection, but they all calibrated their camera to a black body source before analyzing data, and so presented their findings as brightness temperature, and not as signal value. This chapter will determine the applicability of using the camera setup at CMU to determine the solidification isotherm directly from a discontinuity in the pixel intensity gradient at the tail of the melt pool. The camera will then be calibrated and the utility of the system characterized.

6.2 Methods

6.2.1 High Speed Camera

The camera used throughout this chapter is the Photron Mini AX200-900K-M-16GB (Photron USA, Inc., San Diego, CA) and has a 12-bit monochrome detector array. The detector array is made up of 1024 x 1024 pixels, each pixel representing a 20 μm square. The light sensitivity following the ISO 12232 Ssat Standard is 40,000. The shutter is a global electronic shutter. The camera is capable of 6,400 frames per second (Hz) when all pixels are active, with

increasing allowable frame rate as the number of active pixels decreases. All information in this section is taken from the company provided technical specifications [184]. All camera images are saved as 12-bit .TIF files with no image compression applied.

6.2.2 Camera Setup at NIST

The high speed camera (Photron Mini AX200) was incorporated into the optical path of the prototyping system developed by NIST, a precursor to NIST's current Additive Manufacturing Metrology Testbed (AMMT) [105][106], as can be seen in Figure 6-1. The camera was placed at a predesigned focal plane within the system that gives a 1:1 magnification [106]. Since no rigorous calculation of spatial resolution had been done for the camera system at the time of data collection [107], the goal of the experiment was to determine what information could be gleaned about the melt pool when no spatial information was used.

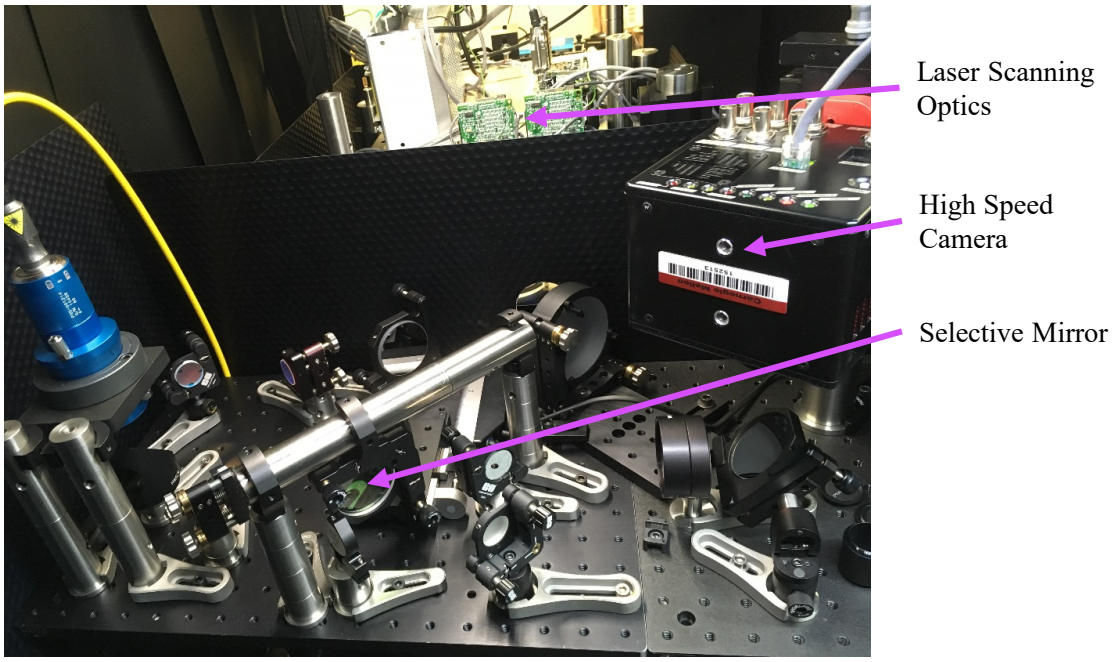

Figure 6-1: High speed camera incorporated into the laser optics of the prototype AMMT at NIST.

This camera system is used to view the single beads that are described in section 3.2.5 and analyzed in section 3.3.5. A frame rate of 50 kHz and an integration time of 0.5 μs (set such that none of camera images saturate) is used for data collection. All camera settings are held constant for all data collected. The optical filter used is a Thorlabs FBH850-40, which has a center wavelength of 850nm and a transmission full width half max (FWHM) of 40nm. A wavelength of 850nm is chosen to be sufficiently high without being sensitive to the laser wavelength of 1070 nm [106]. The particular wavelength range was pre-determined and the optical path for the NIST system was designed to reduce aberrations at this wavelength [106]. An example melt pool top view image, cross sectional area image, and thermal emission image can be seen in Figure 6-2.

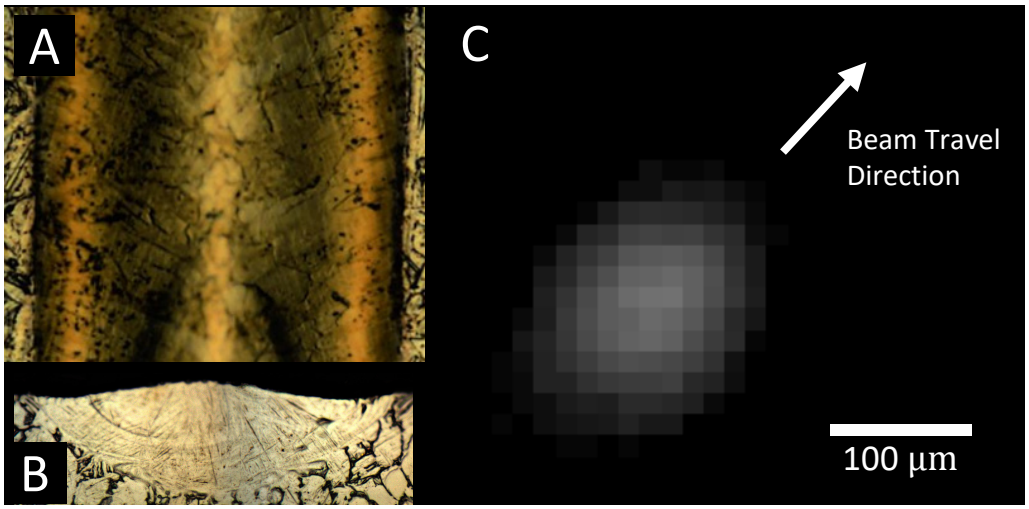

Figure 6-2: All images are for the same scan track (P = 250 W, V = 600 mm/s, T = 25 ˚C) and at the same scale. (A) Microscope image of the top surface of the scan track. (B) Microscope image of the cross sectional melt pool area (sectioned, polished, and etched). (C) Example thermal emission image from the scan track.

The total in-band thermal emission from each melt pool is determined by adding up the values of all pixels above a threshold of 20 DL in the camera images and averaging over the available images for that scan track. The threshold value is set 3σ above the average signal noise.

To generate a process map of constant thermal emission, the same procedure as outlined in section 3.3.5 is used. The total in-band thermal emission values can be found in Appendix 6.

6.2.3 Camera Setup at CMU

In order to view melt pools in the EOS M290 at the length and time scales necessary for in-situ monitoring, a high speed camera system is developed and characterized. The high magnification lens used is an Infinity K2 Distamax with the addition of two, 2x NTX tubes (Infinity Photo-Optical Company, Boulder, CO). The camera system (camera and lens) is able to view melt pools through a port on the roof of the EOS M290 chamber. The camera setup can be seen in Figure 6-3.

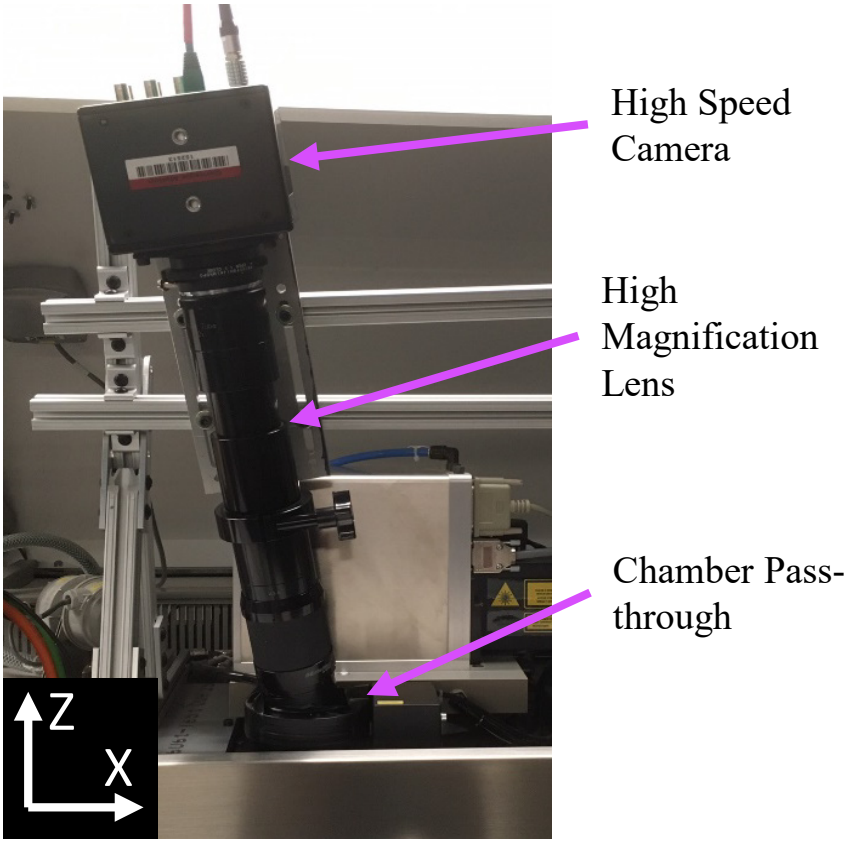

Figure 6-3: High speed camera and high magnification lens attached to the top of the EOS M290 at CMU.

A target viewing area for the high speed camera is chosen to be within the smaller build plate of the resistive heating insert described in section 3.2.1 while being reasonably far from the bolt holes and edges of the plate. The location is not the direct center of the build plate because moving it closer to the chamber door reduced the angle between the camera and the EOS M290's build plane. The viewable area of the high speed camera relative to the standard EOS M290 build plate and the build plate of the resistive heating insert is shown in Figure 6-4. Each grey square in the image is 10 mm on a side. The distance from the tip of the camera lens to the center of the viewable area is approximately 70 mm in *X*, 95 mm in *Y*, and 475 mm in *Z* (out of the page in Figure 6-4). This gives an angle between the camera axis and the build plane of approximately 14 degrees.

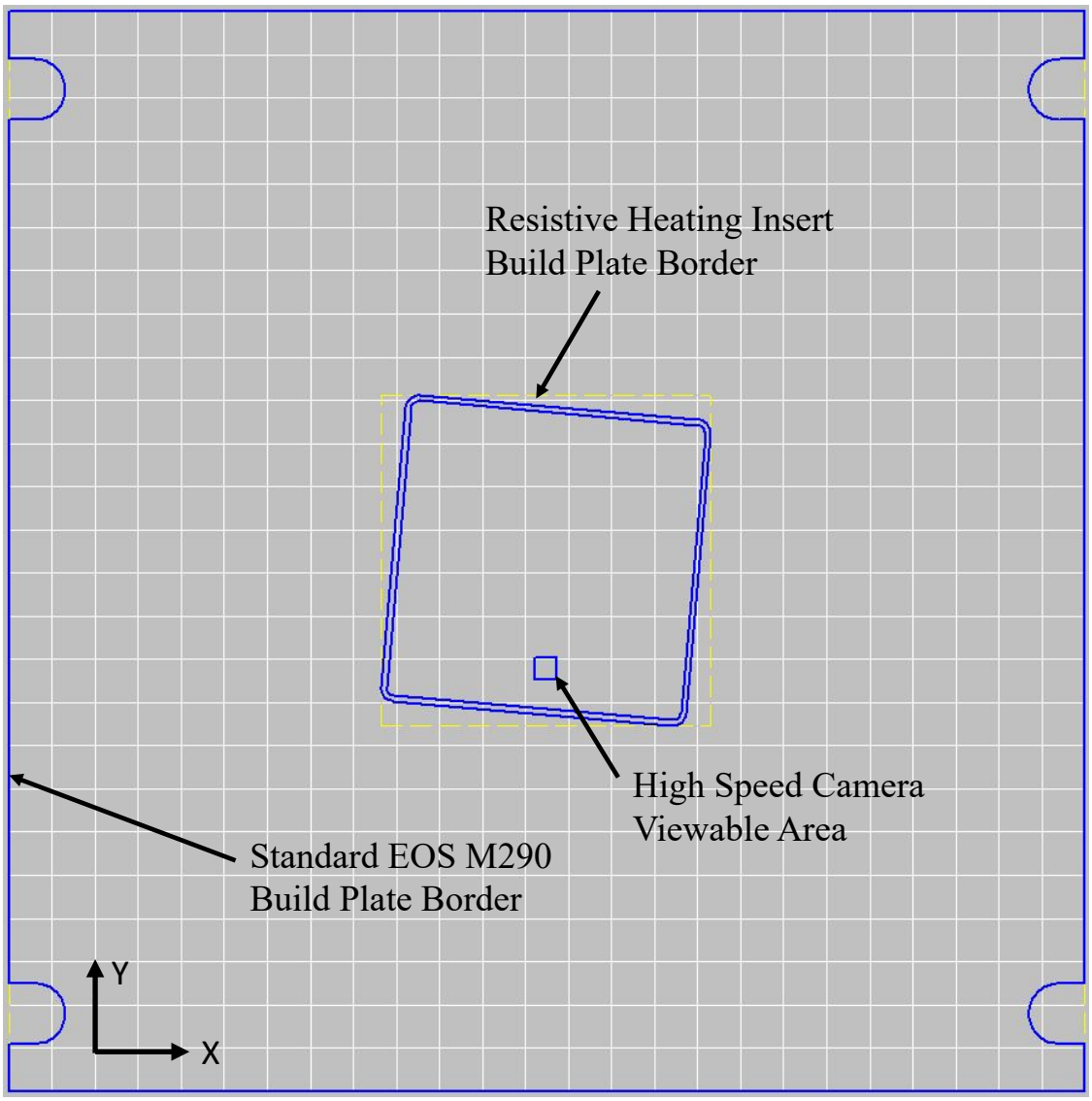

Figure 6-4: View of the standard build plate for the EOS M290, the build border for the high temperature resistive insert, and the viewable area for the high speed camera. Each grey box is a 10 mm square. The view is from above the build surface and the chamber door would be in the negative *Y* direction.

Once the target area is chosen, the resolution and FOV of the camera can be characterized. First, a square is lased onto a test plate, imaged with the high speed camera, and then imaged with an optical microscope. The optical microscope image and camera image can be seen in Figure 6-5. The inside of each vertex of the square is used as a fiducial marker. With the optical microscope,

each edge s measured as 4.6±0.05 mm and each angle between edges of the box are measured as 90 degrees. Because of the angle between the camera axis and build plane, this square feature is warped in the high speed camera image. The camera image and corresponding spatial information are then used to determine edge lengths (in pixels) of the square. Table 6-1 shows the results of this analysis.

Table 6-1: The distance between fiducial makers in a high speed camera image of a square.

Side	X Distance (pixels)	Y Distance (pixels)	Angle (degrees)
A	719	28	A-B = 92.2
B	0	716	B-C = 87.5
C	723	31	C-D = 92.5
D	0	706	D-A = 87.8

Though the edge lengths are all different and the angle between sides of the square are not 90 degrees, the differences in values between edges are relatively small. For ease of further analysis the projected area of the pixels are considered square with an instantaneous FOV of each pixel of 6.38 μm on a side. This gives a full FOV of the camera of approximately 6.53 mm square. The area of each pixel on the camera array is 20 μm, giving a magnification of approximately 3.1. Taking into account the angle of the camera axis to the build plane and the full FOV of the camera, when the center of the camera image is at focus the maximum distance that any location within the camera image can be out of focus is ±1.1 mm.

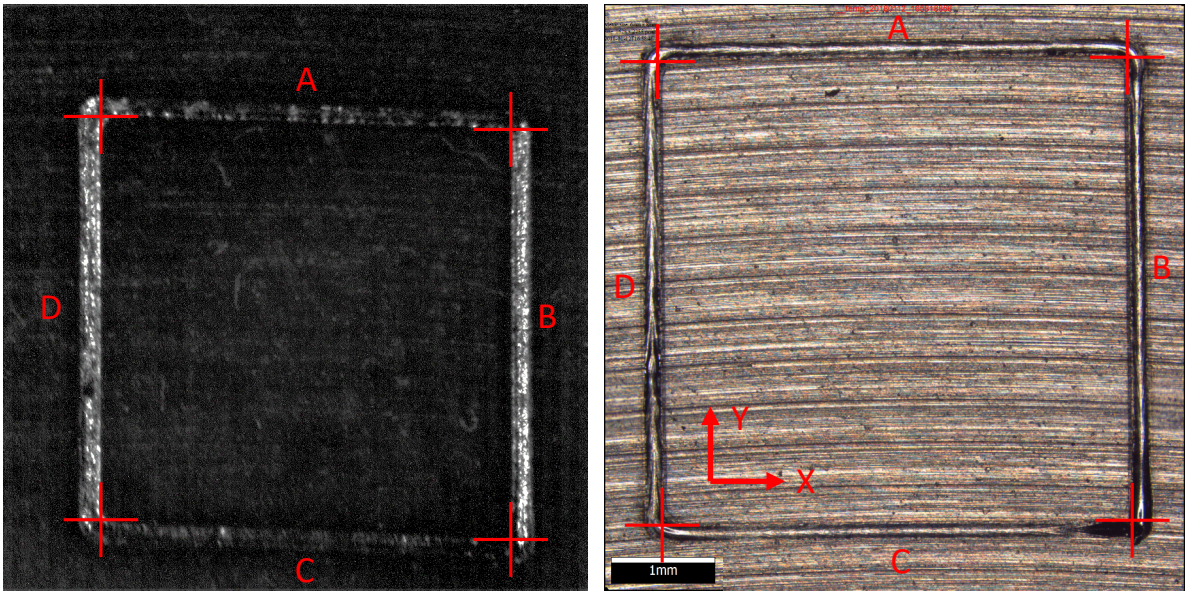

Figure 6-5: On the left is the high speed camera image of a box that was lazed in the EOS M290. On the right is that same box imaged under a microscope. The red crosses show where fiducial markers are located to determine the FOV of the camera. Each side of the box is labeled with a letter.

To characterize the camera resolution, apertures of 100 ± 4 µm, 200 ± 6 µm and 300 ± 8 µm (Thorlabs P100H, P200S, and P300H respectively) (Thorlabs Inc., Newton, NJ) are then placed in the center of the camera frame and imaged based on a procedure by Lane et al. [107]. An LED illumination source is covered with several layers of tissue paper and placed under the apertures to mimic a uniform light source. In order to determine the extent to which the light source is uniform, the light source is imaged without an aperture in place. Figure 6-6 shows the no aperture image with an inner box that covers the area encompassing all of the aperture readings. A histogram of all of the pixel intensities within the inner box are also displayed in Figure 6-6. While the field is not uniform, the variability is small enough that useful measurements can still be taken.

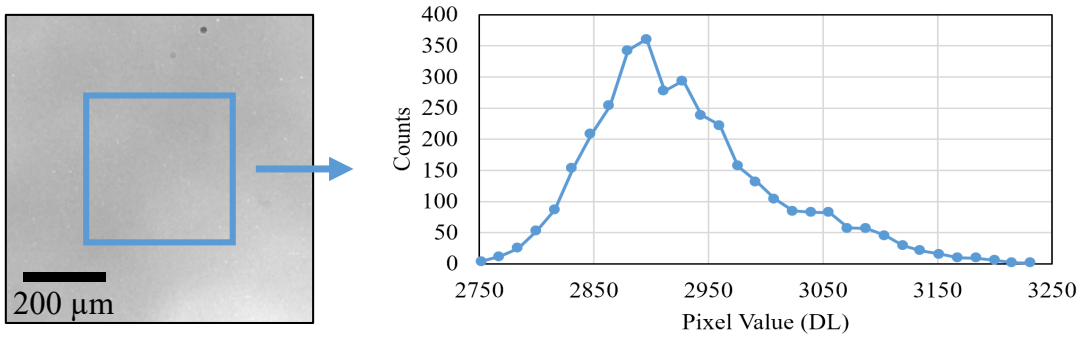

Figure 6-6: The no aperture image of the light source is shown on the left, with the blue box showing the location where the apertures will be placed. The histogram on the right shows the pixel values measured from within the blue box.

Images are taken for each aperture at the focal plane, 1.1 mm above the focal plane, and 1.1 mm below the focal plane in order to mimic what would be viewed at any point in the camera FOV. Figure 6-7 shows representative images of each aperture at focus, 1.1 mm above the focal plane (Closer than Focal Plane), and 1.1 mm below the focal plane (Farther than Focal Plane).

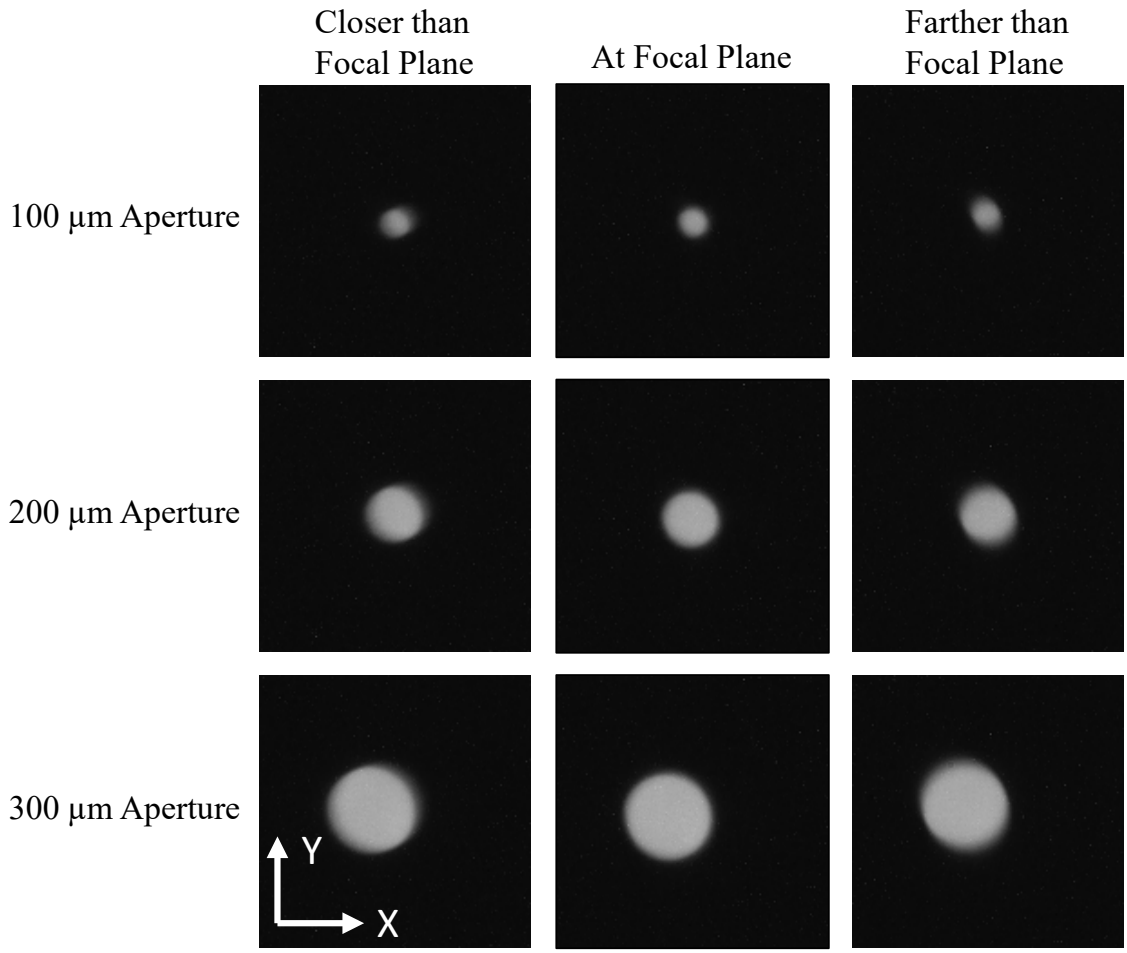

Figure 6-7: Representative camera images for the 100 µm, 200 µm, and 300 µm apertures at focus, above the focal plane, and below the focal plane.

Figure 6-8 shows high speed camera images of the three focal heights for the 100 µm aperture. The choice of axes will be the same for the 200 µm and 300 µm apertures. The distortion axis rotated 90 degrees when focus was crossed, as evidenced by the 90 degree shift in the along axis direction (yellow dotted line) between images *A* and *C* in Figure 6-8. The centroid of each aperture is determined and because of the obvious distortion along preferential axes that did not line up with the *X* and *Y* axes, profiles are taken along and across the distortion axis for the closer than the focal plane (Figure 6-9), and further than the focal plane (Figure 6-10) cases. There is no

preferential axis in the at focus images, however, so an *X* and *Y* profile is generated from the at focus images (Figure 6-11). The profiles in Figure 6-9, Figure 6-10, and Figure 6-11 are taken along the axis directions shown in Figure 6-8. A line profile of the no aperture case is shown in each figure for reference.

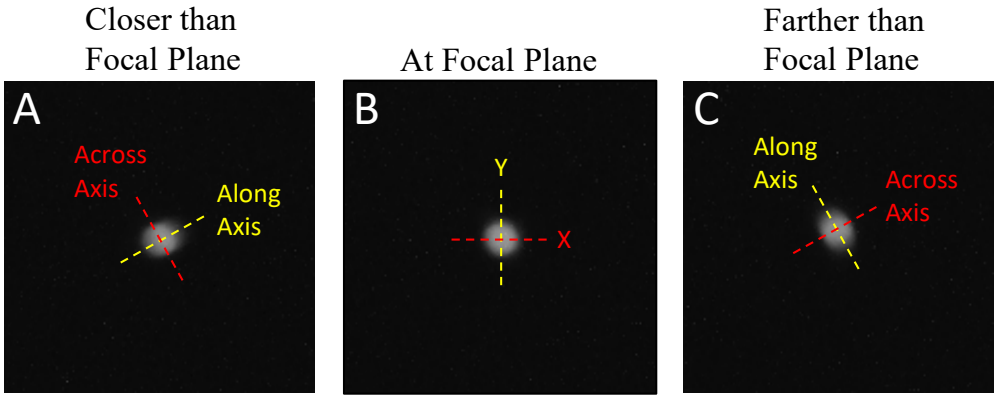

Figure 6-8: Images *A*, *B*, and *C* show the axes used to generate pixel intensity profiles for each focal height. Note that the axis rotates 90 degrees between images *A* and *C* due to the rotation of the distortion.

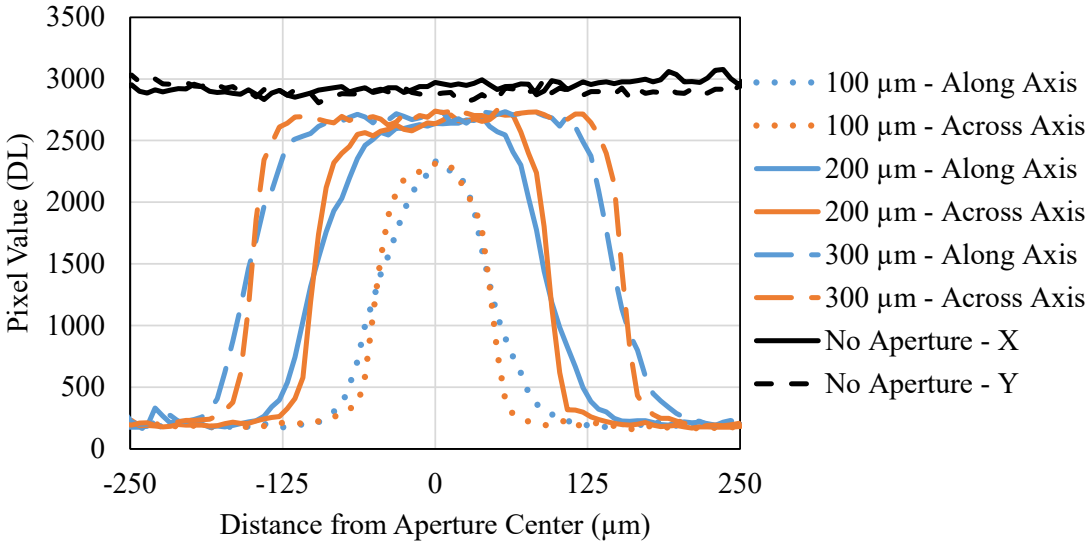

Figure 6-9: Pixel Intensity profiles for the three apertures as well as the no aperture case when the aperture is placed closer to the camera than the focal plane.

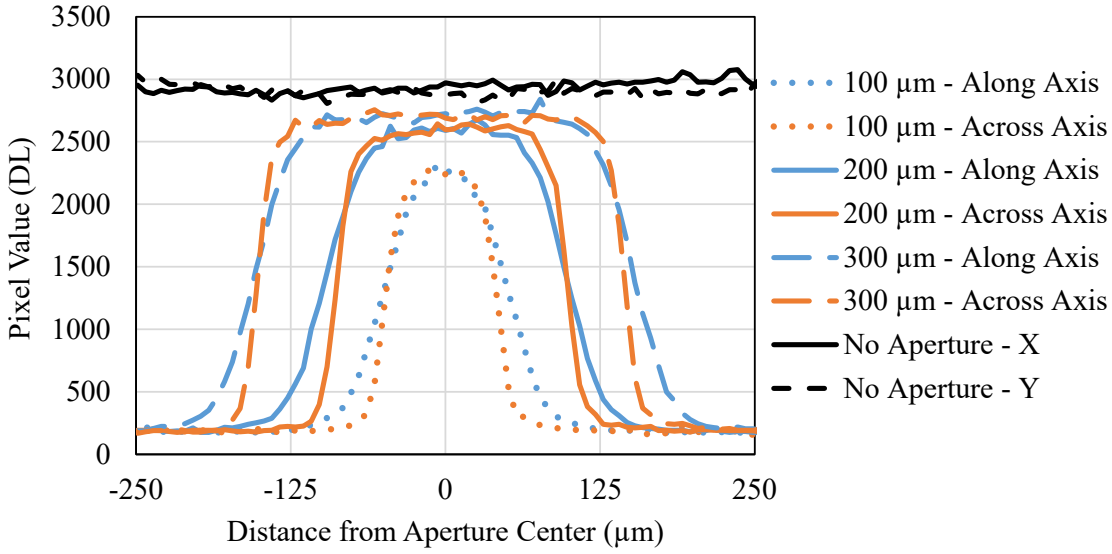

Figure 6-10: Pixel Intensity profiles for the three apertures as well as the no aperture case when the aperture is placed farther from the camera than the focal plane.

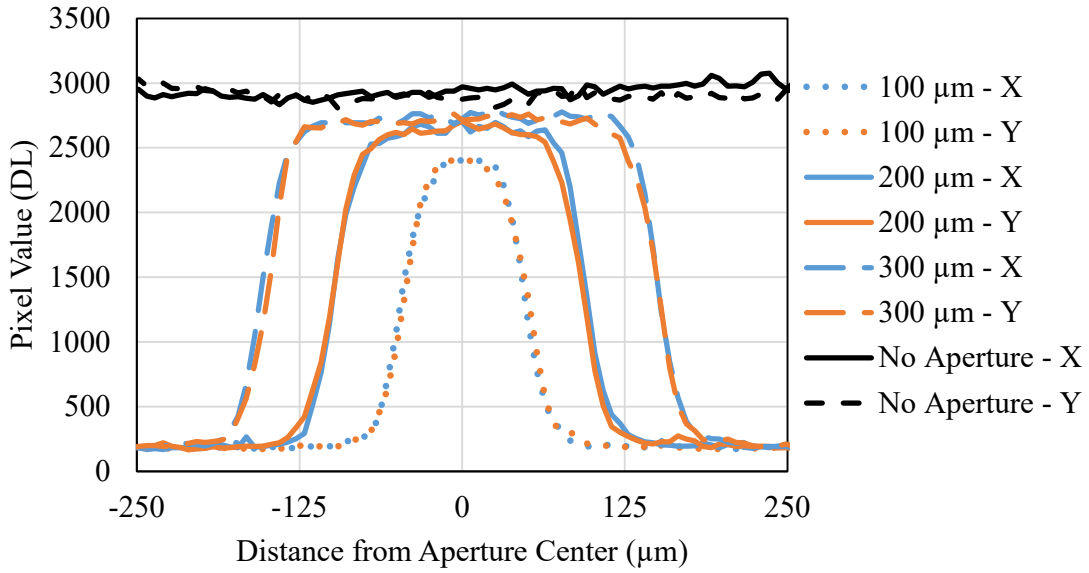

Figure 6-11: Pixel Intensity profiles for the three apertures as well as the no aperture case when the aperture is placed at the focal plane.

At focus (Figure 6-11), the *X* and *Y* profiles for each aperture are similar, meaning that there should not be significant distortion of features within the central region of an image. Closer and further than the focal plane, however, have different profiles along and across the axis. This means that the melt pool images at the edges of the field of view may be skewed relative to those at the center. This non-uniform distortion may lead to variability between images for melt pools generated with the same parameters as well as variability between different parameter sets. Therefore a determination of melt pool shape may prove difficult with the current camera setup.

Figure 6-12 shows all of the profiles for the edges of each aperture at focus. This figure is generated by averaging together the profile for the leading and trailing edges of each profile in Figure 6-11. All of the curves lie along the same characteristic curve of pixel intensity vs distance from the edge of the aperture. This characteristic curve is the edge spread function (ESF), a standard metric for camera resolution [107]. The *X* and *Y* profiles for the 100 μm aperture do not start at a distance of zero because, similar to the findings in Lane et al. [107], the maximum pixel value for the 100 μm detector is roughly 80-85% of the no aperture value. This shows that the resolution of the imaging system is causing an attenuation of the signal due to the high spatial frequency associated with a small feature. The camera resolution at the edges of the FOV are worse than at the center, which is unavoidable in a fixed field of view camera unless the camera axis is perpendicular to the build plane. Though it was not possible in this work due to the placement constraints of the high temperature insert (section 3.2.1), the camera axis should be aligned as close to perpendicular to the build plane as possible for all future monitoring applications.

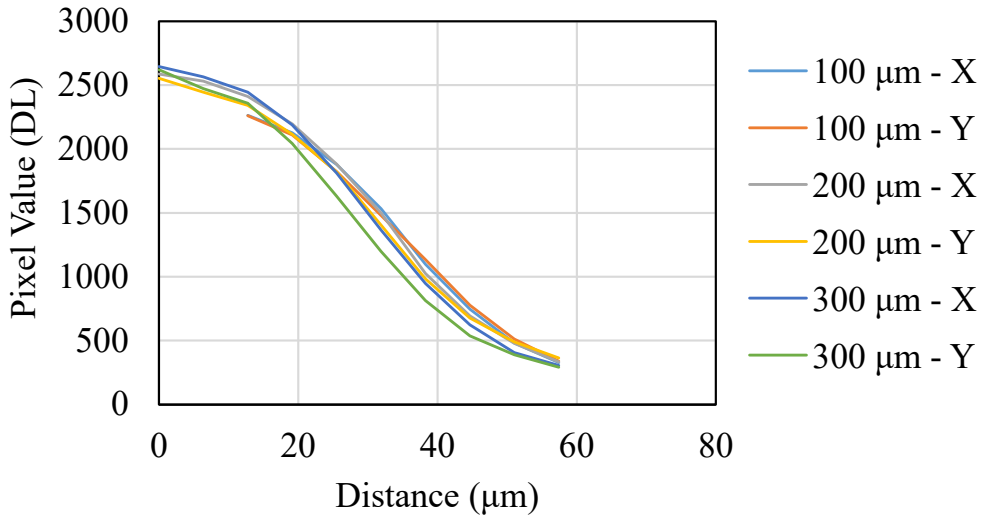

Figure 6-12: All of the profiles for the edges of each aperture at focus. Each curve is the average of both edges for the labeled intensity profile.

6.2.4 Optical Filter Selection

A fixed FOV is used instead of a coaxial orientation because incorporating a camera system into the existing laser optics of the EOS M290 is not practical for these experiments. Because the melt pool passes by the camera instead of constantly being viewed in center frame, optical blur becomes much more of an issue[68]. In addition, the thermal emission from the hottest part of the melt pool will be significantly higher than the thermal emission from colder liquid or solidifying material, so longer integration times, and therefore more optical blur, are necessary when imaging solidification rather than the hotter parts of the melt pool.

The camera detector is sensitive to wavelengths between roughly 400 nm and 1000 nm and has a peak sensitivity around 700 nm [184]. This brackets the sensitivity range of the camera system. The optical filter further refines the wavelength range that the camera system is sensitive

[68] Optical blur refers to the distance that an object moves while light is being collected for each camera image, and shows up as a blurring or elongation of the object.

to. In order to minimize the optical blur and still be able to look at solidification, a filter that passes a wide range of wavelengths, but still attenuates the laser wavelength of 1064 nm [125], is chosen. The optical filter used for the experiments at CMU is a Thorlabs FESH0950, which is sensitive to wavelengths of light between 500nm and 950nm.

6.2.5 Temperature Calibration of the CMU camera system

Once the camera settings and optics were set on the EOS M290 at CMU, the camera system was disassembled, brought to NIST, and a temperature calibration of the camera system was performed using a high temperature blackbody source with a 1 inch diameter orifice. The calibration setup can be seen in Figure 6-13 and the internals of the black body can be seen in Figure 6-14. The same optics, camera settings, and working distance was used during the calibration as is used for the experiments in the EOS machine.

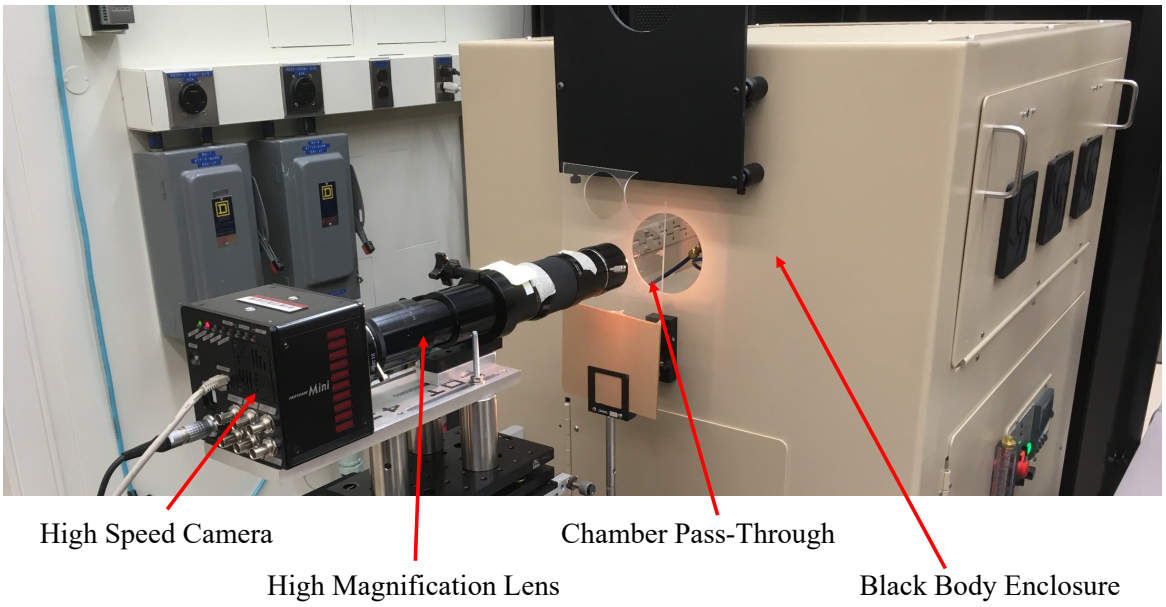

Figure 6-13: The camera setup used for temperature calibration at NIST. This setup is meant to mimic the camera position and optics on the EOS M290 at CMU. The camera and lens settings were fixed before transportation to NIST.

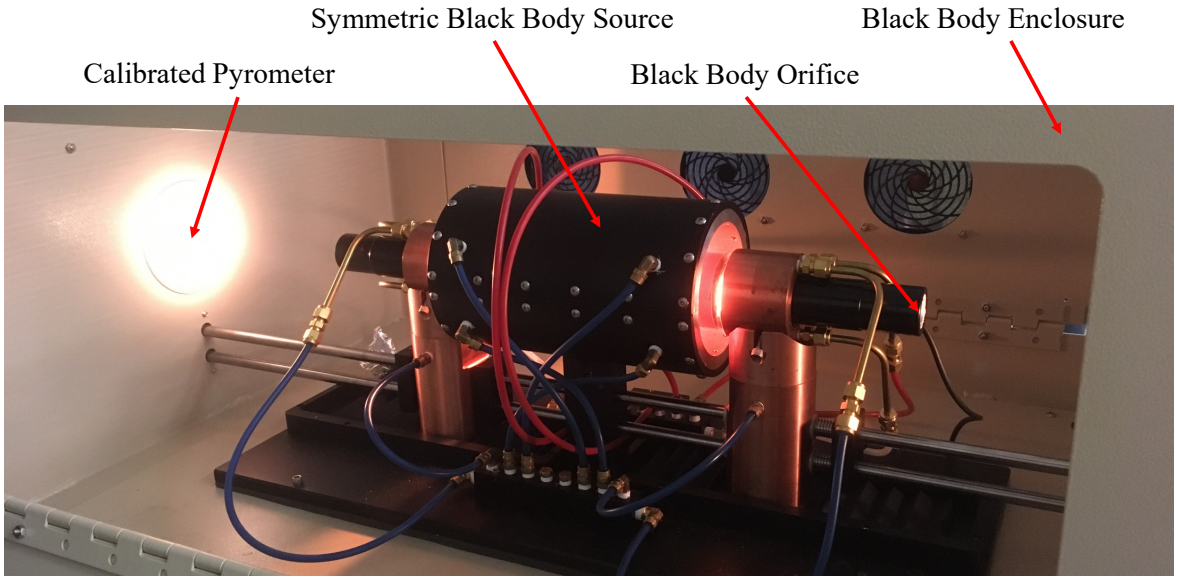

Figure 6-14: A view of the internals of the high temperature black body source at NIST.

Figure 6-15 gives a sense of the emission from a high temperature black body source and is only meant to give the reader an understanding of the level of light emission at elevated temperature. A series of images were taken of the high speed camera in front of the black body orifice at 1000 °C (*A*), 1600 °C (*B*), and 2000 °C (*C*).

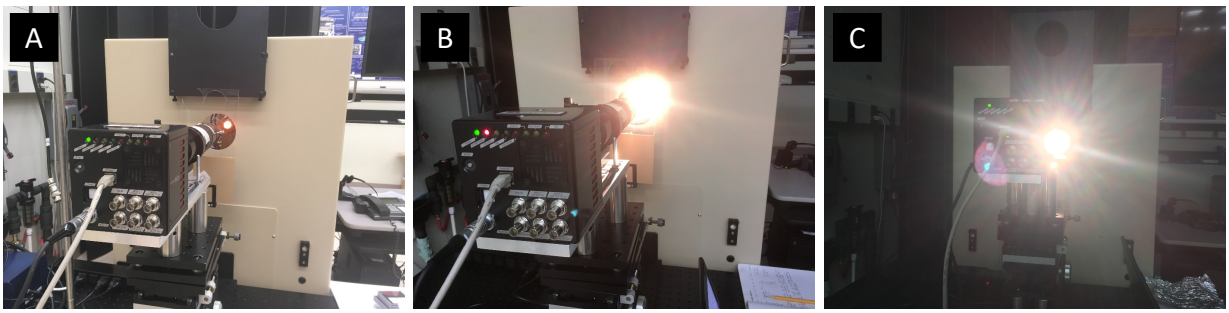

Figure 6-15: Images of successively higher temperatures emitted by the high temperature black body source at NIST. The brightness of the background changes as the images move from *A* to *C* to keep the light emitted from the black body source from saturating the image.

To see solidification of the Ti64 melt pools, it is necessary to have the camera calibrated to the correct temperature range. The appropriate temperature range depends on the expected solidification temperature and emissivity of the material. The solidification temperature of Ti64 is between 1600 ˚C and 1650 ˚C [27]. Because the solidifying material does not emit as a black body (a true black body has an emissivity of 1), the brightness temperature of solidification is lower than the actual temperature. The difference between the brightness and actual temperature is dependent on the emissivity of the material and the sensitivity of the camera system within the wavelength range that is being imaged (called 'spectral responsivity') [111]. The spectral responsivity for some of the components within the camera system are not known, but the spectral responsivity for the two components that have the largest effect are known from product literature (the camera detector and the optical filter) [184], [185]. Figure 6-16 shows the normalized spectral responsivity for the camera detector, optical filter (Thorlabs FESH0950), and the combination of the responsivity from both components, labeled as "Camera System".

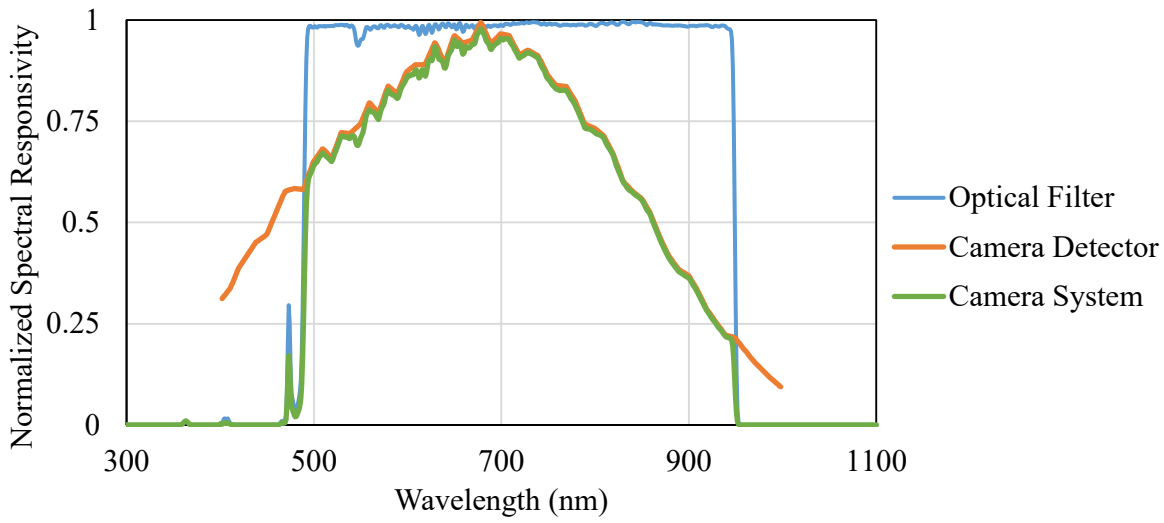

Figure 6-16: A figure of the normalized spectral responsivity of the camera components. The camera system is assumed to be the combined effect of the spectral responsivity of the optical filter and camera detector only.

The following assumptions are made in order to use Equation 3[69] to understand how emissivity affects the conversion between brightness and actual temperature: 1) emissivity is constant (not dependent on wavelength, temperature, or material[70]) and 2) the spectral responsivity of the camera system is based solely on the combined spectral responsivity of the camera detector and lens (all other components are assumed to have a constant spectral responsivity). The "Camera System" spectral responsivity from Figure 6-16 is then used as the weighting and the emissivity is assumed to be constant. Based on these assumptions, an integration time of 40 μs[71] is chosen for camera calibration, giving a usable brightness temperature range of the camera system between 1150 ˚C and 1600 ˚C. Using Equation 3 to find solidification within this temperature range, the emissivity of the melt pool boundary must be between 0.04 and 0.78. It is very likely that the emissivity is found to be within this range [27], [109], [141], [177], [186].

In order to generate a pixel-by-pixel temperature calibration from the image data, each pixel is treated separately. 100 images are taken at each calibration temperature and the individual pixel values are averaged together[72]. For each pixel, the calibration data is fit to the inverse Sakuma-Hattori equation [129], Equation 7, using a least squares regression and following the procedure outlined in Lane et al. [127]. The inverse version of the equation is used because it directly calculates the brightness temperature (T_b) from the camera signal (S):

[69] Equation 3 is reproduced here from section 1.3.7. $S \propto \int w_\lambda * \varepsilon_\lambda * L_\lambda(T)\, d\lambda + \beta$

[70] This assumption is incorrect, but the wavelength dependence of Ti64's emissivity is likely small for the wavelength range used in this work [196]. In addition, the spectral emissivity of Ti-Al alloys does not change significantly with composition up to roughly 50 atomic percent Al and does not have a large dependence on temperature above or below solidification [177], [188], [197].

[71] Even with the choice of optical filter meant to allow as much light as possible to pass, the necessary integration time is relatively high. For the span of velocities used in this chapter (500 mm/s to 2500 mm/s), the optical blur in a single image will be between 20 μm and 100 μm.

[72] The camera settings are: 6400 FPS, 1024 x 1024 active pixels, and an integration time of 40 μs.

Equation 7

$$F^{-1}(S) = T_b = \frac{c_2}{A * \ln\left(\frac{C}{S} + 1\right)} - \frac{B}{A}$$

where c_2 is the second radiation constant (14388 μm*K), and A, B and C, are fit coefficients to be determined from the calibration data. It is important to weight the fit toward the lower temperature region of the calibration because of the greater uncertainty in temperature at the lower range of the calibration curve, as evidenced by the relatively high slope of the calibration curve at low camera signal [127]. As part of the least squares regression, S is weighted by $1/S$ to favor the lower temperature values in the calibration. The r^2 and RMSE values for the fit at each pixel are determined[73]. The average r^2 value is 0.9992, the standard deviation of r^2 values is 0.000134, and the total range of r^2 values is 0.985 to 1.00. The average RMSE value is 0.3038 °C, the standard deviation of RMSE values is 0.0261 °C, and the total range of RMSE values is .0136 °C to 2.709 °C. The fit parameters for the average pixel values are: A = 1.036, B = 57.43, and C = 15,240,000.

Figure 6-17 shows the calibration curve for the average pixel values, and is meant to be representative. It is clear that the data is well fit to the inverse Sakuma-Hattori equation and the use of this equation as the basis for the calibration curve is appropriate. By applying a unique calibration curve to each pixel, nonlinearity in camera signal between pixels is accounted for.

[73] The r^2 value is a scale invariant measure of the proportion of the variation that can be explained by the model, with a maximum value of 1. A complimentary measure of error is RMSE, which is a scale dependent measure of how concentrated the data is around the fit line, and is in units of the dependent variable [198, pp. 369–376]. Both of these metrics are important to understanding how well the data is fit and what absolute temperature errors can be expected.

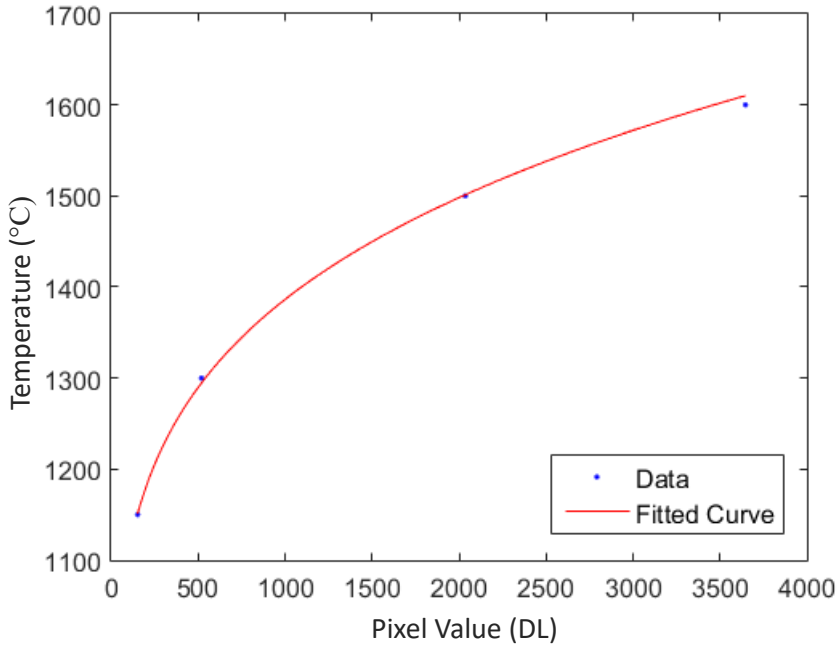

Figure 6-17: A representative calibration curve for the high speed camera system at an integration time of 40 µs.

The inverse Sakuma-Hattori equation solves for the brightness temperature, and not the actual temperature, because it does not account for the effects of material emissivity. To understand how the calibration curve may change due to the effects of emissivity, Equation 3 must be modified and is shown as Equation 8.

Equation 8

$$I(T) = \int_{\lambda_2}^{\lambda_1} \left[\frac{w_\lambda}{\lambda^5} * \left(\exp\left(\frac{c_2}{\lambda * T}\right) - 1\right)\right] d\lambda$$

where *I(T)* is the intensity function generated from a combination of Equation 2 and Equation 3, λ is wavelength, T is temperature, λ_1 and λ_2 bound the detectible wavelength range from Figure 6-16, and w_λ is the normalized responsivity (used as a weighting function) from Figure 6-16. Because the target material and surroundings are not absorbing all light (as is the case with a black body) the reflections from the ambient environment must now be considered because the

surrounding environment will affect the measurement of temperature. The temperature from the melt pool and surrounding material (the material of interest) is much greater than the ambient temperature (T_{amb}, the rest of the build chamber), however, so the effect ambient temperature will be small. With all of this considered, Equation 9 is used to convert between brightness temperature (T_b) and true temperature (T_{true}) assuming a constant emissivity (ε).

Equation 9

$$I(T_{true}) = \frac{I(T_b) - (1-\varepsilon) * I(T_{amb})}{\varepsilon}$$

Figure 6-18 shows the calibration curve taken from Figure 6-17 (labeled as ε=1.0) as well as that same curve if the emissivity were less than 1 (generated from Equation 9). The red horizontal band in Figure 6-18 shows the range of temperatures over which solidification may occur. The same calibration was used to convert all of the images taken at an integration time of 40 µm, regardless of the frame rate or number of active pixels.

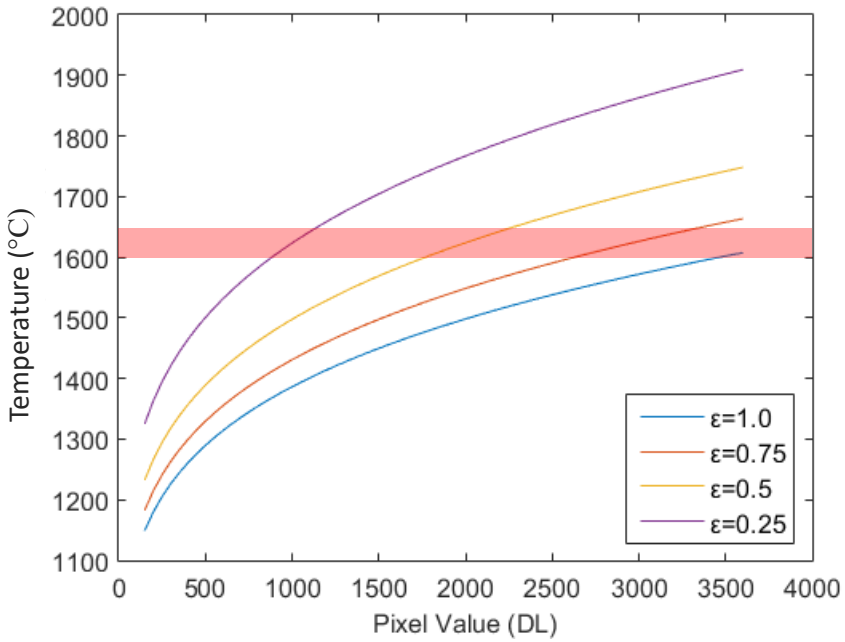

Figure 6-18: A plot of the camera calibration curve assuming different values for the emissivity of the melt pool surface. The red horizontal band shows the solidification range of Ti64.

The ESF generated in Figure 6-12 can then be converted to brightness temperature. In this way, the maximum detectible thermal gradient for the camera system can be determined. In addition, brightness temperature (an emissivity of 1) will have the smallest change in temperature with signal (the lowest slope), and will therefore be a conservative estimate for the maximum thermal gradient that can be attained when viewing real materials. Figure 6-19 shows the average curve from Figure 6-12 as well as those values after being converted to brightness temperature. The slope of the line for the linear portion of the resultant curve is 7.84 °C/µm, or 7.84×10^6 °C/m.

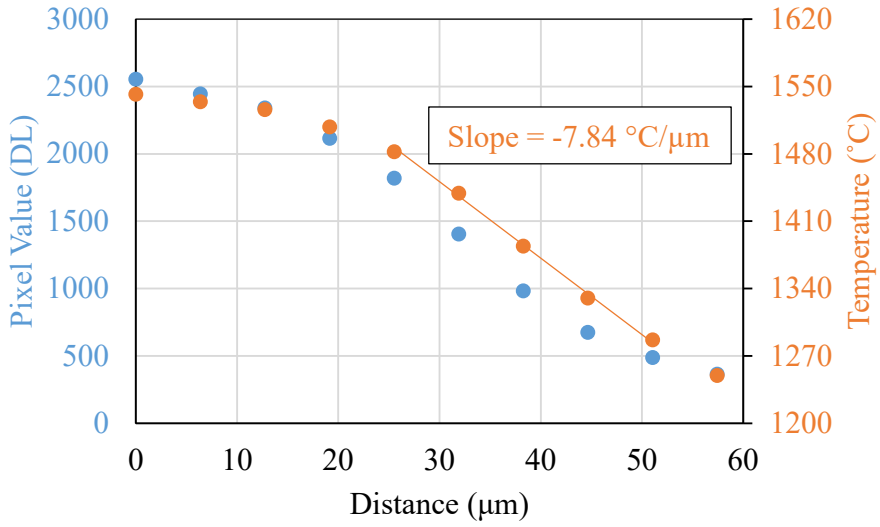

Figure 6-19: Determination of the maximum detectible thermal gradient using the ESF of the camera system from Figure 6-12 and the calibration curve for brightness temperature from Figure 6-17.

6.2.6 Thresholding to Find Melt Pool Dimensions

The high speed camera software has preset values for allowable integration times. In order to set an appropriate integration time for viewing the melt pool emission, two factors are considered. The first is that the integration time should be as long as practical in order to get as much signal at solidification as possible. The competing factor is that the oversaturated portion of

the melt pool should not be wider than the actual melt pool width so that melt pool dimensions can be determined. Trial and error done by viewing the emission from single beads on a sacrificial Ti64 plate is used to determine an acceptable integration time of 1.05 μs[74]. This integration time is the longest possible without have a saturated width greater than the expected width of the melt pool[75].

The same power, velocity, and substrate temperature combinations used in section 3.3.2 are used in this section. Each parameter combination is lased within the FOV of the high speed camera and the thermal emission recorded. The individual images are made coaxial [187] and the pixel intensities along the length of the melt pool and across the width of the melt pool, in both cases passing through the centroid of the saturated region of the melt pool, are extracted. An example intensity image with the lines along which the intensity values were extracted is shown in Figure 6-20. Anything over a detector saturation of 98% is considered saturated and anything under a detector saturation of 3% is considered below the noise threshold. These values are chosen to avoid the non-linearity in camera signal encountered at the extremes of the detection range.

The pixel intensities are then subsampled by a factor of 4 using the Matlab function 'interp' to linearly interpolate between pixel values. The intensity values for each image for a given parameter set are then averaged and the variability quantified. An example intensity profile can be seen in Figure 6-21.

[74] With this integration time, the expected optical blur is only 0.53 μm to 2.63 μm, and is therefore considered negligible.
[75] Expected melt pool width is determined from the melt pool dimensions in section 3.3.2.

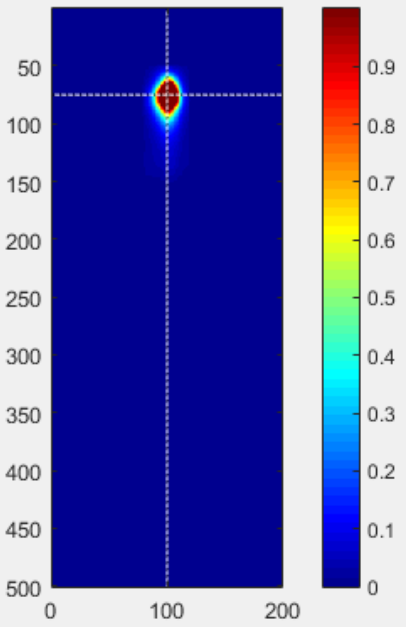

Figure 6-20: The intensity profile of a representative melt pool after being made coaxial. The color scale is % of detector saturation and the axes are pixel value.

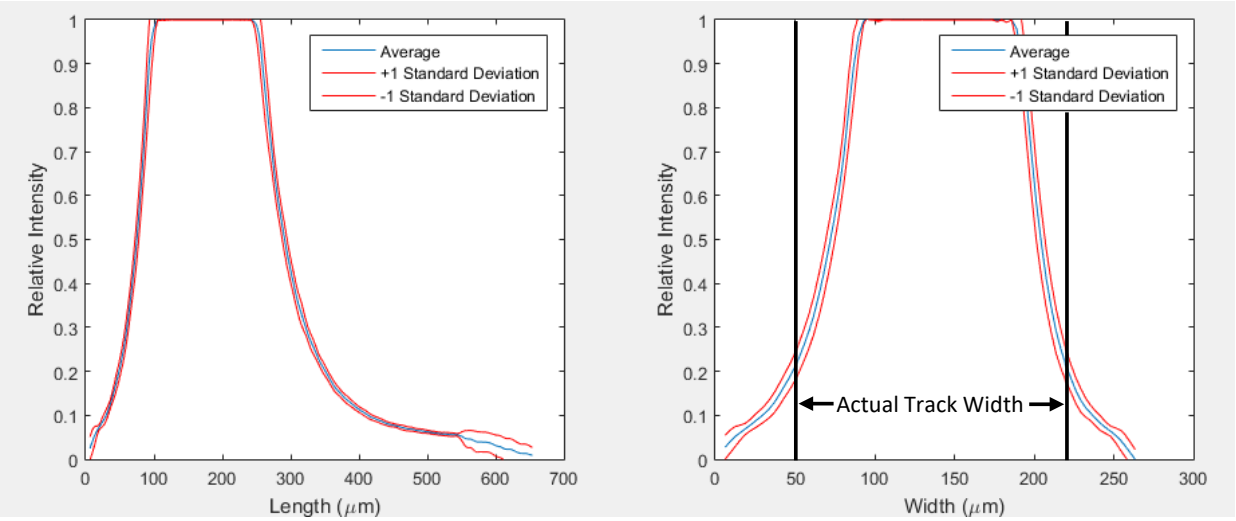

Figure 6-21: Vertical (left) and horizontal (right) scans passing through the centroid of the saturated region of the representative melt pool shown in Figure 6-20. Black bars are overlaid on the horizontal scan to represent the actual track width for the melt pool.

6.2.7 Solidification Discontinuity Detection

If a discontinuity can be seen down the length of each melt pool, then that pixel value can be used to threshold the solidification boundary. All of the images for a particular parameter set are made coaxial by matching the centroid of the oversaturated pixels in each image [187]. The pixel intensity values are then extracted down the length of each melt pool passing through the centroid of the oversaturated pixels. In order to smooth the data enough to get a slope and curvature that is not overly affected by noise, 5 pixel values on each side of the target value (for a total of 11 values) are included in a 3rd order polynomial fit and the second derivative of this polynomial is taken at the target value. This procedure is done at each pixel value in order to get a curve of the second derivative. The minimums of the second derivative curve are found for the pixel value interval from the center of the melt pool toward the tail[76] using the 'islocalmin' function in Matlab 2017b. This method requires a significant number of pixels along the melt pool length, and may not be suitable for lower magnification camera systems. Nicholas Jones, a colleague at CMU, assisted with generating the Matlab script to implement this detection method.

This method should capture the discontinuity due to the solidification isotherm (as long as this region is not obscured), but will also capture anomalous readings from fluid flow within the melt pool, spatter crossing the centerline of the melt pool, and weld products ejected above the melt pool. To filter out the anomalous data, all of the second derivatives are weighted by the intensity of the detection (each location is given a weight using the 'prominence' feature in the 'islocalmin' Matlab function). A histogram of the data is then generated with the weighting incorporated by counting the individual detections between 0 and 1000 times. A count of 1000 is

[76] Minimums in the second derivative are only recorded for the data that is below 95% of the maximum pixel value at the tail of the melt pool to avoid false readings when the pixels transition from saturated to not saturated.

reserved for the most intense detection and all other detections are scaled linearly between a value of 0 for no detection and a value of 1000 for the most intense detection, then rounded to the nearest whole number value.

In this way, small anomalies that happen often (like fluid surface perturbations or noise in the data) will be counted but not weighted heavily. Large anomalies that are rare (like spatter passing over the centerline of the melt pool or rapid variations in plume intensity) will also be counted, but not preclude the solidification isotherm from being counted as well[77]. The solidification isotherm should show up above the anomalous detections in a histogram because of a combination of intensity and frequency of detection in a small pixel value range. The spatter may still obscure the data because of the intensity of the detection; however, the individual spatter detections should be at discrete pixel values and will therefore show up as single valued peaks. In order to reduce the effect of the spatter detections, the histogram is smoothed using the 'smooth' function utilizing the 'rlowess' method with a span of 5 in Matlab 2017b. This smoothing function is based on local averaging, but is specifically tailored to remove outliers. The largest peak in the smoothed data is then isolated and the pixel value equating to solidification is taken as the average value of that peak. The uncertainty in the solidification pixel value is taken as two standard deviations on either side of that average for that peak.

The pixel value for solidification (with uncertainty) is then combined with the temperature range for solidification to determine a range for the emissivity value of the material at the solidification boundary [112] . This pixel value range found using this method could be represented

[77] If only the most intense detection is counted at the expense of all others, then the solidification isotherm would be discarded when there is a more intense, anomalous detection.

by a vertical bar in Figure 6-18. The emissivity value is then considered constant over the range of temperatures when determining true temperature[78].

6.3 Results

6.3.1 Total Melt Pool Emission

In order to determine the melt pool information that can be gleaned when high temperature information is retained, camera settings for the NIST camera setup are set such that no part of the thermal images saturates. In addition, because of the coaxial orientation of the camera, the melt pool is always in center frame and a large number of images can be taken. These images are compared to ex-situ measurements of the resultant melt pools to determine if correlations can be made.

The process maps for melt pool cross sectional area for the single beads conducted at NIST can be found in section 3.3.5, and are shown here as one plot (Figure 6-22). The corresponding map for total in-band melt pool thermal emission is shown in Figure 6-23. In both cases, it is clear from the slope of the curves of constant metric in power-velocity space as well as the shifts in those curves due to changes in substrate temperature that all three parameters tested (power, velocity, and substrate temperature) have significant effects on both melt pool cross sectional area and total in-band thermal emission. Furthermore, each successive curve constitutes a 2X change in the metric of interest, with the largest values chosen to start in similar locations in process space:

[78] The Author understands that the assumption of a constant emissivity is most likely incorrect due to variations in the angle of the material surface relative to the camera axis, the unknown temperature dependence of the emissivity, and the unknown influence of participating media between the material surface and the camera system. The lack of information about the possible emissivity changes due to these factors, however, necessitates the constant emissivity assumption in order to convert from radiant temperature to true temperature.

6 000 µm^2 at 25 ˚C in Figure 6-22 and 40 000 DL at 25 ˚C in Figure 6-23 (blue squares with dotted connecting lines).

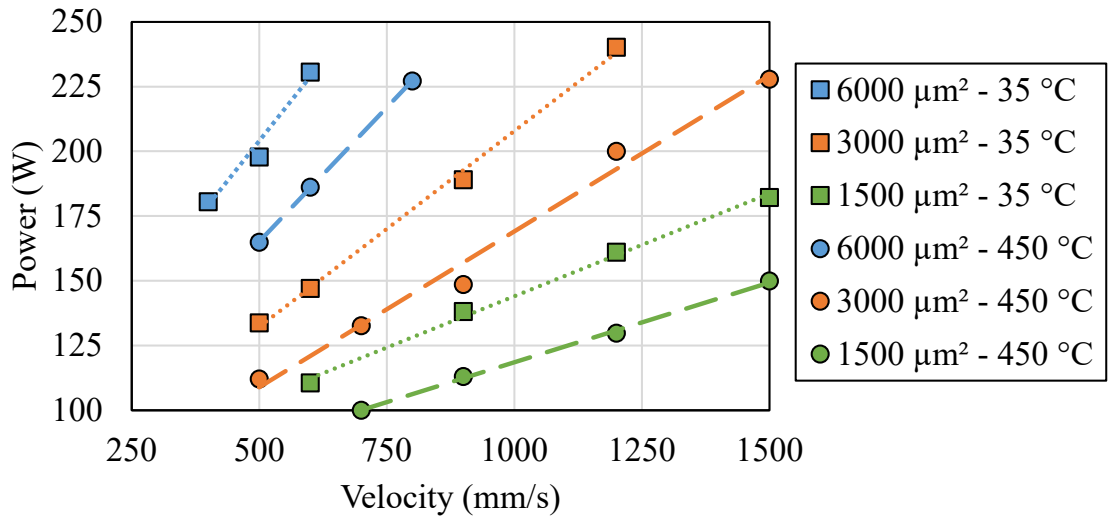

Figure 6-22: Curves of constant melt pool cross sectional area measured ex-situ for the single beads deposited at a substrate temperature of 35 ˚C.

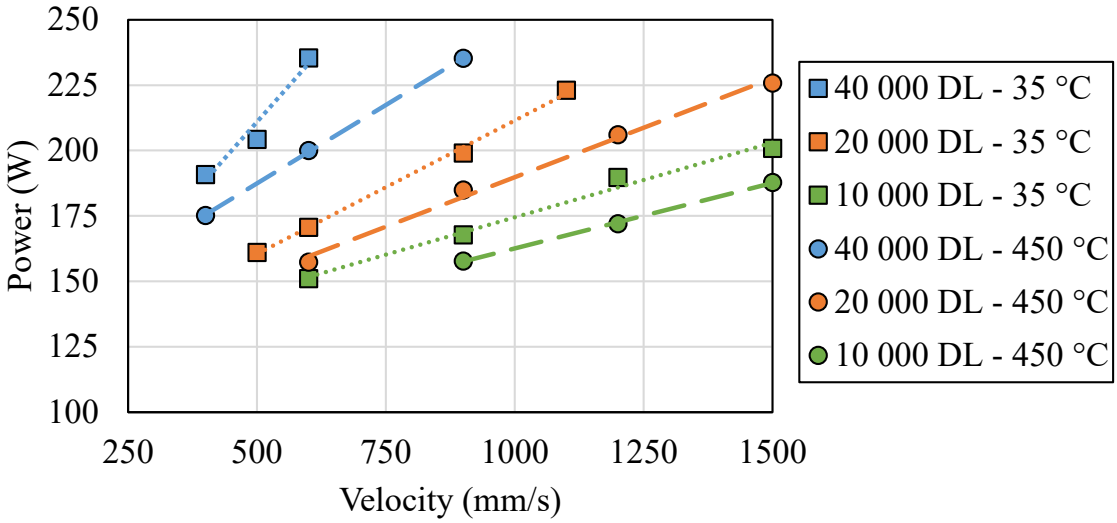

Figure 6-23: Curves of constant total in-band melt pool emission obtained from in-situ melt pool images for the single beads deposited at a substrate temperature of 35 ˚C.

The curves in Figure 6-22 and Figure 6-23 are similar, though with different magnitudes of process variable changes necessary to create the 2X jumps between curves. This means that correlations based on mapping of values between figures is possible, and therefore thermal emission can be used as a metric for cross sectional area, which is an important melt pool characteristic [30] that is nearly impossible to measure directly in-situ. An example of a correlation that can be made is as follows. If power is held at 200 W and substrate temperature is held at 25 ˚C, the curve of melt pool cross sectional area vs. thermal emission for the velocity range measured is linear with a slope of roughly 7 DL/μm^2.

To determine how strong the correlation between melt pool cross sectional area and total thermal emission is as substrate temperature is changed, the melt pool cross sectional area and the melt pool thermal emission for each parameter set is normalized to its value at 25 ˚C and plotted in Figure 6-24. The error bars are one standard deviation on the mean values and best fit curves are added for clarity. While there is significant scatter in the data, the trends show a very strong correlation between melt pool cross sectional area and total in-band thermal emission as substrate temperatures change. This means that if the melt pool emission is tracked throughout a raster or even throughout a build, the difference in melt pool cross sectional area can also be tracked since the power and velocity of the beam at any time is known.

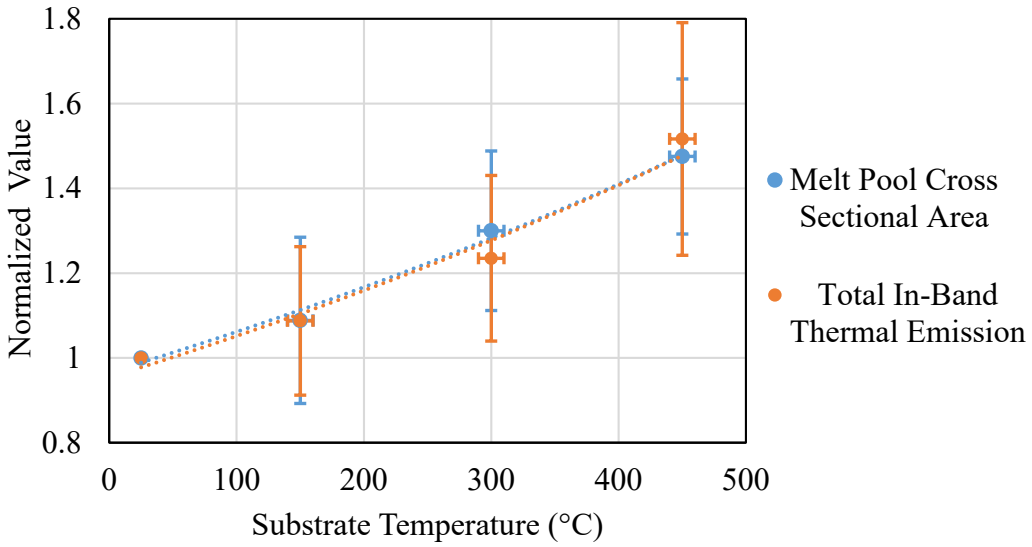

Figure 6-24: Normalized melt pool cross sectional area and the melt pool thermal emission for each parameter set, with error bars representing one standard deviation on the mean for each data point.

6.3.2 Thresholding for Melt Pool Dimensions

The pixel value across the width of each melt pool for the single beads taken on the EOS M290 is compared to the actual width of that melt pool from section 3.3.2. A linear regression line that passes through the origin is fit to a plot of width generated from pixel intensity on the *Y* axis and actual width on the *X* axis. This regression is done at each pixel value in order to generate a curve of regression line slope vs pixel intensity threshold. The analysis is then re-run comparing two additional cases: 1) the pixel value is one standard deviation above the mean and the actual width is one standard deviation below the mean and 2) the pixel value is one standard deviation below the mean and the actual width is one standard deviation above the mean. Cases 1) and 2) are meant to give a representation of the error that may be present in the pixel value threshold. Figure 6-25 shows curves of the regression line slope vs pixel value threshold for the average

values in blue, case 1 in orange, and case 2 in green. The pixel values for a slope of 1 are extracted for each curve: 695 DL for the average curve, 520 DL for case 1, and 885 DL for case 2.

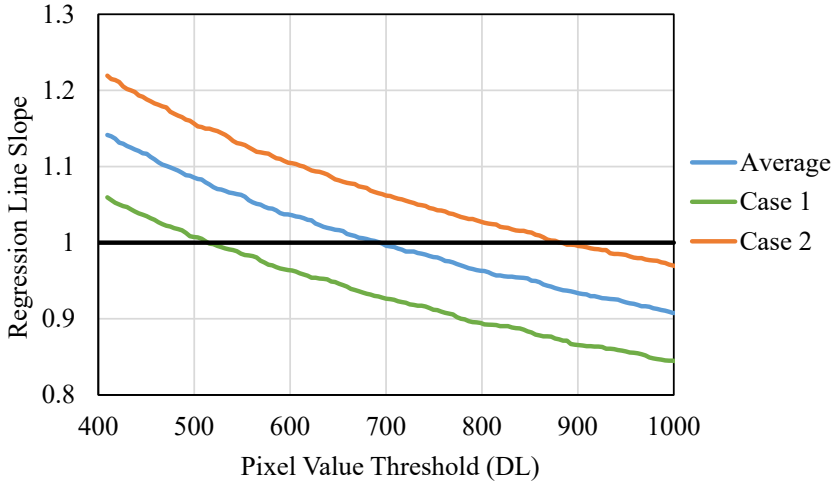

Figure 6-25: Figure of the slope of the regression line plotted against the intensity value chosen to threshold the data.

The average pixel value of 695 DL is then used as the threshold of the pixel value across the width of each melt pool for the single beads taken on the EOS M90 and is compared to the actual width of that melt pool from section 3.3.2. This information is shown in Figure 6-26. The blue hollow circles represent each single bead. The error bars represent one standard deviation on the mean for both *X* and *Y*. The blue line is the average regression line with a slope of 1. The regression line slope from the average curve is then determined for the pixel values for case 1 (slope of 1.07) and case 2 (slope of 0.94) in order to present the uncertainty derived from case 1 (green line) and case 2 (orange line) on Figure 6-26.

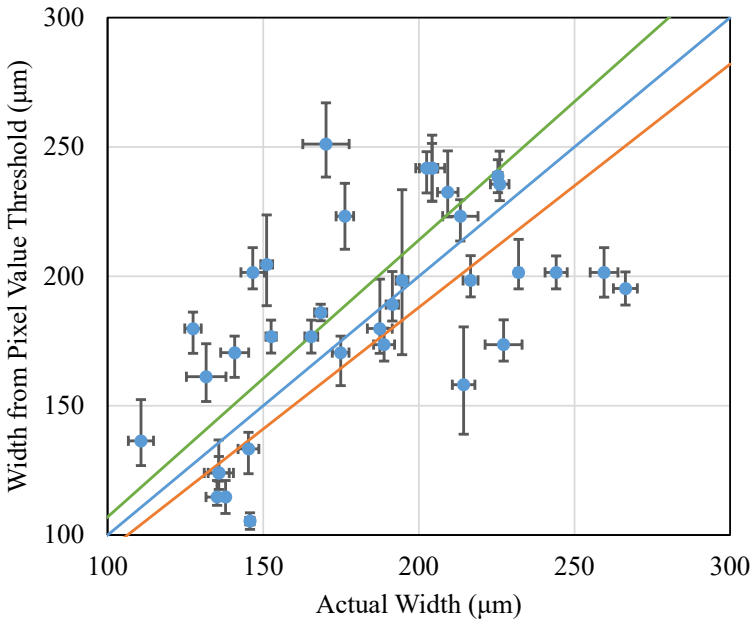

Figure 6-26: A figure of the width measured by thresholding the data plotted against the actual width. The blue and red lines equate to those in the previous image.

There is a correlation between larger width of the melt pool and larger width of the emitted radiation, but the r^2 value for the blue regression line in Figure 6-26 is only 0.19, meaning that the fit is not strong. The poor fit means that using thresholding of pixel values is not necessarily an appropriate method to determine the melt pool width in-situ when using these camera settings to detect melt pool emission. It is likely that the plume being ejected from the hottest part of the melt pool is adding significantly to the measured pixel intensities, increasing the apparent width of the melt pool. If this is the case, then it is possible that the width measured from pixel intensity is the width of the plume, and not the width of the melt pool track. 'Blooming'[79] from the hottest part of the melt pool likely also contributes to the increase in apparent width.

[79] Blooming refers to the spill-over of excess electrons from a pixel that is oversaturated to its neighboring pixels. This would have the effect of raising the signal from those neighboring pixels and artificially increasing their intensity. An analysis of the effects of blooming in this work is not done, but its effect would be the same as the addition of intensity from the plume: the melt pool would appear wider than it actually is.

6.3.3 Detecting the Solidification Isotherm

6.3.3.1 Low Integration Time

The camera images from section 6.3.2 are also used in this section (taken at an integration time of 1.05 μs). Figure 6-27 shows the procedure outlined in section 6.2.7 applied to a representative image of nominal parameters for the EOS M290 (280 W, 1200 mm/s, 35 °C preheat). A line scan down the center of the melt pool creates a pixel intensity profile, two derivatives are taken, and the local minima of the second derivative are determined. For the three plots in Figure 6-27, the *X* axis is pixel number and the *Y* axis is pixel value. The red line down the length of the melt pool image shows the path for the pixel intensity profile and subsequent derivatives.

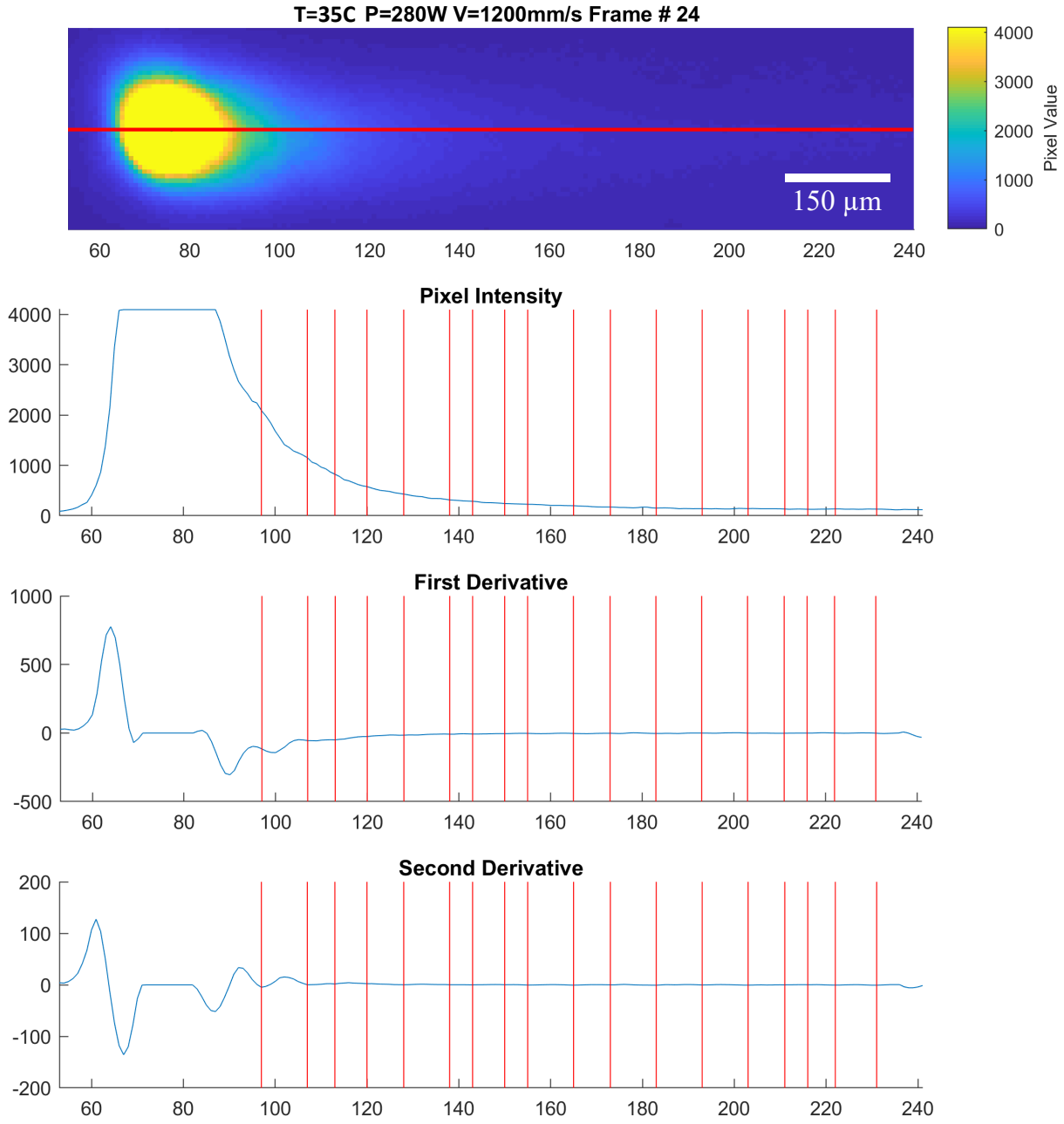

Figure 6-27: A schematic showing the steps in the analysis to find the solidification discontinuity. The red line overlaid on the melt pool image represents the line scan down the centerline of the melt pool. The x axis for all portions of the figure is the pixel value along that line scan.

The histogram for detections of the solidification discontinuity can be seen in Figure 6-28. It is clear that even though Figure 6-27 has a large number of detections, when the data for all of the images taken at all of the parameter sets is analyzed, there is one detection that is clearly the most prominent. The histogram bin with the most counts has a span of 117 to 136 DL and is highlighted in red. These values are not considerably above the camera's noise floor, meaning that the choice of integration time is too low because the metric of interest is in a range of camera signal that induces considerable amounts of uncertainty. The integration time should be increased in order to increase the likelihood that the solidification detections shown in Figure 6-28 are not just noise.

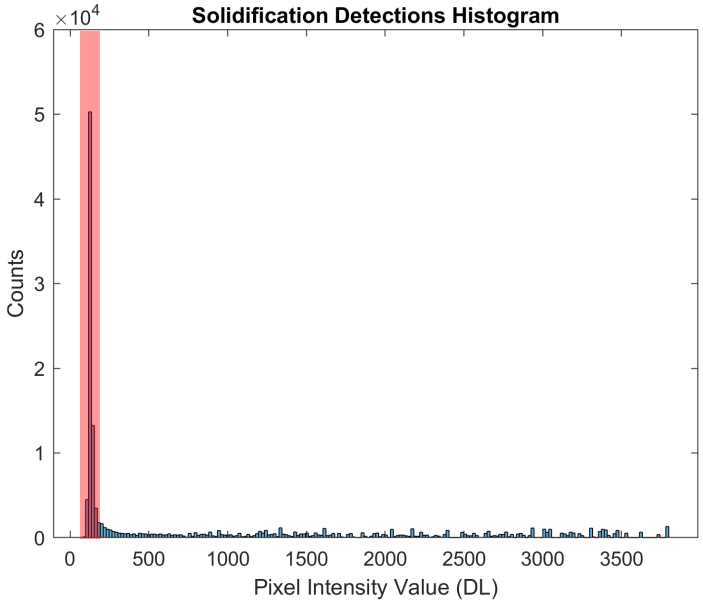

Figure 6-28: A histogram of detection frequency for the entire data set at an integration time of 1.05 µs.

Assuming that the algorithm has correctly identified the solidification discontinuity means that the pixel value equating to the solidification isotherm found from thresholding the melt pool width (520 DL to 885 DL, section 6.3.1) is considerably higher than the pixel value found in this section. One observation from the thresholding analysis is that the plume may be playing a

significant role in the melt pool emission and calculation of melt pool width. Looking at the tail of the melt pool would likely be affected less by plume emission because the plume has had time to cool. The discrepancy in values between the two methods is consistent with this observation, but leads to the conclusions that the camera settings used to find the solidification isotherm are not appropriate and the integration time needs to be increased.

6.3.3.2 The Effect of Bright Features

After temperature calibration is completed on the camera, it becomes clear that the 1.05 μs integration time used in sections 6.3.2 and 6.3.3.1 is not appropriate. The integration time used to calibrate the camera for a temperature range of 1150 °C to 1600 °C is 40 μs, or roughly 38 times longer than the integration time of 1.05 μs. A first approximation of the brightness temperature of solidification from literature information is 1435 °C (generated by assuming an emissivity of 0.35 at a true temperature of 1620 °C [109], [188]). From the camera calibration, an brightness temperature of 1435 °C at a 40 μs integration time will be 1370 DL, and a rough approximation[80] of the intensity value at a 1.05 μs integration time would be 38 times less, or 36 DL. This value is very low, and can easily be overshadowed by noise, pixel value non-linearity, or stray light from the plume. In addition, it is considerably lower than the values found in sections 6.3.2 and 6.3.3.1, further indicating that the plume is artificially increasing the pixel value for solidification.

It has been shown from prior literature that the effects of the plume are significant [116]. Depending on the process parameters used for melting, and especially the velocity of the beam, the plume will be ejected from under the beam spot at a different angle relative to the build plane,

[80] This approximation assumes that the camera's stated integration time is linearly related to the pixel value, which is not necessarily true, though it should be close. Therefore, this is a rough approximation for estimation purposes only.

independent of shielding gas flow [189]. High velocity melt pools will have plume ejection toward the back of the melt pool, while low velocity melt pools will have a more vertical plume ejection. This difference stems from the liquid flows within the melt pool. In either case, plume formation can obscure the melt pool surface and can have a significant effect on the shape and brightness temperature of the melt pool thermal image.

A qualitative analysis shows that using the 40 μs integration time, it would not be possible to use the melt pool width as a method to determine the solidification isotherm because for all of the melt pools imaged, the saturated region of the image is significantly wider than the melt pool itself. Figure 6-29 shows an example thermal image with the saturated region and actual track width highlighted. This means that an emissivity greater than 1 would be required to calculate a true temperature that matches the ex-situ measured track width. This leads to the conclusion that three phenomenon are likely happening to obscure the thermal emission from the melt pool surface: 1) the hottest part of the melt pool is causing blooming, 2) the plume ejected from the hottest part of the melt pool is also emitting significant amounts of thermal radiation, and 3) the thermal emission from the hottest part of the melt pool is reflecting off of the plume and back onto the material surface, artificially increasing its brightness temperature.

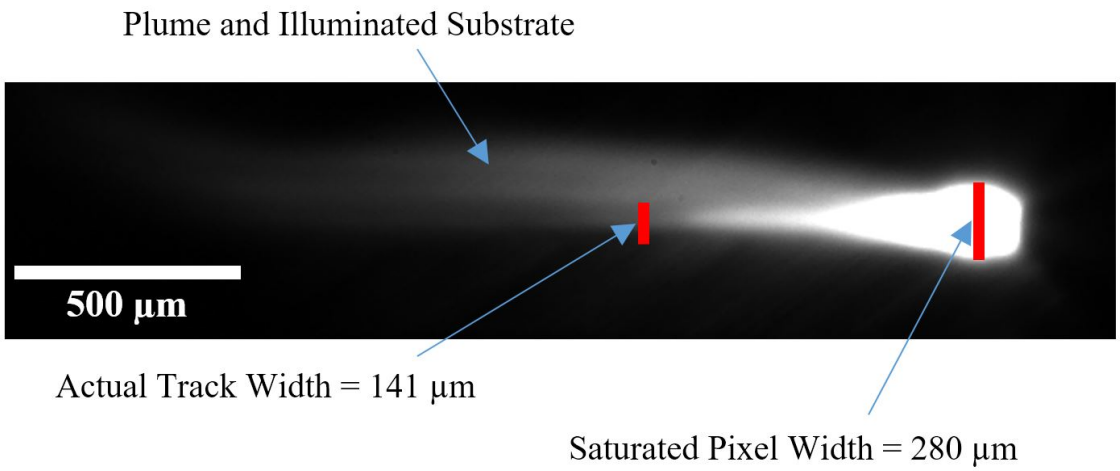

Figure 6-29: A representative image of the EOS Ti64 nominal parameters. The actual track width was determined from cross sectional measurements in section 3.3.2.

6.3.3.3 High Integration Time

Even with the obscuring effects mentioned in the previous section, the solidification isotherm should still be discernable as long as that signal value is within the detectible limits of the camera. In order to determine this, the analysis outlined in section 6.2.7 is completed for thermal images taken at an integration time of 40 µs. If the thermal images are converted to temperature, this step happens before coaxializing the melt pools so that a pixel-by-pixel calibration can be implemented.

It is clear that the plume is emitting a significant amount of thermal radiation. Figure 6-30 shows a progression of melt pool images for parameters that will generate roughly the same melt pool cross sectional area (determined from section 3.3.2). In addition, as the velocity of the beam is increased, the direction of plume formation moves toward the tail of the melt pool and becomes more intense. All melt pools, however, have plumes that are intense enough to significantly obscure the melt pool boundaries.

From the images in Figure 6-30, it looks like there is considerably more light emitted from the melt pools at higher power and velocity, which at first seems like a contradiction with the results from section 6.3.1. The center of the brightest part of the melt pool is saturated in these images, however, so it is impossible to know how intense the total in-band thermal emission actually is. Section 6.3.1 suggests that even though these images look significantly different, they should have roughly the same total in-band thermal emission.

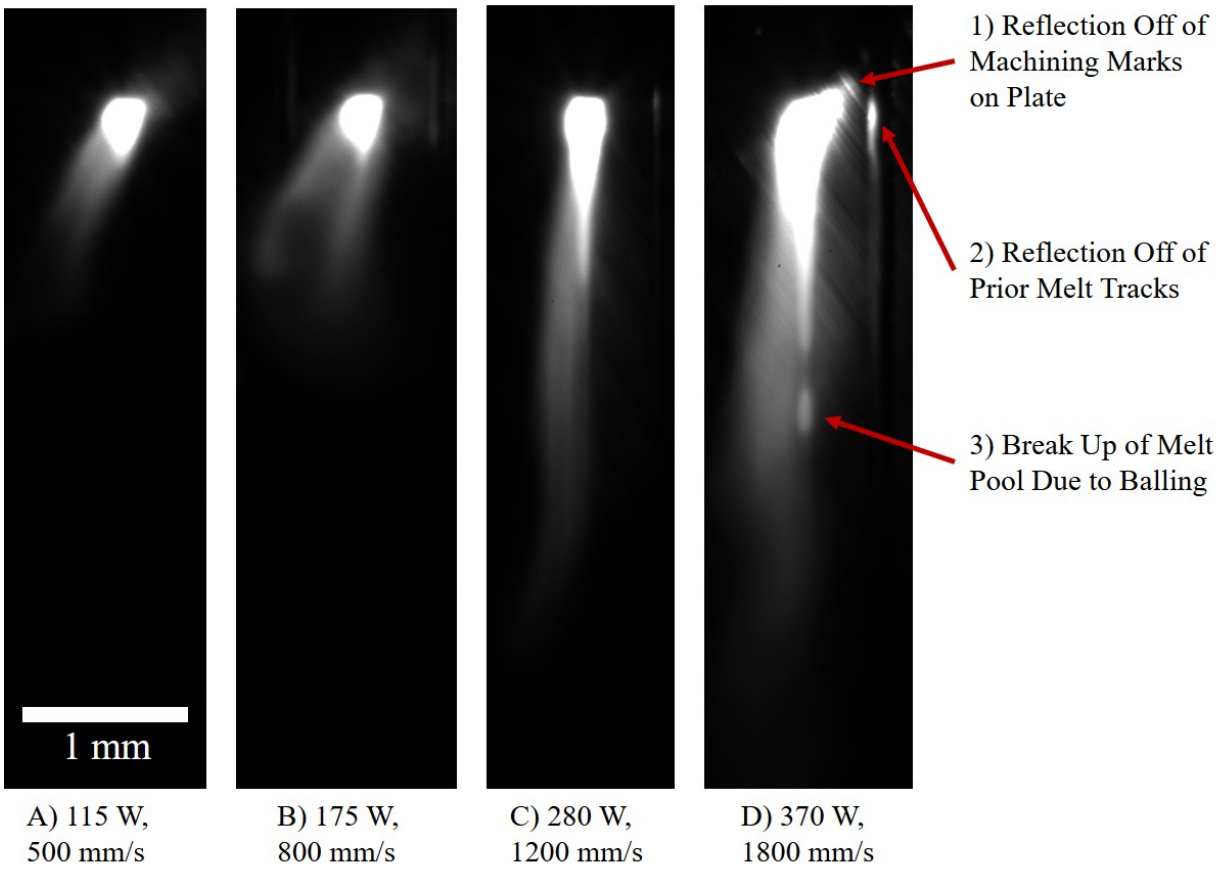

Figure 6-30: Representative images of several parameter sets (each at a substrate temperature of 35 ˚C) meant to have roughly the same melt pool cross sectional area. The plume emission and melt pool length seem to increase from image *A* to image *D*.

In Figure 6-30.D, three particular anomalies are highlighted. Anomalies 1) and 2) are reflections off of existing material, and illustrate the difficulty in isolating the melt pool itself. A connected components analysis[81] is not necessarily sophisticated enough to eliminate either of these anomalies because the pixel values surrounding these anomalies may not be low enough to generate the required contrast. Anomaly 3) is a break up of material at the tail of the melt pool and shows the balling phenomenon. This means that even with the obscuring nature of the hottest part of the melt pool and plume, it is possible to determine melt pool morphological features from an observation of the melt pool thermal emission. While a trained user would not have trouble differentiating anomaly 2) as a feature to discard and anomaly 3) as a feature of interest, the automation of this process by a computer may be non-trivial [160, Ch. 7].

Heigel and Lane [112] found that as melt pools became larger, the solidification discontinuity became easier to find. Taking this to its logical conclusion, if the melt pool were extremely large and moving slowly, the melt pool boundaries should be outside of the region of plume interference. For this reason, a very large melt pool[82] is generated as a way to easily determine the pixel value for the solidification discontinuity without the plume obscuring the tail of the melt pool. Figure 6-31 shows a representative image of this very large melt pool.

[81] A connected components analysis identifies discrete objects assuming that they are not connected. Once multiple objects are identified, it is possible to remove all but the largest object, which would be the melt pool. For further information on this topic, please refer to [187].

[82] Parameters of 370 W and 50 mm/s are used to make the largest melt pool that the EOS software allows. No heating of the build plate is employed when generating this melt pool, so the substrate temperature was roughly 35 °C.

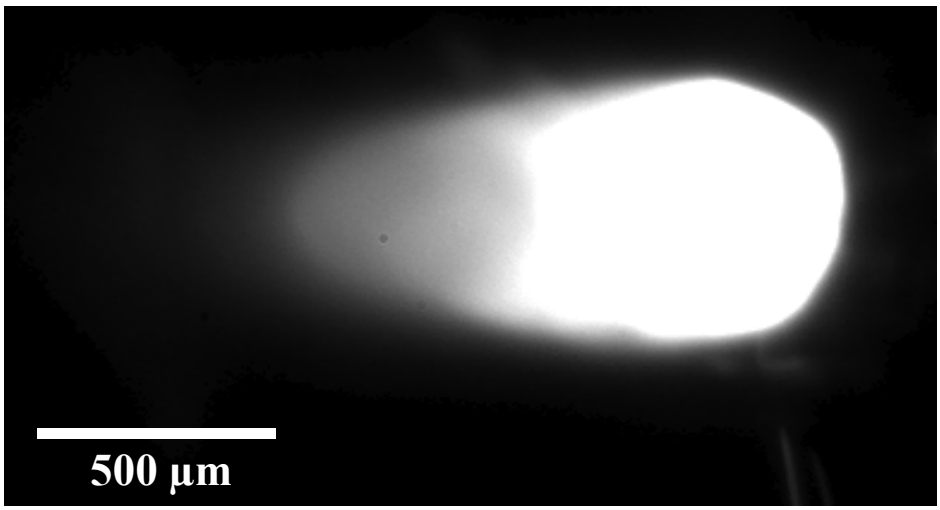

Figure 6-31: A representative image of the very large melt pool used to get unobscured images of the tail of a melt pool. The parameters for this melt pool are 370 W, 50 mm/s, and 35 °C substrate temperature.

Figure 6-32 shows the procedure outlined in section 6.2.7 for the melt pool seen in Figure 6-31. The tail region of the melt pool is symmetric and a significant discontinuity in the pixel intensity curve at a pixel value of roughly 1500 is visible. A pixel value of 1500 is in the range expected for solidification based on the likely emissivity from literature (0.35 [109], [188]) and temperature calibration discussed in the previous section. Therefore, it is likely that the solidification isotherm is visible in this melt pool without significant effects from the plume. In addition, because the melt pool is moving so slowly, the optical blur is reduced to only 2.0 µm.

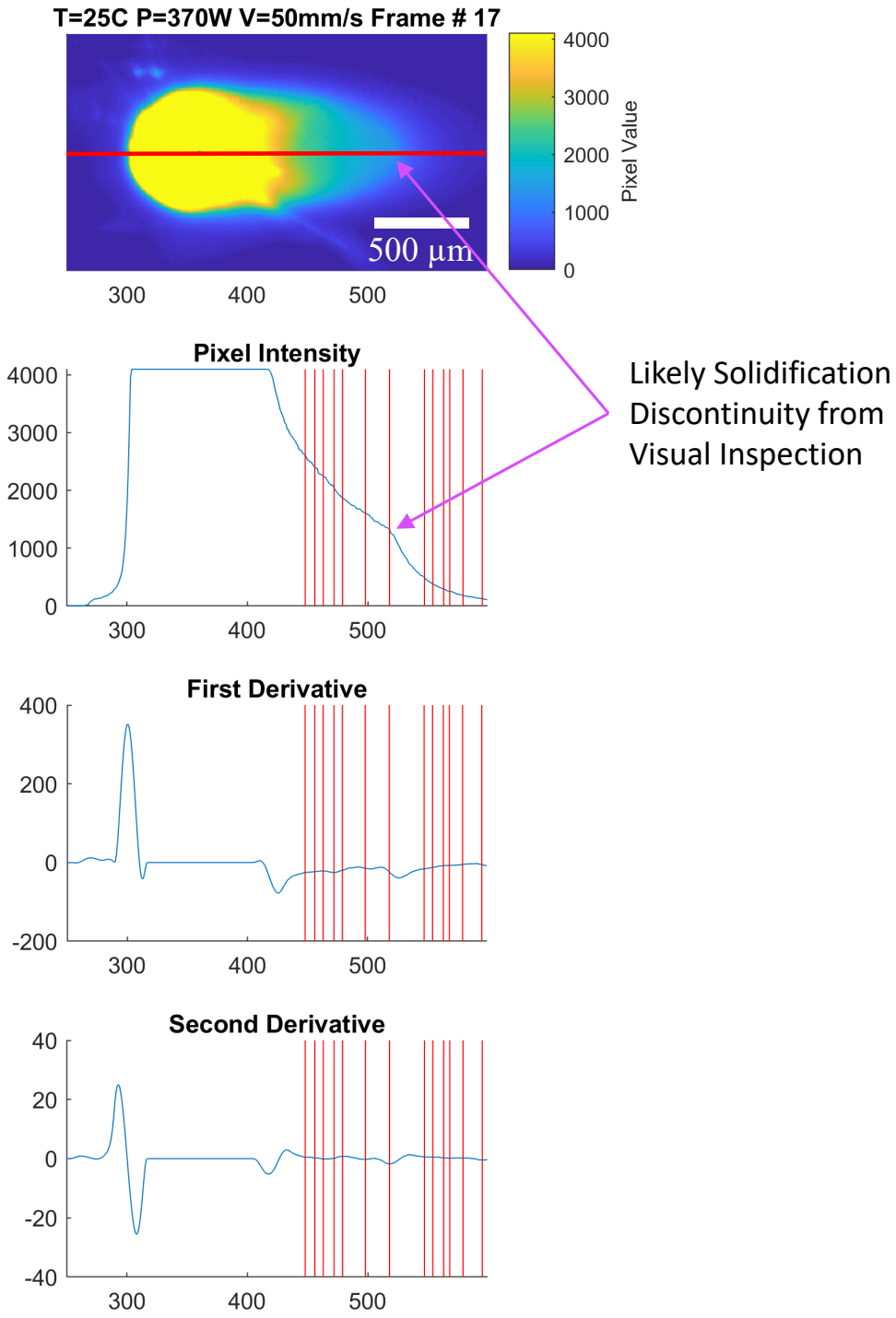

Figure 6-32: The same schematic as Figure 6-27, but for the large melt pool described in Figure 6-31 imaged at an integration time of 40 µs. The red line overlaid on the melt pool image represents the line scan down the centerline of the melt pool. The x axis for all portions of the figure is the pixel value along that line scan.

It is clear that a large percentage of the vertical red lines in Figure 6-32 do not equate to a value that makes sense visually and are likely anomalous, but the weighting used for the detections reduces the influence of the multiple anomalous detections. Figure 6-33 shows the same analysis for the nominal Ti64 parameters (280 W, 1200 mm/s). The yellow highlight inside of the dotted region represents the zoomed in region at the tail of the melt pool based on the Author's visual inspection. This region is blown up and shown in Figure 6-34. Again the multiple anomalous detections can be seen, but when more detail is shown for the tail region, it becomes clear that the largest weighted detection is occurring at what looks to be the solidification discontinuity. The weights chosen by the algorithm for each detection are overlaid on the figure (numbers in black boxes in the Second Derivative plot in Figure 6-34). The largest weight is at the location that the Author would expect from visual inspection of the melt pool image and pixel intensity curve. The normalized intensity of this detection is more than an order of magnitude larger than the anomalous detections surrounding it.

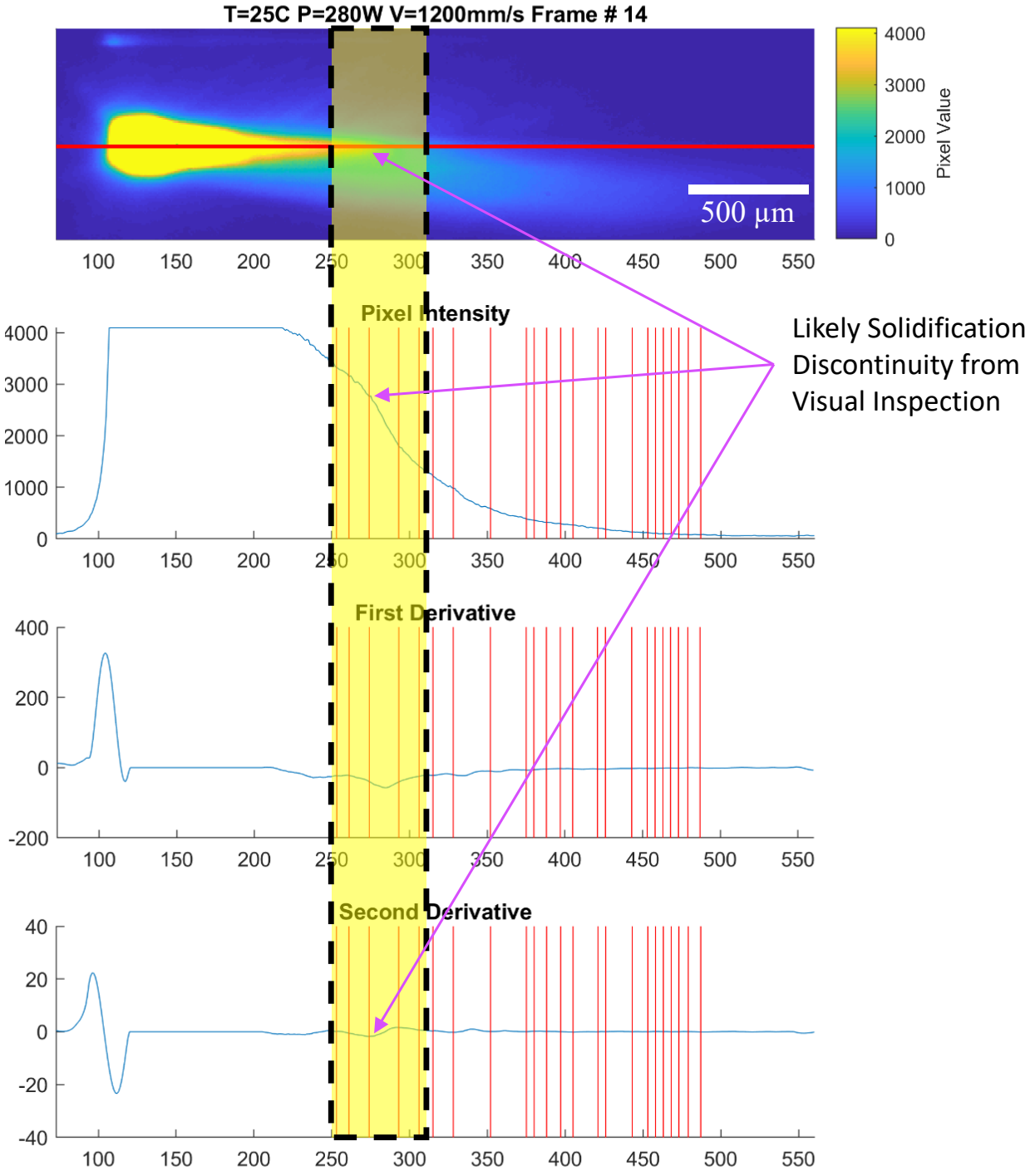

Figure 6-33: The same schematic as Figure 6-27, but for the EOS nominal parameters for 30 µm Ti64 layers. The red line overlaid on the melt pool image represents the line scan down the centerline of the melt pool. The x axis for all portions of the figure is the pixel value along that line scan.

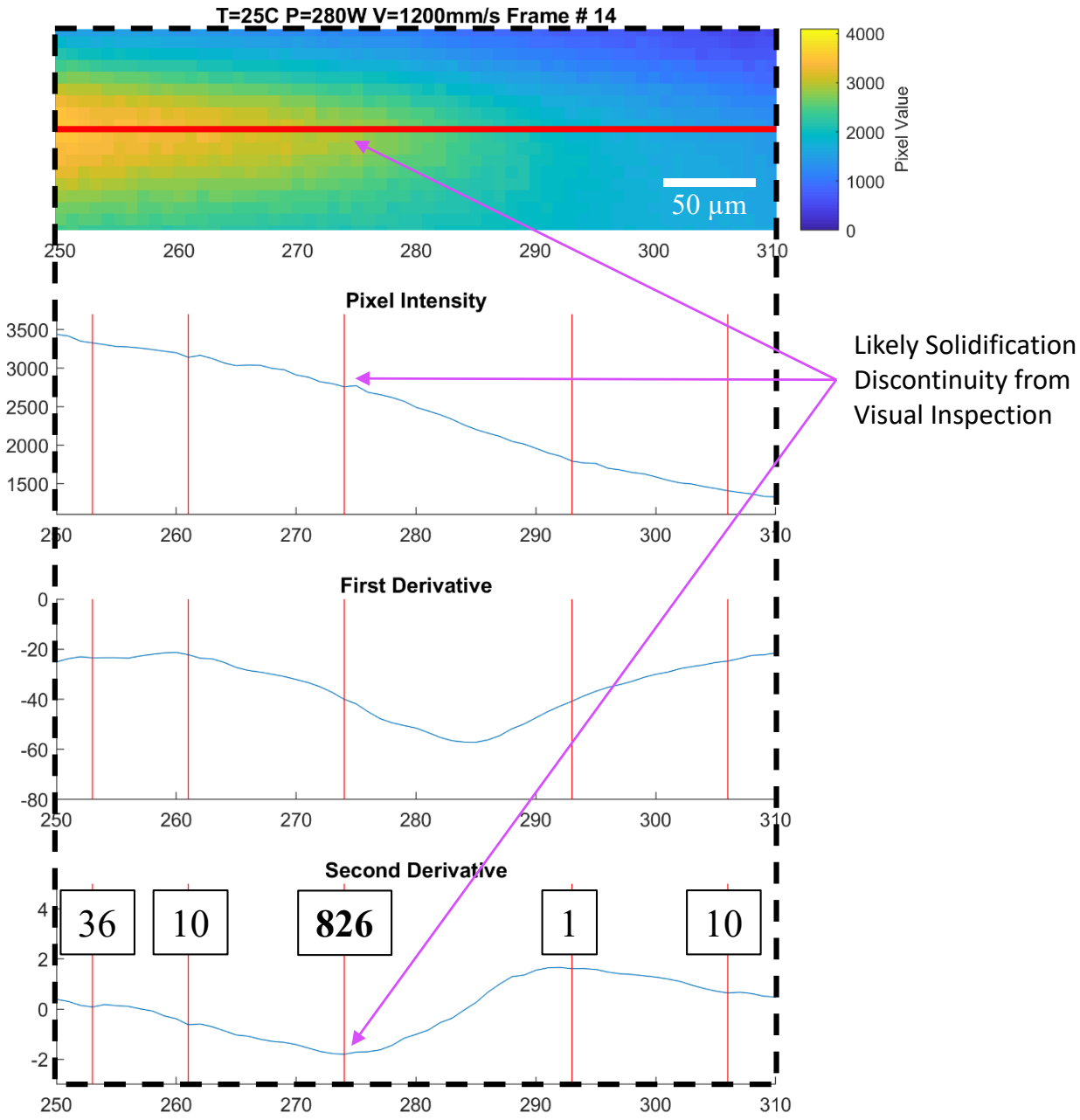

Figure 6-34: A zoomed in view of the highlighted section of Figure 6-33. The numbers equating to each local minima detection show its weighting. The red line overlaid on the melt pool image represents the line scan down the centerline of the melt pool. The x axis for all portions of the figure is the pixel value along that line scan.

It is clear from a comparison of the pixel intensity plots in Figure 6-32 and Figure 6-33 that the solidification discontinuity is at significantly different pixel intensities (roughly 1500 DL and 2700 DL respectively). This is a result of the plume emission that can be seen in Figure 6-33, and shows that even though the solidification discontinuity can be seen, the plume is combining with the emission from the surface of the melt pool to give artificially high pixel intensity values. Because of the variability of the plume thermal emission, however, it is not clear how to subtract the effect of the plume from the images. For this reason, the images are not modified. The plume emission is likely the reason for the variability seen in the reported melt pool lengths in prior research [112], though the difference in viewing angle and spectral responsivity of the two camera setups, as well as the difference in material, makes comparison difficult.

All of the images for the melt pool seen in Figure 6-32 (a total of 244 images) are analyzed and a weighted histogram of the solidification discontinuity detections is generated (Figure 6-35.A). It is clear that there is significant noise in this data, but when smoothing is applied (Figure 6-35.B), two peaks are clearly more significant than the others and are highlighted in red. The first peak occurs at a pixel value close to the image noise and is likely due to the steep drop off in pixel intensity at the edges of the original camera frames. This first peak occurs at the same pixel value range as the single peak in section 6.3.3.1, indicating that this peak is likely generated by the same mechanism and is due to the analysis procedure itself and not a physical phenomenon. Therefore, this peak should be discounted both in this analysis and in section 6.3.3.1. The second peak makes physical sense and is chosen as the pixel value that equates to solidification. The average value for this peak is 1434 DL and the standard deviation of this peak is 80 DL. For ease of future analysis, the single value of 1434 DL is used as the pixel value for solidification for a 40 μs integration time.

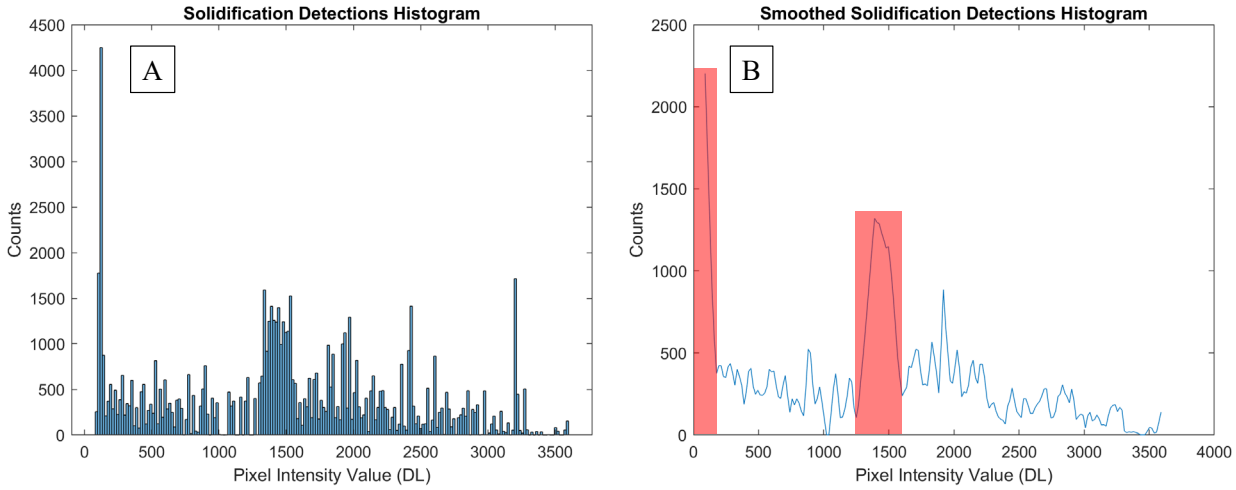

Figure 6-35: A) A histogram of the detections for all of the data taken for the melt pool in Figure 6-31. B) The plot in A, smoothed to remove outliers. The red highlights show the possible location of the solidification discontinuity for an integration time of 40 µs.

The same histograms are generated for the melt pool seen in Figure 6-33, though there are only 14 usable images available, and can be seen in Figure 6-36. As noted earlier, the solidification discontinuity detection is at a considerably higher pixel value than for the very large melt pool.

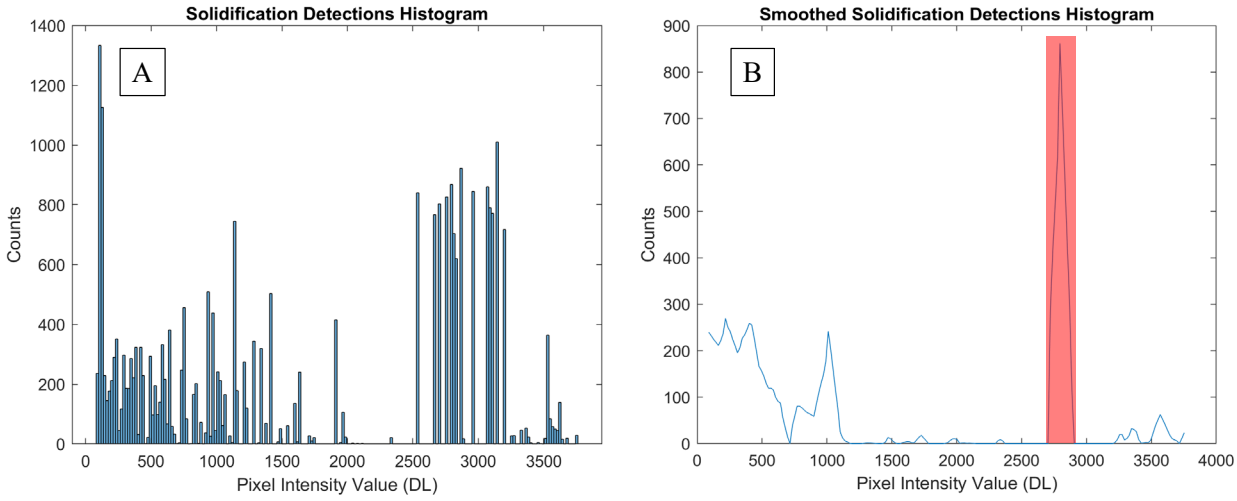

Figure 6-36: The same information as Figure 6-35, but for the EOS nominal parameters for 30 µm Ti64 layers.

When the images for all of the melt pools analyzed in section 3.3.2 are analyzed as one data set (for a total of 147 images), the histograms generated (Figure 6-37) show no distinct solidification peak, though there are a large number of detections between roughly 1800 and 3200 DL. The red highlighting in Figure 6-37.B represents the range for solidification found from this data while the blue highlighting represents the range found from the very large melt pool that was only minimally affected by the plume. Aggregating the images in this way incorporates different plume morphologies, melt pool shapes, and substrate temperatures. It is clear that there is too much noise and too many anomalous detections to generate a usable pixel value for solidification.

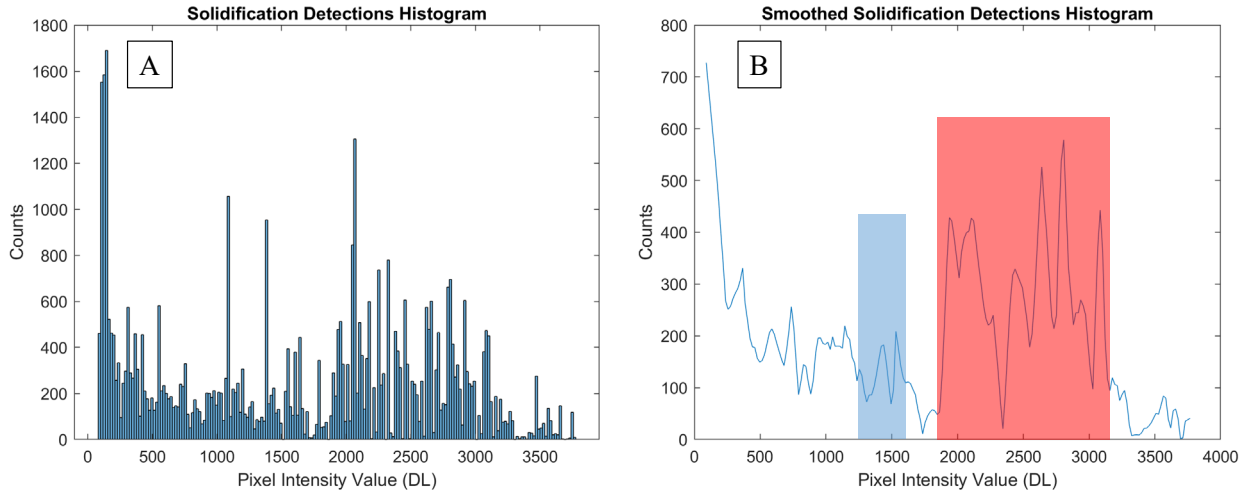

Figure 6-37: The same information as Figure 6-35, but for all of the parameter sets described in section 3.3.2.

Figure 6-37 shows that different parameter sets are generating anomaly detections at different pixel values, likely due to varying levels of plume intensity. In order to understand the average effect of the plume on the solidification detection across different parameter sets, a larger data set than is available in this work would be necessary. These data do show, however, that there is a distinct effect of the plume in the aggregated data and there seems to be a varying effect as

parameters are changed. This result is due to the variation in plume intensity and angle of plume emission as parameters are changed.

6.3.4 Melt Pool Emissivity and Melt Pool Dimensions

The pixel value for solidification determined from the previous section (1434 ± 160 DL[83]) is converted to a brightness temperature (1443 $^{+17}_{-19}$ °C) using the average temperature calibration fitting parameters from section 6.2.5. Each image is still converted to brightness temperature on a pixel by pixel basis, however. If the brightness temperature were at the high end of the uncertainty range (1460 °C) and the actual temperature were at the low end of the solidification range (1600 °C), the emissivity would be 0.45. If the brightness temperature were at the low end of the uncertainty range (1424 °C) and the actual temperature were at the high end of the solidification range (1650 °C), the emissivity would be 0.28. If the brightness temperature were at the average value (1443 °C) and the actual temperature were at 1620 ° C [109], the emissivity would be 0.37. This gives an emissivity range for solidifying Ti64 of 0.37 $^{+0.08}_{-0.09}$, which is in good agreement with literature values for liquid, solid, and solidifying material [27], [109], [141], [177], [186], [188].

A representative brightness temperature image taken from nominal Ti64 parameters (280 W, 1200 mm/s, 35 °C) can be seen in Figure 6-38 with the solidification boundary highlighted in red. It is clear that the plume is artificially increasing length because the melt pool is not symmetric about the beam travel axis and the plume is visible. In addition, optical blur will be artificially increasing the melt pool length because the heat source is moving while light is being collected in each image (for this velocity, the optical blur will be 48 μm). The width is also affected because it

[83] The standard deviation of the peak in section 0 was 80 DL. Two standard deviations on either side of the mean are chosen to represent the variability in this measurement.

is considerably larger than the measured width from section 3.3.2. Because the length and width are affected, the total melt pool surface area will also be artificially large. Due to the inability to get accurate values from these images, the values for melt pool dimensions are not presented here.

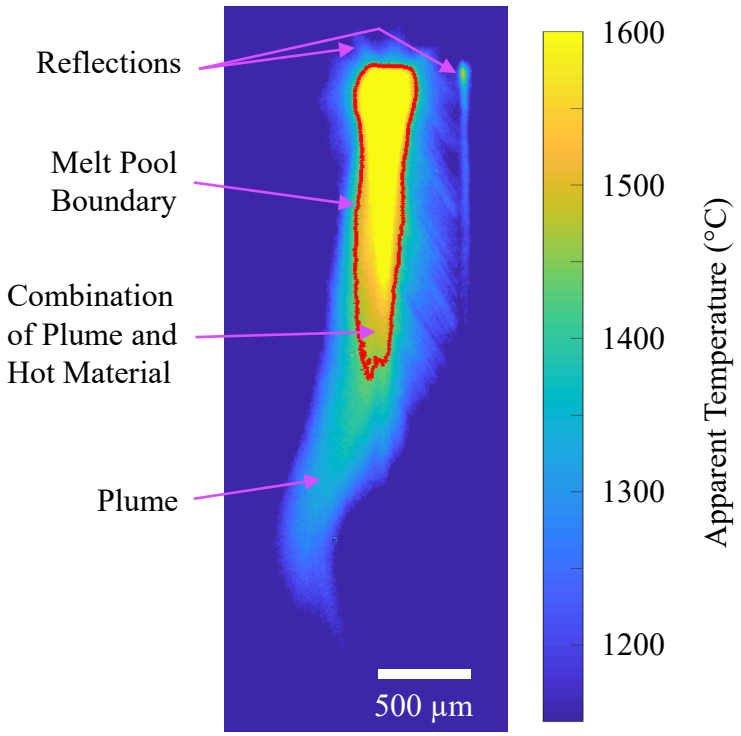

Figure 6-38: A false color image showing the brightness temperature of the EOS nominal parameters for 30 µm Ti64 layers, highlighting several anomalies as well as the melt pool boundary determined from the previous section.

6.3.5 The Effect of Temperature on the Melt Pool

The beam turns off at the edge of a stripe during a raster before turning back on to produce the next pass in that raster. The previous melt pool cools during this time. By imaging the melt pool when the beam turns off, information about temperatures within the melt pool and the time required for the melt pool to solidify can be determined without being obscured. This has the added benefit of eliminating the optical blur in the image because the melt pool is no longer moving. In

order to have the greatest possible temporal resolution, the camera's active pixels are reduced to 1024 pixels wide by 320 pixels tall and the frame rate is increased to 20,000 Hz, but the integration time is maintained at 40 μs. The images are converted to brightness temperature using a pixel by pixel calibration, then converted to true temperature using a constant emissivity of 0.37 (found from the previous section).

The cooling progression for nominal parameters can be seen in Figure 6-39. The field of view of the camera is stationary, so both the leading edge and tail of the melt pool shrink in toward the center, though the tail shrinks considerably more. The uncertainty in the time that the beam turns off is between +0 μs and +50 μs as defined by when the plume decreases in intensity significantly. The red highlight in each image represents the solidification boundary as determined from the 1620 ˚C isotherm (the solidification temperature [109]).

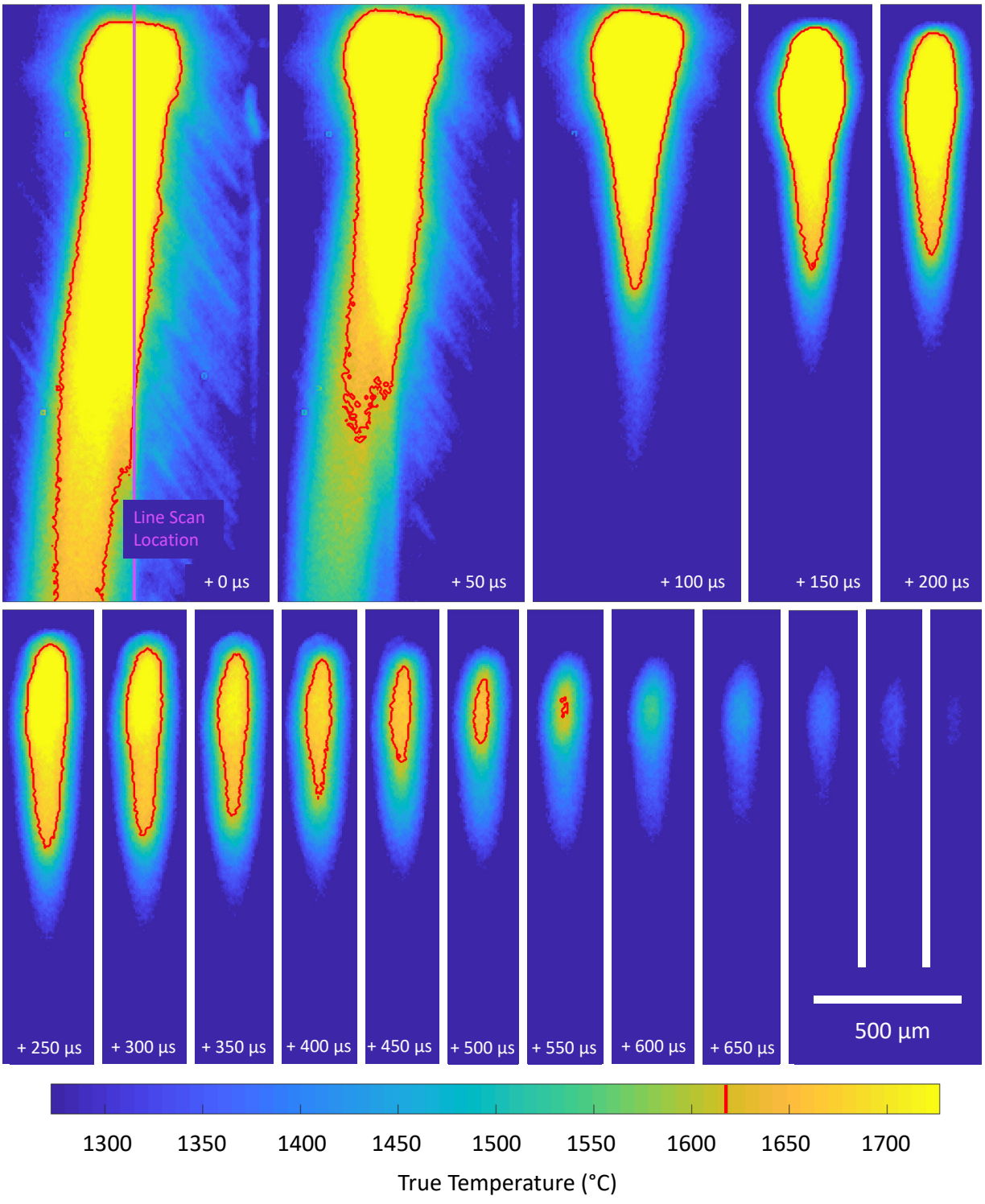

Figure 6-39: A series of images showing the EOS Ti64 nominal parameters cooling after the beam is turned off. The red contour shows the solidification temperature (1620 °C [109]).

It is clear that the plume and the hottest part of the melt pool obscure the melt pool surface when the plume is emitting thermal radiation. This makes determination of melt pool dimensions difficult and subject to significant error and uncertainty. When the beam is off, however, the melt pool surface should be the only object emitting significant thermal radiation, and information about the melt pool itself can be determined with much greater accuracy. As Figure 6-39 shows, the time it takes for the melt pool to solidify (+550 μs) is considerably longer than the time it takes for the plume to stop being visible (roughly +150 μs). The effect of blooming is likely very small after roughly +250 μs since the melt pool width drops below the measured melt pool width at this time. Based on work by Zhao et al. the maximum melt pool cross sectional dimensions do not significantly change for roughly the first 40% of the time required for the melt pool to fully solidify, likely due to superheated liquid and the recalescence phenomenon[84] [88]. In the case of Figure 6-39, this means that the actual melt pool width should not start decreasing significantly until roughly 220 μs after the beam turns off, which coincides well with the time required for blooming to no longer affect melt pool dimensions.

A purple line can be seen in the +0 μs image in Figure 6-39 showing the location used to extract the data for Figure 6-40. This same location is used to generate the data for all subsequent time steps. It is clear that the temperature at any location monotonically decreases with time, as expected. The solidification temperature of 1620 ° C [109] is shown as a horizontal red bar for reference.

[84] The recalescence phenomenon refers to the stabilization or even increase of temperature due to the release of latent heat of fusion as a material solidifies, even though heat is continually be extracted from the solidifying liquid by the surrounding material [199, p. 259].

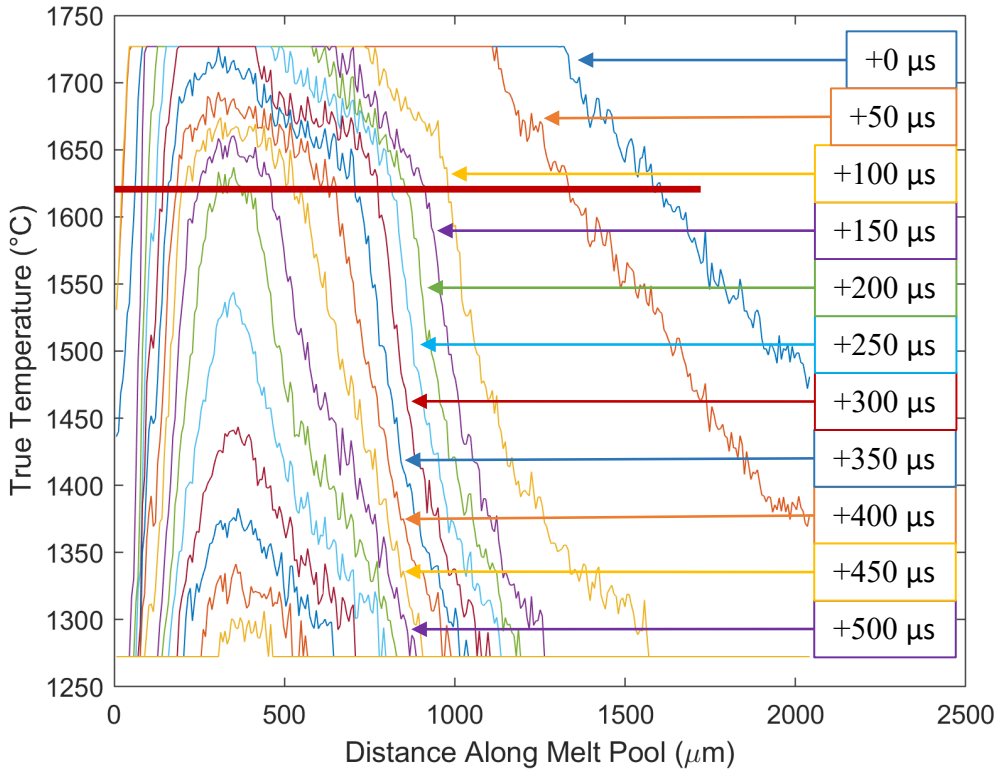

Figure 6-40: The temperature profile down the center of the melt pool shown in Figure 6-39 as it cools after the beam is turned off.

From Figure 6-40, the thermal gradients at the tail of the melt pool look fairly constant for the first half of melt pool solidification (roughly +100 μs and +350 μs), equating to the time that the melt pool cross sectional area stays fairly constant. The leads to the assumption that the thermal gradients at the tail of the melt pool after the plume has dissipated should not change significantly from their values when the laser beam is on. The average thermal gradient at the tail of the melt pool just below solidification for this time range (over the temperature range from 1500 °C to 1620 °C) is 1.45×10^6 °C/m, which is considerably below the 7.84×10^6 °C/m maximum thermal gradient that the camera system can detect (from section 6.2.5). Figure 6-41 shows this same analysis done

for each parameter set, normalized to its corresponding value at 35 °C, and plotted[85]. The normalized thermal gradient from simulation (taken from the simulations completed as part of Chapter 3) is also shown on the same axis. There is good agreement between the conduction based simulations and the experimental data[86], which is expected because the measured thermal gradients are all in the solid material, and therefore fluid flow within the melt pool will not affect the results. While there is scatter in the data, the trend is clearly to lower thermal gradients with higher substrate temperatures.

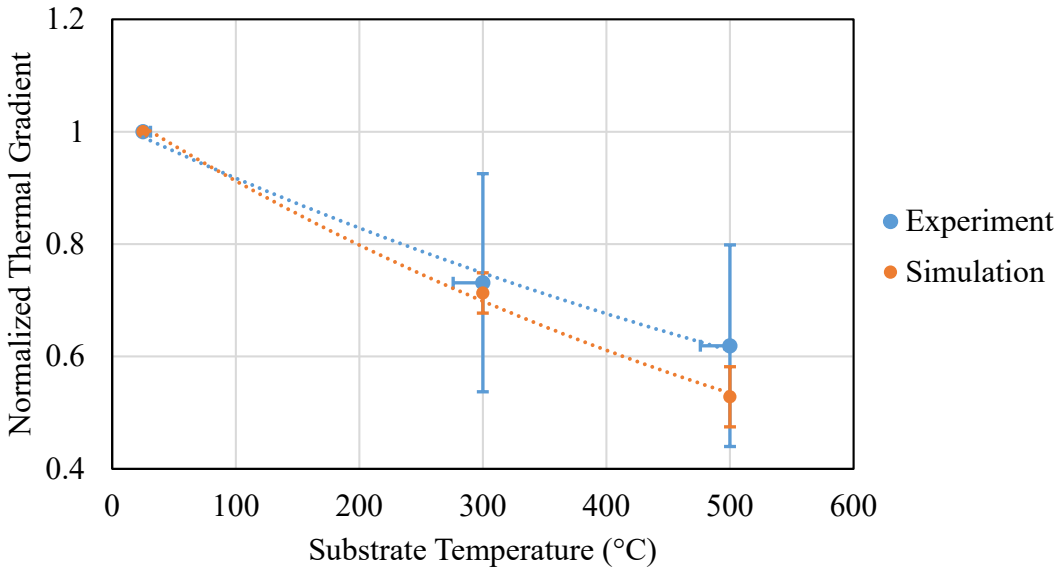

Figure 6-41: Normalized thermal gradient at the tail of the melt pool for a range of power-velocity combinations at different temperatures. The error bars in the *Y* direction are one standard deviation on the mean. The error bars in *X* are the range of temperatures measured from section 3.2.4.

[85] A figure similar to Figure 6-40 is generated for each parameter set, the time increments just after the melt pool tail becomes clear and while the thermal gradient is still roughly steady state are determined, the average thermal gradient at the melt pool tail for those time increments is determined between 1500 °C to 1620 °C, and that value is recorded. Cases where balling occurs are excluded due to the variable thermal gradients at the tail.

[86] The simulations are taken as an aggregate to eliminate the need for an effective or absolute absorptivity to correlate the simulations to particular parameter sets.

The maximum temperature in each frame in Figure 6-39 is extracted and plotted in Figure 6-42 along with the melt pool surface area. From this analysis, coupled with information from Zhao et al. [88][87], three regions can be identified. The first, highlighted in green, is where the plume and hottest part of the melt pool are obscuring the melt pool width and overestimating the melt pool surface area. The second, highlighted in purple, is where most of the melt pool cross sectional area change occurs. The third, highlighted in yellow, is the rapid cooling after the melt pool has solidified due to the lack of latent heat of fusion. This rapid cooling starts when the maximum surface temperature is between 1600 and 1650 °C, as expected, and further validates that the solidification isotherm has been correctly determined. In addition, the tail of the cooling curve (after 650 μs) starts to have a lower slope (or 'tail off') due to the lower temperature difference between the maximum temperature and the existing substrate temperature (in this case, 35 °C). This suggests that the camera system is accurately tracking the solid state cooling of the melt pool.

[87] Negligible melt pool cross sectional area change is seen for roughly the first 40% of the time required for the melt pool to solidify.

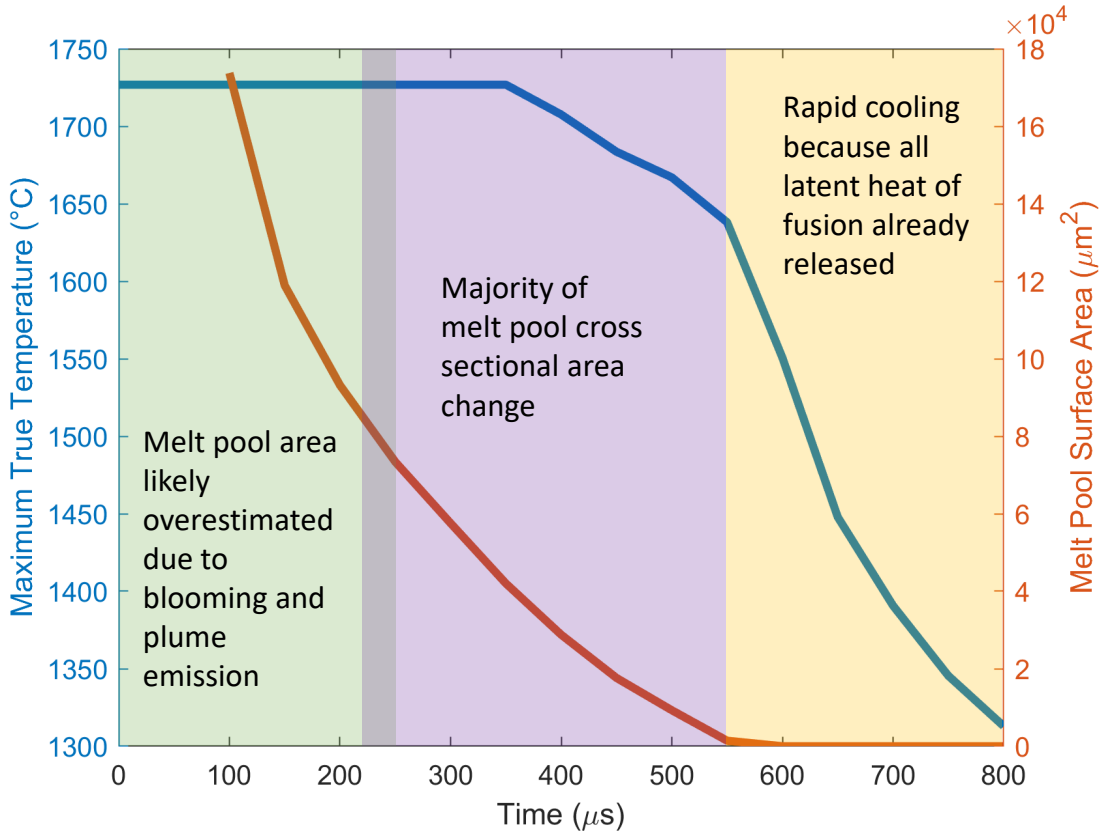

Figure 6-42: A figure of the melt pool surface area decrease and maximum temperature for the EOS Ti64 nominal parameters after the beam is turned off. The purple region is based off of data from Zhao et al. [88].

To understand how the time to solidify changes as the substrate temperature increases, melt pool surface area and maximum temperature are plotted for nominal parameters (280 W, 1200 mm/s) for each of three substrate temperatures: 35 °C, 300 °C, and 500 °C. Those curves can be seen in Figure 6-43. Due to the lower thermal gradients associated with higher substrate temperatures, it is anticipated that the time to solidify would increase as the substrate temperature increases. This does seem to be the general trend, though there is some overlap of the 25 °C and 300 °C cases. In addition, the maximum temperature is expected to be higher at all time steps for a higher substrate temperature, again because of the lower thermal gradients. Again, this is the

general trend, but there is overlap of the 35 °C and 300 °C cases. It is likely that this overlap is due to uncertainty in exactly when the beam turns off relative to when the images are acquired, as a time of 0 is based on visual inspection of the plume and is in increments of 50 µs.

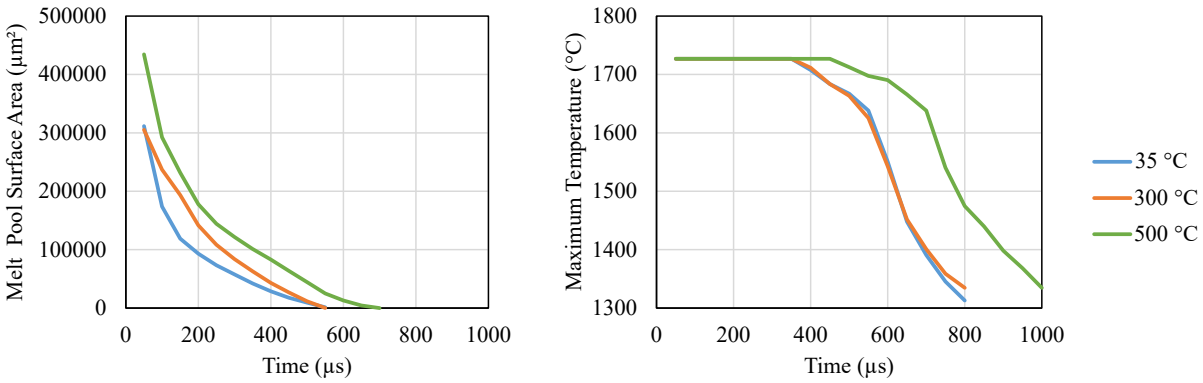

Figure 6-43: Left) A figure of the melt pool surface area decrease and Right) maximum temperature for the EOS nominal parameters for 30 µm Ti64 layers after the beam is turned off for each of three substrate temperatures.

The same cooling progression is measured for all melt pools. The time to solidify for each parameter set is normalized to its value at 35 °C, plotted in Figure 6-44 and combined with the same curve generated for simulations (Figure 5-13). There is a definite upward trend in the time to solidify with substrate temperature, but there is a significant amount of scatter in the experimental values. It is unlikely that the scatter can be completely attributed to uncertainty in the time that the beam is turned off, though this will have a significant contribution to the scatter. The increases in time to solidify are on the order of 100-400 µs. The time step between frames is 50 µs, so the uncertainty in the time to solidify may be as much as 2 frames or 100 µs, the same order of magnitude as the differences being measured. Because the uncertainty due to the time between frames is random, however, trends should still be valid as long as enough data is taken at each temperature. Said another way, over a large sample size, the uncertainty in time to solidify

should average out and the inherent differences between data taken at different substrate temperatures become apparent (as seen in Figure 6-44). While there is scatter in the experimental data, the trend is clearly to higher time for the melt pool to solidify with higher substrate temperatures.

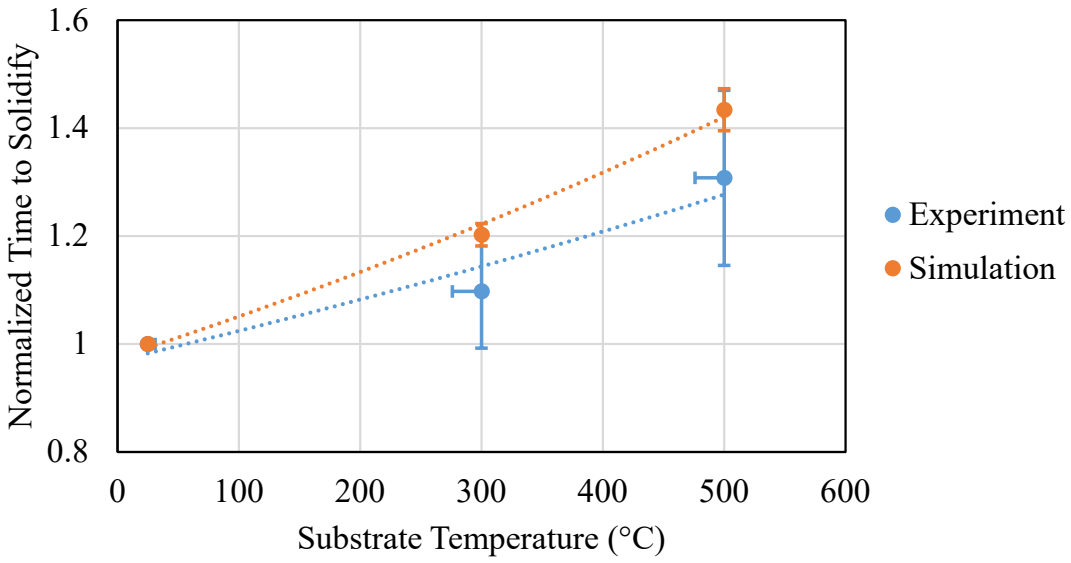

Figure 6-44: Experimental and simulation results for normalized time to solidify for a range of power-velocity combinations at different substrate temperatures. An exponential best fit line is shown for each data set for reference. The error bars in the *Y* direction are one standard deviation on the mean. The error bars in *X* direction are the range of temperatures measured from section 3.2.4.

The error bars between the experimental and simulation data in Figure 6-44 overlap, though the average change seen in the experimental data is lower than what conduction based simulations would predict, meaning that simulations are likely overestimating the time required for a melt pool to solidify as the substrate temperature is increased. This is likely due to the omission of fluid flow within the melt pool in simulations, therefore overestimating the effect of thermal gradients on conduction into the substrate.

One noteworthy result of looking at the melt pool as the beam turns off is that in some large melt pools, the shape of the plume changes after the beam is turned off, as can be seen in Figure 6-45. This is likely due to the melt pool cavity changing shape after the beam turns off. When the beam is on, there is a jet of hot, fast moving liquid moving from under the beam toward the back of the melt pool due to recoil pressure and surface tension gradients [40]. When the beam turns off, the driving force for this jet is removed, allowing the liquid that was bunched toward the back of the melt pool to fall back toward the front of the melt pool, making a more circular spot. The result is a short time where there is a more vertically formed plume (or better aligned with the camera axis) while the cavity is still very hot and before the plume dissipates as the liquid cools. This phenomenon is most evident at +100 μs in Figure 6-45. From section 5.3.4, however, it is clear that the liquid does not fully fill in the cavity under the beam spot, so there must not be enough liquid available to flow back into the cavity after the beam is turned off.

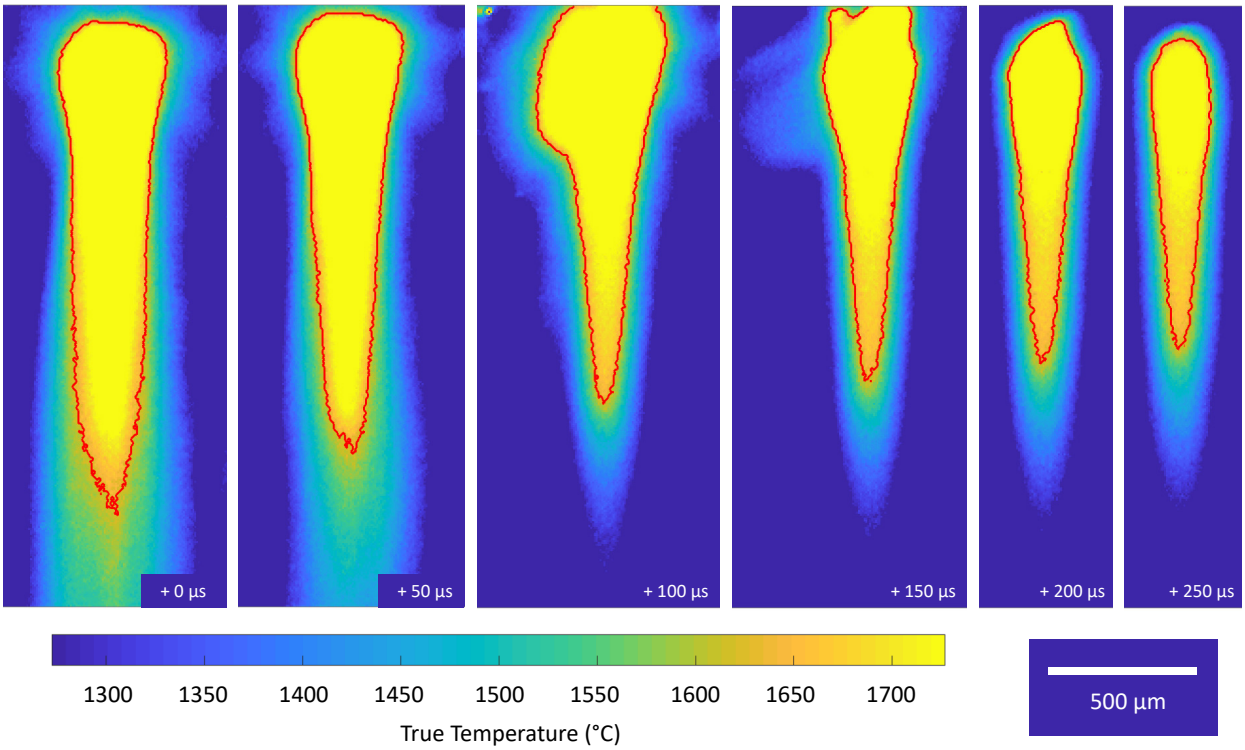

Figure 6-45: A progression of images for a large melt pool (250 W, 800 mm/s, 35 °C substrate temperature) showing the direction change of the plume after the beam is turned off.

6.3.6 Melt Pool Emission Variations during a Raster Stripe

It is possible to use the information from the previous experiments in this chapter to determine the thermal gradients seen during the generation of the stripe described in section 5.3.3. Because of the fixed field of view camera, only a portion of that stripe is visible. The camera is oriented, as seen in Figure 6-46, such that one side of the stripe is visible, meaning that the beam turn on and turn off of single beads are visible. This allows for an analysis of the time for the melt pool to solidify and the thermal gradients at the tail of the melt pool for all even numbered passes as the stripe is built up. The data is taken at only 6,400 Hz to have as large a field of view as possible, however, meaning that each frame is separated by 156 µs. This precludes an analysis of the time to solidify because the temporal resolution is not fine enough. This same restriction is not

imposed on thermal gradients because of the relatively long time that the thermal gradients will be stable (as noted from section 6.3.5). The data for the nominal parameter set (280 W, 1200 mm/s, 35 °C) from section 6.3.5 is used as the value for the first pass in this stripe because the beam turn off for the first pass in this stripe is not viewed, but is equivalent to the average thermal gradient for the nominal parameter set from section 6.3.5. Figure 6-46 shows an image taken by the high speed camera of the raster after deposition in order to show where the FOV is located. The beam turn on and turn off of interest is at the top of the image.

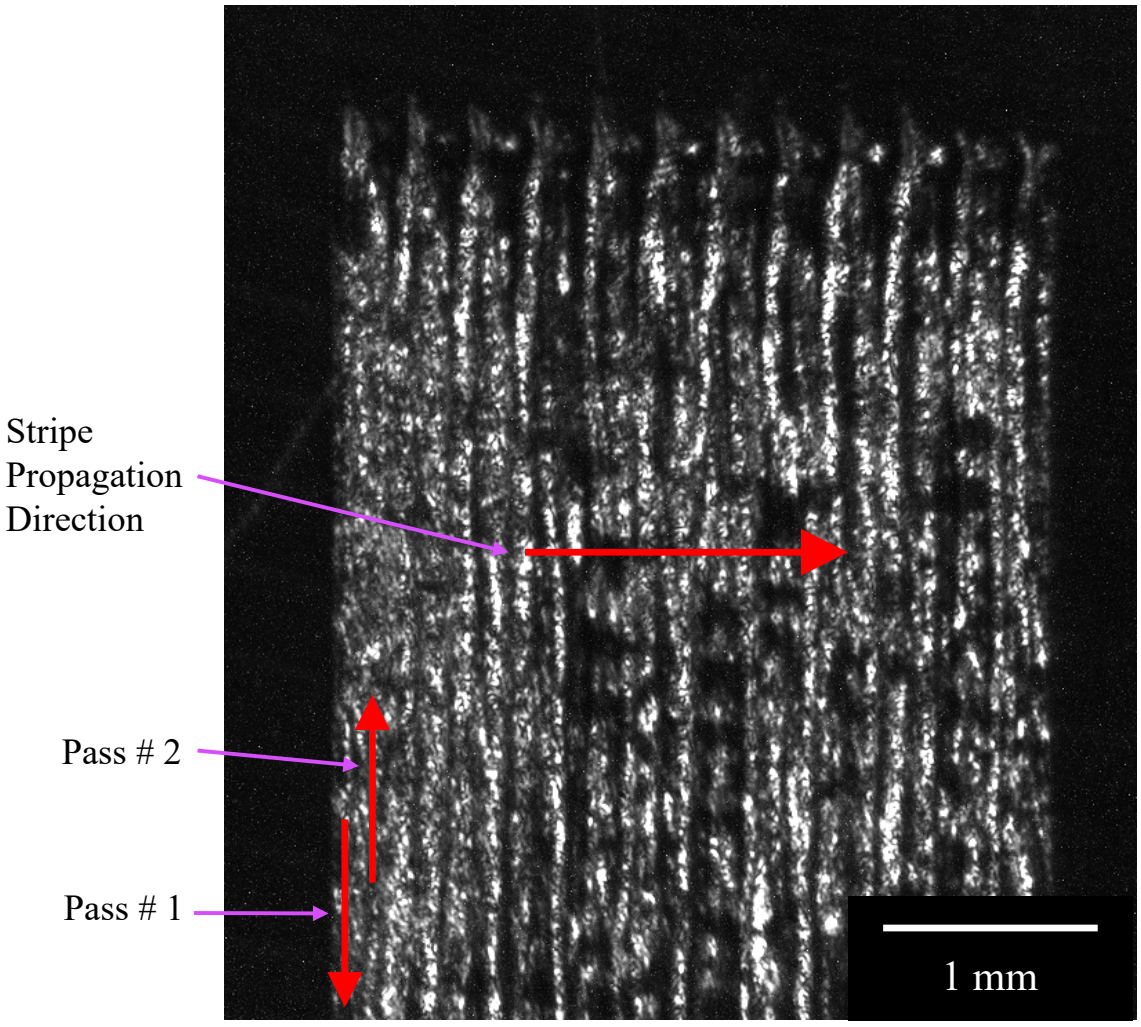

Figure 6-46: A camera image after the stripe is deposited showing the section of the raster within the camera view.

The thermal gradients from the stripe shown in Figure 6-46 are measured according to the procedure outlined in section 6.3.5 (measure the distance required for the temperature to drop from 1620 °C to 1500 °C). Each thermal gradient value is then normalized by the average value found for the single bead analysis for that parameter set. The plot of normalized thermal gradient at the tail of the melt pool for successive passes of the raster stripe is shown in Figure 6-47. It is clear that the thermal gradients decrease quickly and significantly as the raster progresses due to the increased local substrate temperature from previous laser passes.

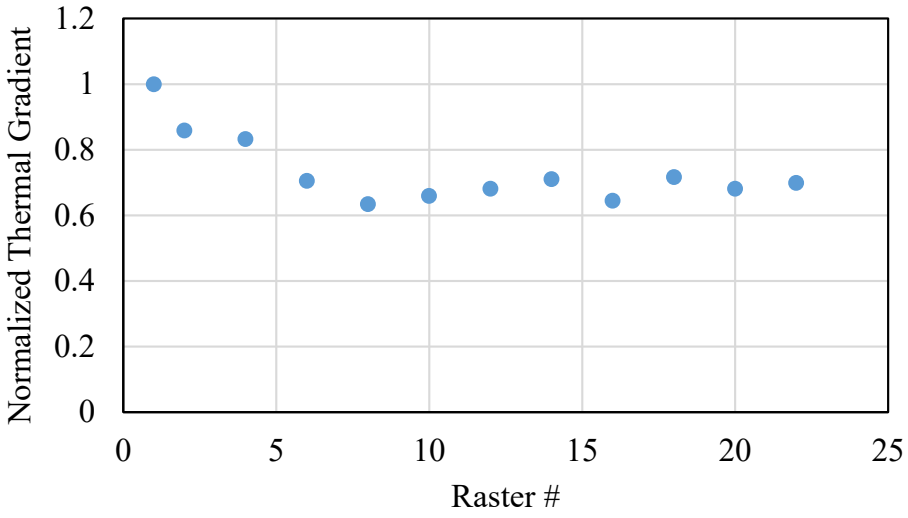

Figure 6-47: The thermal gradients measured for each raster pass in the stripe (labeled raster #), normalized to the value for the first pass.

The best fit curve for simulations from Figure 6-41 can be used convert Figure 6-47 into substrate temperatures during the beam turnaround for that raster pass, and can therefore be compared to the simulated substrate temperatures during a raster from Chapter 5. Figure 6-48 shows the calculated temperatures from the measured thermal gradients as blue dots as well as the range of temperatures calculated from the constant power and velocity simulation for nominal

parameters that was conducted in Chapter 5[88] as an orange overlay. The upper and lower bounds of the orange overlay are the simulated temperatures for an absorptivity of 40% and 80% respectively.

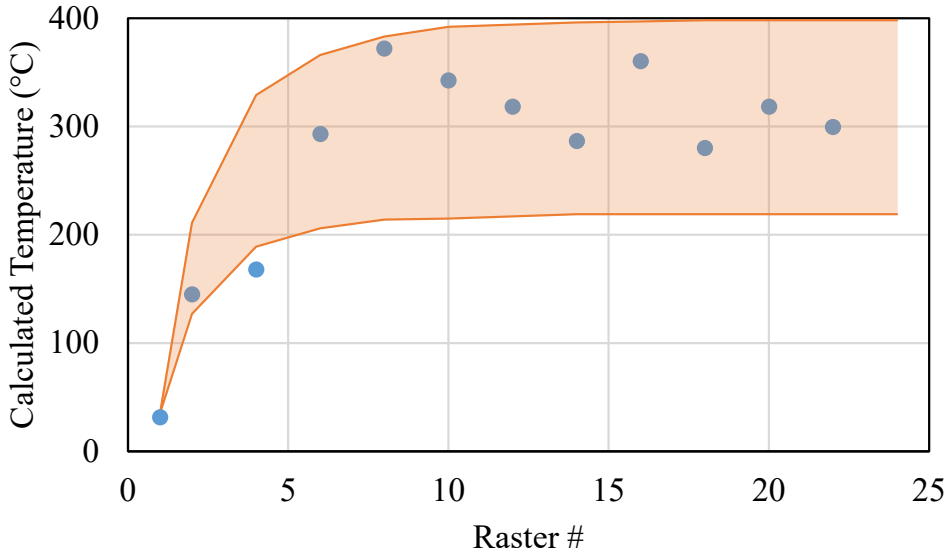

Figure 6-48: Temperatures calculated from the measured thermal gradients for each pass of the stripe (labeled raster #) as well as the range of temperatures predicted from simulations done as part of Chapter 5.

There is good agreement between the experimental data and the simulations, both for the number of raster passes need to get to steady state as well as the steady state temperature at the edge of a raster, meaning that the conduction based simulations discussed in Chapter 5 are a good representation of the local substrate temperatures encountered by the melt pool, even though they are designed to be course and run quickly. This helps validate the analysis in Chapter 5 and shows that an optimized scan strategy can be accurately determined. Figure 6-48 also indicates that the range of actual absorptivity values in Chapter 5 was appropriate. Since the data seems to be close

[88] The particular simulations being referenced are the first iteration for Cases 1 and 2 in section 5.3.3. The temperatures presented here are the same temperatures as were used to generate the expected melt pool depths for Figure 5-25.

to the center of the range, it is likely that the actual absorptivity is also toward the middle of the range (near 0.6, which is in line with literature values for the melt pool cross sectional shape [155]), though further research would be necessary to accurately determine this value.

Finally, Figure 6-48 shows that it is possible to determine the local substrate temperature directly from the melt pool thermal gradients in-situ. While it would also be possible to use a second thermal camera calibrated to a lower temperature range to directly view the local substrate temperatures, space within commercial laser powder bed fusion machines is limited, making it advantageous to use as few sensors as possible to gather the requisite data. In addition, the reason a high speed, visible light camera is chosen for this application is its relatively low price and relatively high frame rate. In order to get high frame rate and high magnification, it is not possible to reduce the temperature range being viewed to any considerable degree[89].

Recall that this same stripe was cross sectioned and analyzed in section 5.3.4. The conclusion from that section was that the variability in the melt pool depth made validation of the simulated substrate temperatures encountered by the melt pool impractical. The use of multiple characterization methods is necessary for this data set due to the complexity of the laser interaction with the material and the significant fluid flows in the melt pool. The ability to validate the methodology developed in Chapter 5 via in-situ melt pool monitoring has the added benefit of being non-destructive, and therefore practical for commercial part production.

[89] The integration time is already long and the optical filter is already passing a wide wavelength range. In order to see lower temperatures, either the integration time would have to be increased significantly or the magnification would need to be reduced significantly. This is because lower temperatures emit less light. Both of these options would detract from the capabilities of the camera system.

6.4 Discussion

While the plume will obscure the melt pool dimensions, useful information can be gleaned from the melt pool emission when no dimensions are available. In addition, a high speed camera takes in so much information that it is difficult and expensive to use it in a real time system. If the sensor were a single pixel instead of the array of pixels used in a camera, the data stream would be multiple orders of magnitude smaller. A single pixel sensor that detects emitted radiation is known as a pyrometer, and is a good tool for non-contact thermography. All spatial information is lost when such a simple sensor is used, but if the information from a pyrometer is adequate, then it is preferred in a control system because it is much less expensive to implement. The thermal data from the single beads conducted at NIST is obtained with a high speed camera, but no spatial information is used in analyzing it, meaning that the same thermal information could be obtained by a simple pyrometer.

This chapter starts with an analysis of what information can be gleaned when no spatial information about the melt pool is used. The term 'total in-band melt pool emission' (or 'melt pool emission') is used to describe all of the thermal emission from the melt pool within a specified wavelength range, requiring that no pixels are over-exposed (saturated). Recorded in this way, the melt pool emission includes the plume and any subsequent reflections, and shows that while the plume seems random and variable, the total emission is fairly stable and follows distinct trends. Unlike findings by Yadroitsev [109] where maximum temperature was almost solely dependent on beam power, this work finds that melt pool emission changes significantly with beam power, beam velocity, and substrate temperature. In addition, the trends seen in total melt pool emission track very well with melt pool cross sectional area, meaning that easily obtainable sensor data can be used as a metric for an important melt pool characteristic that is nearly impossible to directly

measure in-situ, even when melt pool surface dimensions are being obscured by the plume. Melt pool emission, therefore, is a better metric than maximum temperature or melt pool surface area for in-situ monitoring applications.

When spatial information is desired, a visible light, high speed camera can be used to accurately view the thermal emission from Ti64 melt pools on the length and time scales necessary to see plume formation, melt pool dimensions, thermal gradients, and cooling rates. This is important because visible light cameras are considerably less expensive than equivalent infrared cameras, and allow users the ability to use considerably higher performing equipment for relatively low cost.

The high speed camera is successfully calibrated to brightness temperatures between 1150 ˚C and 1600 ˚C. A variety of methods to determine the pixel value for solidification are employed and the most suitable is used to generate a pixel value of 1434 DL. This value, coupled with information about the camera system, yields an emissivity at solidification of roughly 0.37, which matches well with literature values. Using this emissivity value, true temperatures are measured between 1272 ˚C and 1727 ˚C.

The plume and hottest part of the melt pool are shown to have a large effect on the apparent dimensions and thermal gradients within the melt pool. Plume emission and blooming are shown to be the reason that thresholding the melt pool width based off of ex-situ measurements is not successful. In addition, the artificially high pixel intensities caused by the plume and blooming means that it is important to calibrate a thermal camera before use to better understand the data that is being collected. If this were done first in these experiments, the integration time of 1.05 μs would not have been used to collect data when the feature of interest was solidification of Ti64.

The plume is superheated gas or plasma [38] and emits strongly in the wavelengths that the high speed camera system is sensitive to. It is also likely that the plume reflects and scatters some of the light being emitted from the hottest part of the melt pool. The effect of the plume is two-fold. The first is that reflected light illuminates some of the substrate surface, artificially increasing the brightness temperature of that surface. This issue is mitigated somewhat in these experiments, however, because the original substrate is machined and the only raised features are previous melt tracks and machining marks. Strong reflections are generally far enough away from the original melt pool to show up as distinct sources, and can therefore be removed in the same way as spatter (using a connected components analysis [187]). The issue of reflected light may become more important when this method is used with rougher surfaces, such as powder or during part production, due to the proximity of strongly reflecting surfaces and therefore the inability to exclude those reflections from the melt pool. The second adverse effect of the plume is that it emits enough light to obscure the lower temperature thermal emission (around solidification), especially for high power, high velocity melt pools when the vapor cavity geometry is such that the plume is ejected toward the tail of the melt pool [189].

In order to view the top surface of the melt pool unobstructed, the melt pool is imaged when the beam is turned off. The time required for solidification of the melt pool is compared to conduction based simulations and shows that the effect of temperature is not as strong as is predicted, likely due to fluid flows within the melt pool distributing heat more effectively than conduction alone, therefore reducing the effect of lower thermal gradients in the solid material.

The thermal gradients just behind the melt pool are then determined for a user defined steady state time frame from when the plume stopped obscuring the melt pool surface until roughly half way through the melt pool solidification process. The measured thermal gradients show that

conduction based simulations accurately predict the thermal gradient differences induced by changes to substrate temperatures and show that conduction based simulations are accurate once the melt pool has solidified. Comparisons are made in aggregate due to the limited data set available and the relatively high scatter in the data. The lack of sufficient data precludes conclusions from individual process parameter sets.

The ability to see changes in substrate temperature from the thermal gradients at solidification is then attempted based on the results of the single bead experiments. A stripe (the same stripe that was discussed in section 5.3.4) is lazed without powder using the standard scan strategy and parameter set for Ti64 in the EOS M290 for two purposes: 1) determine if the temperature information generated by the methodology developed in Chapter 5 is accurate and 2) determine if substrate temperature can be determined from thermal gradients behind the melt pool if power and velocity are held constant. Using the measured difference in thermal gradients induced by temperature from single beads, temperatures are calculated at the ends of each raster pass within the stripe. These calculated temperatures match very well with simulations, both in terms of the number of raster passes necessary to reach a steady state and the substrate temperatures encountered by the melt pool. This validates the simulations discussed in Chapter 5 and shows that temperatures can be determined in a feed forward manner, and therefore accounted for in a control system.

Chapter 7 – Conclusions

7.1 Summary

It is important to characterize the response of a material to increases in temperature and understand the advantages and disadvantages of allowing or forcing that temperature to be outside the nominal ranges for the processes being studied. Due to the variability seen in the powder bed processes, it is also important to be able to monitor parts on various time and size scales in order to ensure part quality and generate optimized process parameter sets. This work presents a body of knowledge, methodologies, and monitoring techniques that can be used as the basis for both feed forward and feedback control systems in powder bed processes. This work investigates the effect of part temperature on resultant part outcomes due to the lack of prior work on this topic.

Chapter 2 shows that there is sufficient time between layers in the EBM process to allow temperature variability induced by deposition to disappear before the start of the subsequent layer. Therefore, the focus of a thermal feedback control strategy for EBM should be on measuring average surface temperature of the deposited material instead of trying to constrain surface temperatures to be constant across a single layer. A relationship between substrate temperature and melt pool cross sectional area for Ti64 is presented for the EBM process based on finite element thermal modelling of the melt pool and verified using single bead experiments. The finite element models are then used to understand the relationship between substrate temperature and solidification cooling rate. The relationship discovered in this work is used to generate a feedback control strategy that adjusts powers in order to constrain prior beta grain widths to remain constant throughout the height of an EBM build, even as the surface of the part increases in temperature throughout the height of the build. Prior beta grain widths are held constant throughout the height

of cylinder builds and the ability to control swelling on the top surface of parts is demonstrated using an automated feedback control strategy utilizing thermal imaging.

The same methodology that is employed in the EBM process is then transferred to the LPBF process for Ti64 in Chapter 3, but because the part bed is not heated significantly in the LPBF process, the analysis focuses on residual stress reduction and the alpha/beta grain morphology instead of the prior beta grain morphology. To understand the effect of substrate temperature in the LPBF process, simulations of the melt pool are completed and a custom heating apparatus that works within the EOS M290 is created to do single bead verification of the resulting relationships. Process maps incorporating power, velocity, and substrate temperature are generated, allowing for the determination of relationships between beam power, melt pool area and aspect ratio. The ability to increase the available processing space while simultaneously increasing the likelihood of a successful build is discussed based on the relationship between melt pool cross sectional area and aspect ratio.

In Chapter 4, an analysis of the effects of increasing substrate temperature in LPBF is extended to full part production. Simple cylindrical specimens are fabricated at a range of temperatures for two target melt pool cross sectional areas to determine the effect of process parameters on part quality. The ability to produce Ti64 parts at elevated temperature with reduced distortion and low porosity is demonstrated. A microstructural characterization shows that parts built at up to 500 ˚C have characteristics similar to the nominal as-built microstructure, but may have some breakdown of the as-deposited martensite during part fabrication. After stress relief, the substrate temperature during deposition (up to 500 ˚C) is shown to have little effect on the alpha grain morphology of the parts. The knowledge gained from this build is then used to build

an industry relevant component at elevated temperature with reduced supports while still maintaining dimensional accuracy, showing the viability of this method for part production.

To this point, only average substrate temperature has been analyzed. Chapter 5 focuses on the local heating resulting from the scan strategy used to fill in an individual layer in the LPBF process. Using the relationship between part temperature and melt pool area generated in Chapter 3, as well as simulations of the increase in temperature associated with a raster scan strategy, a methodology is developed to control melt pool areas during a raster scan strategy. The required power adjustment to keep melt pool cross sectional area constant during a raster stripe is then determined for select cases relevant to Ti64 part production in the EOS M290. The ability to efficiently determine the temperatures throughout a stripe is shown, as is the need to control power during the entire stripe and not just at the edges. This methodology can be easily implemented into a feed forward scan strategy and allow the user to reduce uncertainty in melt pool dimensions during production.

To determine the validity of model predictions without destructive testing, monitoring of the melt pool with high fidelity and at high frequency is necessary. Chapter 6 utilizes a high speed camera to understand the effect of beam power, beam velocity, and substrate temperature on the melt pool. Various methods for determining melt pool dimensions are presented and the characterization of the camera system is completed. The effect of the plume is shown to be significant and the ability to view the melt pool surface is investigated. Finally, an understanding of the time required for a melt pool to solidify and the thermal gradients that can be expected at the tail of the melt pool are presented. The thermal gradients seen in-situ are compared to model predictions and help validate the temperature fields generated in Chapter 5.

7.2 Implications

The temperature of a part during deposition in PBF processes can have significant effects on resultant part quality, especially when processing near the border of keyholing space due to the possibility of keyholing porosity. These effects can be either advantageous or detrimental depending on whether the temperatures observed are expected and accounted for. Control of temperature has been identified by AM machine manufacturers as an important step in ensuring consistency and part quality, and new products are being developed to give users more temperature history information. The ability to understand the consequences of the information gathered by the available sensors requires an understanding of how temperatures relate to other process parameters and how to account for any temperature changes. This research adds to the body of knowledge concerning how temperatures affect outcomes and can be used as the basis for thermal feed forward and feedback control strategies. Some important implications of this research are presented below.

- The determination of the effects of surface temperature in the EBM process and the development and verification of a feedback control strategy to control solidification microstructure during deposition by controlling solidification cooling rates. This work allows for greater microstructural control during part production and has the added benefit of reducing swelling, allowing users to more easily produce parts with intended properties without having to constrain surface temperatures during production.

- Process mapping of temperature in the LPBF process for Ti64. The ability to generate substrate temperatures of up to 500 ˚C in an EOS M290 is developed in order to verify

simulated trends in melt pool cross sectional area with temperature. The ability to expand processing space and produce more semicircular melt pools is shown and an understanding of how to keep melt pool cross sectional area constant as temperature changes is developed.

- The ability to produce parts at elevated temperature and reduce part distortion without significantly affecting as-built microstructure. Two mechanisms for distortion reduction are discussed (reduction of induced residual stress and the relaxation of residual stress) and the benefit of even small increases in substrate temperature is shown. The reduction in distortion of industry relevant part geometries and the ability to use more easily removable supports shows the utility of increasing substrate temperature during deposition. The similarity in the as-built and stress relieved microstructural development for samples printed at both nominal and elevated temperatures shows that the substrate temperature at deposition will not substantively change the microstructure after heat treatment for Ti64 parts produced at substrate temperatures up to at least 500 °C.

- The development of a multi-scale modelling methodology to determine the temperatures encountered by the melt pool during deposition of a raster stripe in the LPBF process. These temperatures are fed into a model to determine the appropriate beam power at any location within a raster stripe to constrain the melt pool cross sectional area to remain constant, even as substrate temperatures are allowed to vary. This beam power profile can easily be implemented into existing path planning to generate a more uniform melt pool during deposition, increasing the available processing space and reducing the potential for defects.

- The characterization of a high speed, high magnification camera system for the monitoring of the melt pool in LPBF processes. The ability of the camera system to detect solidification and characterize the effects of plume formation on the measurement of melt pool dimensions provides the basis for future monitoring applications and an understanding of the challenges involved with thermal monitoring of the process on the length and time scales over which melt pool dynamics occur. The utility of the system is shown via the verification of model predictions and highlights the differences in the melt pool that occur as local substrate temperature is changed.

- The total in-band thermal emission from the melt pool is shown to vary with power, velocity, and substrate temperature in a similar way to melt pool cross sectional area. Therefore, a simple photodetector can be used to determine melt pool dimensions by utilizing correlations between melt pool cross sectional area and total in-band thermal emission. Eliminating the use of spatial information in the thermal data makes the correlations more easily incorporated into a feedback control system because of the multiple order of magnitude reduction in data acquisition rate afforded by a pyrometer over a camera.

7.3 Future Work

While this research adds significantly to the understanding of the effects of part temperature during deposition in PBF processes, more work is still needed. Several areas for future work are suggested below.

- This work focuses exclusively on Ti64. Future applications should extend the methodologies used in this work to other AM suitable, industry relevant alloys. The particular temperatures of interest and thermal properties will change for different alloys, but the methodologies should still be applicable.

- Better characterization of material properties specifically tailored to additive manufacturing. The determination of material properties such as laser absorptivity within the vapor cavity of a melt pool and temperature and geometry dependence of the material's emissivity at high temperature would allow for future model development, a greater understanding of the physics involved in the process, and more reliable implementation of feed forward path planning algorithms.

- This work shows that the microstructure and hardness for Ti64 parts produced at a substrate temperature of 500 °C should not be considerably different from the nominal substrate temperature as-built parts. Additional characterization of the high temperature as-built Ti64 parts with respect to microstructure, mechanical properties, and chemical composition should be completed to determine what, if any, changes are induced by the increased substrate temperature during deposition.

- Determine the effect of temperature on the keyholing porosity threshold for AM suitable alloys. This work shows that the melt pool aspect ratio and melt pool cross sectional area increase with an increase in substrate temperature for the LPBF process. Future work should identify the keyholing porosity threshold and determine the effect of temperature on this threshold for both Ti64 and other alloys of interest.

- Determine the threshold for part swelling in the EBM process. Part swelling is likely a combination of substrate temperature and power density of the heat source. This work shows that the control of solidification cooling rates can suppress the onset of swelling, but further work is needed to determine the threshold at which swelling occurs and the most efficient ways to avoid it during production.

- Further investigate the thermal radiation emitted by the plume and hottest part of the melt pool. This work shows that the plume and hottest part of the melt pool artificially increase melt pool dimensions and obscure other important features like thermal gradients. This work also shows that the entire in-band thermal emission from the melt pool (including the plume) can be correlated to melt pool dimensions. A greater understanding of the variability in the plume emission and the generation of strategies to mitigate its effect on imaging would allow for considerably better measurement of melt pool surface characteristics during deposition.

References

[1] "Ti6Al4V Titanium Alloy," *Arcam AB*. [Online]. Available: http://www.arcam.com/wp-content/uploads/Arcam-Ti6Al4V-Titanium-Alloy.pdf. [Accessed: 26-Sep-2017].

[2] T. Wohlers and T. Caffrey, "Wohlers Report 2013," Fort Collins, CO, 2013.

[3] H. Yeung, J. Neira, B. Lane, J. Fox, and F. Lopez, "Laser Path Planning and Power Control Strategies for Powder Bed Fusion Systems," in *Solid Freeform Fabrication Proceedings*, 2016, pp. 113–127.

[4] ASTM Standard 52900, "Standard Terminology for Additive Manufacturing," West Conshohocken, PA, 2015.

[5] J. Beuth *et al.*, "Process Mapping for Qualification Across Multiple Direct Metal Additive Manufacturing Processes," in *Solid Freeform Fabrication Proceedings*, 2013, pp. 655–665.

[6] M. Tang, P. Chris Pistorius, and J. L. Beuth, "Prediction of lack-of-fusion porosity for powder bed fusion," *Addit. Manuf.*, vol. 14, pp. 39–48, 2017.

[7] T. DebRoy *et al.*, "Additive manufacturing of metallic components – Process, structure and properties," *Prog. Mater. Sci.*, vol. 92, pp. 112–224, 2018.

[8] K. M. Taminger and R. A. Hafley, "Electron Beam Freeform Fabrication for Cost Effective Near-Net Shape Manufacturing," Hampton, VA, 2006.

[9] F. Wang, J. Mei, and X. Wu, "Microstructure study of direct laser fabricated Ti alloys using powder and wire," *Appl. Surf. Sci.*, vol. 253, pp. 1424–1430, 2006.

[10] I. Gibson, D. Rosen, and B. Stucker, *Additive Manufacturing Technologies*, 2nd Editio. Verlag New York: Springer, 2015.

[11] M. Seifi, M. Dahar, R. Aman, O. Harrysson, J. Beuth, and J. J. Lewandowski, "Evaluation of Orientation Dependence of Fracture Toughness and Fatigue Crack Propagation Behavior of As-Deposited ARCAM EBM Ti-6Al-4V," *JOM*, vol. 67, no. 3, pp. 597–607, 2015.

[12] L. Parry, I. A. Ashcroft, and R. D. Wildman, "Understanding the effect of laser scan strategy on residual stress in selective laser melting through thermo-mechanical simulation," *Addit. Manuf.*, vol. 12, pp. 1–15, 2016.

[13] G. Kasperovich and J. Hausmann, "Improvement of fatigue resistance and ductility of TiAl6V4 processed by selective laser melting," *J. Mater. Process. Tech.*, vol. 220, pp. 202–214, 2015.

[14] M. Donachie, *Titanium: A Technical Guide, Second Edition*. Materials Park, OH: ASTM International, 2000.

[15] O. Hedin, "The Arcam EBM ® process: A walkthrough," Rosemont, IL, 2012.

[16] "Additive Manufacturing Process Software," *EOS GMBH*, 2017. [Online]. Available: https://www.eos.info/systems_solutions/software_data-preparation. [Accessed: 26-Sep-2017].

[17] J. Sieniawski, W. Ziaja, K. Kubiak, and M. Motyka, "Microstructure and Mechanical Properties of High Strength Two-Phase Titanium Alloys," in *Titanium Alloys - Advances in Properties Control*, 2013, pp. 69–80.

[18] T. Ahmed and H. J. Rack, "Phase transformations during cooling in α+β titanium alloys," *Mater. Sci. Eng. A*, 1998.

[19] M. R. Plichta, J. C. Williams, and H. I. Aaronson, "On the Existence of the Beta-Massive Alpha Transformation in Ti-Ag, Ti-Au, and Ti-Si," *Metall. Trans. A*, vol. 8A, pp. 1885–1892, 1977.

[20] J. W. Elmer, T. A. Palmer, S. S. Babu, W. Zhang, and T. DebRoy, "Phase transformation dynamics during welding of Ti–6Al–4V," *J. Appl. Phys.*, vol. 95, no. 12, pp. 8327–8339, 2004.

[21] L. Thijs, F. Verhaeghe, T. Craeghs, J. Van Humbeeck, and J. P. Kruth, "A study of the microstructural evolution during selective laser melting of Ti-6Al-4V," *Acta Mater.*, vol. 58, pp. 3303–3312, 2010.

[22] R. Filip, K. Kubiak, W. Ziaja, and J. Sieniawski, "The effect of microstructure on the mechanical properties of two-phase titanium alloys," *J. Mater. Process. Technol.*, vol. 133, pp. 84–89, 2003.

[23] P. W. Early and S. J. Burns, "Improved Toughness From Prior Beta Grains in Ti-6Al-4V," *Scr. Metall.*, vol. 11, pp. 867–869, 1977.

[24] K. P. Rao, K. Angamuthu, and P. B. Srinivasan, "Fracture toughness of electron beam welded Ti6Al4V," *J. Mater. Process. Technol.*, vol. 9, pp. 185–192, 2007.

[25] D. Rosenthal, "The Theory of Moving Sources of Heat and its Application to Metal Treatments," *Trans. ASME*, pp. 849–866, 1946.

[26] T. W. Eagar and N.-S. Tsai, "Temperature Fields Produced by Traveling Distributed Heat Sources," *Weld. Res. Suppl.*, pp. 346–355, 1983.

[27] M. Boivineau *et al.*, “Thermophysical properties of solid and liquid Ti-6Al-4V (TA6V) alloy,” *Int. J. Thermophys.*, vol. 27, no. 2, pp. 507–529, 2006.

[28] E. Kaschnitz, P. Reiter, and J. L. Mcclure, “Thermophysical Properties of Solid and Liquid 90Ti–6Al–4V in the Temperature Range from 1400 to 2300 K Measured by Millisecond and Microsecond Pulse-Heating Techniques,” *Int. J. Thermophys.*, vol. 23, no. 1, 2002.

[29] J. J. Z. Li, W. L. Johnson, and W. K. Rhim, “Thermal expansion of liquid Ti-6AI-4V measured by electrostatic levitation,” *Appl. Phys. Lett.*, vol. 89, no. 11, pp. 10–12, 2006.

[30] J. Gockel, J. Beuth, and K. Taminger, “Integrated control of solidification microstructure and melt pool dimensions in electron beam wire feed additive manufacturing of Ti-6Al-4V,” *Addit. Manuf.*, vol. 1–4, no. 4, pp. 119–126, 2014.

[31] Z. Francis, “The Effects of Laser and Electron Beam Spot Size in Additive Manufacturing Processes,” Carnegie Mellon University, 2017.

[32] T. Mukherjee, W. Zhang, and T. DebRoy, “An improved prediction of residual stresses and distortion in additive manufacturing,” *Comput. Mater. Sci.*, vol. 126, pp. 360–372, 2017.

[33] M. F. Gouge, J. C. Heigel, P. Michaleris, and T. A. Palmer, “Modeling forced convection in the thermal simulation of laser cladding processes,” *Int. J. Adv. Manuf. Technol.*, vol. 79, pp. 307–320, 2015.

[34] N. Patil *et al.*, “A Generalized Feed Forward Dynamic Adaptive Mesh Refinement and Derefinement Finite Element Framework for Metal Laser Sintering—Part I: Formulation and Algorithm Development,” *J. Manuf. Sci. Eng.*, vol. 137, 2015.

[35] D. Pal *et al.*, “A Generalized Feed-Forward Dynamic Adaptive Mesh Refinement and Derefinement Finite-Element Framework for Metal Laser Sintering—Part II: Nonlinear Thermal Simulations and Validations,” *J. Manuf. Sci. Eng.*, vol. 138, 2016.

[36] J. Romano, L. Ladani, J. Razmi, and M. Sadowski, “Temperature distribution and melt geometry in laser and electron-beam melting processes – A comparison among common materials,” *Addit. Manuf.*, vol. 8, pp. 1–11, 2015.

[37] I. Yadroitsev, A. Gusarov, I. Yadroitsava, and I. Smurov, “Single track formation in selective laser melting of metal powders,” *J. Mater. Process. Technol.*, vol. 210, pp. 1624–1631, 2010.

[38] J. Zhou, H.-L. Tsai, and P.-C. Wang, “Transport Phenomena and Keyhole Dynamics during Pulsed Laser Welding,” *Trans. ASME*, vol. 128, pp. 680–690, 2006.

[39] Y. S. Lee and W. Zhang, “Mesoscopic Simulation of Heat Transfer and Fluid Flow in Laser Powder Bed Additive Manufacturing,” in *Solid Freeform Fabrication Proceedings*, 2015, pp. 1154–1165.

[40] S. A. Khairallah, A. T. Anderson, A. Rubenchik, and W. E. King, “Laser powder-bed fusion additive manufacturing: Physics of complex melt flow and formation mechanisms of pores, spatter, and denudation zones,” *Acta Mater.*, vol. 108, pp. 36–45, 2016.

[41] M. Courtois *et al.*, “A new approach to compute multi-reflections of laser beam in a keyhole for heat transfer and fluid flow modelling in laser welding,” *J. Phys. D Appl. Phys.*, vol. 46, 2013.

[42] W. J. Seufzer, “Additive Manufacturing Modeling and Simulation: A Literature Review for Electron Beam Free Form Fabrication,” Hampton, VA, 2014.

[43] N. W. Klingbeil, J. L. Beuth, R. K. Chin, and C. H. Amon, “Measurement and Modeling of Residual Stress-Induced Warping in Direct Metal Deposition Processes,” in *Solid Freeform Fabrication Proceedings*, 1998, pp. 367–374.

[44] N. W. Klingbeil, J. W. Zinn, and J. L. Beuth, “Measurement of Residual Stresses in Parts Created by Shape Deposition Manufacturing,” in *Solid Freeform Fabrication Proceedings*, 1997, pp. 125–132.

[45] J. Beuth and N. Klingbeil, “The Role of Process Variables in Laser-Based Direct Metal Solid Freeform Fabrication,” *JOM*, pp. 36–39, 2001.

[46] A. Vasinonta, J. L. Beuth, and M. L. Griffith, “A Process Map for Consistent Build Conditions in the Solid Freeform Fabrication of Thin-Walled Structures,” *J. Manuf. Sci. Eng.*, vol. 123, no. 4, pp. 615–622, 2001.

[47] S. Bontha, N. W. Klingbeil, P. A. Kobryn, and H. L. Fraser, “Effects of process variables and size-scale on solidification microstructure in beam-based fabrication of bulky 3D structures,” *Mater. Sci. Eng. A*, pp. 311–318, 2009.

[48] J. E. Gockel, “Integrated Control of Solidification Microstructure and Melt Pool Dimensions in Additive Manufacturing of Ti-6Al-4V,” Carnegie Mellon University, 2014.

[49] E. Soylemez, J. L. Beuth, and K. Taminger, “Controlling Melt Pool Dimensions Over a Wide Range of Material Deposition Rates in Electron Beam Additive Manufacturing,” in *Solid Freeform Fabrication Proceedings*, 2010, pp. 571–582.

[50] H. Gong *et al.*, “Melt Pool Characterization for Selective Laser Melting of Ti-6Al-4V Pre-

alloyed Powder," in *Solid Freeform Fabrication Proceedings*, 2014, pp. 256–267.

[51] C. Montgomery, J. Beuth, L. Sheridan, and N. Klingbeil, "Process Mapping of Inconel 625 in Laser Powder Bed Additive Manufacturing," in *Solid Freeform Fabrication Proceedings*, 2015, pp. 1195–1204.

[52] S. P. Narra, R. Cunningham, J. Beuth, and A. D. Rollett, "Location specific solidification microstructure control in electron beam melting of Ti-6Al-4V," *Addit. Manuf.*, vol. 19, pp. 160–166, 2018.

[53] R. Cunningham, S. P. Narra, T. Ozturk, J. Beuth, and A. D. Rollett, "Evaluating the Effect of Processing Parameters on Porosity in Electron Beam Melted Ti-6Al-4V via Synchrotron X-ray Microtomography," *JOM*, vol. 68, no. 3, pp. 765–771, 2016.

[54] R. Cunningham, S. P. Narra, C. Montgomery, J. Beuth, and A. D. Rollett, "Synchrotron-Based X-ray Microtomography Characterization of the Effect of Processing Variables on Porosity Formation in Laser Power-Bed Additive Manufacturing of Ti-6Al-4V," *JOM*, vol. 69, no. 3, pp. 479–484, 2017.

[55] H. Gong, K. Rafi, H. Gu, T. Starr, and B. Stucker, "Analysis of defect generation in Ti–6Al–4V parts made using powder bed fusion additive manufacturing processes," *Addit. Manuf.*, vol. 1, no. 4, pp. 87–98, 2014.

[56] A. Ladewig, G. Schlick, M. Fisser, V. Schulze, and U. Glatzel, "Influence of the shielding gas flow on the removal of process by-products in the selective laser melting process," *Addit. Manuf.*, vol. 10, pp. 1–9, 2016.

[57] R. Fabbro, K. Hirano, and S. Pang, "Analysis of the physical processes occurring during deep penetration laser welding under reduced pressure," *J. Laser Appl.*, vol. 28, no. 2, 2016.

[58] P. A. Kobryn and S. L. Semiatin, "Microstructure and texture evolution during solidification processing of Ti–6Al–4V," *J. Mater. Process. Technol.*, 2003.

[59] K. Puebla, L. E. Murr, S. M. Gaytan, E. Martinez, F. Medina, and R. B. Wicker, "Effect of Melt Scan Rate on Microstructure and Macrostructure for Electron Beam Melting of Ti-6Al-4V," *Mater. Sci. Appl.*, vol. 3, pp. 259–264, 2012.

[60] A. Klassen, T. Scharowsky, and C. Körner, "Evaporation model for beam based additive manufacturing using free surface lattice Boltzmann methods," *J. Phys. D. Appl. Phys.*, vol. 47, no. 27, 2014.

[61] A. Anam, J. J. S. Dilip, D. Pal, and B. Stucker, "Effect of Scan Pattern on the

Microstructural Evolution of Inconel 625 during Selective Laser Melting," in *International Solid Freeform Fabrication Proceedings*, 2014, pp. 363–376.

[62] R. R. Dehoff *et al.*, "Site specific control of crystallographic grain orientation through electron beam additive manufacturing," *Mater. Sci. Technol.*, vol. 31, no. 8, pp. 931–938, 2015.

[63] J. Raplee *et al.*, "Thermographic Microstructure Monitoring in Electron Beam Additive Manufacturing," *Nat. Sci. Reports*, vol. 7, no. 43554, pp. 1–16, 2017.

[64] A. A. Antonysamy, J. Meyer, and P. B. Prangnell, "Effect of build geometry on the beta-grain structure and texture in additive manufacture of Ti6Al4V by selective electron beam melting," *Mater. Charact.*, vol. 84, pp. 153–168, 2013.

[65] P. Michaleris and A. DeBiccari, "Prediction of Welding Distortion," *Weld. Res. Suppliment*, vol. 76, no. 4, pp. 172–181, 1997.

[66] M. V. Deo and P. Michaleris, "Migration of welding induced buckling distortion using transient thermal tensioning," *Sci. Technol. Weld. Join.*, vol. 8, pp. 49–54, 2003.

[67] H. E. Coules, "Contemporary approaches to reducing weld induced residual stress," *Mater. Sci. Technol.*, vol. 29, no. 1, pp. 4–18, 2013.

[68] N. W. Klingbeil, J. L. Beuth, R. K. Chin, and C. H. Amon, "Residual stress-induced warping in direct metal solid freeform fabrication," *Int. J. Mech. Sci.*, vol. 44, pp. 57–77, 2002.

[69] K. Dai and L. Shaw, "Distortion minimization of laser-processed components through control of laser scanning patterns," *Rapid Prototyp. J.*, vol. 8, no. 5, pp. 270–276, 2002.

[70] A. Vasinonta, J. Beuth, and M. Griffith, "Process Maps for Controlling Residual Stress and Melt Pool Size in Laser-Based SFF Processes," in *Solid Freeform Fabrication Proceedings*, 2000.

[71] E. R. Denlinger, J. C. Heigel, P. Michaleris, and T. A. Palmer, "Effect of inter-layer dwell time on distortion and residual stress in additive manufacturing of titanium and nickel alloys," *J. Mater. Process. Tech.*, vol. 215, pp. 123–131, 2015.

[72] A. J. Dunbar, E. R. Denlinger, M. F. Gouge, T. W. Simpson, and P. Michaleris, "Comparisons of laser powder bed fusion additive manufacturing builds through experimental in situ distortion and temperature measurements," *Addit. Manuf.*, vol. 15, pp. 57–65, 2017.

[73] X. Tan *et al.*, "Graded microstructure and mechanical properties of additive manufactured

Ti6Al4V via electron beam melting," *Acta Mater.*, vol. 97, pp. 1–16, 2015.

[74] L. E. Murr *et al.*, "Microstructures and mechanical properties of electron beam-rapid manufactured Ti-6Al-4V biomedical prototypes compared to wrought Ti-6Al-4V," *Mater. Charact.*, 2009.

[75] E. Rodriguez *et al.*, "Integration of a Thermal Imaging Feedback Control System in Electron Beam Melting," in *Solid Freeform Fabrication Proceedings Proceedings*, 2012, pp. 945–961.

[76] J. Mireles, C. Terrazas, S. M. Gaytan, D. A. Roberson, and R. B. Wicker, "Closed-loop automatic feedback control in electron beam melting," *Int. J. Addit. Manuf. Technol.*, vol. 78, pp. 1193–1199, 2015.

[77] D. Porter, K. Easterling, and M. Sherif, *Phase Transformations in Metals and Alloys*. London: Chapman and Hall, 1981.

[78] F. J. Gil and J. A. Planell, "Behaviour of normal grain growth kinetics in single phase titanium and titanium alloys," *Mater. Sci. Eng. A283*, pp. 17–24, 2000.

[79] L. E. Criales, Y. M. Arısoy, B. Lane, S. Moylan, A. Donmez, and T. Özel, "Laser powder bed fusion of nickel alloy 625: Experimental investigations of effects of process parameters on melt pool size and shape with spatter analysis," *Int. J. Mach. Tools Manuf.*, vol. 121, no. March, pp. 22–36, 2017.

[80] S. Tammas-Williams *et al.*, "XCT analysis of the influence of melt strategies on defect population in Ti-6Al-4V components manufactured by Selective Electron Beam Melting," *Mater. Charact.*, vol. 102, pp. 47–61, 2015.

[81] M. A. Groeber, E. Schwalbach, S. Donegan, K. Chaput, T. Butler, and J. Miller, "Application of characterization, modelling, and analytics towards understanding process-structure linkages in metallic 3D printing," *IOP Conf. Ser. Mater. Sci. Eng.*, vol. 219, 2017.

[82] D. Clymer, J. Cagan, and J. Beuth, "Power–Velocity Process Design Charts for Powder Bed Additive Manufacturing," *J. Mech. Des.*, vol. 139, 2017.

[83] K. Mills, R. Keene, R. Brooks, and A. Shirali, "Marangoni effects in welding," *Phil. Trans. R. Soc. Lond. A*, vol. 356, pp. 911–925, 1998.

[84] U. Gratzke, P. D. Kapadia, J. Dowden, J. Kroos, and G. Simon, "Theoretical approach to the humping phenomenon in welding processes," *J. Phys. D. Appl. Phys.*, vol. 25, pp. 1640–1647, 1992.

[85] W. E. King *et al.*, “Observation of keyhole-mode laser melting in laser powder-bed fusion additive manufacturing,” *J. Mater. Process. Technol.*, pp. 2915–2925, 2014.

[86] R. Rai, J. W. Elmer, T. A. Palmer, and T. Debroy, “Heat transfer and fluid flow during keyhole mode laser welding of tantalum, Ti–6Al–4V, 304L stainless steel and vanadium,” *J. Phys. D. Appl. Phys.*, vol. 40, pp. 5753–5766, 2007.

[87] J. H. Cho, D. F. Farson, J. O. Milewski, and K. J. Hollis, “Weld pool flows during initial stages of keyhole formation in laser welding,” *J. Phys. D. Appl. Phys.*, vol. 42, no. 17, 2009.

[88] C. Zhao *et al.*, “Real-time monitoring of laser powder bed fusion process using high-speed X-ray imaging and diffraction,” *Sci. Rep.*, vol. 7, 2017.

[89] P. S. Wei and T. C. Chao, “The Effects of Entrainment on Pore Shape in Keyhole Mode Welding,” *J. Heat Transfer*, vol. 137, 2015.

[90] M. Pastor, H. Zhao, R. Martukanitz, and T. Debroy, “Porosity, Underfill and Magnesium Loss during Continuous Wave Nd:YAG Laser Welding of Thin Plates of Aluminum Alloys 5182 and 5754,” *Weld. Res. Suppl.*, pp. 207–216, 1999.

[91] J. Norris, C. Robino, D. Hirschfeld, and M. Perricone, “Effects of Laser Parameters on Porosity Formation: Investigating Millimeter Scale Continuous Wave Nd:YAG Laser Welds,” *Weld. J.*, vol. 90, 2011.

[92] F. Verhaeghe, T. Craeghs, J. Heulens, and L. Pandelaers, “A pragmatic model for selective laser melting with evaporation,” *Acta Mater.*, vol. 57, pp. 6006–6012, 2009.

[93] J. Schwerdtfeger, R. F. Singer, and C. Körner, “In situ flaw detection by IR-imaging during electron beam melting,” *Rapid Prototyp. J.*, vol. 18, no. 4, pp. 259–263, 2012.

[94] R. B. Dinwiddie, R. R. Dehoff, P. D. Lloyd, L. E. Lowe, and J. B. Ulrich, “Thermographic In-Situ Process Monitoring of the Electron Beam Melting Technology used in Additive Manufacturing,” *Proc. SPIE*, vol. 8705, pp. 1–9, 2013.

[95] F. Bardin *et al.*, “Closed-loop power and focus control of laser welding for full-penetration monitoring,” *Appl. Opt.*, vol. 44, no. 1, pp. 13–21, 2005.

[96] F. M. Haran, D. P. Hand, C. Peters, and J. D. C. Jones, “Focus control system for laser welding,” *Appl. Opt.*, vol. 36, no. 21, pp. 5246–5251, 1997.

[97] S. Kaierle, “Process Monitoring and Control of Laser Beam Welding: Measuring Quantifiable Data for Improved Processing Results,” *Macro Mater. Process.*, pp. 41–43, 2008.

[98] Y. Kawahito, T. Ohnishi, and S. Katayama, “In-process monitoring and feedback control for stable production of full-penetration weld in continuous wave fibre laser welding,” *J. Phys. D Appl. Phys. J. Phys. D Appl. Phys*, vol. 42, pp. 1–8, 2009.

[99] D. Y. You, X. D. Gao, and S. Katayama, “Review of laser welding monitoring,” *Sci. Technol. Weld. Join.*, 2014.

[100] S. Price, J. Lydon, K. Cooper, and K. Chou, “Experimental Temeprature Analysis of Powder-Based Electron Beam Additive Manufacturing,” in *Solid Freeform Fabrication Proceedings*, 2013, pp. 162–173.

[101] S. Clijsters, T. Craeghs, S. Buls, K. Kempen, and J. P. Kruth, “In situ quality control of the selective laser melting process using a high-speed, real-time melt pool monitoring system,” *Int. J. Adv. Manuf. Technol.*, pp. 1089–1101, 2014.

[102] T. Craeghs, F. Bechmann, S. Berumen, and J. P. Kruth, “Feedback control of Layerwise Laser Melting using optical sensors,” *Phys. Procedia*, vol. 5, pp. 505–514, 2010.

[103] T. Craeghs, S. Clijsters, E. Yasa, F. Bechmann, S. Berumen, and J. P. Kruth, “Determination of geometrical factors in Layerwise Laser Melting using optical process monitoring,” *Opt. Lasers Eng.*, pp. 1440–1446, 2011.

[104] J. P. Kruth, P. Mercelis, J. Van Vaerenbergh, and T. Craeghs, “Feedback control of Selective Laser Melting,” Leuven, Belgium, 2007.

[105] M. L. Vlasea, B. Lane, F. Lopez, S. Mekhontsev, and A. Donmez, “Development of Powder Bed Fusion Additive Manufacturing Test Bed for Enhanced Real-Time Process Control,” *Solid Free. Fabr. Symp.*, pp. 527–539, 2015.

[106] B. Lane *et al.*, “Design, Developments, and Results from the NIST Additive Manufacturing Metrology Testbed (AMMT),” *Solid Free. Fabr. Symp.*, pp. 1145–1160, 2016.

[107] B. Lane, S. Grantham, H. Yeung, C. Zarobila, and J. Fox, “Performance Characterization of Process Monitoring Sensors on the NIST Additive Manufacturing Metrology Testbed,” *Solid Free. Fabr. Symp.*, 2017.

[108] B. Lane, E. Whitenton, and S. Moylan, “Multiple sensor detection of process phenomena in laser powder bed fusion,” vol. 9861, no. May 2016, pp. 1–9, 2016.

[109] I. Yadroitsev, P. Krakhmalev, and I. Yadroitsava, “Selective laser melting of Ti6Al4V alloy for biomedical applications: Temperature monitoring and microstructural evolution,” *J. Alloys Compd.*, pp. 404–409, 2014.

[110] M. Grasso and B. Colosimo, “Process defects and in situ monitoring methods in metal powder bed fusion: a review,” *Meas. Sci. Technol.*, vol. 28, 2017.

[111] B. Lane, S. Moylan, E. P. Whitenton, and L. Ma, “Thermographic measurements of the commercial laser powder bed fusion process at NIST,” in *Solid Freeform Fabrication Proceedings*, 2015, pp. 575–591.

[112] J. C. Heigel and B. M. Lane, “Measurement of the melt pool length during single scan tracks in a commercial laser powder bed fusion process,” in *International Manufacturing Science and Engineering Conference Proceedings*, 2017.

[113] J. C. Heigel and B. M. Lane, “The Effect of Powder on Cooling Rate and Melt Pool Length Measurements Using In Situ Thermographic Tecniques,” *Solid Free. Fabr. Proc.*, 2017.

[114] T. Scharowsky, F. Osmanlic, R. F. Singer, and C. Körner, “Melt pool dynamics during selective electron beam melting,” *Appl. Phys. A*, vol. 114, pp. 1303–1307, 2014.

[115] P. Bidare, R. R. J. Maier, R. J. Beck, J. D. Shephard, and A. J. Moore, “An open-architecture metal powder bed fusion system for in-situ process measurements,” *Addit. Manuf.*, vol. 16, pp. 177–185, Aug. 2017.

[116] P. Bidare, I. Bitharas, R. M. Ward, M. M. Attallah, and A. J. Moore, “Fluid and particle dynamics in laser powder bed fusion,” *Acta Mater.*, vol. 142, pp. 107–120, 2017.

[117] G. Repossini, V. Laguzza, M. Grasso, and B. M. Colosimo, “On the use of spatter signature for in-situ monitoring of Laser Powder Bed Fusion,” *Addit. Manuf.*, vol. 16, pp. 35–48, 2017.

[118] M. Abdelrahman, E. W. Reutzel, A. R. Nassar, and T. L. Starr, “Flaw detection in powder bed fusion using optical imaging,” *Addit. Manuf.*, vol. 15, pp. 1–11, 2017.

[119] L. Scime and J. Beuth, “Anomaly detection and classification in a laser powder bed additive manufacturing process using a trained computer vision algorithm,” *Addit. Manuf.*, vol. 19, pp. 114–126, 2018.

[120] T. Purtonen, A. Kalliosaari, and A. Salminen, “Monitoring and adaptive control of laser processes,” *Phys. Procedia*, pp. 1218–1231, 2014.

[121] G. Tapia and A. Elwany, “A Review on Process Monitoring and Control in Metal-Based Additive Manufacturing,” *J. Manuf. Sci. Eng.*, vol. 136, 2014.

[122] S. K. Everton, M. Hirsch, P. Stravroulakis, R. K. Leach, and A. T. Clare, “Review of in-situ process monitoring and in-situ metrology for metal additive manufacturing,” *Materials and*

Design. 2016.

[123] Arcam AB, "Just Add." [Online]. Available: http://www.arcam.com/wp-content/uploads/justaddbrochure-web.pdf. [Accessed: 27-Sep-2017].

[124] EOS GMBH, "Monitoring of industrial 3D printing processes." [Online]. Available: https://www.eos.info/software/monitoring-software. [Accessed: 27-Sep-2017].

[125] A. Saharan, "Additive Manufacturing : Transitioning from Prototyping to Production," 2017. [Online]. Available: https://www.nfpa.com/NFPA/marchfpic5.pdf. [Accessed: 17-Jan-2018].

[126] E. A. Sharkov, "Black-body radiation," in *Passive Microwave Remote Sensing of the Earth*, Springer-Verlag Berlin Heidelberg, 2003, pp. 203–221.

[127] B. Lane and E. P. Whitenton, "Calibration and Measurement Procedures for a High Magnification Thermal Camera," *Natl. Inst. Stand. Technol.*, 2015.

[128] "The Ultimate Infrared Handbook for Research and Development Professionals," FLIR Systems, Inc., Wilsonville, OR, 2012.

[129] F. Sakuma and S. Hattori, "Establishing a practical temperature standard by using a narrow-band radiation thermometer with a silcon detector," in *Temperature: its measurement and control in science and industry*, New York: AIP, 1982, pp. 421–427.

[130] P. Saunders, "General interpolation equations for the calibration of radiation thermometers," *Metrologia*, vol. 34, pp. 201–210, 1997.

[131] Arcam AB, "Arcam A2X."

[132] J. Mireles, "Process Study and Control of Electron Beam Melting Technology Using Infrared Thermography," University of Texas at El Paso, 2013.

[133] S. S. Al-Bermani, M. L. Blackmore, W. Zhang, and I. Todd, "The Origin of Microstructural Diversity, Texture, and Mechanical Properties in Electron Beam Melted Ti-6Al-4V," *Metall. Mater. Trans. A*, vol. 41A, pp. 3422–3434, 2010.

[134] J. C. Fox, "Transient Melt Pool Response in Additive Manufacturing of Ti-6Al-4V," Carnegie Mellon University, 2015.

[135] A. Klassen, A. Bauereiß, and C. Körner, "Modelling of electron beam absorption in complex geometries," *J. Phys. D. Appl. Phys.*, vol. 47, no. 6, 2014.

[136] D. Dobranich and R. C. Dykhuizen, "Scoping Thermal Calculations of the LENS Process," Livermore, CA, 1998.

[137] “E3-11 - Standard Guide for Preparation of Metallographic Specimens,” West Conshohocken, PA, 2011.

[138] “Buehler SUM-MET - The science Behing Materials Preparation,” USA, 2007.

[139] V. A. Nemchinsky, “The role of thermocapillary instability in heat transfer in a liquid metal pool,” *Int. J. Heat Mass Transf.*, vol. 40, no. 4, pp. 881–891, 1997.

[140] E. Rodriguez, “Development of a Thermal Imaging Feedback Control System in Electron Beam Melting,” University of Texas at El Paso, 2013.

[141] E. Rodriguez, J. Mireles, C. A. Terrazas, D. Espalin, M. A. Perez, and R. B. Wicker, “Approximation of absolute surface temperature measurements of powder bed fusion additive manufacturing technology using in situ infrared thermography,” *Addit. Manuf.*, 2015.

[142] S. Price, B. Cheng, J. Lydon, K. Cooper, and K. Chou, “On Process Temperature in Powder-Bed Electron Beam Additive Manufacturing: Process Parameter Effects,” *J. Manuf. Sci. Eng.*, vol. 136, no. 6, p. 61019, 2014.

[143] S. P. Narra, “Melt Pool Geometry and Microstructure Control Across Alloys in Metal Based Additive Manufacturing Processes,” Carnegie Mellon, 2017.

[144] “E112 - Standard Test Methods for Determining Average Grain Size,” West Conshohocken, PA, 1996.

[145] “EOS M 290 - industrial 3D printed parts from metal materials.” [Online]. Available: https://www.eos.info/eos-m290. [Accessed: 02-Nov-2017].

[146] V. Saphronov, R. S. Khmyrov, and A. V Gusarov, “Experimental and theoretical study of residual deformations and stresses at additive manufacturing by fusion.”

[147] H. Peng *et al.*, “Part-scale model for fast prediction of thermal distortion in DMLS additive manufacturing; Part 2: a quasi-static thermomechanical model.”

[148] “AMS5662N: Nickel Alloy, Corrosion and Heat-Resistant, Bars, Forgings, and Rings,” 2016.

[149] “A564/A564M: Standard Specification for Hot-Rolled and Cold-Finished Age-Hardening Stainless Steel Bars and Shapes,” West Conshohocken, PA, 2013.

[150] “High temp. Substrate-plate heating for SLM 280,” *SLM Solutions*, 2017. [Online]. Available: https://slm-solutions.com/products/machines/selective-laser-melting-machine-slm-280-20. [Accessed: 17-Jan-2018].

[151] F. F. Schmidt and R. A. Wood, “Heat Treatment of Titanium and Titanium Alloys,” 1966.

[152] T. Mukherjee, J. S. Zuback, A. De, and T. Debroy, “Printability of alloys for additive manufacturing,” *Nat. Sci. Reports*, 2015.

[153] R. S. Rosen, R. W. Lowry, and M. E. Kassner, “High Temperature Properties of Alloys Being Considered for Design of a Concentric Canister Launcher,” Livermore, CA, 1998.

[154] *A Designers’ Handbook Series No 9004: High-Temperature Characteristics of Stainless Steels*. Nickel Development Institute.

[155] J. Trapp, A. M. Rubenchik, G. Guss, and M. J. Matthews, “In situ absorptivity measurements of metallic powders during laser powder-bed fusion additive manufacturing,” *Appl. Mater. Today*, vol. 9, pp. 341–349, 2017.

[156] “Iso/TR11146-3:2004 - Lasers and laser-related equipment -- Test methods for laser beam widths, divergence angles and beam propagation ratios -- Part 3: Intrinsic and geometrical laser beam classification, propagation and details of test methods,” Switzerland, 2004.

[157] R. E. Laureijs, J. B. Roca, S. P. Narra, C. Montgomery, J. L. Beuth, and E. R. H. Fuchs, “Metal Additive Manufacturing: Cost Competitive Beyond Low Volumes,” *J. Manuf. Sci. Eng.*, vol. 139, no. 8, p. 81010, 2017.

[158] D. S. Thomas and S. W. Gilbert, “Costs and Cost Effectiveness of Additive Manufacturing A Literature Review and Discussion,” Gaithersburg, MD, 2014.

[159] J.-P. Kruth, J. Deckers, E. Yasa, and R. Wauthlé, “Assessing and comparing influencing factors of residual stresses in selective laser melting using a novel analysis method,” *J. Eng. Manuf.*, vol. 226, no. 6, pp. 980–991, 2012.

[160] L. Scime, “Methods for the Expansion of Additive Manufacturing Process Space and the Development of In-Situ Monitoring Methodologies,” Carnegie Mellon University, 2018.

[161] G. E. Lloyd, “Atomic number and crystallographic contrast images with the SEM: a review of backscattered electron techniques,” *Mineral. Mag.*, vol. 51, pp. 3–19, 1987.

[162] S. A. Speakman, “Basics of X-Ray Powder Diffraction,” 2014. [Online]. Available: http://prism.mit.edu/xray/Basics of X-Ray Powder Diffraction.pdf. [Accessed: 12-Apr-2017].

[163] V. K. Pecharsky and P. Y. Zavalij, *Fundamentals of Powder Diffraction and Structural Characterization of Materials*. New York: Springer Science and Business Media, 2003.

[164] R. Li, L. Riester, T. R. Watkins, P. J. Blau, and A. J. Shih, “Metallurgical analysis and

nanoindentation characterization of Ti–6Al–4V workpiece and chips in high-throughput drilling," *Mater. Sci. Eng. A*, vol. 472, pp. 115–124, 2008.

[165] B. Wysocki, P. Maj, R. Sitek, J. Buhagiar, K. Kurzydłowski, and W. Święszkowski, "Laser and Electron Beam Additive Manufacturing Methods of Fabricating Titanium Bone Implants," *Appl. Sci.*, vol. 7, no. 657, 2017.

[166] R. Li, L. Riester, T. R. Watkins, P. J. Blau, and A. J. Shih, "Metallurgical analysis and nanoindentation characterization of Ti–6Al–4V workpiece and chips in high-throughput drilling," *Mater. Sci. Eng. A*, vol. 472, pp. 115–124, 2008.

[167] B. Wysocki, P. Maj, R. Sitek, J. Buhagiar, K. Kurzydłowski, and W. Święszkowski, "Laser and Electron Beam Additive Manufacturing Methods of Fabricating Titanium Bone Implants," *Appl. Sci.*, vol. 7, no. 657, 2017.

[168] C. Yan, L. Hao, A. Hussein, and P. Young, "Ti – 6Al – 4V triply periodic minimal surface structures for bone implants fabricated via selective laser melting," *J. Mech. Behav. Biomed. Mater.*, vol. 51, pp. 61–73, 2015.

[169] "ASTM E384-11e1 Standard test method for knoop and Vickers hardness of materials," West Conshohocken, 2011.

[170] P. Promoppatum, R. Onler, and S.-C. Yao, "Numerical and experimental investigations of micro and macro characteristics of direct metal laser sintered Ti-6Al-4V products," *J. Mater. Process. Tech.*, vol. 240, pp. 262–273, 2017.

[171] W. Xu *et al.*, "Additive manufacturing of strong and ductile Ti-6Al-4V by selective laser melting via in situ martensite decomposition," *Acta Mater.*, vol. 85, pp. 74–84, 2015.

[172] B. Baufeld, E. Brandl, and O. Van Der Biest, "Wire based additive layer manufacturing: Comparison of microstructure and mechanical properties of Tiâ€"6Alâ€"4V components fabricated by laser-beam deposition and shaped metal deposition," *J. Mater. Process. Tech.*, vol. 211, pp. 1146–1158, 2011.

[173] M. Koike *et al.*, "Evaluation of titanium alloys fabricated using rapid prototyping technologies-electron beam melting and laser beam melting," *Materials (Basel).*, vol. 4, no. 10, pp. 1776–1792, 2011.

[174] L. E. Murr, S. M. Gaytan, E. Martinez, F. Medina, and R. B. Wicker, "Next Generation Orthopaedic Implants by Additive Manufacturing Using Electron Beam Melting," *Int. J. Biomater.*, 2012.

[175] S. Specification, “ASTM B367-06, Standard Specification for Titanium and Titanium Alloy Castings,” West Conshohocken, PA, 2006.

[176] E. Yasa, J. Deckers, T. Craeghs, M. Badrossamay, and J.-P. Kruth, “Investigation on Occurrence of Elevated Edges in Selective Laser Melting,” in *Solid Freeform Fabrication Proceedings*, 2009, pp. 673–685.

[177] H. Kwon, W.-K. Baek, M.-S. Kim, W.-S. Shin, and J. J. Yoh, “Temperature-dependent absorptance of painted aluminum, stainless steel 304, and titanium for 1.07 mm and 10.6 mm laser beams,” *Opt. Lasers Eng.*, vol. 50, pp. 114–121, 2011.

[178] M. Tang, P. C. Pistorius, S. Narra, and J. Beuth, “Rapid Solidification: Selective Laser Melting of AlSi10Mg,” *JOM*, vol. 68, no. 3, 2016.

[179] C. Dunsky, “Process Monitoring in Laser Additive Manufacturing,” *Industrial Laser Solutions*, 2014. [Online]. Available: http://www.industrial-lasers.com/articles/print/volume-29/issue-5/features/process-monitoring-in-laser-additive-manufacturing.html. [Accessed: 17-Jul-2017].

[180] T. Toeppel *et al.*, “3D Analysis in Laser Beam Melting Based on Real-Time Process Monitoring,” *Mater. Sci. Technol. Conf.*, 2016.

[181] L. Nickels, “Improving the QA of 3D-printed parts,” *Met. Powder Rep.*, vol. 71, no. 4, pp. 249–251, 2016.

[182] K. W. Westerberg *et al.*, “Analysis of the E-Beam Evaporation of Titanium and Ti-6Al-4V,” Livermore, CA, 1998.

[183] M. Doubenskaia, M. Pavlov, S. Grigoriev, and I. Smurov, “Definition of brightness temperature and restoration of true temperature in laser cladding using infrared camera,” *Surf. Coat. Technol.*, vol. 220, pp. 244–247, 2013.

[184] “Image Sensor Technical Data,” *Photron USA Inc.*, 2015. [Online]. Available: http://photron.com/wp-content/uploads/2015/11/Mini-AX-REV16.9.29.pdf. [Accessed: 17-Jan-2018].

[185] “Premium Hard-Coated Edgepass Filters,” *Thorlabs Inc.* [Online]. Available: https://www.thorlabs.com/newgrouppage9.cfm?objectgroup_id=6082&pn=FESH0950#7294. [Accessed: 25-Jan-2018].

[186] J. Yang, S. Sun, M. Brandt, and W. Yan, “Experimental investigation and 3D finite element prediction of the heat affected zone during laser assisted machining of Ti6Al4V alloy,” *J.*

Mater. Process. Technol., vol. 210, pp. 2215–2222, 2010.

[187] L. Scime, B. Fisher, and J. Beuth, "Using coordinate transforms to improve the utility of a fixed field of view high speed camera for additive manufacturing applications," *Manuf. Lett.*, Jan. 2018.

[188] S. Krishnan, C. D. Anderson, J. K. R. Weber, P. C. Nordine, W. H. Hofmeister, and R. J. Bayuzick, "Optical Properties and Spectral Emissivities at 632.8 nm in the Titanium-Aluminum System," *Metall. Trans. A*, vol. 24, no. 1, pp. 67–72, 1993.

[189] S. Ly, A. M. Rubenchik, S. A. Khairallah, G. Guss, and M. J. Matthews, "Metal vapor micro-jet controls material redistribution in laser powder bed fusion additive manufacturing," *Sci. Rep.*, vol. 7, no. 1, p. 4085, 2017.

[190] L. Reimer, "Electron Scattering and Diffusion," in *Scanning Electron Microscopy: Physics of Image Formation and Microanalysis*, 2nd Editio., New York: Springer, 1988.

[191] H. K. Rafi, N. V Karthik, H. Gong, T. L. Starr, and B. E. Stucker, "Microstructures and Mechanical Properties of Ti6Al4V Parts Fabricated by Selective Laser Melting and Electron Beam Melting," *J. Mater. Eng. Perform.*, vol. 22, no. 12, pp. 3872–3883, 2013.

[192] T. Bergman, A. Lavine, F. Incropera, and D. DeWitt, *Fundamentals of Heat and Mass Transfer*, 7th ed. Jefferson City: John Wiley and Sons Inc, 2011.

[193] "CCD Spatial Resolution." [Online]. Available: http://www.andor.com/learning-academy/ccd-spatial-resolution-understanding-spatial-resolution. [Accessed: 26-Apr-2018].

[194] A. Baddeley and E. Jensen, *Stereology for Statisticians - Adrian Baddeley, Eva B. Vedel Jensen - Google Books*. Boca Raton, FL: Chapman and Hall, 2004.

[195] X. Zhao *et al.*, "Comparison of the microstructures and mechanical properties of Ti–6Al–4V fabricated by selective laser melting and electron beam melting," *Mater. Des.*, vol. 95, no. December, pp. 21–31, 2016.

[196] H. Watanabe, M. Susa, H. Fukuyama, and K. Nagata, "Phase (Liquid/Solid) Dependence of the Normal Spectral Emissivity for Iron, Cobalt, and Nickel at Melting Points," *Int. J. Thermophys.*, vol. 24, no. 2, 2003.

[197] J. K. R. Weber, S. Krishnan, R. Schiffman, and P. C. Nordine, "OPTICAL AND THERMODYNAMIC PROPERTY MEASUREMENTS OF LIQUID METALS AND ALLOYS," *Adv. Sp. Res*, vol. 11, no. 7, pp. 43–52, 1991.

[198] M. Baron, *Probability and Statistics for Computer Scientists*, 2nd Editio. Boca Raton, FL: Taylor & Francis Group, 2014.

[199] J. A. Dantzig and M. Rappaz, *Solidification*. Boca Raton, FL: EPFL Press, 2009.

Appendix 1: Arcam Single Bead Experimental Parameters and Cross Sectional Areas

Target Substrate Temperature (°C)	Beam Power (W)	Beam Velocity (mm/s)	Cross Sectional Area 1 (µm²)	Cross Sectional Area 2 (µm²)
700	417	500	52740	49207
700	417	800	25202	26641
700	472	500	63725	53337
700	472	800	24789	33156
700	556	500	84621	87820
700	556	800	41716	43539
700	639	500	103280	102391
700	639	800	53816	50160
700	722	500	139726	147946
700	722	800	83695	87506
700	833	500	177562	159000
700	833	800	95134	91382
700	944	500	193215	183386
700	944	800	109039	110661
700	1111	500	212445	208143
700	1111	800	133767	123760
750	417	500	52058	51995
750	417	800	34317	29396
750	472	500	63873	73347
750	472	800	34155	38089
750	556	500	93788	89124
750	556	800	44390	49872
750	639	500	103372	114264
750	639	800	51403	62537
750	722	500	140803	148449
750	722	800	87308	86385
750	833	500	170713	167169
750	833	800	100296	102146
750	944	500	178856	186879
750	944	800	115003	112355
750	1111	500	232878	238772
750	1111	800	133446	140397
800	417	500	61112	61455
800	417	800	35141	34057
800	472	500	77824	71850

800	472	800	33190	33543
800	556	500	99880	98066
800	556	800	46473	50023
800	639	500	113311	114404
800	639	800	59317	60838
800	722	500	158305	161058
800	722	800	89476	87846
800	833	500	189977	180076
800	833	800	102136	102940
800	944	500	205604	220015
800	944	800	117649	117622
800	1111	500	246367	244591
800	1111	800	143383	138267
850	417	500	65263	61158
850	417	800	38372	32937
850	472	500	80760	87536
850	472	800	37297	37605
850	556	500	104073	99440
850	556	800	42890	48806
850	639	500	120819	118953
850	639	800	65602	63897
850	722	500	141930	159863
850	722	800	92003	88121
850	833	500	195039	197781
850	833	800	108360	108951
850	944	500	214922	212617
850	944	800	121521	117514
850	1111	500	242503	254100
850	1111	800	146353	153668

Appendix 2: EOS Single Bead Experimental Parameters and Cross Sectional Areas

Target Substrate Temp. (°C)	Beam Power (W)	Beam Velocity (mm/s)	Average Cross Sectional Area (µm²)	Standard Deviation in Cross Sectional Area (µm²)	Average Width (µm)	Standard Deviation in Width (µm)	Average Depth (µm)	Standard Deviation in Depth (µm)
35	115	500	10748	418	154	2.6	115	4.7
300	115	500	12491	404	166	5.7	131	6.4
500	115	500	14308	377	174	3.4	143	4.6
35	115	800	4487	232	119	3.8	57	2.6
300	115	800	5305	262	127	4.0	63	2.4
500	115	800	5974	247	135	3.3	67	2.6
35	175	800	11239	542	171	6.4	109	4.4
300	175	800	13123	497	178	7.4	120	5.1
500	175	800	14759	456	184	4.1	132	3.2
35	175	1200	5288	162	117	3.3	65	1.8
300	175	1200	6274	258	124	2.8	73	2.0
500	175	1200	7241	254	132	2.7	80	1.7
35	175	1800	3113	96	102	1.3	44	1.2
300	175	1800	3522	117	107	0.9	48	1.7
500	175	1800	4106	115	111	0.8	53	1.4
35	250	800	19831	507	178	4.5	187	5.7
300	250	800	22523	557	188	4.7	204	6.2
500	250	800	25109	640	197	5.9	221	6.5
35	250	1800	5811	176	120	1.9	71	1.7
300	250	1800	6660	189	126	1.7	77	2.2
500	250	1800	7579	204	132	1.4	83	2.4
35	280	1200	12401	350	141	2.1	128	3.1
300	280	1200	14169	367	153	3.5	139	2.7
500	280	1200	16155	647	162	3.6	150	4.7
35	340	1250	15610	437	140	3.4	156	2.8
300	340	1250	18090	432	151	3.6	170	2.9
500	340	1250	19718	558	159	3.8	179	3.9
35	370	1200	18939	751	156	4.5	181	5.3
300	370	1200	22099	486	170	3.5	199	4.3
500	370	1200	24341	402	177	4.0	209	3.8

35	370	1800	10771	239	132	2.0	115	2.4
300	370	1800	12170	264	138	3.0	125	2.5
500	370	1800	13636	308	143	2.4	133	2.8
35	370	2500	6525	199	125	1.9	78	1.8
300	370	2500	7409	193	129	1.8	84	1.9
500	370	2500	8317	212	133	1.9	91	1.9

Appendix 3: NIST Single Bead Experimental Parameters and Cross Sectional Areas

Target Substrate Temperature (°C)	Beam Power (W)	Beam Velocity (mm/s)	Cross Sectional Area (µm²)	Width (µm)	Depth (µm)
35	100	400	1883	112	21
300	100	400	2084	116	24
450	100	400	2449	124	27
35	100	400	2815	131	27
300	100	600	1240	101.5	16
450	100	600	1442	105.5	16
35	100	600	1616	110	19
300	100	600	2010	121	21
450	100	900	668	82	12
35	100	900	827	93	13
300	100	900	925	96	15
450	100	900	1052	99	15
35	100	1200	484	76	9
300	100	1200	547	84	10
450	100	1200	738	89	10
35	100	1200	753	91	11
300	150	400	4687	154	38
450	150	400	4736	158	38
35	150	400	5118	165	43
300	150	400	6097	168	45
450	150	600	3304	138	32
35	150	600	3516	140	32
300	150	600	3972	148.5	35
450	150	600	4310	164	37
35	150	900	1872	119	17
300	150	900	1925	118	18
450	150	900	2427	120	24
35	150	900	3118	137	31
300	150	1200	1392	105	19
450	150	1200	1602	99	18
35	150	1200	1810	110	22
300	150	1200	1925	119	24
450	150	1500	975	80	15

35	150	1500	1173	99	14
300	150	1500	1230	97	16
450	150	1500	1555	109	19
35	200	400	7442	182	53
300	200	400	8097	186	60
450	200	400	8648	197	61
35	200	400	9406	198	64
300	200	600	5418	161	46
450	200	600	5552	167	45
35	200	600	6210	172	48
300	200	600	6940	174	51
450	200	900	3513	143	34
35	200	900	2167	153	19
300	200	900	3802	86	13
450	200	900	4258	152	37
35	200	1200	2098	128	23
300	200	1200	1714	148	22
450	200	1200	2441	129	26
35	200	1200	3349	146	30
300	200	1500	2001	111	21
450	200	1500	1565	144	16
35	200	1500	1832	132	21
300	200	1500	2580	129	28
450	250	600	6920	188	51
35	250	600	6768	223	42
300	250	600	7359	228	43
450	250	600	8642	190	61
35	250	900	4731	153	41
300	250	900	5233	156	43
450	250	900	5357	164	45
35	250	900	5868	158	51
300	250	1200	3314	139	33
450	250	1200	3547	179	29
35	250	1200	3875	152	33
300	250	1200	4377	147	38
450	250	1500	2274	146	21
35	250	1500	2992	140	30
300	250	1500	3329	146	30
450	250	1500	3691	144	33

Appendix 4: EOS Bulky Part Build Conditions List

Cylinder Label (condition # _ parameter letter)	Target Substrate Temperature (˚C)	Power (W)	Velocity (mm/s)	Hatch Spacing (µm)
1_A	35	280	1200	140
1_B	35	280	1200	140
1_C	35	168	690	140
1_D	35	280	2050	90
1_E	35	280	2050	90
1_F	35	168	1200	90
2_A	150	280	1200	140
2_B	150	272	1200	140
2_C	150	162	690	140
2_D	150	280	2050	90
2_E	150	272	2050	90
2_F	150	162	1200	90
3_A	300	280	1200	140
3_B	300	261	1200	140
3_C	300	156	690	140
3_D	300	280	2050	90
3_E	300	261	2050	90
3_F	300	156	1200	90
4_A	500	280	1200	140
4_B	500	238	1200	140
4_C	500	144	690	140
4_D	500	280	2050	90
4_E	500	238	2050	90
4_F	500	144	1200	90

Appendix 5: EOS Melt Pool Time to Solidify at a 35 °C Substrate Temperature

Beam Power (W)	Beam Velocity (mm/s)	Beam Turnaround Time with Skywriting (µs), Group 1	Beam Turnaround Time with Skywriting (µs), Group 2	Beam Turnaround Time without Skywriting (µs), Group 1	Beam Turnaround Time without Skywriting (µs), Group 2
50	200	850	600	530	270
50	500	640	550	310	210
50	1000	600	530	280	200
50	2500	600	530	280	200
50	7000	630	540	280	200
150	200	840	590	510	260
150	500	610	520	280	200
150	1000	590	510	260	190
150	2500	590	520	260	190
150	7000	610	520	260	190
370	200	830	580	510	250
370	500	610	520	280	190
370	1000	580	510	260	190
370	2500	580	500	260	190
370	7000	600	510	250	180

Beam Power (W)	Beam Velocity (mm/s)	Simulated Time for Melt Pool to Solidify at 35 °C Substrate Temperature (µs)*	Simulated Time for Melt Pool to Solidify at 300 °C Substrate Temperature (µs)*	Simulated Time for Melt Pool to Solidify at 500 °C Substrate Temperature (µs)*
50	200	230	290	352
50	500	126	151	184
50	1000	73.66	89.09	107
50	2500	34.78	41.44	49.5
50	7000	-	-	-
150	200	987	1190	1430
150	500	477.1	576.84	681.39
150	1000	267.3	317.68	376.53
150	2500	119.26	141.68	166.32

150	7000	-	-	-
370	200	2280	2760	3310
370	500	1060	1270	1510
370	1000	586.3	693.12	812.8
370	2500	253.44	301.04	355
370	7000	-	-	-

*NOTE: An absorptivity of 40% is used to match simulation to experiment. This means that the beam power used in simulations would have to be multiplied by 2.5 to match the actual beam power.

Appendix 6: NIST Total In-Band Melt Pool Emission

Target Substrate Temperature (°C)	Beam Power (W)	Beam Velocity (mm/s)	Total Melt Pool Emission (DL)	Standard Deviation of Total Melt Pool Emission (DL)
35	150	400	17659	343
35	150	600	10186	504
35	150	900	3916	347
35	150	1200	2046	662
35	150	1500	125	53
35	200	400	45049	652
35	200	600	33337	396
35	200	900	20286	453
35	200	1200	12130	1134
35	200	1500	9893	1161
35	250	600	42681	2847
35	250	900	32890	5158
35	250	1200	20011	3539
35	250	1500	16822	2437
300	150	400	23005	337
300	150	600	12852	211
300	150	900	4977	301
300	150	1200	2299	323
300	150	1500	669	92
300	200	400	48746	467
300	200	600	33445	1903
300	200	900	22037	1508
300	200	1200	13987	1169
300	200	1500	3537	1003
300	250	600	48251	4062
300	250	900	38652	1539
300	250	1200	25894	1361
300	250	1500	21112	1343
500	150	400	27046	303
500	150	600	16536	278
500	150	900	7043	308
500	150	1200	3546	323
500	150	1500	1904	734
500	200	400	52791	819
500	200	600	39856	368

500	200	900	25492	557
500	200	1200	18039	753
500	200	1500	12618	812
500	250	600	66185	3116
500	250	900	45568	958
500	250	1200	33734	1060
500	250	1500	26863	1057

Appendix 7: Temperature Dependent Properties of Ti64

The temperature dependent properties used in the finite element modelling of Ti64 in this work are shown below and are taken from Boivineau et al. [27], Kaschnitz et al. [28], and Li et al. [29]. All intermediate values are linearly interpolated from the data shown. Properties for temperatures outside of the ranges shown are held constant at the value for the maximum or minimum temperature at which properties are available.

Solidus Temperature = 1893 K

Liquidus Temperature = 1927 K

Latent Heat of Fusion = 285,000 J/kg*K

Temperature (K)	Thermal Conductivity (W/m*K)
423	5.72
662	8.51
914	11.69
1105	14.31
1229	16.18
1276	17.11
1375	19.68
1417	20.50
1551	22.47
1716	24.88
1839	26.63
1879	27.23
1902	28.49
2041	30.95
2233	34.29
2650	42.00

Temperature (K)	Heat Capacity (J/(kg*K))
500	650
800	700
1200	720
1400	730
1500	737
1600	752
1700	775
1800	807
1900	848
2000	931
2300	931

Temperature (K)	Density (kg/m³)
300	4470
1000	4390
1200	4370
1400	4340
1600	4310
1800	4270
1893	4250
1927	4120
2000	4110